In Situ Parameter Estimation of a Single-Phase Voltage Source Inverter using Pseudo-Random Impulse Sequence Perturbation

Ian Paul Gerber

Thesis presented in partial fulfilment of the requirements for the degree of Master of Engineering (Electrical) in the Faculty of Engineering at Stellenbosch University.

Supervisors: Dr F. M. Mwaniki, Prof H. J. Vermeulen
Department of Electrical and Electronic Engineering

December 2022

Stellenbosch UNIVERSITY IYUNIVESITHI UNIVERSITEIT

forward together
sonke siya phambili
saam vorentoe

Plagiaatverklaring / *Plagiarism Declaration*

1. Plagiaat is die oorneem en gebruik van die idees, materiaal en ander intellektuele eiendom van ander persone asof dit jou eie werk is.
   Plagiarism is the use of ideas, material and other intellectual property of another's work and to present is as my own.

2. Ek erken dat die pleeg van plagiaat 'n strafbare oortreding is aangesien dit 'n vorm van diefstal is.
   I agree that plagiarism is a punishable offence because it constitutes theft.

3. Ek verstaan ook dat direkte vertalings plagiaat is.
   I also understand that direct translations are plagiarism.

4. Dienooreenkomstig is alle aanhalings en bydraes vanuit enige bron (ingesluit die internet) volledig verwys (erken). Ek erken dat die woordelikse aanhaal van teks sonder aanhalingstekens (selfs al word die bron volledig erken) plagiaat is.
   Accordingly all quotations and contributions from any source whatsoever (including the internet) have been cited fully. I understand that the reproduction of text without quotation marks (even when the source is cited) is plagiarism

5. Ek verklaar dat die werk in hierdie skryfstuk vervat, behalwe waar anders aangedui, my eie oorspronklike werk is en dat ek dit nie vantevore in die geheel of gedeeltelik ingehandig het vir bepunting in hierdie module/werkstuk of 'n ander module/werkstuk nie.
   I declare that the work contained in this assignment, except where otherwise stated, is my original work and that I have not previously (in its entirety or in part) submitted it for grading in this module/assignment or another module/assignment.

Abstract

DC-AC inverters are important in the shift towards renewable energy as they are used to integrate solar and wind power systems with the electrical grid. Inverters influence the power quality and stability of the grid. Inverter-based generation need to adhere to certain power quality and technical requirements. Accurate inverter models and parameters are, therefore, required for the analysis, design and simulation of inverters in grid studies.

In this project, a methodology for estimating inverter model parameters is presented. Various inverter models exist. In this project electromagnetic transient models of inverters are used, as it is allows for the most accurate representation of inverters. Parameter estimation studies are applied to inverters to populate the electromagnetic models with accurate model parameters.

This project makes use of excitation signals to perturb inverters to aid inverter modelling and parameter estimation of inverter parameters. A wideband pseudo-random impulse sequence source is applied to an inverter to characterize the output impedance of the inverter. The pseudo-random impulse sequence signal is a wideband excitation signal that is suitable for system identification and can be used in high-power, high-voltage environments, such as inverter systems. The output impedance of the inverter contains information about the inverter's filter parameters, as well as the control-loop parameters and can subsequently be of great value during parameter estimation studies. The output impedance, as well as the output voltage and current of the inverter are used during parameter estimation to estimate the inverter's filter and controller parameters.

The proposed inverter parameter estimation methodology is first evaluated through two simulation case studies. Parameter estimation is performed on a single-phase, stand-alone inverter with output voltage control to obtain five filter and controller parameters as a first case study. As another case study, seven filter and controller parameters of a single-phase, grid-connected, current-controlled inverter are estimated. An experimental approach is then adopted to estimate five controller parameters for a practical single-phase, stand-alone, current-controlled inverter. The output impedance frequency response of a practical half-bridge inverter is also investigated and non-linearities present in the output impedance are identified.

During this project the output impedance of inverters are characterized in a practically implementable way. This project accurately estimated parameters of inverters *in situ* to aid accurate inverter modelling.

Uittreksel

GS-WS wisselrigters is toenemend belangrik in die skuif vanaf nie-hernubare na hernubare energiebronne, omdat dit gebruik word om wind- en sonplase te integreer met die elektriese netwerk. Wisselrigters beïnvloed die kwaliteit en stabiliteit van die netwerk. Wisselrigter gebaseerde generasie moet tot seker drywing kwaliteite en tegniese vereistes voldoen. Analise, ontwerp en simulasie van wisselrigters is belangrik vir netwerk studies.

In hierdie projek word 'n metode om wisselrigters se parameters te bekom vir akkurate modellering voorgestel. Verskeie modellering tegnieke bestaan vir wisselrigters, in hierdie projek word elektromagnetiese modelle gebruik, omdat dit die mees akkurate voorstelling van 'n wisselrigter is. Parameter bepalings studies word aangewend to wisselrigters om die elektromagnetiese modelle met akkurate parameters te populeer.

Hierdie projek maak gebruik van breëband seine om wisselrigter modellering te verbeter. In hierdie projek word 'n pseudo-lukrake impuls volgorde bron gebruik om 'n wisselrigter se uittree impedansie te karakteriseer. Die pseudo-lukrake impuls volgorde is 'n opwekkingsein wat onlangs voorgestel is. Dit kan in hoë drywing, hoë spanning omgewings gebruik word. Die pseudo-lukrake impuls volgorde is 'n breëband sein wat oor die vermoë beskik om 'n breë frekwensie band op te wek. 'n Wisselrigter se uittree impedansie kan gekarakteriseer word deur 'n pseudo-lukrake impuls volgorde sein aan te wend om die wiselrigter oor 'n wye frekwensie band op te wek. Die uittree impedansie bevat inligting rakende die wisselrigter se filter en beheerder parameters en kan gevolglik doeltreffend gebruik word in parameter bepalings studies. Deur die uittree impedansie, spanning en stroom te gebruik kan die wisselrigter se parameters bepaal word.

In hierdie projek word verskeie wisselrigters uitleggings ondersoek. Die uittree impedansie van die wisselrigters word gevind en gebruik in parameter bepaling studies. Parameter bepaling word toegepas op 'n enkelfase wisselrigter wat die uittree spanning oor 'n alleenstaande las reguleer om vyf beheer en filter parameters te bepaal. Vir 'n ander gevalle studie word sewe beheer en filter parameters van 'n enkelfase, netwerk gekoppelde, stroom beheerde wisselrigter bepaal. 'n Simulink model vir 'n praktiese enkelfase, alleenstaande, stroom beheerde wisselrigter word ook afgelei en die vyf beheer parameters van die wisselrigter word bepaal deur gebruik te maak van praktiese metings. Die uittree impedansie van 'n half-brug wisselrigter word ook ondersoek.

In hierdie projek word die uittree impedansie van wisselrigters op 'n prakties behaalbare wyse gevind. Die projek kry dit reg om die parameters van wisselrigters wat aangeskakel is te bepaal.

Acknowledgements

All the glory to God the Father, the Son and the Holy Spirit.

Great thanks to Doctor Mwaniki, Professor Vermeulen and Mr. Bekker for your technical and academic guidance, keeping me on the right track whenever and so often as I went adrift. Many thanks for your continuous direction and sitting through all the long meetings. Thank you for the opportunity to study a postgraduate degree. Thank you for your patience and guidance with the writing. Thank you for sending us to Prague.

Thanks to Francois du Plessis and Doctor Beukes from the Power Electronics laboratories for their wealth of knowledge regarding inverters and help with obtaining an inverter.

Thanks to Bateljon E222! Daniel Banks, thanks for being a friend. Sorry for all the procrastination and thanks for getting the hang of the HPC, building the PRIS source and always listening to my complaints. Thanks Zandile Moyo for looking after us guys (and feeding us cookies) and always being an instigator of good conversations. Doctor Chantelle van Staden, thank you for your kindness and logistical proficiency.

Paul Gerber, I probably wouldn't have ended up studying this degree, doing what I do if it wasn't for you. Thank you for giving us opportunities that you had to work for so hard. You are my hero and will always be. Moeder, thank you for all your love and phone calls.

My fiancé, Jeanri Nel, thank you for you unconditional love and for being ever present. I'm looking forward to our future together.

Publications

- **2021 56th International Universities Power Engineering Conference (UPEC)**, Paper: *Parameter Estimation of a Ferro-Resonance Damping Circuit using Pseudo-Random Impulse Sequence Perturbations.*
- **2022 22nd International Conference on Environmental and Electrical Engineering (EEEIC)**, Paper: *Parameter Estimation of a Single-Phase Voltage Source Inverter using Pseudo-Random Impulse Sequence Perturbation.*
- *Co-author. **2022 57th International Universities Power Engineering Conference (UPEC)**, Paper: *Synthesis and Characterization of Multi-level Pseudo-Random Sequences as Excitation Signals for System Identification.*

Contents

List of Figures

List of Tables

Nomenclature

Variables and functions

v, V	Voltage
i, I	Current
t	Time
f	Frequency
L	Inductance
C	Capacitance
R	Resistance
Z	Impedance
K	Gain
ω	Angular frequency
s	Laplace operator
$\mathbf{A}$	State matrix
$\mathbf{b}$	Input vector
$\mathbf{c}$	Output vector
d	Feedthrough constant
$\mathbf{V}$	Observability matrix
ρ	Rank of matrix
n	Order of polynomial
G	Audiosusceptibility
Y	Admittance
H	Backcurrent gain

Acronyms and abbreviations

AC	Alternating Current
AHDL	Altera Hardware Description Language
ARMAX	Autoregressive Moving Average with Exogenous
ARX	Autoregressive with Exogenous
AVM	Average-Value Modeling
VSI	Voltage Source Inverter
BJ	Box-Jenkins
BS	Binary Sequence
DC	Direct Current
EDIF	Electronic Design Interchange Format
EMT	Electromagnetic Transient
FPGA	Field Programmable Gate Array
GA	Genetic Algorithm
GPIO	General Purpose Input/Output
GS	Global Search
GUI	Graphical User Interface
HDL	Hardware Description Language
IGBT	Insulated-Gate Bipolar Transistor
LFSR	Linear Feedback Shift Register
MAE	Mean Absolute Error
MSE	Mean Squared Error
MPPT	Maximum Power Point Tracker
NARX	Non-linear Autoregressive with Exogenous
OE	Output Error
PRBS	Pseudo-Random Binary Sequence
PRIS	Pseudo-Random Impulse Sequence
PCB	Printed Circuit Board
PLL	Phase Locked Loop
PE	Parameter Estimation
PS	Particle Swarm
RMS	Root Mean Square

RMSE	Root Mean Squared Error
SE	Squared Error
SI	System Identification
SISO	Single-Input Single-Output
TCL	Tool Command Language
VHDL	Very High-Speed Integrated Circuit Hardware Description Language
XOR	Exclusive Or

Chapter 1

Introduction

1.1. Introduction

This thesis focuses on applying system identification and parameter estimation methodologies on single-phase inverters to aid in accurate inverter modelling. Inverter modelling is essential for power system analysis, for instance, in stability studies, grid integration studies and for simulation purposes [1].

This chapter gives an overview of the project. The project motivation and description section describes the importance of inverter modelling as well as the application of system identification and parameter estimation methodologies on inverters, to obtain inverter parameters. This chapter also explains the objectives of the project and gives a brief layout of the thesis.

1.2. Project Motivation and Description

Inverters are power electronic devices that make use of switching and filtering to convert DC power to AC power. Although the application of inverters are not limited to renewable energy, increased deployment of Voltage Source Inverters (VSIs) are mainly due to the recent development in Renewable Energy Sources (RESs). Inverters are, within the renewable energy sector, used to convert the DC power that is generated by solar panels to AC power to enable integration with the utility grid. Inverters are also utilized in doubly-fed induction and variable-speed synchronous generators that are commonly used in wind turbines. Inverters are used in both residential renewable energy applications and on industrial and utility scale renewable power plants.

The stability of the power system as well as the power quality of the grid is influenced by the rapid increase of inverters within the power system. The impact of inverters on the grid is the subject of several studies [2–5]. Inverter-based generation need to adhere to specific requirements for network integration purposes. These standards address the quality of power delivered by the inverter-based generation [6, 7], as well as technical requirements to maintain safe and functional grid operation [8].

Modelling of inverters is increasingly important within this context [9–13]. The circuit

topologies, control mechanisms and corresponding parameters of inverters are essential for studying, analysing and simulating the electrical utility grid. Customarily, no information regarding the circuit topology and control strategy of inverters are available, as these are protected by the manufacturer [14]. This effectively prohibits system designers and customers to model VSIs in distributed utility networks.

Different inverter modelling approaches exist in literature [15–19]. These can be categorised as parametric and black-box modelling approaches. A parametric modelling approach requires detailed knowledge regarding the operation of the inverter, including its parameters [20]. On the other hand, a black-box model relates the input and output of the inverter by means of a mathematical model and no internal knowledge of the inverter is required [21–27].

Information regarding the low-pass filter topology and filter parameters, the control-loop topology and controller parameters and the non-linearities within the control-loop of an inverter is not necessarily available or accessible for commercial inverters to implement a parametric model [14]. If *a priori* information regarding the switching circuit and filter topologies is not available, it may be determined by visually inspecting the inverter, if the topology or housing allows for inspection. The modulation and control loop are normally controlled digitally. This makes access to the control topology and controller parameters difficult, and parametric inverter modelling without *a priori* information virtually impossible.

If the inverter model topology, modulation scheme and non-linearities are known, filter and control-loop parameters are required. System identification and parameter estimation methodologies can be applied to determine or verify these parameters.

System identification and parameter estimation methodologies typically involve perturbation of the Device Under Test (DUT) using a suitable excitation signal [28]. The response of the DUT as well as its input signals are used to characterize the system. The excitation signal requires suitable time- and frequency domain characteristics to ensure sufficient perturbation of the target system.

The Pseudo-Random Impulse Sequence (PRIS) is a wideband excitation signal consisting of a deterministic series of bipolar impulse waveforms [28]. The signal characteristics can easily be manipulated to suit the system identification experiment. The PRIS source topology is, furthermore, suitable for application in high-voltage, high-power system identification applications [28].

Using the PRIS source to perturb the AC output side of the voltage source inverter allows for practically viable *in situ* measurements. The inverter is able to operate at nominal voltage and current whilst being perturbed, allowing continuous conversion of power. Furthermore, it allows the parameters being estimated and the system under investigation to be determined more accurately due to the inverter operating at almost normal operating conditions with regards to its fundamental frequency voltage and current [29].

Time-domain output waveforms as well as frequency responses can be used during system identification. By using a wideband perturbation source, such as the PRIS, the device under test is excited over a wide frequency band. Subsequently, frequency responses are obtained and can be used during system identification.

This project presents a parametric methodology to characterize and model single-phase inverters. The approach uses a wideband perturbation signal, the PRIS signal, to perturb the AC output of an inverter. The output impedance of an inverter is characterized and subsequently used to determine the filter and controller parameters.

1.3. Project Objectives

As mentioned, this project applies system identification and parameter estimation studies on single-phase voltage source inverters. This section expands on the objectives of the project. The research objectives are:

- *Investigate the use of a customizable pseudo-random impulse sequence excitation source for in situ perturbation of an inverter*: Perturbation is applied during system identification. Whilst perturbing an inverter, perturbation is required to be sufficient to excite all relevant dynamic modes of the system, yet allow the inverter to operate at its nominal values. This project specifically investigates the suitability of PRIS perturbations for voltage source inverters. PRIS perturbation is applied to an inverter, without damaging any inverter components or causing non-linear behaviour.
- *Characterize the output impedance frequency response of an inverter*: Using the wideband PRIS signal, the voltage source inverter is excited over a wide frequency range. Its output impedance frequency response is subsequently estimated.
- *Model a single-phase inverter*: A voltage source inverter is modelled in simulation. An appropriate parametric model is chosen for the voltage source inverter. This model is validated by comparing it to an experimental inverter.
- *Perform system identification and parameter estimation studies on a single-phase voltage source inverter*: System identification and parameter estimation are performed on single-phase inverters to obtain model parameters and accurate model outputs.

1.4. Thesis Structure

This thesis consists of 6 chapters, with the following content:

- **Chapter 1**: The project overview is presented in chapter 1. A high-level description of the project is provided. Furthermore, the rationale and applicability of the project are discussed. Research objectives are presented.

- **Chapter 2**: In chapter 2, a literature review is conducted on the most applicable aspects of the project. Spectral estimation techniques that will be used to characterize the frequency response of inverters are discussed. Wideband excitation signals used to characterize power system equipment are presented. Parameter estimation methodologies and system identification studies implemented on inverters found in literature are discussed.

- **Chapter 3**: Chapter 3 explains the design of the PRIS source used in this investigation. The implementation of the Pseudo-Random Binary Sequence (PRBS) on a Field Programmable Gate Array (FPGA) to control the switching of the PRIS source is discussed. Other hardware choices are presented.

- **Chapter 4**: In chapter 4 two case studies are presented. Two single-phase, full-bridge, feedback-controlled inverters are perturbed and parameter estimation is applied to determine the parameters. The inverters under investigation are idealized, as it makes use of perfect switching, no DC-link capacitor, assumes a stiff DC source and has no deadtime.

- **Chapter 5**: In chapter 5 a practical full-bridge, feedback-controlled, single-phase voltage source inverter is investigated. The inverter is modelled in Simulink. The model is used to perform parameter estimation on a practical inverter using wideband perturbation.

- **Chapter 6**: Chapter 6 discusses the results obtained in this project, presents conclusions and expands on the limitations of this project and possible solutions for these limitations.

- **Appendix A**: In Appendix A, a practical open-loop half-bridge inverter is investigated. The inverter is perturbed experimentally to obtain its output impedance. Various non-linear characteristics are described.

Chapter 2

Literature Review

2.1. Overview

This literature study is divided into six sections. The concept of system identification of power system equipment is introduced, along with system identification studies applied to inverters that is found in literature. Appropriate inverter models are discussed. The parameter estimation process is introduced, including optimization algorithms and objective functions applicable to this project. Perturbation and its use in frequency-domain estimation are explained. Spectral estimation techniques that are used in this investigation are discussed.

2.2. System Identification of Power System Equipment

2.2.1. Overview of System Identification of Power System Equipment

Accurate models are required for power system equipment, such as transformers, motors, generators and inverters, to aid accurate power system analysis and design [30, 31]. System identification aims to construct an accurate mathematical model of power system equipment using measured data [28].

Model parameters may depend on specific operating conditions or change over time due to ageing. Accurate model parameters are thus also important for condition monitoring [32].

System identification studies of power system equipment frequently make use of excitation signals to perturb the target device. These excitation signals are chosen according to their frequency- and time-domain characteristics. The measured input and output signals are subsequently used to populate models using parameter estimation methodologies [28].

Spectral estimation can be used to extract frequency-domain data from measured signals to subsequently use during parameter estimation methodologies [33]. Alternatively, time-domain data can also be used. Various optimization algorithms and techniques exist that can be used during parameter estimation.

2.2.2. System Identification of Voltage Source Inverters

System identification studies applied to voltage source inverters have generally aimed at either populating a parametric model of an inverter, or modelling the inverter as a black-box.

2.2.2.1. Parametric System Identification of Voltage Source Inverters

Various system identification studies in literature aimed to find the parameters of parametric inverter models [34–37], using different perturbation methods and optimization algorithms. These system identification studies perturbed the DC voltage reference [34], introduced a three-phase short-circuit fault [35], disturbed the DC voltage and reactive power references [36] and varied the DC voltage magnitude [37]. All of these studies investigated three-phase systems. Table. 2.1 summarizes these parameter estimation studies. The perturbation techniques used are as follows:

- **DC voltage reference perturbation**: Chang *et al.* [34] performed a parameter estimation study on a photovoltaic inverter. The authors focused on obtaining parameters used in the control-loop of the VSI. The inverter included a DC-DC converter connected to the input, operating as a Maximum Power Point Tracker (MPPT). The DC voltage reference of the inverter was perturbed and a damped least square method was used to estimate the parameters. Four controller gains were estimated, of which the greatest error was 27%. The design of a specific VSI may prohibit the possibility of accessing the reference signal as was done in this study.

- **Three-phase short-circuit fault and disturbing the DC voltage reference**: Zhongqian *et al.* [35] introduced a three-phase short-circuit fault and disturbed the DC voltage reference of an inverter as perturbation. Thereafter, a two-step identification method was used to obtain 4 controller gains and the filter inductor value of a three-phase VSI with errors below 20.5%. To obtain accurate model parameters, *in situ* parameter estimation of a VSI operating under normal conditions is required. Introducing a three-phase short-circuit fault in the VSI may lead to non-linear distortion in the inverter that may prohibit the controller gains and filter parameters to be accurately estimated.

- **DC voltage and reactive power references disturbance**: By disturbing the reference DC voltage and reference reactive power and also using a damped least-squares optimization method, four control loop gains and the filter inductor of a three-phase VSI were estimated by Shen *et al.* [36] with a maximum error of 5.6%.

- **Varying DC voltage**: Dong *et al.* [37] varied the DC voltage and employed a particle swarm optimization method to estimate eight controller gains within 2%

error.

- **Introducing voltage and current transients**: Jiayu *et al.* [38] perturbed the inverter by varying sunlight intensity, causing voltage and current to fluctuate. A least squares optimization algorithm was employed to solve for eight controller and filter parameters.

TABLE 2.1: Summary of the parametric parameter estimations studies found in literature.

Paper Title	Perturbation Method	Frequency/Time-domain data used in Objective Function	Optimization Algorithm	Parameters Estimated	Biggest Error [%]	Experimental Verification
Parameter Identification of Controller for Photovoltaic Inverter Based on L-M Method [34]	Sinusoidal sweep of DC voltage reference	Frequency	Damped Least Squares	Controller	35	No
Two-step method for identifying photovoltaic grid-connected inverter controller parameters based on the adaptive differential evolution algorithm [35]	Three-phase fault and DC voltage reference varied to introduce change in real power	Time	Direct Evolution	Filter and Controller	20.50	Yes
d-q axis decoupling parameter identification strategy for the grid-connected inverter of photovoltaic generation system [36]	DC voltage reference and reference reactive power varied	Time	Damped Least Squares	Filter and Controller	5.60	No
Parameter identification of grid-connected photovoltaic inverter based on adaptive - improved GPSO algorithm [37]	Sunlight intensity and temperature varied to change output current	Time	Particle Swarm	Controller	0.97	No
Modelling of Photovoltaic Grid Connected Generation System Based on Parameter Identification Method [38]	Sunlight intensity varied to introduce transients in voltages and currents	Time	Least Squares	Controller	x	No

2.2.2.2. Critical Discussion of Perturbation Methods used in System Identification Studies

In this project it is assumed that the internal reference signals of the inverter are not accessible during system identification studies. Inverters are generally controlled by a discrete controller. The reference signals are implemented within the controller and are not accessible except by the inverter manufacturer. This means that from the mentioned studies only Dong *et al.* [37] and Jiayu *et al.* [38] applied practically implementable perturbation strategies to the inverter.

The DC input to the inverter can be perturbed by either using an excitation signal or by increasing or decreasing the DC voltage, mimicking a change in irradiation supplied to photovoltaic panels [37, 38]. Some inverters determine the reference output power and subsequent reference currents and voltages required to produce this power based on the DC input. In these cases the DC side could be perturbed by introducing a step-change in the DC voltage or current, subsequently changing the amplitude of the reference signals.

As an alternative to perturbing the DC input side of the inverter, the AC output side can be perturbed. The switching circuit of an inverter produces a modulation voltage. The modulated voltage is filtered by a low-pass filter to filter high-frequency harmonics. Amongst others, the output current and voltage are continuously measured by the digital controller, and could be used to generate the PWM signal supplied to the full-bridge, based on the reference signal supplied to the control loop. Perturbing the controlled output voltage and current would thus perturb not only the time-domain output waveforms, but also the control-loop, if the perturbation technique is sufficient.

In this work, inverters are perturbed at the AC output side by a PRIS perturbation source. The PRIS source is suitable for high-power, high-voltage environments, and can be designed to perturb the AC output of the inverter whilst online.

2.2.2.3. Black-Box System Identification of Voltage Source Inverters

Due to the aforementioned challenges associated with obtaining a parametric model for a commercial VSI [14], studies have also focused on obtaining a black-box model of the VSI. This method was first implemented on DC-DC converters [39–42] and was later extended to VSIs [21–27]. The input to output signals are related with dynamic systems, such as the input admittance, back current gain, audiosusceptibility and output impedance [21], or using non-linear models. Black-box modelling of inverters might be more realistic with regards to the lack of available parametric models of inverters. System identification studies using black-box modelling approaches found in literature include the following:

- Valdivia *et al.* [21] implemented a three-input three-output network to characterize a three-phase voltage source inverter. The dynamic models included in the three-input three-output network included the output impedance, input admittance, back-current gain and audiosusceptibility. The dynamic models were either a transfer function model, Wiener model or polytopic model, described in the DQ domain. For perturbation, output current steps in both the D and Q axis were introduced by a resistive and capacitive load reduction. Furthermore, the DC voltage is stepped by including either a resistor or diodes in series with the input of the inverter and then short-circuiting this resistive or diode network. A method to decouple the unwanted effects of perturbation from the resultant dynamic models were also introduced. The study included experimental results and good correlation between the obtained model and practical measurements were obtained. The results are specific for a specific operating point, i.e. a small-signal model was obtained. Some of the dymanic systems were assumed to be linear, neglecting deadtime.

- The previous methodology was also extended to a large signal black-box model by Guarderas *et al.* [26]. In this paper, small-signal models were combined using weighting functions to model an inverter at multiple operating points. The input

voltage, output voltage, fundamental output frequency as well as the real and reactive power reference are passed to the black-box model. The outputs of the model are the output current and input current. This work was originally published in 2017 and later extended to a journal in 2020.

- A Hammerstein-Wiener black-box model was implemented by Abdelsamad *et al.* [23]. The harmonics of the grid voltage are distorted as perturbation. The investigation focused on the harmonics produced by the inverter.

- Neural Networks were employed by Stender *et al.* [22] to obtain a black-box model for an inverter and induction machine arrangement.

- Ala *et al.* [27] obtained a black-box model to describe the output current of a 700 W SMA inverter if the grid voltage is known. A transfer function was obtained to describe the current to voltage relationship.

- Patcharaprakiti *et al.* [43] compared various models of inverters. This included a Autoregressive with Exogenous (ARX) model, a Box-Jenkins (BJ) model, an Output Error (OE) model, an Autoregressive Moving Average with Exogenous (ARMAX) model, a Non-linear Autoregressive with Exogenous (NARX) model, a Hammerstein-Wiener model, a Hammerstein model and a Wiener model. The study found that a Hammerstein-Wiener model is most accurate. The inverter operated in steady-state.

2.3. Voltage Source Inverter Modelling

The inverters investigated in this project are primarily feedback-controlled, single-phase inverters. These inverters typically consists of a switching circuit, low-pass filter, modulation scheme and a control system, as shown in the block diagram in Fig. 2.1. The inverter is supplied with a DC source. The inverter converts the DC power to AC power to supply a load or the grid.

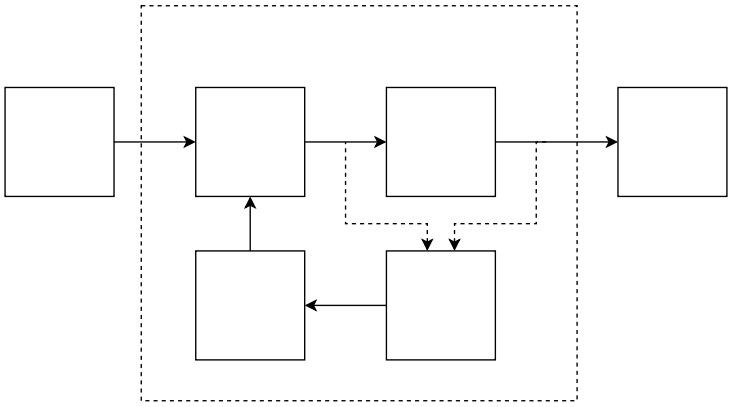

Figure 2.1: Block diagram of a typical voltage source inverter.

To obtain an accurate Electromagnetic Transient (EMT) or parametric model of a single-phase inverter, the following information of an inverter arrangement are typically required:

- *DC source voltage and current input*: This could be solar panels, batteries, a wind-turbine with its output connected to a AC-DC converter or a DC-DC converter.
- *Switching circuit topology*: The switching circuit of a single-phase inverter is typically a half- or full-bridge switching circuit consisting of IGBTs or MOSFETs.
- *Pulse-width modulation scheme*: Different Pulse-Width Modulation (PWM) schemes could be incorporated to control the switching circuit. The modulation scheme generates logic signals to control the switching circuit based on a control signal.
- *Low-pass filter topology and parameters*: A low-pass filter is usually used to filter the modulated voltage created by the switching to a smooth sinusoidal output.
- *Control loop topology and parameters* - Although an inverter can operate as an open-loop system, it is generally required to output a specific voltage and/or current to interface with the grid or load. Feedback control is implemented to maintain certain voltage and current levels. In Fig. 2.2 the continuous plant is controlled by comparing the output signal to a reference signal. The error is fed into the controller. The output of the controller allows the actuator to control the plant and in the case of the inverter, the control signal will be used to control the switches with a PWM scheme.

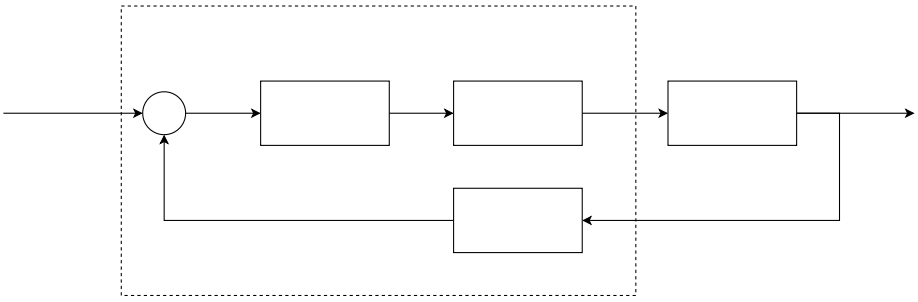

Figure 2.2: Adapted block diagram of the high-level digital control system design [44].

- *Non-linearities of the controls*: Non-linear constraints are added in the control loop for internal and external protection as well as network integration compliance.
- *Load/grid characteristics*: The inverter converts DC power to AC power and dispatches the AC power to a load or into the grid.

Parameter estimation studies aim to populate models of power system equipment with accurate parameter values. Various inverter modelling methodologies and techniques exist.

An applicable model needs to be populated for specific power system studies [45]. Some of the different inverter models are:

- **Electromagnetic transient model**: An Electromagnetic Transient (EMT) model of an inverter, models the inverter as a detailed power electronic device, including all circuitry and digital control into the model [20]. EMT models of inverters are the most accurate way of modelling an inverter, as it is a direct representation of its internal structure. EMT models, however, can only be simulated in software environments, such as Simulink, PLECS, LTspice, etc [46]. EMT models could be computationally complex to execute for inverters. EMT models are used in this project, due to the accuracy of the model.
- **Average model**: Inverters contain non-linear elements that can be modelled as continuous elements using an average modelling approach [47]. The continuous element aims to model the average behaviour of the non-linear element. Average models thus do not include all the information about the system, but only its average representation. Models of systems that contain complex switching can be executed much faster by using an average model. Guha *et al.* [48] implemented an average model for a three-phase voltage source inverter to investigate grid-stability. During this project the average model is used to approximate the output impedance of the inverter.
- **Thévenin/Norton equivalent model**: Inverters could also be modelled as a Thévenin or Norton equivalent [49–53]. A Norton equivalent is especially applicable, as a grid-connected inverter injects current into the grid, while maintaining the grid voltage at the point of coupling. However, a Thévenin or Norton equivalent does not inherently contain switching information, making the model less accurate. Fig. 2.3 shows a Thévenin equivalent inverter connected to the grid, where both the grid and the inverter consists of a Thévenin voltage source and a series output impedance.

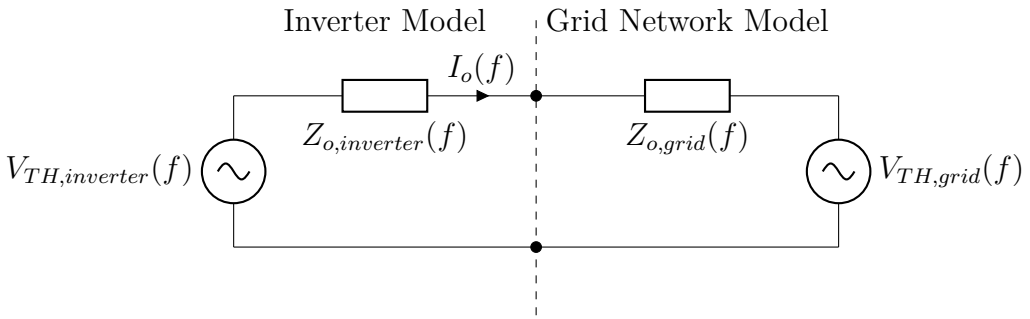

Figure 2.3: The Thévenin representation of an inverter connected to the grid.

- **Black-box model**: Black-box models describes the input-output characteristics of an inverter without any knowledge of the inverter topology, control loop and modulation

scheme. Several black-box models of inverters have been implemented [21–27, 43], and are described in more detail in section 2.2.2.3.

- **Dynamic phasor model**: Periodic waveforms can be described by the Fourier series. During transients, these waveforms are not entirely periodic. In dynamic phasor models the Fourier coefficients are time-variant, as opposed to the time-invariant Fourier coefficients of a normal Fourier series. Dynamic phasor models are thus more suitable to describe the modulation schemes in voltage source inverters [54–58].
- **Switching-function-based model**: Another mathematical model used to describe inverters aim at describing the switching events of the switching bridge [59–61]. Each state of the switch are given a logical high or low and the relationship between circuit elements, the modulation schemes and the switching functions are derived.

2.3.1. Voltage Source Inverter Output Impedance Frequency Response

2.3.1.1. Application of Inverter Output Impedance Frequency Response in Power System Analysis

The characterization of the output impedance frequency response of an inverter is important for power system analysis [62]. The output impedance of inverters is required when investigating the stability of inverters and determining the harmonic contributions of an integrated network.

2.3.1.1.1 Stability of Inverters

Grid-connected inverters are prone to instability. If the grid to which it is connected has a high impedance, the current control loop of the inverter can become unstable, causing instability complications and continuous harmonic resonances [63]. Various methods exist to analyze the stability criteria of grid-connected inverters. Most of these methodologies rely on using the impedance frequency response of the inverter and the grid to determine the stability of the interconnected system [64–67]. The output impedance of the inverter inherently contains information regarding the control loop, i.e. the control loop manifests within the output impedance. Therefore, the control loop can be adjusted to manipulate the output impedance of the inverter [68].

2.3.1.1.2 Harmonic Emissions of Inverter Based Generation

A mixture of Renewable Power Plants (RPPs) and residential inverter systems are increasingly integrated with the utility grid. The inverter systems that feed power into the grid are required to adhere to certain power quality regulations. Various factors are considered

when determining the quality of power supplied, amongst others voltage fluctuations, high-frequency current and voltage harmonics as well as voltage and current unbalances [8]. Harmonic current and voltage emissions can be caused by various power plants or loads connected to the grid. To determine the source of emissions, obtaining the magnitude of the output impedance of inverter-based RPPs at specific frequencies, $|Z_{hc}|$, is vital to determine the source of dominant harmonic emissions [69]. The accumulation of measured voltage-current RMS values of harmonic emissions at the point of coupling on the locus of the grid impedance magnitude at a specific frequency, $|Z_h|$, implies that the RPP is the source of emission and vice versa. Fig. 2.4 displays this approach.

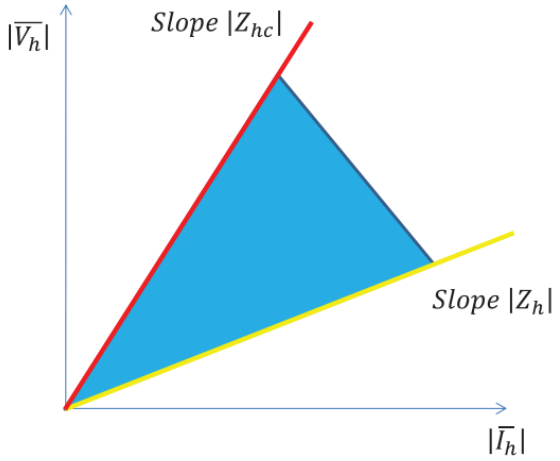

Figure 2.4: The measured RMS voltage-current harmonics are compared to the impedance loci of the inverter based plant and the grid to determine the dominant source of harmonics [69].

2.3.1.2. Determining the Output Impedance of a Voltage Source Inverter

The output impedance of an inverter has been characterized using various different approaches in literature.

- **Average model**: Yoon *et al.* [64] made use of the average switching model to obtain an analytical expression of the output impedance of an voltage source inverter. Fig. 2.5a displays the single-phase representation of the DUT, while Fig. 2.5b shows the magnitude and phase plots of the average switching model output admittance.

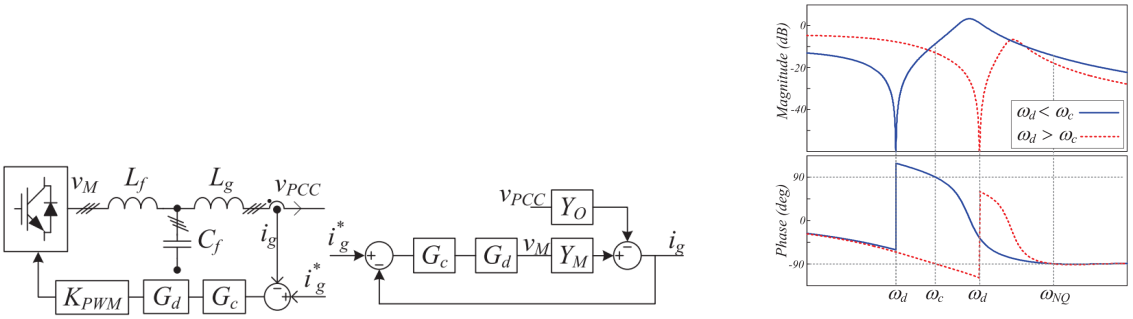

(a) The circuit topology of the inverter alongside its average switching model [64].

(b) Magnitude and phase plots of the output admittance [64].

- **Differential impedance spectroscopy**: Rogalla *et al.* [70] used differential impedance spectroscopy to determine Thévenin equivalent circuits of an inverter. Two different frequency bins were excited during separate measurements. The measurements are then used to cancel out the internal voltage of the device under test.

- **Perturbation**: Output or AC side perturbations of a three-phase inverter were used to analytically describe the output impedance of the voltage source inverter by Cespedes [67]. Analytical expressions were verified with an experimental arrangement that made use of a frequency response analyzer to obtain measurements. The methodology made use of sequence networks.

2.4. Parameter Estimation

2.4.1. Overview

Typically, during the parameter estimation process a mathematical or simulated model is populated with the correct parameters of a measured system. The parameters are estimated by iteratively minimizing the error between the outputs of the model and target system using a suitable optimization algorithm [71]. Time-domain and frequency-domain information of the measured signals can be used during parameter estimation [33].

A block diagram of the parameter estimation process using frequency-domain data is presented in Fig. 2.6. The same input signal, $x(t)$, is applied to the system and the model of the system. The objective function is subsequently calculated by comparing the measured frequency responses of the actual system, $Y_S(\omega)$, with the frequency responses of the model, $Y_M(\omega)$. The optimisation algorithm iteratively updates the model parameters such that the objective function is minimized and the model and system outputs are the same [72].

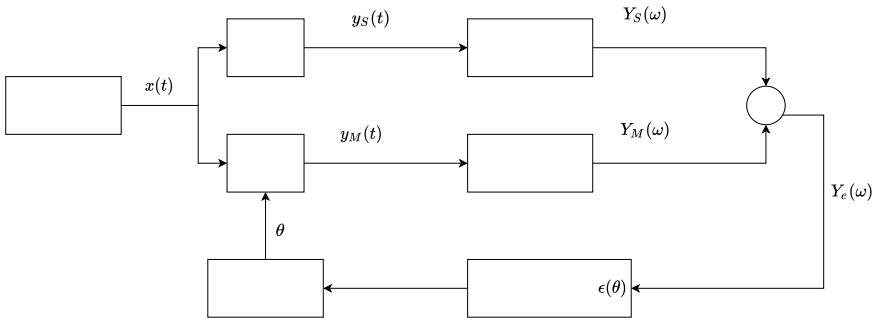

Figure 2.6: Frequency-domain parameter estimation process [72].

A block diagram of the parameter estimation process using time-domain data is shown in Fig. 2.7. Instead of the frequency-domain output being compared in the objective function, the time-domain signals of the actual system, $y_S(t)$, and of the model, $y_M(t)$ are compared.

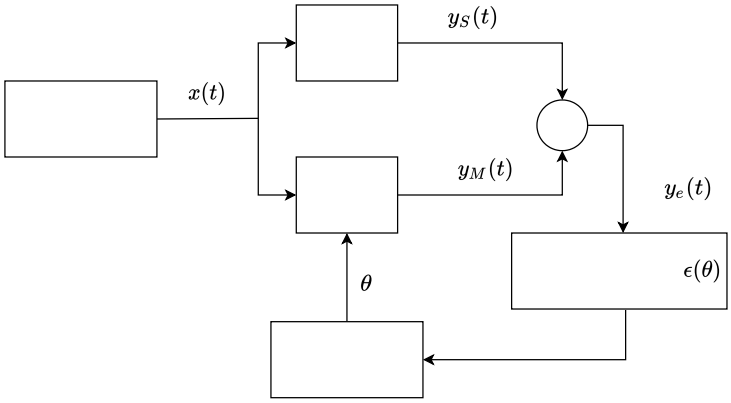

Figure 2.7: Time-domain parameter estimation process [72].

The time- and frequency-domain estimation processes could also be combined by including both time- and frequency-domain information in the objective function.

2.4.2. Objective Function

During parameter estimation an objective function is minimized by the optimization algorithm. The optimization algorithm iteratively changes the parameters of the model. Each set of parameters causes the output of the model to change. For each output an objective function value is calculated to measure its similarity with respect to the output of the system based on the error between the model and the system.

The estimated output of the model, Y_M, and the true output of the system, Y_S, are passed to the objective function. The outputs, Y_S and Y_M, could be a time-domain signal or frequency-domain response of length R. Various different cost functions exist. The objective functions used in this project include:

- **Pearson Correlation**: Pearson correlation, $\rho(Y_M, Y_S)$, can be calculated as [73]

$$\rho(Y_M, Y_S) = \frac{1}{R-1}\sum_{r=1}^{R}(\frac{Y_S - \mu_S}{\sigma_S})(\frac{Y_M - \mu_M}{\sigma_M}), \tag{2.1}$$

where σ_S and σ_M are standard deviations of the system and model respectively and μ_S and μ_M are the means of the system and model outputs [73]. Correlation is a metric that describes the linear dependence between two signals [74, 75].

- **Mean Absolute Error (MAE)**: The MAE objective function sums the absolute error between the system and model outputs and averages it with respect to the number of samples, R [76]:

$$\text{MAE}(Y_S, Y_M) = \frac{1}{R}\sum_{r=1}^{R}|Y_S - Y_M| \tag{2.2}$$

- **Mean Squared Error (MSE)**: The MSE objective function sums the squared error between the system and model outputs and averages it with respect to the number of samples, R [77]:

$$\text{MSE}(Y_S, Y_M) = \frac{1}{R}\sum_{r=1}^{R}(Y_S - Y_M)^2 \tag{2.3}$$

- **Root Mean Squared Error (RMSE)**: The RMSE objective function obtains the square root of the squared error between the system and model outputs which is averaged with respect to the number of samples, R [78]:

$$\text{RMSE}(Y_S, Y_M) = \sqrt{\frac{1}{R}\sum_{r=1}^{R}(Y_S - Y_M)^2} \tag{2.4}$$

2.4.3. Optimization Algorithms

The optimization algorithm iteratively updates the parameters of the model in order to minimize the difference in the estimated and true outputs. An optimization algorithm should effectively search through a large search space, without converging to a local minima to obtain the global minimum of an objective function.

Various different optimization algorithms exist. The following optimization algorithms are utilized in this investigation:

- **Grey wolf optimization**: The Grey Wolf Optimization (GWO) algorithm is a meta-heuristic optimization method mimicking the collaborative hunting methodology of grey wolves. Making use of an hierarchical structure, the algorithm mimics how grey wolves *hunt*, *encircle* and finally *attack* their prey [79, 80].

- **Pattern search optimization**: Pattern search iteratively evaluates the objective function along the dimensions of the parameters. If the objective function value is decreased at a certain point the algorithm creates a new *mesh*. If no better objective function value is achieved the *mesh* shrinks [81, 82].
- **Surrogate optimization**: The surrogate optimization algorithm evaluates a number of points and use these points to approximate a function that it uses to obtain the minimum. This algorithm is not computationally expensive and does not have stopping criteria [83, 84].
- **Genetic algorithm**: The Genetic Algorithm (GA) makes use of a random and brute force approach to obtain the global minima. The GA creates a random initial population inside the upper and lower bounds. Subsequent sequences of populations are created by using the individuals from previous generations. Individuals undergo *selection*, *mutation* and *crossover* to obtain a solution that minimizes the objective function. Individuals can mutate with random changes to its parameters or crossover with other promising individuals to form a new generation [85–87].
- **Particle swarm**: Particle Swarm Optimization (PSO) creates a population of points in the search space, these points are also called particles. These particles move with a specified velocity to a possible minimum to improve their position. The swarm of particles move to the best neighbour and to the best neighbourhood with specific velocities, allowing the swarm to zoom in on the best region over time [88, 89].

2.4.4. Observability

Observability implies that a unique parameter set exists for a system, i.e. a different combination of parameter values will not be able to produce the same output for a specific input. The observability of a system can be determined using a linear state-space model of the system. If the input, $x(t)$, and output, $y(t)$, of a system can be used to determine the initial states of the system, the system is observable [90].

2.5. Perturbation Signals used for System Identification

2.5.1. Overview

During system identification and parameter estimation studies, perturbation is often applied to the device or system under test. Non-parametric frequency-domain techniques require that the system under test is perturbed using an external excitation [91]. This could be accomplished by passive perturbation or an excitation signal [92]. During perturbation the response of the system is captured and used to determine the characteristics of the Device Under Test (DUT) [28]. Perturbation could be mechanical, e.g. increasing the speed

of rotation of a wind turbine, in which case the wind turbine or some system connected to it is the DUT [32]. Perturbation could also be electrical, e.g. changing the load connected to a generator to cause a change in the demand current, in which case the generator is the DUT [93].

Perturbation using an excitation signal is a commonly-used approach of perturbation for power system equipment. Various perturbation signals exist. These include, but are not limited, to the stepped-sine signal, swept-sine/chirp signal, multi-sine signal, random burst signal, impulse excitation signal, pseudo-random noise signal, periodic noise signal, pseudo-random binary sequence, discrete-interval binary sequence and random noise signal [94].

Different types of linear and non-linear systems require different suitable excitation signals [95]. Care must be taken that the voltage and current ratings of the DUT is not exceeded by the perturbation technique. The perturbation technique must also be able to excite all the dynamic modes of the device under test [28].

In case of *in situ* or online perturbation, the DUT is operating continuously while perturbation is applied. *In situ* perturbations are important if the DUT exhibits device specific nature and dependency on the operating point, as is the case with inverters. Careful considerations is required to choose a perturbation technique that is capable of *in situ* measurements for high-power, high-voltage power system equipment [29].

2.5.2. Wideband Excitation Signals

2.5.2.1. Overview

Power system equipment are designed to operate at the fundamental frequency. The ever increasing penetration of renewable energy sources in the utility grid has caused an increase in the higher-frequency harmonics injected into the utility grid [72]. Models of power system equipment, subsequently, need to be accurate over a large range of frequencies [96].

Wideband frequency responses have been used in parameter estimation studies [97–100]. Frequency responses are typically less noisy than time-domain signals, aiding optimization algorithms to find the global minima [101]. While a pure sinusoidal signal concentrates its voltage and current at its fundamental frequency, a wide frequency band can be excited using wideband perturbation signals [94].

2.5.2.2. Swept-Sine Signal

The frequency of a swept-sine signal change with time. The power is distributed over a wide frequency band, as the signal sweeps through all these frequencies. The swept-sine signal can be implemented in practice by making use of an operational-amplifier. A limitation of such a perturbation source is that the bandwidth of the signal is limited by

the specifications of the operational amplifier [102].

The swept sine signal starts with an initial frequency, f_1, and ends with a final frequency, f_2. The signal sweeps between these two frequencies over some period, T_p. The signal, $f(t)$, can be described as

$$f(t) = sin[(\alpha t + \beta)t], \tag{2.5}$$

within some period, $0 \leq t \leq T_p$, where $\alpha = \frac{2\pi(f_2 - f_1)}{T_p}$ and $\beta = 2\pi f_1$ [28].

A swept-sine signal requires a long measurement time for sufficient frequency resolution. A practical swept-sine source requires infinite different signal levels to produce a continuous amplitude range. For these reasons, practical implementation of a swept-sine signal is difficult [103].

2.5.2.3. Pseudo-Random Binary Sequence (PRBS)

A Pseudo Random Binary Sequence (PRBS) is a binary sequence that is generated deterministicly. Its characteristics approximate a random sequence as its logic state at a discrete time *appears* to be independent of any previous state. The logic state changes at multiples of the clock frequency, f_{clk} [104, 105].

A PRBS can be practically implemented with logic circuits. A Linear Feedback Shift Register (LFSR), together with XOR gates that feed outputs from specific bits in the LFSR back to the input of the LFSR can be used to generate a PRBS. The order, m, of the PRBS refers to the number of bits used in the LFSR. A PRBS can be described by a polynomial that describes which bits in the LFSR is fed back via the XOR gates. The total number of bits in a PRBS period is equal to $2^m - 1$. Table 2.2 shows possible PRBS polynomials [106]. Shift registers are practically implemented using flip-flops.

TABLE 2.2: A table of possible PRBS polynomials [106].

m	$h(x)$	m	$h(x)$
2	$x^2 + x + 1$	21	$x^{21} + x^{19} + 1$
3	$x^3 + x^2 + 1$	22	$x^{22} + x^{21} + 1$
4	$x^4 + x^3 + 1$	23	$x^{23} + x^{18} + 1$
5	$x^5 + x^3 + 1$	24	$x^{24} + x^{23} + x^{21} + x^{20} + 1$
6	$x^6 + x^5 + 1$	25	$x^{25} + x^{22} + 1$
7	$x^7 + x^6 + 1$	26	$x^{26} + x^{25} + x^{24} + x^{20} + 1$
8	$x^8 + x^6 + x^5 + x^4 + 1$	27	$x^{27} + x^{26} + x^{25} + x^{22} + 1$
9	$x^9 + x^5 + 1$	28	$x^{28} + x^{25} + 1$
10	$x^{10} + x^7 + 1$	29	$x^{29} + x^{27} + 1$
11	$x^{11} + x^9 + 1$	30	$x^{30} + x^{29} + x^{26} + x^{24} + 1$
12	$x^{12} + x^{11} + x^8 + x^6 + 1$	31	$x^{31} + x^{28} + 1$
13	$x^{13} + x^{12} + x^{10} + x^9 + 1$	32	$x^{32} + x^{30} + x^{26} + x^{25} + 1$
14	$x^{14} + x^{13} + x^{11} + x^9 + 1$	33	$x^{33} + x^{20} + 1$
15	$x^{15} + x^{14} + 1$	34	$x^{34} + x^{31} + x^{30} + x^{26} + 1$
16	$x^{16} + x^{14} + x^{13} + x^{11} + 1$	35	$x^{35} + x^{33} + 1$
17	$x^{17} + x^{14} + 1$	36	$x^{36} + x^{25} + 1$
18	$x^{18} + x^{11} + 1$	37	$x^{37} + x^{36} + x^{33} + x^{31} + 1$
19	$x^{19} + x^{18} + x^{17} + x^{14} + 1$	38	$x^{38} + x^{37} + x^{33} + x^{32} + 1$
20	$x^{20} + x^{17} + 1$	39	$x^{39} + x^{35} + 1$

The PRBS signal has been applied to numerous power system equipment system identification studies, including the following:

- Synchronous generators [32]
- Batteries [107]
- Converter systems [103]
- Transformers [97]
- DC Systems [108]
- Automatic Voltage Regulators [109]

2.5.2.4. Pseudo-Random Impulse Sequence (PRIS)

The Pseudo-Random Impulse Sequence (PRIS) signal is a wideband excitation signal developed by Mwaniki [94]. Fig. 2.8 shows a practical PRIS source, implemented by supplying a H-bridge with a DC voltage and controlling the gating signals of the switches with a PRBS signal. A series RLC circuit is used as filter to create the impulses. The clock frequency of the PRBS gating signal, PRBS order and the series RLC circuit can be configured to manipulate the spectral characteristics of the PRIS signal. The PRIS source topology is suitable for application in high-voltage, high-power system identification applications, as the capacitor allows protection of the source from excess voltages [94].

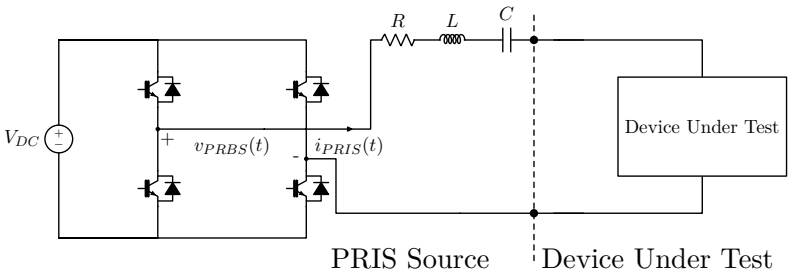

Figure 2.8: Pseudo-random impulse sequence test arrangement to perturb a device under test.

Fig. 2.9 displays a PRIS current consisting of bipolar impulses, enveloped by the PRBS voltage that is supplied as gating signal to the H-bridge.

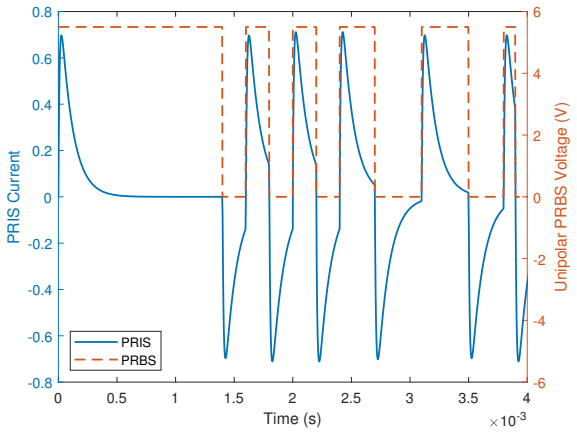

Figure 2.9: Bipolar pseudo-random impulse sequence current and unipolar pseudo-random binary sequence voltage waveforms [72].

An ideal bipolar PRIS can be mathematically described in the time-domain as [94]

$$f^{B}_{PRIS}(t) = \sum_{i=0,2,4}^{((N+1)/2)-1} f_i(t-t_i) f_{p,t_i,t_{i+1}}(t) - \sum_{i=1,3,5}^{((N+1)/2)} f_i(t-t_i) f_{p,t_i,t_{i+1}}(t), \tag{2.6}$$

where

$$f_{p,t_i,t_{i+1}}(t) = u(t-t_i) - u(t-t_{i+1}). \tag{2.7}$$

The logic state of the PRBS source change at multiples of the clock frequency. The time instances at which it changes are pseudo-random. Time instances t_i and t_{i+1} indicates the i^{th} and $(i+1)^{th}$ change in state [94].

A bipolar PRIS can be mathematically described in the frequency-domain as [28]

$$\begin{aligned} F_{PRIS}(\omega) = &\sum_{i=0,2,4}^{((N+1)/2)-1} \frac{A\tau_1\tau_2(\frac{1}{\tau_1}+j\omega) - B\tau_1\tau_2(\frac{1}{\tau_2}+j\omega)}{(1+j\omega\tau_1)(1+j\omega\tau_2)} \\ &- \sum_{i=1,3,5}^{((N+1)/2)} \frac{A\tau_1\tau_2(\frac{1}{\tau_1}+j\omega) - B\tau_1\tau_2(\frac{1}{\tau_2}+j\omega)}{(1+j\omega\tau_1)(1+j\omega\tau_2)}, \end{aligned} \tag{2.8}$$

where

$$A = U[e^{-j\omega t_i} - e^{\frac{t_i}{\tau_2} - t_{i+1}(\frac{1}{\tau_2}+j\omega)}], \tag{2.9}$$

and

$$B = U[e^{-j\omega t_i} - e^{\frac{t_i}{\tau_2} - t_{i+1}(\frac{1}{\tau_1}+j\omega)}]. \tag{2.10}$$

The suitability of the PRIS source in high-power applications is due to the possibility of lower power ratings of the source, as compared to a PRBS source. Fig. 2.10 compares the power losses in the series resistor used in a PRBS and PRIS source. The power losses

in the PRBS source is 10 times more than the power losses in the PRIS source in this case [94].

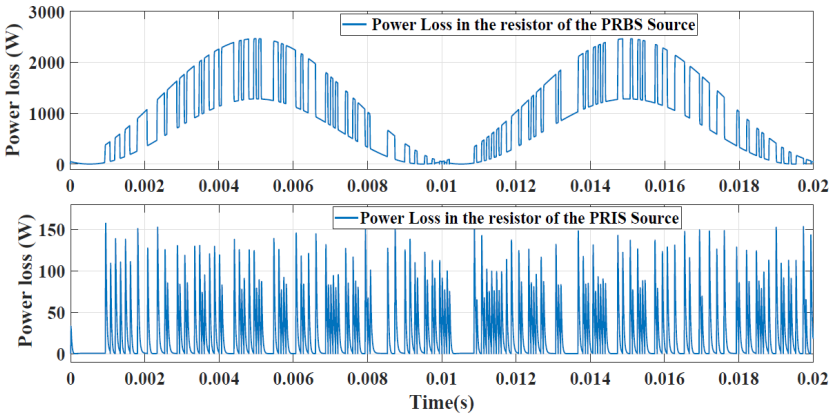

Figure 2.10: Power losses in the resistor of a PRBS and PRIS source [94].

PRIS perturbations has been applied in various system identification studies of power system equipment, including the following:

- Grid Impedance [110]
- Transformers [99, 100]
- Capacitive Voltage Transformers [72, 98]

2.6. Spectral Estimation

Wideband perturbation signals, such as the Pseudo-Random Binary Sequence (PRBS), Pseudo-Random Impulse Sequence (PRIS) and swept-sine signals, excite its target system over a wide frequency bandwidth. This allows the broadband frequency response of the system to be obtained to model power system equipment over this wide frequency band. The input and output signals are captured as time-domain signals and the associated frequency responses are subsequently extracted using spectral estimation.

A time-domain signal or the relationship between time-domain signals can be described with various different approaches in the frequency-domain. These include, but are not limited to the Fourier transform, Fourier series, fast Fourier transform, discrete Fourier transform, energy spectral density and power spectral density.

2.6.1. Power Spectral Density

A Power Spectral Density (PSD) describes the power contained in a time-domain signal over some frequency range [111–113]. The magnitude of the power is normalized with

regards to the frequency resolution or frequency bin size. A PSD is commonly used to describe wideband signals, whereas sinusoidal signals are rather described using the autopower function.

The autocorrelation function, $R_{xx}(\tau)$, of a time-domain real power signal, $x(t)$, is described by [111]

$$R_{xx}(\tau) = \lim_{T\to\infty} \frac{1}{T} \int_{-\infty}^{\infty} x(t)x(t+\tau)d\tau. \tag{2.11}$$

Using (2.11) the PSD, $P_{xx}(f)$, can be calculated as [111]

$$P_{xx}(f) = \int_{-\infty}^{\infty} R_{xx}(\tau)e^{-j2\pi f\tau}d\tau. \tag{2.12}$$

Various estimators can be used to determine the PSD. These estimators can be implemented numerically. Parametric estimators assume that the time-domain signal is a stationary process and include autoregressive models, Yule-Walker estimators, Burg estimators and maximum likelihood estimators. Examples of non-parametric estimators are the periodogram, Bartlett's method, Welch's method, multitaper, singular spectrum analysis and the critical filter theory [111–113].

Various non-parametric estimators, such as Bartlett's method, Welch's method, multitaper and the Blackman-Tukey method are variations of the periodogram. The periodogram makes use of (2.12). Welch's method, on the other hand, segments the input signal into different windows that overlap and determines the average periodogram of these windows [114, 115].

Different types of windows, such as the Hanning, Flattop, Tukey, Blackman, Kaiser and Hamming window, can be used to window the signal. Windowing the signal is necessary to reduce leakage, but does introduce bias [116, 117]. When windowing a signal, a trade-off exists between the bias introduced and the reduction of variance in the estimated frequency response.

2.6.2. Cross Power Spectral Density

The Cross Power Spectral Density (CPSD) compares the power between two signals [118, 119]. The cross-correlation function, $R_{xy}(\tau)$, of two real power signals, $x(t)$ and $y(t)$, can be calculated as [118]

$$R_{xy}(\tau) = \lim_{T\to\infty} \frac{1}{T} \int_{-\infty}^{\infty} x(t)y(t-\tau)d\tau = R_{yx}(-\tau). \tag{2.13}$$

The cross-correlation function, (2.13), could subsequently be used to obtain the CPSD, $P_{xy}(f)$, of these two time-domain signals with the use of [118]

$$P_{xy}(f) = \int_{-\infty}^{\infty} R_{xy}(\tau)e^{-j2\pi f\tau}d\tau. \tag{2.14}$$

The CPSD can be calculated using the same spectral estimators used to determine a PSD, as discussed in section 2.6.1.

2.6.3. Transfer Function or Frequency Response

The PSDs and CPSD of the input, $x(t)$, and output, $y(t)$, time-domain signals of a linear time invariant system could be used to estimate the transfer function of the system, i.e. the frequency response of the Single-Input Single-Output (SISO) system [120].

Two approximations for the transfer function exist [121, 122]. The first estimate uses the CPSD, $P_{yx}(f)$, of the two signals and the PSD of the input signal, $P_{xx}(f)$ [120]:

$$H_1(f) = \frac{P_{yx}(f)}{P_{xx}(f)} \tag{2.15}$$

The transfer function could also be estimated using the CPSD, $P_{xy}(f)$, of the two signals and the PSD of the output signal, $P_{yy}(f)$ [120]:

$$H_2(f) = \frac{P_{yy}(f)}{P_{xy}(f)} \tag{2.16}$$

$H_1(f)$ and $H_2(f)$ are estimations of the transfer function, and should be equal. However, if noise exists on the input and/or output signals and the spectral estimator makes use of windowing, the estimates will differ. The H_1 estimator assumes no noise exists on the input signal, whereas the H_2 operator assumes no noise exists on the output signal. If noise does exist on the input or output signal, some error would exist in the estimated frequency response [123]. The transfer function can also be calculated using the same spectral estimators used to determine a PSD, as discussed in section 2.6.1.

Chapter 3

Design and Analysis of the Pseudo-Random Impulse Sequence Perturbation Source

3.1. Overview

In this project, a Pseudo-Random Impulse Sequence (PRIS) source is used to perturb voltage source inverters during system identification studies. This chapter discusses the generation of a Pseudo-Random Binary Sequence (PRBS) gating signal used in a PRIS source and the design of the PRIS source.

The PRBS gating signal is generated by integrating multiple software components and utilizing a Field Programmable Gate Array (FPGA). The hardware design of the PRIS source is discussed, including its switching topology, RLC filter and any additional circuitry. Measurement equipment used during experimental results is also discussed in this chapter. The PRIS source was designed and developed based on the proposed methodology from Mwaniki *et al.* [94].

Fig. 3.1 presents the circuit topology of a PRIS source [28]. It consists of a PRBS generator that controls the switching of a H-bridge. The H-bridge is supplied by a DC voltage source, V_{DC}, and the output of the H-bridge is filtered by a RLC filter before it is connected to the Point of Common Coupling (PCC) to perturb a target system.

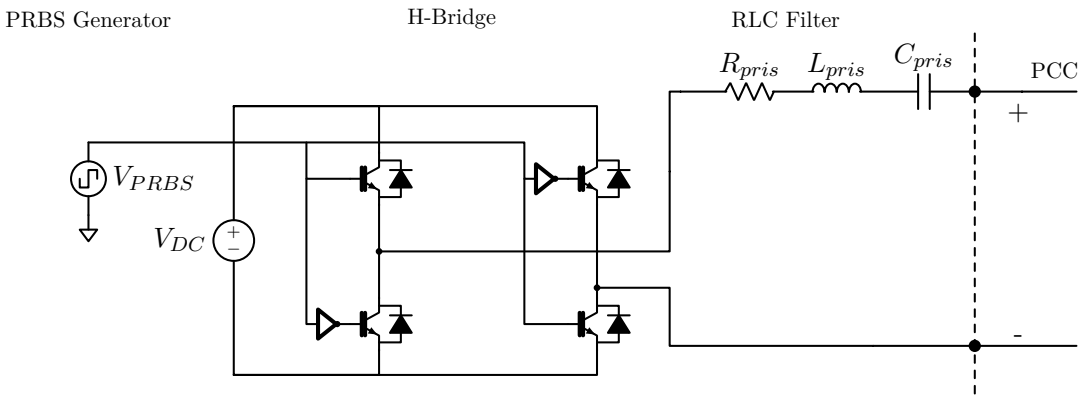

Figure 3.1: Circuit configuration of a pseudo-random impulse sequence source.

3.2. Pseudo-Random Binary Sequence Design and Generation

3.2.1. Overview

The H-bridge of the PRIS source is controlled using a PRBS gating signal. A requirement of the PRIS source is a user-controllable PRBS generator to customize the PRBS characteristics and thus also the time- and frequency-domain characteristics of the PRIS source, enhancing controllability of the PRIS source. A FPGA is used to generate the PRBS signal.

A Graphical User Interface (GUI) is developed in Python to allow the user to input variables such as the clock frequency, PRBS order and length and the number of PRBS periods. This information is processed in Python. A PRBS sequence consisting of low and high logic states is created and written to a VHDL file which can be loaded onto the FPGA. The VHDL code executes the PRBS sequence and displays it on the FPGA output pins. A Tool Command Language (TCL) is used to synthesize the VHDL file and upload the required files to the FPGA. Fig. 3.2 illustrates this process.

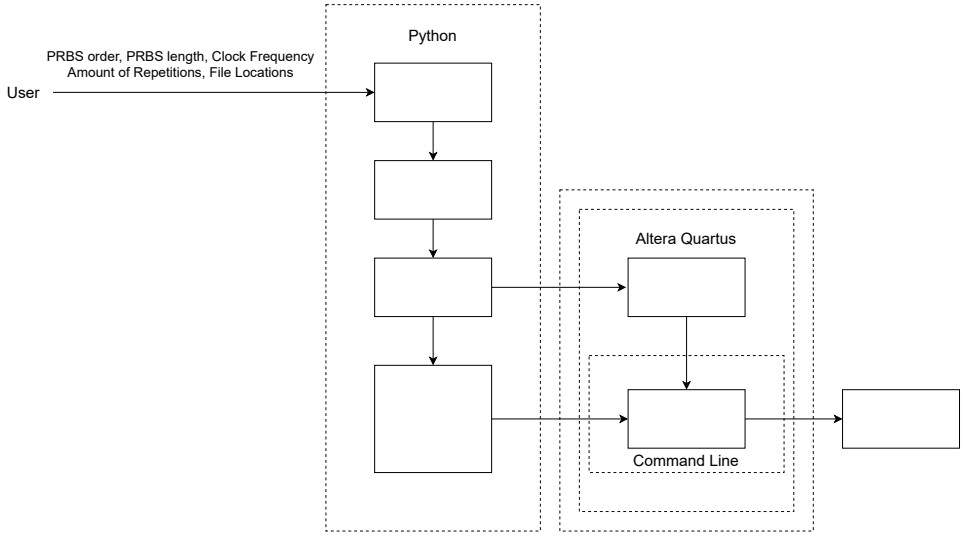

Figure 3.2: Block diagram illustrating the process of generating a pseudo-random binary sequence on a field programmable gate array.

3.2.2. Software used to Generate the Pseudo-Random Binary Sequence

3.2.2.1. Python Firmware Integration

Python is an interactive software language that can be used to integrate various software applications and systems [124]. It has a wide range of available libraries, aiding easy adaption of existing code to user-specific applications. During the generation of a PRBS sequence for this project, Python is used to execute most of the firmware programming. The following components of the PRBS generator are implemented using Python:

- *Graphical user interface*: Making use of the *tkinter* library [125], a GUI is created for user-friendly customization of a PRBS sequence. The GUI is used to obtain user inputs. These inputs are used to create a custom PRBS sequence. The user is required to provide the GUI with the PRBS order, PRBS length, clock frequency and the number of times the PRBS signal is repeated. This allows the PRIS source to be easily reconfigured for different applications. The programming of the GUI is aided with the use of *Python Automatic GUI Generator (PAGE)*. Fig. B.1 in appendix B shows a screenshot of the GUI.
- *PRBS generation*: The Python library, *Decida*, has a class called *Pattern* that is used to generate a PRBS bit pattern for a given length and order.
- *Updating VHDL code and uploading it to the FPGA*: Using the *os* module in Python, the command-line can be accessed. Subsequently, VHDL code can be altered via the command-line and TCL commands for the Altera Quartus software can be used.

3.2.2.2. Programming of the Field Programmable Gate Array

VHDL code is uploaded onto the FPGA. A timer is used to iteratively loop through the PRBS array consisting of logical lows and highs and make the corresponding GPIO pins low and high to output the PRBS on the appropriate FPGA General Purpose Input/Output (GPIO) pins. Additionally, an enable as well as a gating signal is implemented. The enable signal is high for the duration the FPGA is outputting a PRBS sequence. The gating signal is high for one PRBS clock period as soon as a PRBS sequence starts or starts repeating to allow future integration with a triggered measurement or perturbation technique. Fig. 3.3 presents a simulated example of a PRBS4 that is repeated twice with the required corresponding enabling and gating signals. The clock frequency is $f_{clk} = 10kHz$.

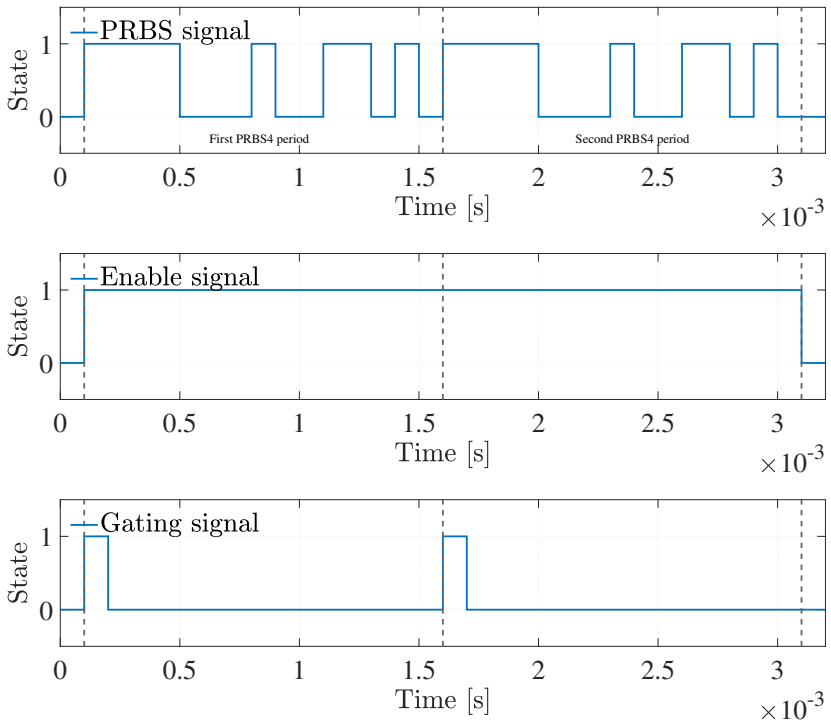

Figure 3.3: A PRBS4 signal that repeats and the enable and gating signals that needs to be implemented on the FPGA.

3.2.2.3. Using Quartus Tool Command Language to Synthesize and Build Code on Field Programmable Gate Array

The Quartus II software can be controlled and used via the command line. This is useful, as the command line can be controlled from a Python script using the *os* library, an operating system interface, from Python. TCL commands are available for Quartus II. TCL commands are used by running a batch file from Python. The contents of the batch file are presented in appendix C.

3.2.3. Hardware Implementation of Pseudo-Random Binary Sequence on a Field Programmable Gate Array Development Board

A Field Programmable Gate Array (FPGA) development board is used to generate the desired PRBS gating signal. A FPGA has an array of programmable logic blocks that can build a circuit using logic gates [126]. A FPGA is favoured to a microcontroller for the design of the high-frequency PRBS signal. An FPGA is more expensive than a microcontroller, its software is more complex to programme and it has little compatibility over different software and hardware configurations. However, the flexibility that re-programmable hardware allows, makes it superior with regards to performance. It has an higher processing speed and its rise and fall times are shorter. Since the only use of the

FPGA will be to control the gate driver, it is more suitable for application in a PRBS generator than a microcontroller.

Terasic, Digilent and Xilinx are some of the predominant FPGA development board manufacturers. Terasic uses Intel FPGAs. These FPGAs can be programmed using the Quartus Software [127]. The DE0 Nano development board, using a Altera Cyclone IV FPGA, is chosen for this project due to its size and its compatibility with the user-friendly Quartus II software.

A push-button is connected to a GPIO pin to allow the user to start a PRBS sequence manually. A high GPIO pin output is 3.3V. The clock frequency of the PRBS generated by the FPGA can be up to 50 MHz. Additionally, fault signals from the IGBT drivers used in the PRIS source are connected to the FPGA. As soon as a fault occur, the FPGA will stop producing a PRBS signal.

3.2.4. PRBS Generation Experimental Results

The designed PRBS generator is tested experimentally. The PRBS voltage used to control the IGBTs are measured and presented in Fig. 3.4. A PRBS4, as defined in Table 2.2, is generated at a clock frequency of 10 kHz, repeating indefinitely. The measured low and high logic states of the PRBS change at multiples of the clock frequency and at pseudo-random instances. The shape of the PRBS4 compares well with the simulated PRBS4 in Fig. 3.3.

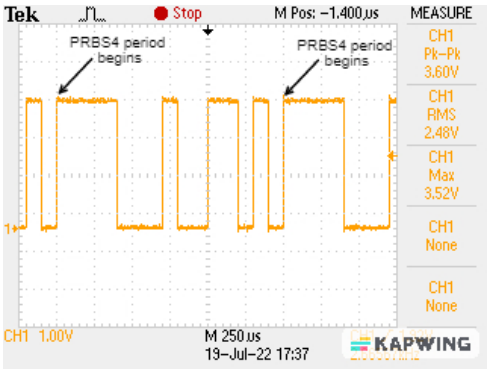

Figure 3.4: Oscilloscope measurement of a repeating PRBS4 sequence voltage with a 10kHz clock frequency.

3.3. Pseudo-Random Impulse Sequence Source Design and Generation

3.3.1. Practical Pseudo-Random Impulse Sequence Source System Overview

Fig. 3.1 illustrates the circuit topology of the constructed PRIS source. The PRBS generator, each leg of the H-bridge and the RLC filter are soldered onto individual Printed Circuit Board (PCB) cards. These PCB cards are housed in a KM6-II subrack and can slot into the subrack using rails. The PCB cards are connected with either 64 or 16 pin DIN connectors to a PCB that is fixed to the backplate of the subrack. A DC voltage power supply that powers the FPGA as well as the IGBT drivers used in the H-Bridge also slots into the subrack and is connected to the backplate. A 220 V_{RMS} AC supply is connected to the back of the subrack to power this DC voltage power supply. Appropriate connections between different PCB cards are made on the PCB on the backplate. Also connected to the backplate is the external DC voltage supplying the H-bridge, V_{DC} in Fig. 3.1. Fig. D.1 in appendix D shows the practical PRIS source. The PRIS source can withstand a maximum voltage of approximately 1.6 kV at the PCC and a maximum current of approximately 25 A.

3.3.2. H-Bridge Design

In designing the H-bridge section of the PRIS source, two FF225R17ME4 IGBT modules are used. Each module contains two IGBTs, i.e. one leg of the H-bridge. These IGBTs have a maximum collector-emitter voltage, V_{ce}, of 1.7kV and nominal collector current of 225 A. FF225R17ME4 gate drivers are mounted on top of each IGBT module. These opto-coupled drivers allow for easy and safe implementation of the H-bridge. The IGBT modules are set to be operated in H-bridge mode. Complimentary signals are sent from the FPGA to the two separate drivers. One driver is controlled by a PRBS sequence, while the other is controlled by the inverted PRBS sequence. Deadtime is implemented within the IGBT drivers to prevent a short-circuit. Each IGBT module is soldered to an individual PCB card that slots into the backplate of the subrack. The IGBT drivers are connected to the PCB on the backplate with a 20 way twisted ribbon cable to allow connection with the FPGA.

3.3.3. RLC Filter Design

The series RLC branch used in the PRIS source is soldered onto an individual PCB card that slots into the PCB on the backplate of the subrack. The RLC component

values and power ratings depend on the system under test and can be configured to suit the application. These passive elements are used to control the time-constants of the PRIS waveform, hence controlling the time- and frequency-domain characteristics of the perturbation signal.

3.3.4. DC Voltage Source Supplying H-Bridge of PRIS Source

The DC voltage source supplying the H-bridge of the PRIS source is connected to the PCB on the backplate of the subrack. An analogue source is preferred to a digitally controlled source, as a digitally controlled source tends to switch between constant voltage and constant current modes when used to power an *in situ* PRIS source. This is unwanted, as the PRIS source is designed using a constant voltage source, not a constant current source. The size of the voltage depend on the application. The DC voltage that supplies the PRIS source can be varied to increase or decrease perturbation energy.

3.3.5. DC Voltage Source Supplying IGBT Driver and FPGA

5V and 15 V DC supplies are required to power the FPGA and IGBT drivers respectively. These voltage rails are supplied by a Bivolt Pk60B DC power supply card that can slot into the subrack and connects to the PCB on the backplate.

3.3.6. Field Programmable Gate Array Printed Circuit Board Card

The Altera DE0 Nano FPGA development board that generates the PRBS signal is placed on a PCB card that slots into the PCB on the backplate of the subrack. Additional circuitry for the GPIO inputs, outputs and a on-button are also implemented on the PCB.

3.3.7. Pseudo-Random Impulse Sequence Source Experimental Results

The PRIS source is tested experimentally with no device under test as presented in Fig. 3.5.

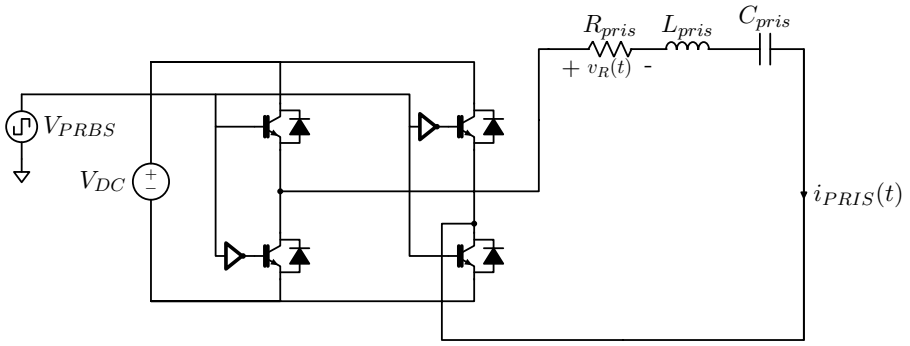

Figure 3.5: Circuit configuration of a pseudo-random impulse sequence source with no device under test.

The RLC filter parameters are chosen as 100Ω, $2.2mH$ and $1\mu F$ respectively to produce an overdamped response [94]. A PRBS4, as defined in Table 2.2, is used at a clock frequency of 10 kHz. The oscilloscope measurement of the voltage across R_{pris}, $v_R(t)$, is presented in Fig. 3.6. The PRIS is programmed to repeat. The PRIS is enveloped by the PRBS4 presented in Fig. 3.3 and the time constants resemble an impulse.

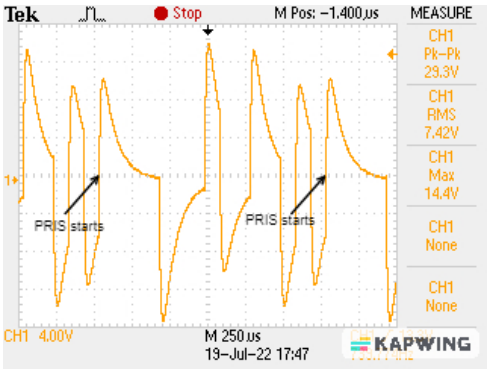

Figure 3.6: Oscilloscope measurement of the pseudo-random impulse sequence generated using a PRBS4, with a 10kHz clock frequency. The voltage across R_{pris}, $v_R(t)$, is measured.

3.4. Configuration of the Pseudo-Random Impulse Sequence Source

The PRBS gating signal and the RLC circuit of the PRIS source can be configured in order to control the spectral characteristics of the excitation signal as required. In this section, the selection of the RLC components and PRBS signal are discussed.

During the investigation in this section, the PRIS source with no device under test, as shown in Fig. 3.5, is simulated in Simulink while examing the current, $i_{PRIS}(t)$ and the PSD of the current. The PRIS source is constructed using the values summarized in Table 3.1, except when explicitly stated otherwise.

TABLE 3.1: PRIS source parameters while investigating the configuration of the PRIS source.

PRBS Order	**Clock Frequency f_{clk}**	R_{pris}	L_{pris}	C_{pris}	V_{DC}
14	$10kHz$	100Ω	$1mH$	$1\mu F$	30 V

The power, voltage and current ratings of the device under test, as well as of the circuit components used to construct the PRIS source should be taken into account when configuring the PRIS source. The circuit components used to construct the PRIS source can be used to limit the voltage and current produced by the source.

3.4.1. Configuration of the PRBS Signal

The PRBS gating signal supplied to the H-bridge of the PRIS source can be configured by changing its clock frequency and PRBS order. Fig. 3.7 presents the PSD of the current, $i_{PRIS}(t)$, as a function of the clock frequency, f_{clk}, while the other parameters of the PRIS source is fixed to the values listed in Table 3.1. As shown in Fig. 3.7, the upper side lobe of the PSD of $i_{PRIS}(t)$ has a width of f_{clk}. The PSD displays minima at integer multiples of f_{clk}. The majority of the energy contained in the excitation signal is contained in the first lobe. The clock frequency of the PRIS source, thus, needs to be chosen to cover the frequency range of the interest of the device under test.

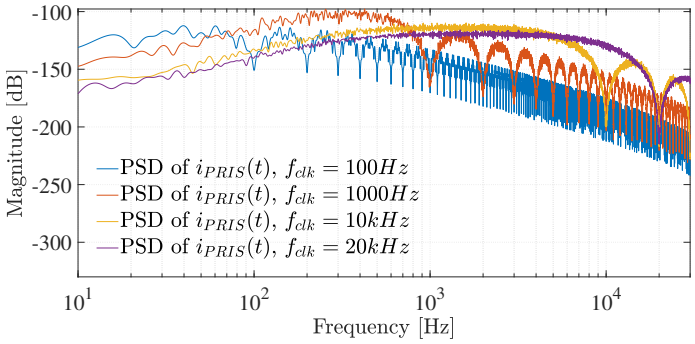

Figure 3.7: Power spectral density of $i_{PRIS}(t)$ as a function of f_{clk}.

After the value of f_{clk} is chosen, the PRBS order needs to be chosen. The length of an PRBS signal with order, m, is $2^m - 1$. A higher PRBS order corresponds to a longer PRBS length, and thus increased randomness of the excitation signal. The period of a PRBS signal, T_{PRBS}, is thus:

$$T_{PRBS} = \frac{2^m - 1}{f_{clk}} \tag{3.1}$$

Therefore, the PRBS order is chosen according to the frequency resolution required for spectral estimation while aiming to keep *in situ* measurement times viable, this would depend on the practical arrangement under test.

3.4.2. Selection of the RLC Circuit Values

3.4.2.1. Selection of the Resistor

Fig. 3.8 shows the time-domain waveform of the current, $i_{PRIS}(t)$, as well as the PSD of $i_{PRIS}(t)$ as a function of the resistor, R_{pris}. As the magnitude of R_{pris} increases, the amplitude of $i_{PRIS}(t)$ decreases and the magnitude of the PSD also decreases. Increasing R_{pris} allows less perturbation energy to reach the device under test. Therefore, intuitively, it is expected that R_{pris} should be chosen as small as possible to increase the perturbation

energy. However, for *in situ* application of the PRIS source, R_{pris}, needs to be designed to protect the rest of the components of the perturbation source and mitigate any voltage differences between the device under test and the perturbation source and limit the current within the perturbation source.

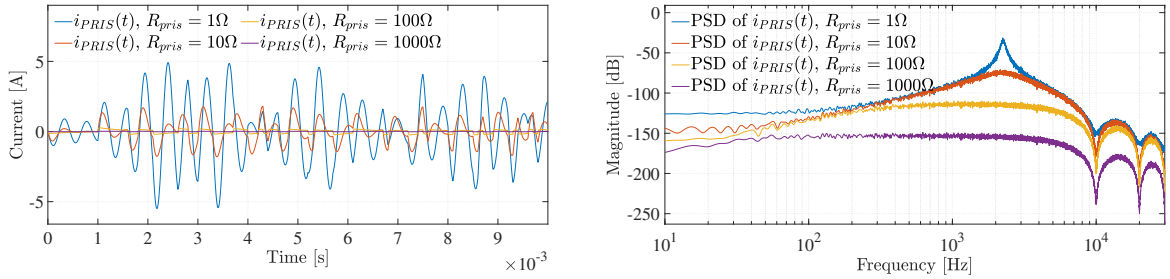

(a) (b)

Figure 3.8: (a) Time-domain waveform of $i_{PRIS}(t)$ as a function of R_{pris}. (b) Power spectral density of $i_{PRIS}(t)$ as a function of R_{pris}.

3.4.2.2. Selection of the Inductor

Fig. 3.8 shows the time-domain waveform of the current, $i_{PRIS}(t)$, as well as the PSD of $i_{PRIS}(t)$ as a function of the inductor, L_{pris}. The inductor has a limited effect on the spectral characteristics of the perturbation source. As the inductance increases, the power contained at frequencies higher than approximately $f_{clk}/3$ decreases. The inductance can also be used to limit the current within the perturbation source. Furthermore, if the device under test controls the current, as in the case of some inverters, the inductance should be increased to allow slower time constants.

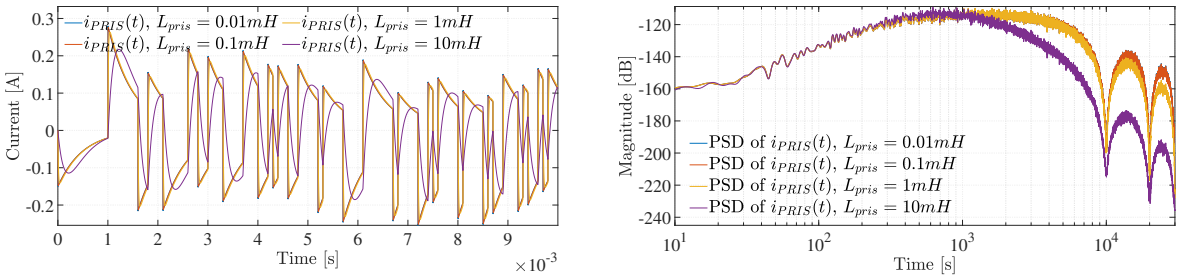

(a) (b)

Figure 3.9: (a) Time-domain waveform of $i_{PRIS}(t)$ as a function of L_{pris}. (b) Power spectral density of $i_{PRIS}(t)$ as a function of L_{pris}.

3.4.2.3. Selection of the Capacitor

Fig. 3.8 shows the time-domain waveform of the current, $i_{PRIS}(t)$, as well as the PSD of $i_{PRIS}(t)$ as a function of the capacitor, C_{pris}. As the capacitance is increased, the time-domain waveform of $i_{PRIS}(t)$ exhibits time-domain characteristics similar to a PRBS

signal. The PSD also contains increased energy at in the first side lobe. Therefore, the capacitor should be chosen to allow adequate low frequency perturbation. However, the capacitor is also used protect the perturbation source by limiting the voltage across the other components of the PRIS source.

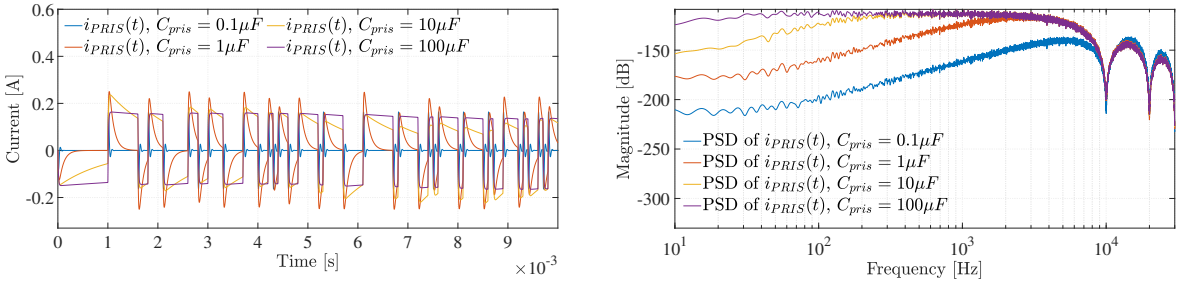

(a) (b)

Figure 3.10: (a) Time-domain waveform of $i_{PRIS}(t)$ as a function of C_{pris}. (b) Power spectral density of $i_{PRIS}(t)$ as a function of C_{pris}.

3.5. Measurement Equipment

A 8-Slot NI cDAQ-9178 chassis is used as a Data Acquisition (DAQ) system. A 4-channel, 16-bit voltage input module, the NI 9223, slots into the chassis. Sampling can be executed up to a sampling frequency of 1MHz. The DAQ system can be use to record data and transfer it via a Universal Serial Bus (USB) cable to a Personal Computer (PC) on which the Data Acquisition Toolbox of MATLAB can be used to process the data.

Three different probes were used during this project to measure voltages and currents, along with a 100kHz low-pass filter manufactured by Thorlabs to filter out high-frequency noise found in the measured output waveforms:

- A high-voltage differential probe from PINTECH, the N1000A, with a maximum voltage of 1400 V_{pp} and a bandwidth of $40MHz$.
- A high-voltage differential probe from GWINSTEK, the GDP-025, with a maximum voltage of 1000 V_{pp} and a bandwidth of $100MHz$.
- An AC/DC current probe from GWINSTEK, the GCP-1000, with a maximum current of 70 A_{DC} and a bandwidth of $1MHz$.

Chapter 4

Parameter Estimation of a Full-Bridge Inverter using a Simulation Approach

4.1. Overview

This chapter focuses on parameter estimation of inverters through simulation. Parameters of a parametric inverter model are estimated. The equivalent output impedance of the inverter is characterized by exciting the inverter using PRIS perturbations. The output impedance is subsequently used in the parameter estimation process. Idealized inverter topologies, without deadtime, parasitic resistances and a DC link capacitor are investigated using an electromagnetic transient model in Simulink. In this chapter, two case-studies are presented. In the first case study a standalone, single-phase, full-bridge inverter with a LC filter is investigated [128]. The second case study expands the approach to a grid-connected, single-phase, full-bridge inverter with an LCL filter.

4.2. Case Study 1: Full-Bridge Voltage Source Inverter with an LC Filter and a Dual-Control Loop

4.2.1. Inverter Topology

Fig. 4.1 shows the circuit configuration of a double-loop, single-phase Voltage Source Inverter (VSI) [129]. An LC low-pass filter is used to filter the harmonics of the modulated voltage, $v_{Ao}(t)$. A Proportional Integrator (PI) controller, $G_c(s)$, and proportional controller, k_{P_i}, is implemented in the control-loop to regulate the measured inductor current, $i_L(t)$, and output voltage, $v_o(t)$. The inverter supplies a resistive load, R_{load}, with a specific voltage.

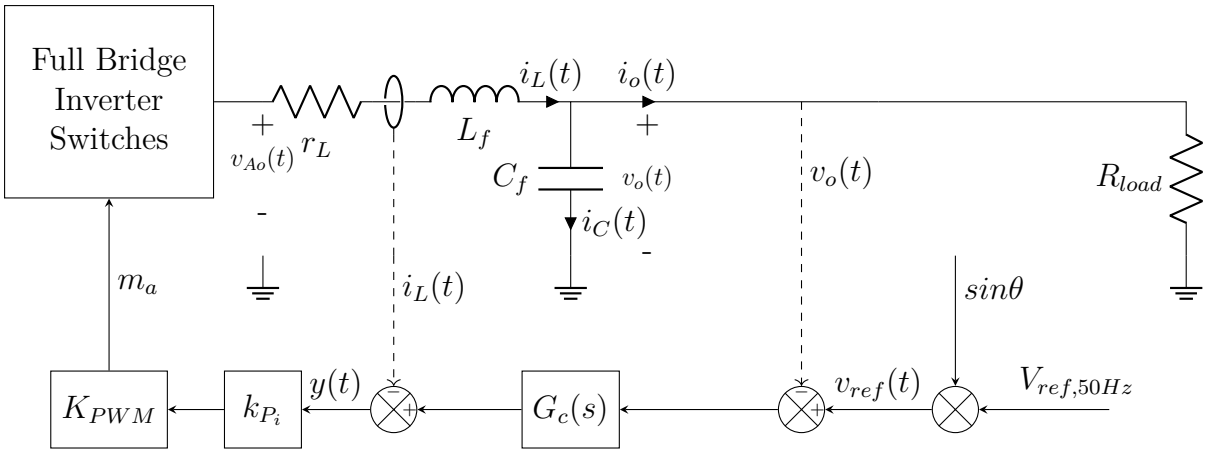

Figure 4.1: Circuit topology of the dual-loop voltage source inverter used in this investigation.

The transfer function, $G_c(s)$, of the PI controller, is expressed by

$$G_c(s) = \frac{k_{pv}s + k_{iv}}{s}, \tag{4.1}$$

where s is the Laplace operator. The gains k_{pv} and k_{iv} are used in the PI controller. Table 4.1 summarizes the controller and filter parameters of the inverter in Fig. 4.1 as presented by Xu *et al.* [129]. The DC input voltage to the inverter, V_d, is 600 V, the fundamental output voltage and current operates at 50 Hz and supplies a resistive load. The inverter controls the output voltage across the load. Therefore, the impedance of the load determines the amplitude of the output current and subsequently the output power. The load is thus chosen as 50 Ω to limit the output current to 2.2 A when supplied with an output voltage with an amplitude of 110 V. The parasitic resistance of the inductor, r_{L_f}, is neglected. The inverter has a switching frequency of $f_{sw} = 20kHz$.

TABLE 4.1: Control-loop and filter parameter values for the circuit shown in Fig 4.1 [129].

Parameter	k_{P_i}	k_{pv}	k_{iv}	C_f [μH]	L_f [mH]
Value	1	5	100	10	10.1

A sinusoidal reference output voltage, $v_{ref}(t)$, with a frequency of 50 Hz and an amplitude of V_{ref} is supplied to the inverter control-loop. Fig. 4.2 shows the inverter in operation with two different reference voltages supplied, $v_{ref}(t) = 50sin(2\pi 50t)$V and $v_{ref}(t) = 110sin(2\pi 50t)$V. The inverter is capable of producing a sinusoidal output voltage. As seen in Fig. 4.2, some error is present in the output voltage, $v_o(t)$, due to the non-ideal passive components of the low-pass filter and the control-loop not being capable of adjusting the output voltage appropriately. A non-linear relationship exists between the reference signal and the output voltage.

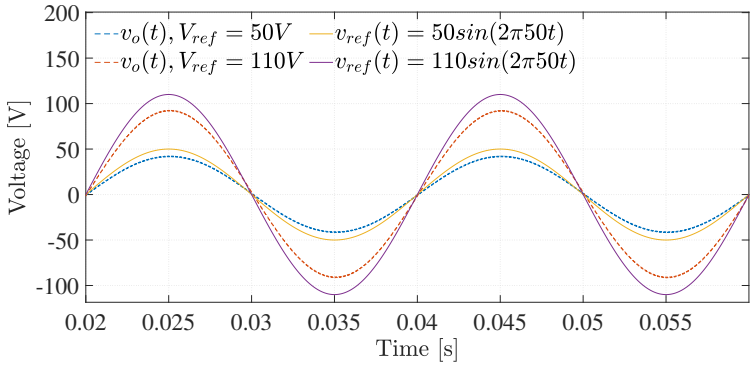

Figure 4.2: Output voltage of the inverter in the time-domain as the reference signal is varied.

During this investigation the inverter is modelled in Simulink with the use of the PLECS blockset as an Electromagnetic Transient (EMT) model. The EMT model describes the various components of the inverter separately. Although it is computationally complex to run an EMT simulation, the accuracy presented by EMT modelling improves the parameter estimation procedure.

4.2.2. Mathematical Analysis of a Double-Loop Voltage Source Inverter

A steady-state average model analysis of the inverter in Fig. 4.1 is conducted. Deadtime, a DC-link capacitor and non-ideal switching and filtering effects are neglected. The modulation voltage, $v_{Ao}(t)$, is described by

$$v_{Ao}(t) = r_L i_L(t) + L\frac{di_L(t)}{dt} + v_o(t). \tag{4.2}$$

The inductor current, $i_L(t)$, is equal to the sum of the capacitor current, $i_C(t)$, and the output current $i_o(t)$. Equation (4.2) thus becomes

$$v_{Ao}(t) = r_L i_o(t) + r_L C\frac{dv_o(t)}{dt} + L\frac{di_o(t)}{dt} + LC\frac{d^2v_o(t)}{dt^2} + v_o(t). \tag{4.3}$$

The Laplace transform of (4.3) yields

$$V_{Ao}(s) = I_o(s)(r_L + sL) + V_o(s)(sr_LC + s^2LC + 1). \tag{4.4}$$

The modulation index, m_a, is related to the peak amplitude of the fundamental frequency component of the modulated voltage, $\hat{V}^1_{Ao}$, and the DC input voltage, V_d, by

$$\hat{V}^1_{Ao} = m_a V_d. \tag{4.5}$$

The amplitude of the triangular carrier wave used in the PWM generator is equal to one. A gain, K_{PWM}, is used to scale the output signal from the control-loop, in order to prevent overmodulation. The modulated voltage, $v_{Ao}(t)$, can thus be described in terms of the control loop as

$$\begin{aligned} v_{Ao}(t) &= k_{P_i}(G_c(t) * (v_{ref}(t) - v_o(t)) - i_L(t)) \\ &= k_{P_i}(G_c(t) * (v_{ref}(t) - v_o(t)) - (C\frac{dv_o(t)}{dt} + i_o(t))). \end{aligned} \tag{4.6}$$

The Laplace transform of (4.6) is defined as

$$V_{Ao}(s) = k_{P_i}((\frac{k_{pvs+kiv}}{s}(V_{ref}(s) - V_o(s)) - (I_o(s) + sCV_o(s)))). \tag{4.7}$$

Equation (4.7) is substituted into (4.4) to obtain

$$\begin{aligned} V_o(s) = V_{ref}(s)&\frac{k_{P_i}k_{pv}s + k_{P_i}k_{iv}}{s^3LC + s^2(r_LC + k_{P_i}C) + s(k_{pv}k_{P_i} + 1) + k_{P_i}k_{iv}} \\ - I_o(s)&\frac{s^2L + s(r_L + k_{P_i})}{s^3LC + s^2(r_LC + k_{P_i}C) + s(k_{pv}k_{P_i} + 1) + k_{P_i}k_{iv}}. \end{aligned} \tag{4.8}$$

Equation (4.8) is written as

$$V_o(s) = G(s)V_{ref}(s) + I_o(s)Z_o(s), \tag{4.9}$$

where

$$G(s) = \frac{k_{P_i}k_{pv}s + k_{P_i}k_{iv}}{s^3LC + s^2(r_LC + k_{P_i}C) + s(k_{pv}k_{P_i} + 1) + k_{P_i}k_{iv}} \tag{4.10}$$

and

$$Z_o(s) = \frac{-(s^2L + s(r_L + k_{P_i}))}{s^3LC + s^2(r_LC + k_{P_i}C) + s(k_{pv}k_{P_i} + 1) + k_{P_i}k_{iv}}. \tag{4.11}$$

The combination of $G(s)V_{ref}(s)$ is defined as the Thévenin voltage source:

$$V_{TH}(s) = G(s)V_{ref}(s) \tag{4.12}$$

From (4.9), the Thévenin equivalent circuit of the inverter in Fig. 4.1 is derived. Fig. 4.3 displays the Thévenin equivalent circuit.

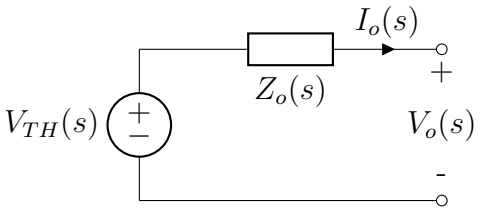

Figure 4.3: Thévenin equivalent circuit of the VSI under investigation.

The output impedance of the inverter is represented by $Z_o(s)$. As shown in (4.11), the output impedance, $Z_o(s)$, is dependant on the filter parameters as well as the control-loop parameters. For this reason $Z_o(s)$ can be used during parameter estimation to estimate the controller and filter parameters of the inverter.

The transfer function, $Z_f(f)$, is the impedance of the LC filter if the modulated voltage is approximated as a constant voltage source and is expressed as

$$Z_f(f) = \frac{sL}{s^2LC + 1}. \tag{4.13}$$

Fig. 4.4 shows the analytical frequency responses $Z_o(f)$, $G(f)$ and $Z_f(f)$ of the VSI. The LC filter causes a resonant point around 500 Hz. This resonant point is shifted to higher frequencies when the filter is included in the closed-loop inverter system. The resonant point of the frequency responses of $Z_o(f)$ and $G(f)$ is between 1kHz and 2kHz.

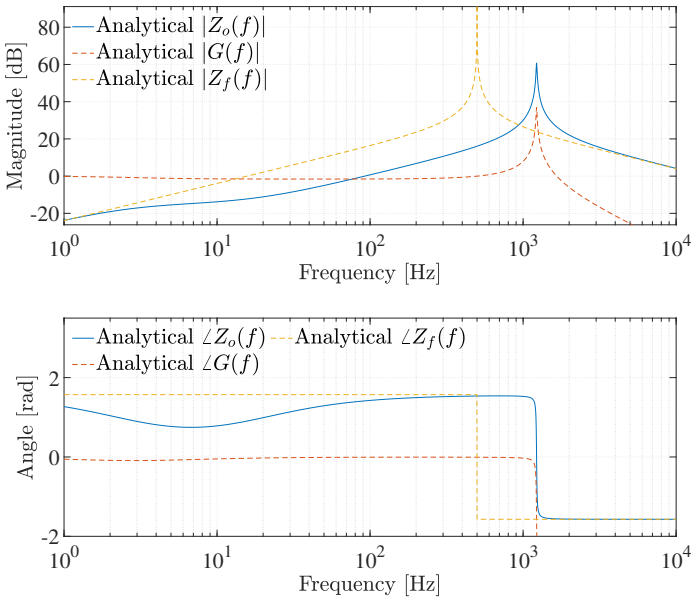

Figure 4.4: Magnitude and phase responses of the analytical $Z_o(f)$, $G(f)$ and $Z_f(f)$.

4.2.3. Observability of the Output Impedance, $Z_o(f)$

$Z_o(f)$ contains all the filter and controller parameters of the inverter and might be suitable for use to estimate the filter and controller parameters. The observability of $Z_o(f)$ is thus investigated. The companion canonical state variable form of the output impedance transfer function is obtained. This yields, amongst others, the state matrix, $\mathbf{A}$,

$$\mathbf{A} = \begin{bmatrix} 0 & 1 & 0 \\ 0 & 0 & 1 \\ -9.87 \times 10^{10} & -4.94 \times 10^{9} & -9879.47 \end{bmatrix}, \tag{4.14}$$

and the output vector, $\mathbf{c}$,

$$\mathbf{c} = \begin{bmatrix} 0 & -9.88 \times 10^{8} & -1 \times 10^{5} \end{bmatrix}. \tag{4.15}$$

The system is observable if the input and output over a finite time interval can be used to determine the initial state of the system [130]. The matrices, $\mathbf{A}$ and $\mathbf{c}$, are used to obtain the observability matrix, $\mathbf{V}$, of $Z_o(f)$ as [130]

$$\mathbf{V} \triangleq \begin{bmatrix} \mathbf{c} \\ \mathbf{cA} \\ \vdots \\ \mathbf{cA}^{n-1} \end{bmatrix} = \begin{bmatrix} 0 & -9.88 \times 10^{8} & -1 \times 10^{-5} \\ 9.87 \times 10^{15} & 4.94 \times 10^{14} & -2.38 \times 10^{-7} \\ 32768 & 9.87 \times 10^{15} & 4.94 \times 10^{14} \end{bmatrix}. \tag{4.16}$$

The transfer function of the equivalent output impedance, $Z_o(f)$, is observable, as the rank, ρ, of the observability matrix, $\mathbf{V}$, is equal to the order of the transfer function, n,

$$\rho(V) = 3 = n. \tag{4.17}$$

4.2.4. Perturbation of a Voltage Source Inverter Using Pseudo-Random Impulses

A broadband excitation signal is used to perturb the device under test, allowing characterization of the frequency responses of the inverter. In this project, the voltage source inverter is perturbed with a PRIS perturbation source. The perturbed measurements are used to obtain the output impedance frequency response of the inverter as a wide frequency band is excited. As discussed in section 2.2.2.2, the AC output side of the inverter is readily accessible for perturbation and more suitable than internal reference signals that would only be accessible in practice within a microcontroller.

4.2.4.1. Perturbation of the Dual-Loop Voltage Source Inverter using Pseudo-Random Impulse Sequence Perturbations

Fig. 4.5 presents the perturbation arrangement used during this investigation. A resistive load, R_{load}, is supplied by the VSI. The PRIS perturbation source is connected in parallel to the load.

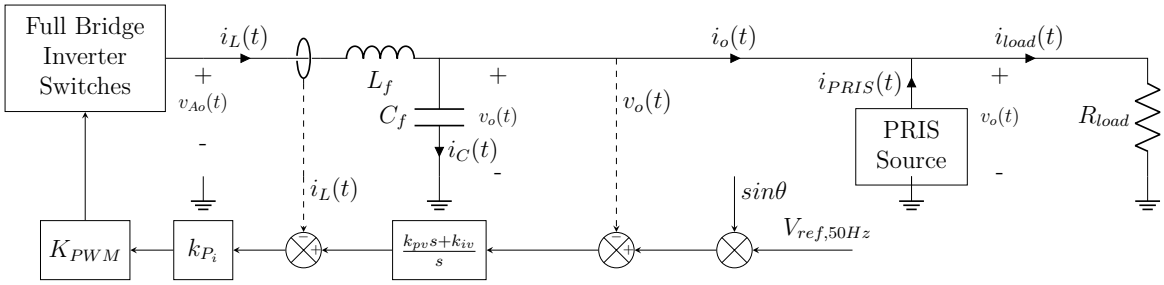

Figure 4.5: Dual-loop voltage source inverter with the perturbation source connected at its AC output.

The circuit implementation of a PRIS source is discussed in chapter 3. An alternative time-domain modelling technique of a PRIS signal is possible [94]. The block diagram in Fig. 4.6 illustrates how a bipolar PRIS can be simulated in Simulink using (2.6). This specific block diagram demonstrates the modelling technique using a PRBS4. When the PRBS has a positive zero-crossing, the PRIS signal generated is greater than zero. When a negative zero-crossing is detected, the PRIS signal is less than zero. The impulses are generated by passing the PRBS signal through two transfer functions, with time-constants τ_1 and τ_2 respectively and summing the output signals.

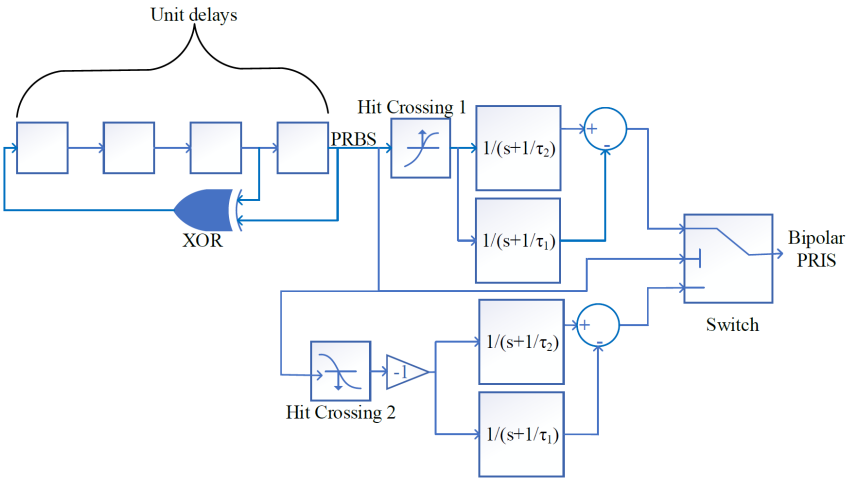

Figure 4.6: Model of a bipolar PRIS signal in Simulink using a PRBS4 [94].

The block diagram model presented in Fig. 4.6 is used with a PRBS14 to generate a PRIS signal in this chapter, instead of the circuit implementation, to allow easier

manipulation of the characteristics of the PRIS perturbation signal. Fig. 4.7 illustrates how the ideal PRIS signal is used in Simulink. The PRIS signal generated as shown in Fig. 4.6 is passed to a controlled voltage source in Simulink to produce the voltage, $v_{PRIS}(t)$. A series resistor is connected to the controlled voltage source to allow for *in situ* connection with the inverter.

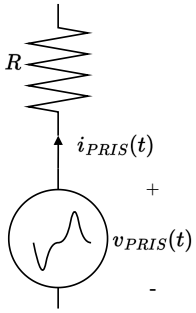

Figure 4.7: Perturbation source arrangement using a time-domain model of the PRIS signal.

A PRBS14 with a clock frequency, f_{clk}, of 2500 Hz is used to construct the ideal PRIS signal. The 2500 Hz clock frequency covers the frequency range of interest, while the order of the PRBS signal is chosen to allow adequate frequency-domain resolution and a viable simulation time. The ideal PRIS signal has time constants, $\tau_1 = 0.1 \times T_{clk}$ and $\tau_2 = 10 \times T_{clk}$ respectively [28].

4.2.4.2. Obtaining the Equivalent Output Impedance of the Voltage Source Inverter

The frequency-domain representation of the measured output voltage and current whilst the inverter is perturbed, $v_{o,p}(t)$ and $i_{o,p}(t)$, can be used to determine the measured output impedance, $Z_{om}(f)$, as the frequencies over a wide band are excited by the PRIS source. The measured output impedance, $Z_{om}(f)$, is defined as

$$Z_{om}(f) = \frac{V_{o,p}(f)}{I_{o,p}(f)}. \tag{4.18}$$

From (4.9) it is known that (4.18) contains a *source*, $G(f)V_{ref}(f)$ within its transfer function. The voltage, $V_{ref}(f)$, is the frequency-domain representation of a 50 Hz reference voltage sine wave. Fig. 4.8 displays the Laplace-domain representation of a 50 Hz sine wave with an amplitude of one. The magnitude at 50 Hz rises sharply.

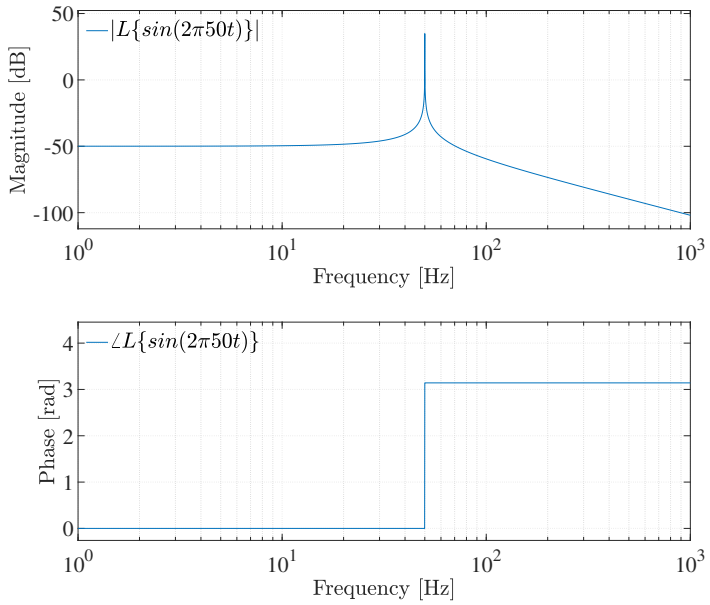

Figure 4.8: Magnitude and phase response of the Laplace-domain representation of a 50 Hz sine wave with an amplitude of unity.

The frequency responses of $G(f)V_{ref}(f)$ and $Z_o(f)$ are shown in Fig. 4.9. As mentioned in section 4.2.2, $Z_o(f)$ contains the shifted resonant point of the LC filter. The combination of $G(f)V_{ref}(f)$ also has this shifted resonant point, as well as the sharp rise in magnitude at 50 Hz, due to the 50 Hz reference sine wave.

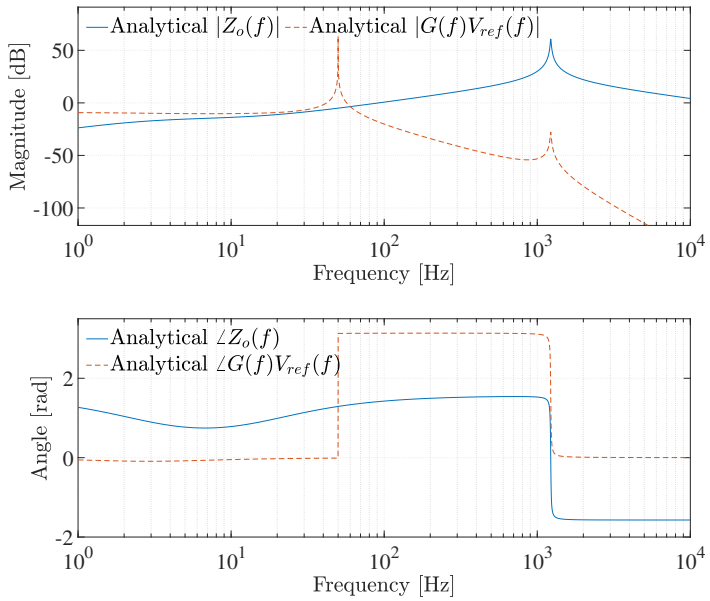

Figure 4.9: Magnitude and phase responses of $G(f)V_{ref}(f)$ and $Z_o(f)$.

The equivalent output impedance of the inverter, $Z_o(f)$, is thus determined using a two-measurement approach. The two-measurement approach aims to remove the 50 Hz

artefact from the measured output impedance, $Z_{om}(f)$. The inverter output voltage and current is measured whilst it is perturbed, $v_{o,p}(t)$ and $i_{o,p}(t)$, and while it is operating under normal conditions, $v_{o,n}(t)$ and $i_{o,n}(t)$. The perturbed output measurements are excited over a wide frequency band. The normal measurements contain the fundamental frequency components and harmonics. The fundamental frequency components and harmonics are also contained in the perturbed measurements. By making use of the two-measurement approach these harmonics are cancelled out when determining $Z_o(f)$. The frequency-domain representations of the measured time-domain signals, $V_{o,p}(f)$ and $I_{o,p}(f)$ as well as $V_{o,n}(f)$ and $I_{o,n}(f)$ are substituted in (4.9) to obtain

$$V_{o,p}(f) = V_{TH}(f) + Z_o(f)I_{o,p}(f), \tag{4.19}$$

and

$$V_{o,n}(f) = V_{TH}(f) + Z_o(f)I_{o,n}(f). \tag{4.20}$$

The output impedance can subsequently be formulated by combining (4.19) and (4.20):

$$Z_o(f) = \frac{V_{o,p}(f) - V_{o,n}(f)}{I_{o,p}(f) - I_{o,n}(f)} \tag{4.21}$$

Fig. 4.10 shows the time-domain output current of the inverter under normal conditions as well as during perturbation. The PRIS perturbations are superimposed on the output current. The current amplitude is also greater under perturbation, due to the PRIS source impedance that is in parallel with the load which creates a smaller combined impedance.

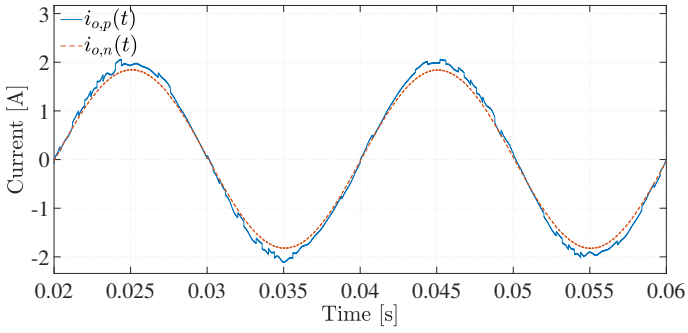

Figure 4.10: Output currents while the inverter is perturbed, $i_{o,p}(t)$, and while under normal operating conditions, $i_{o,n}(t)$, respectively.

Welch's method is utilized to obtain $Z_o(f)$ using the measured time-domain waveforms, $i_{o,p}(t)$, $i_{o,n}(t)$, $v_{o,p}(t)$ and $v_{o,n}(t)$ and (4.21). Welch's method is used to obtain frequency responses as it makes use of averaging to reduce the variance in the estimated frequency response, whilst providing adequate frequency resolution. Fig. 4.11 compares the estimated $Z_o(f)$ using Welch's method and the analytical $Z_o(f)$ from (4.11). The estimated and

analytical representations of $Z_o(f)$ correspond well, as the frequency responses lie on top of each other.

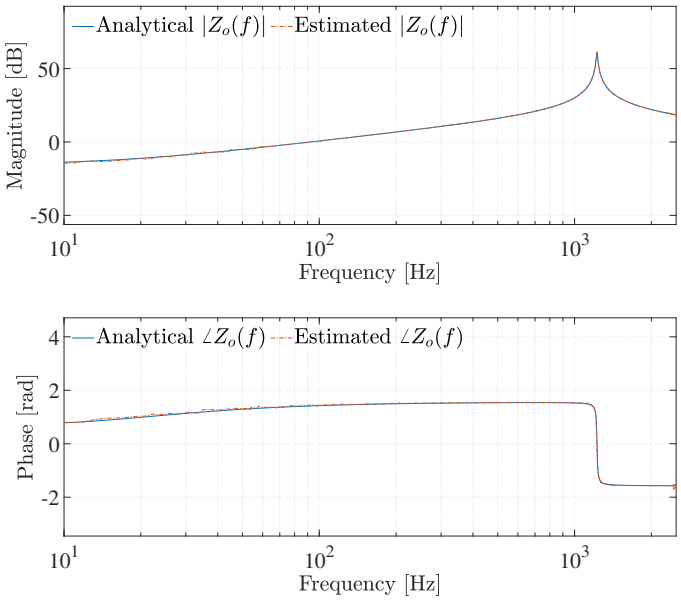

Figure 4.11: Magnitude and phase response of the estimated output impedance, $Z_o(f)$, of the VSI, using the two-measurement approach compared to the magnitude and phase response of the analytical output impedance.

Fig. 4.12 compares the output impedance obtained by using the two-measurement approach with the measured output impedance, $Z_{om}(f)$, that is obtained using (4.18). The 50 Hz artefact can clearly be seen in $Z_{om}(f)$. The two-measurement approach removes this artefact around 50 Hz to produce $Z_o(f)$.

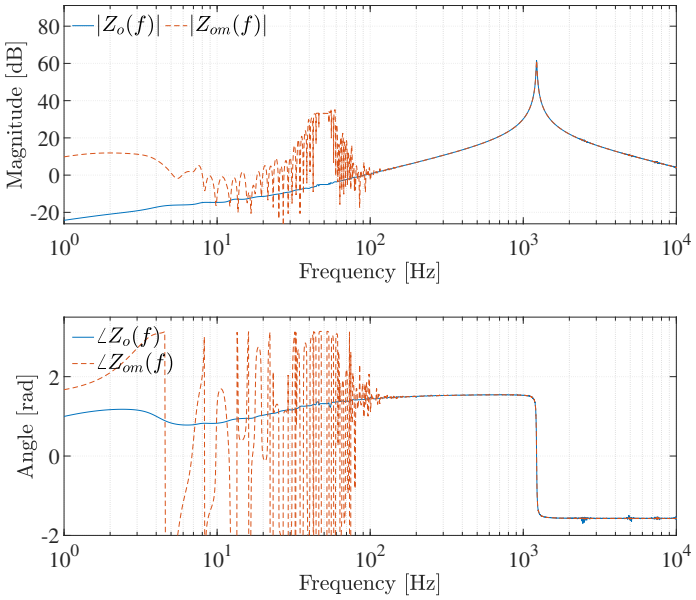

Figure 4.12: Magnitude and phase response of the estimated output impedance, $Z_o(f)$, of the VSI, using the two-measurement approach compared to the magnitude and phase response of the measured output impedance, $Z_{om}(f)$.

4.2.4.3. Sensitivity Analysis of the Controller and Filter Parameters

The vector, θ, contains the controller and filter parameters of interest:

$$\theta = [k_{P_i}, k_{pv}, k_{iv}, C_f, L_f] \tag{4.22}$$

Varying these parameters with values ten times lower and higher than its true value and observing the effect of these changes on the analytical output impedance frequency response gives insight in using the output impedance during parameter estimation. The effect of these changes is also observed in the time-domain. The time-domain sensitivity analysis is presented in appendix E.

Fig. 4.13a shows the influence of k_{P_i} on $Z_o(f)$. Increasing k_{P_i} shifts the resonant frequency to higher frequencies and reduces its magnitude. Fig. 4.13b shows the frequency response of the output impedance as a function of k_{pv}. The gain k_{pv} has a similar influence on the frequency response of the output impedance as k_{P_i}, also shifting the output impedance to higher frequencies as it is increased.

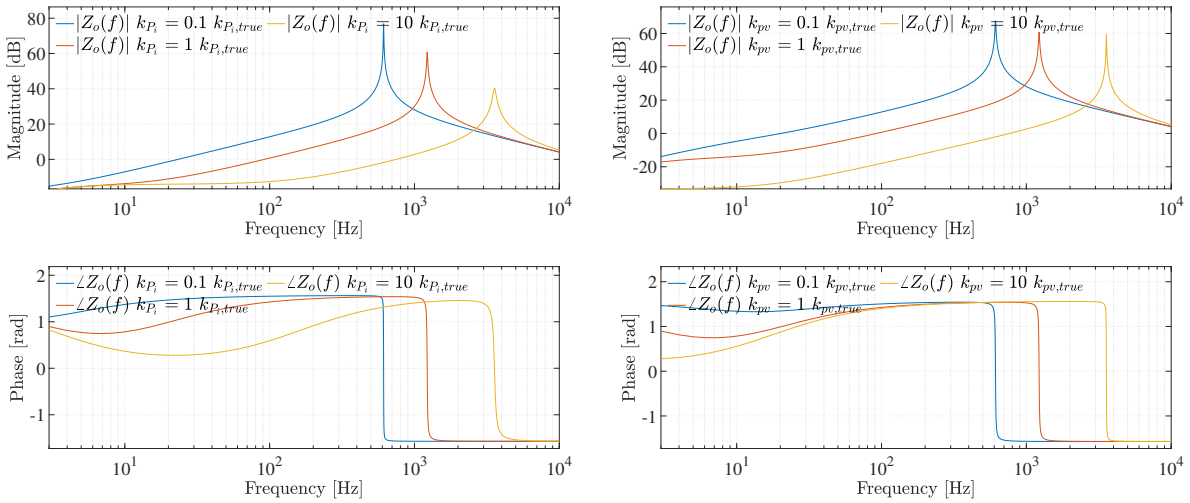

(a) (b)

Figure 4.13: (a) The magnitude and phase response of $Z_o(f)$ as a function of k_{P_i}. (b) The magnitude and phase response of $Z_o(f)$ as a function of k_{pv}.

Fig. 4.14a shows the frequency response of the output impedance as a function of k_{iv}. The gain k_{iv} only affects frequencies lower than 100 Hz of the frequency response of the output impedance. As k_{iv} is increased, the magnitude of the output impedance frequency response in the lower frequency band is reduced. Fig. 4.14b shows the effect of C_f on the frequency response of the output impedance. Increasing the capacitor, C_f, makes the resonant point of the output impedance shift to lower frequencies as shown in Fig. 4.14b. Similar to the capacitor, increasing the inductor, L_f, makes the resonant point of the output impedance shift to lower frequencies as illustrated in Fig. 4.15. This is due to the parallel resonant frequency of the LC filter.

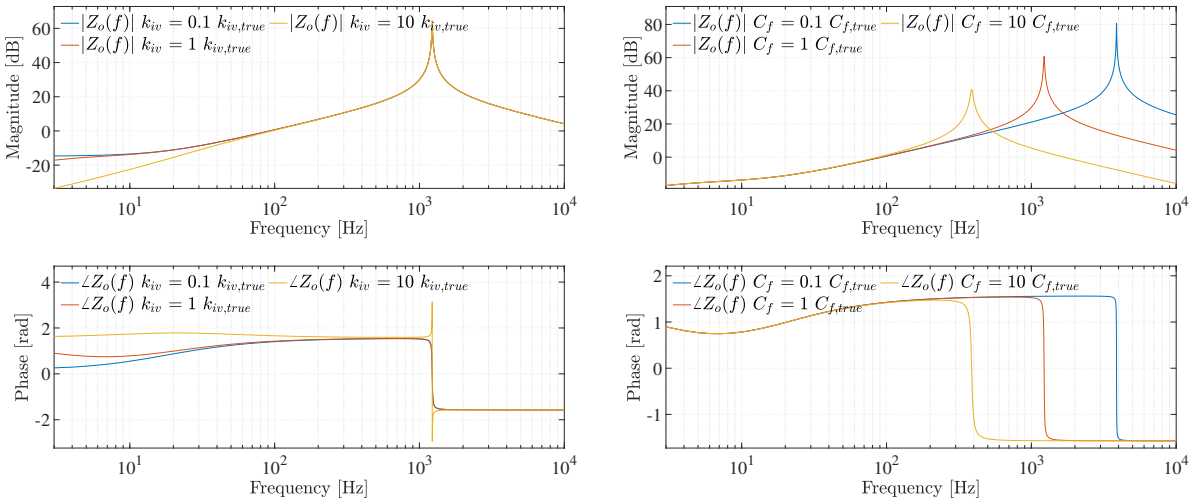

(a) (b)

Figure 4.14: (a) The magnitude and phase response of $Z_o(f)$ as a function of k_{iv}. (b) The magnitude and phase response of $Z_o(f)$ as a function of C_f.

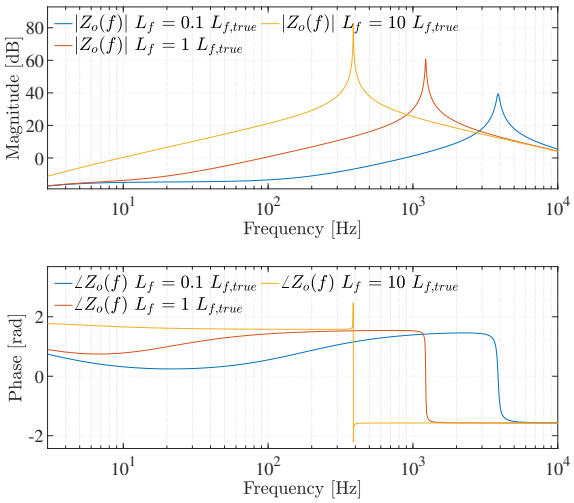

Figure 4.15: The magnitude and phase response of $Z_o(f)$ as a function of L_f.

4.2.5. Parameter Estimation Methodology

The parameter estimation methodology is presented in Fig. 4.16. The filter and controller parameters, θ, of the system are estimated. The parameters of the model are iteratively updated by the optimization algorithm until the output of the model is the same as that of the target system and the objective function is minimized. The output voltage and output current of the target system are measured while under perturbation, $v_{o,S,p}(t)$ and $i_{o,S,p}(t)$, as well as $v_{o,M,p}(t)$ and $i_{o,M,p}(t)$, and while in normal operation, $v_{o,S,n}(t)$ and $i_{o,S,n}(t)$, as well as $v_{o,M,n}(t)$ and $i_{o,M,n}(t)$. The two-measurement approach is used to determine the output impedance of the model, $Z_{o,M}(f)$, as well as of the target system, $Z_{o,S}(f)$. The objective function is calculated as a combination of the errors between the frequency-domain output impedance of the target system and model, as well as the errors between the output current and voltages of the system and model. The objective function is calculated with the MSE as well as the scaled correlation coefficient, ρ.

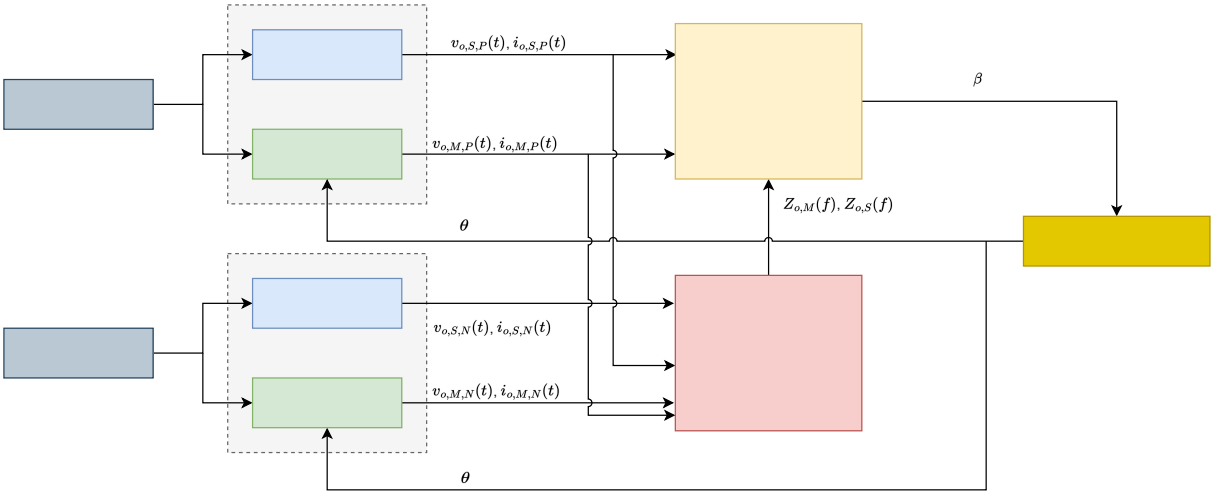

Figure 4.16: Block diagram of the parameter estimation process.

A three-step methodology is implemented to estimate θ:

- **Step 1:** Based on prior knowledge of the inverter, the bounds for θ are chosen. The upper bounds are 100 times larger than the lower bounds. The Grey-Wolf Optimization algorithm is used to minimize the objective function. In this specific optimization process, the Grey-Wolf Optimization algorithm proved to arrive at the global minima whilst being computationally less expensive than the genetic algorithm and particle swarm optimization. The estimated parameters after the first step are labelled θ_1.

- **Step 2:** Using the estimated parameters after step 1, θ_1, the lower and upper bounds are reduced to $\theta_1 \div 3$ and $\theta_1 \times 3$ respectively. The Grey-Wolf Optimization algorithm is used again. The parameters, θ_2, are estimated in step 2.

- **Step 3:** Similarly to step 2, the lower and upper bounds are decreased to $\theta_2 \div 2$ and $\theta_2 \times 2$ respectively, using the estimated parameters after step 2, θ_2. The parameters, θ_2, are also used as the initial input to the pattern search algorithm. The pattern search algorithm is used during refinement, as it is proven to obtain the local minima for an optimization problem more efficiently than global solvers. The estimated parameters, θ_3, are the final estimated parameters.

The parameter estimation process was limited to three steps, as adding more steps might increase the accuracy of the estimated parameters but will also increase the complexity of the process and be time-consuming while not really adding significant precision. Table 4.2 describes the bounds set for the estimated parameters in the optimization algorithms used in steps 1 to 3.

TABLE 4.2: Bounds set in steps 1-3 for the parameters being estimated.

Step	k_{P_i}		k_{pv}		k_{iv}		C_f [μF]		L_f [mH]	
	Lower Bound	**Upper Bound**	**Lower Bound**	**Upper Bound**	**Lower Bound**	**Upper Bound**	**Lower Bound**	**Upper Bound**	**Lower Bound**	**Upper Bound**
1	0.01	10	1	100	10	1000	1.000	100.000	1.010	101.000
2	0.571	5.141	0.974	8.765	19.173	172.56	3.400	30.597	3.316	29.846
3	0.502	2.007	2.650	10.598	35.43	141.72	5.027	20.108	5.285	21.141

Table 4.3 presents the algorithms and objective functions used to estimate θ. A combination of time- and frequency-domain data are used in the objective function in step 1 and 2. In step 3 only the time-domain data is used.

TABLE 4.3: Algorithms and objective functions used in the three-step parameter estimation process.

Step	**Algorithm**	**Objective Function Value, β**
1	Grey Wolf Optimization	MSE($v_{o,S,p}(t)$, $v_{o,M,p}(t)$) + MSE($Z_{o,S}(f)$, $Z_{o,M}(f)$)
2	Grey Wolf Optimization	MSE($v_{o,S,p}(t)$, $v_{o,M,p}(t)$) $\times$ MSE($Z_{o,S}(f)$, $Z_{o,M}(f)$) $\times$ $\rho(Z_{o,S}(f), Z_{o,M}(f))$
3	Pattern Search	MSE($v_{o,S,p}(t)$, $v_{o,M,p}(t)$) + MSE($i_{o,S,p}(t)$, $i_{o,M,p}(t)$)

4.2.6. Results

Table 4.4 shows the estimated parameters, θ_1, θ_2 and θ_3 after steps 1 to 3. Although big errors exist after step 1, the bounds for step 2 can be significantly reduced using the estimated parameters after step 1, θ_1. The accuracy of the estimation is improved in step 2, but a big error still exist in k_{iv}. The final step only makes use of time-domain signals to reduce this error. After step 3 all parameters are estimated within 5.23% accuracy.

TABLE 4.4: Resultant parameter values for each step in the parameter estimation process.

Step	k_{P_i}	k_{P_i} **error** [%]	k_{pv}	k_{pv} **error** [%]	k_{iv}	k_{iv} **error** [%]	C_f [μF]	C_f **error** [%]	L_f [mH]	L_f **error** [%]
1	1.714	71.35	2.921	41.57	57.52	42.48	10.199	1.99	9.949	1.50
2	1.004	0.37	5.299	5.98	70.86	29.14	10.054	0.54	10.571	4.66
3	0.951	4.90	5.252	5.04	105.23	5.23	9.997	0.03	10.094	0.06

Fig. 4.17 and Fig. 4.18 compare the output current and output impedance of the system, using the true parameter values, and the model, using the estimated values. This is done to validate results in Table 4.4. The frequency responses of the output impedances and the output currents of the estimated model and target system are similar, indicating sufficient identification precision.

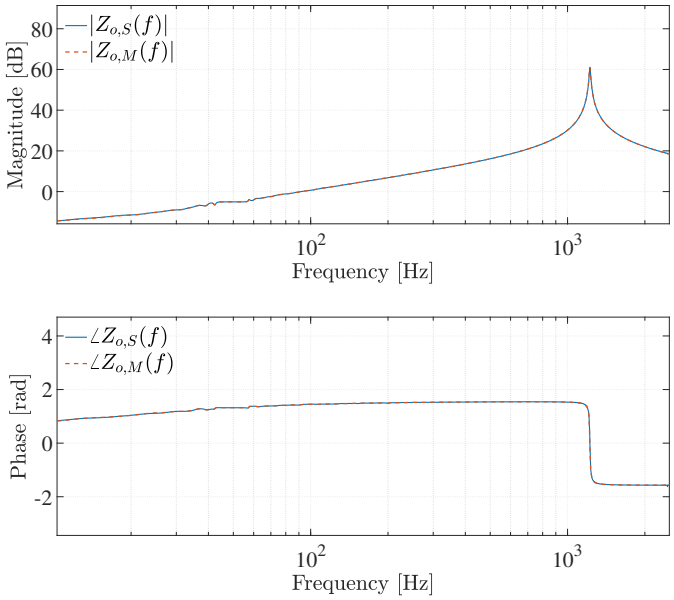

Figure 4.17: Magnitude and phase response of the output impedance of the target, $Z_{o,S}(f)$, and the final estimated model, $Z_{o,M}(f)$.

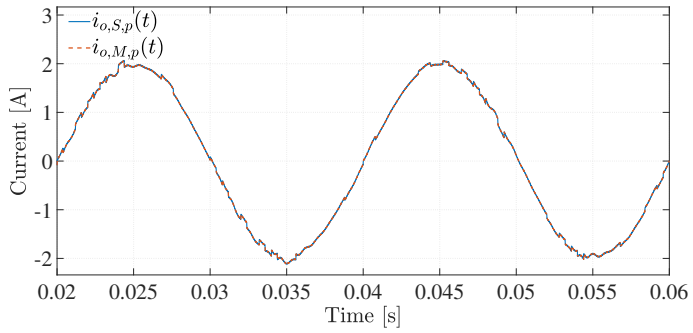

Figure 4.18: The perturbed output current of the system, $i_{o,S,p}(t)$, and the final estimated model, $i_{o,M,p}(t)$.

4.3. Case Study 2: Single-Phase LCL Filter Grid-Connected Voltage Source Inverter

4.3.1. Overview

Another single-phase full-bridge voltage source inverter topology is investigated as a case study. This VSI has the added complexity of a LCL filter and is connected to an AC-source to simulate a grid-tied inverter.

4.3.2. Characterization of Single-Phase AC-connected LCL Filter Voltage Source Inverter with Current Feedback

4.3.2.1. Inverter Topology

Fig. 4.19 presents the topology of the VSI under investigation. It contains a LCL filter at its output, which is connected to an AC voltage source through a series resistor, R_g, and inductor, L_g, to simulate the grid. The inductor current, $i_L(t)$, is fed back to the control loop, where it is compared to a reference inductor current with a 50 Hz fundamental frequency, $i_{L,ref}(t)$. This signal is passed through a controller $G_c(s)$ before it is scaled by the PWM gain, $K_{PWM} = \frac{1}{V_d}$. A full-bridge topology is implemented.

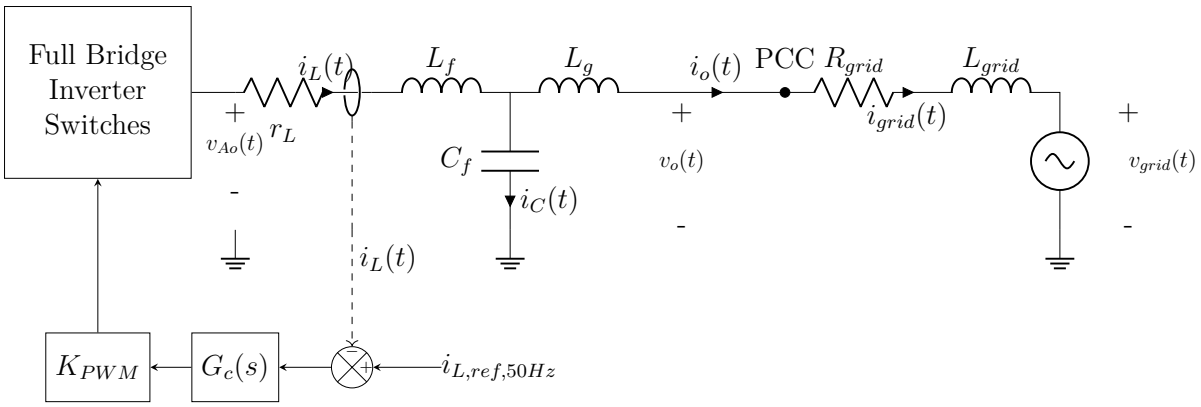

Figure 4.19: Circuit topology of the voltage source inverter used in this investigation.

Fig. 4.20 shows the controller, $G_c(s)$, which consists of the sum of a proportional controller, k_p, and the controller $G_{pr}(s)$. Only the inductor current, $i_L(t)$ is fed into the control loop.

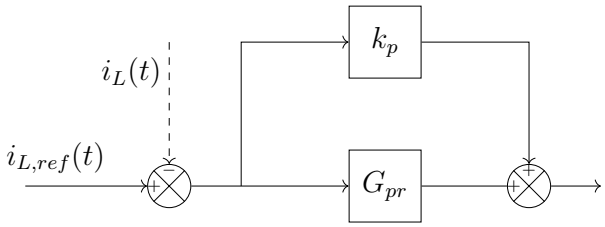

Figure 4.20: The controller, $G_c(s)$.

The Laplace representation of the controller $G_{pr}(s)$ is

$$G_{pr}(s) = \frac{2k_i\omega_{pr}s}{s^2 + 2\omega_{pr}s + {w_g}^2}. \tag{4.23}$$

Table 4.5 summarizes the parameter values of the voltage source inverter that will be estimated in this case study. This includes the controller parameters, as well as that of the filter.

TABLE 4.5: Parameter values of the grid-connected inverter under investigation.

Parameter	k_p	k_i	ω_{pr}	ω_g	C_f [μF]	L_f [mH]	L_g [μ H]
Value	5.4	400	1	314.16	5.3	18	9

4.3.2.2. Mathematical Analysis of Voltage Source Inverter

As seen in Fig. 4.19, the modulation voltage, $v_{Ao}(t)$, can be expressed in the Laplace domain as

$$V_{Ao}(s) = sL_fI_L(s) + sL_gI_o(s) + V_o(s), \tag{4.24}$$

where $s = j2\pi f$. The inductor current, $I_L(s)$, is the sum of the output current, $I_o(s)$, and the capacitor current, $I_C(s)$. This can also be expressed in the Laplace domain as

$$I_L(s) = I_c(s) + I_o(s). \tag{4.25}$$

The capacitor voltage, $V_C(s)$ is expressed as

$$V_c(s) = \frac{I_c(s)}{sC_f}. \tag{4.26}$$

The capacitor voltage, $V_C(s)$ can also be expressed in terms of the output voltage:

$$V_c(s) = sL_gI_o(s) + V_o(s) \tag{4.27}$$

Combining (4.26) and (4.27) results in

$$I_c(s) = s^2C_fL_gI_o(s) + sC_fV_o(s). \tag{4.28}$$

Using (4.28) and (4.25), (4.24) can, therefore, be expressed as

$$V_{Ao}(s) = sL_f(s^2L_gC_fI_o(s) + V_o(s)sC_f + I_o(s)) + sL_gI_o(s) + V_o(s). \tag{4.29}$$

Focusing on the control loop, $V_{Ao}(s)$ can be expressed in the Laplace-domain as

$$\begin{aligned} V_{Ao}(s) &= (k_p + G_{pr})(I_{ref}(s) - I_L(s)) \\ &= (k_p + G_{pr})I_{ref}(s) - (k_p + G_{pr})(I_o(s) + s^2 L_g C_f I_o(s) + V_o(s) s C_f) \\ &= (k_p + G_{pr})I_{ref}(s) - k_p I_o(s) - k_p s^2 L_g C_f I_o(s) - k_p V_o(s) s C_f \\ &- G_{pr} I_o(s) - G_{pr} s^2 L_g C_f I_o(s) - G_{pr} V_o(s) s C_f. \end{aligned} \tag{4.30}$$

Combining (4.29) and (4.30) results in

$$\begin{aligned} &V_o(s)(s^2 L_f C_f + 1 + k_p s C_f + G_{pr} s C_f) \\ &= I_o(s)(-k_p - k_p s^2 L_g C_f - G_{pr} - s^2 L_g C_f G_{pr} - s^3 L_f L_g C_f - s L_f - s L_g) \\ &+ (k_p + G_{pr}) I_{ref}(s). \end{aligned} \tag{4.31}$$

The equivalent output impedance of the inverter, $Z_o(s)$, can be obtained using (4.31) if $I_{ref}(s) = 0A$. The transfer function of the equivalent output impedance of the inverter in Fig. 4.19 has the form

$$Z_o(s) = \frac{V_o(s)}{I_o(s)}|_{I_{ref}(s)=0A} = \frac{b_0 s^5 + b_1 s^4 + b_2 s^3 + b_3 s^2 + b_4 s + b_5}{a_0 s^5 + a_1 s^4 + a_2 s^3 + a_3 s^2 + a_4 s + a_5}. \tag{4.32}$$

Table 4.6 lists the values of the coefficients of the output impedance, $Z_o(f)$, from (4.32).

TABLE 4.6: Coefficients of $Z_o(s)$.

Coefficient	**Value**
b_0	$C_f L_f L_g$
b_1	$C_f L_g (k_p + 2 L_f \omega_{pr})$
b_2	$L_f + L_g + 2 C_f L_g k_i \omega_{pr} + 2 C_f L_g k_p \omega_{pr} + 2 C_f L_g \omega_g^2$
b_3	$k_p + 2 L_f \omega_{pr} + C_f L_g k_p \omega_g^2$
b_4	$2 k_i \omega_{pr} + L_f \omega_g^2 + L_g \omega_g^2$
b_5	$k_p \omega_g^2$
a_0	0
a_1	$C_f L_f$
a_2	$C_f k_p + 2 C_f L_f \omega_{pr}$
a_3	$1 + 2 C_f k_i \omega_{pr} + 2 C_f k_p \omega_{pr} + C_f L_f \omega_g^2$
a_4	$2 \omega_{pr} + C_f k_p \omega_g^2$
a_5	ω_g^2

4.3.3. Parameter Estimation of Filter and Controller Parameters

4.3.3.1. Observability of the Controller and Output Admittance

For the transfer function $G_{pr}(s)$ used in the control loop, the state matrix, $\mathbf{A}$, is determined as

$$\mathbf{A} = \begin{bmatrix} -1.00 & 314.16 \\ -314.16 & -1.00 \end{bmatrix}, \tag{4.33}$$

and its output vector, $\mathbf{c}$, as

$$\mathbf{c} = \begin{bmatrix} 24.00 & -0.16 \end{bmatrix}. \tag{4.34}$$

Using $\mathbf{A}$ and $\mathbf{c}$, the observability matrix, $\mathbf{V}$ is determined as (4.35).

$$\mathbf{V} = \begin{bmatrix} 24.00 & -0.16 \\ 24.40 & 7853.87 \end{bmatrix} \tag{4.35}$$

The rank, ρ, of the observability matrix is not equal to the order, n, of the system:

$$\rho(V) = 1 \neq n = 2 \tag{4.36}$$

This implies that $G_{pr}(s)$ is not observable.

Due to the output impedance not being causal, the observability investigation shifts to the output admittance in the Laplace domain, $Y_o(s)$.

$$Y_o(s) = \frac{1}{Z_o(s)|_{I_{ref}(s)=0}} = \frac{a_1 s^4 + a_2 s^3 + a_3 s^2 + a_4 s + a_5}{b_0 s^5 + b_1 s^4 + b_2 s^3 + b_3 s^2 + b_4 s + b_5} \tag{4.37}$$

The state-space representation of the output admittance, $Y_o(s)$, in the modal canonical form is

$$\mathbf{A} = \begin{bmatrix} -302 & -20.99 \times 10^9 & -6.33 \times 10^{12} & -3.00 \times 10^{15} & -0.62 \times 10^{18} \\ 1 & 0 & 0 & 0 & 0 \\ 0 & 1 & 0 & 0 & 0 \\ 0 & 0 & 1 & 0 & 0 \\ 0 & 0 & 0 & 1 & 0 \end{bmatrix}, \tag{4.38}$$

$$\mathbf{b} = \begin{bmatrix} 1 \\ 0 \\ 0 \\ 0 \\ 0 \end{bmatrix}, \tag{4.39}$$

$$\mathbf{c} = \begin{bmatrix} 0.11 \times 10^6 & 29.92 \times 10^6 & 1.18 \times 10^{12} & 5.10 \times 10^{12} & 0.11 \times 10^{18} \end{bmatrix} \tag{4.40}$$

and

$$d = \left[17.34 \times 10^{-3}\right]. \tag{4.41}$$

Using the matrix, $\mathbf{A}$, and vector, $\mathbf{c}$, the observability matrix, $\mathbf{V}$ can be determined as

$$\mathbf{V} = \begin{bmatrix} 433.24 & -905.66 \times 10^{3} & 442.08 \times 10^{-3} & 266.26 \times 10^{-3} & 1.80 \\ 131.13 \times 10^{3} & 62.76 \times 10^{6} & -109.66 & 147.66 & -419.61 \\ -9.09 \times 10^{12} & 18.99 \times 10^{9} & -48.60 \times 10^{3} & -043.98 \times 10^{3} & 97.72 \times 10^{3} \\ -2.75 \times 10^{15} & -1.32 \times 10^{18} & 017.27 \times 10^{6} & -015.73 \times 10^{6} & -22.76 \times 10^{6} \\ 190.80 \times 10^{21} & -398.04 \times 10^{18} & 4.98 \times 10^{9} & 6.67 \times 10^{9} & 5.30 \times 10^{9} \end{bmatrix}. \tag{4.42}$$

The rank, ρ, of the observability matrix, $\mathbf{V}$, can be determined as

$$\rho(\mathbf{V}) = 2. \tag{4.43}$$

The output admittance is not observable as the rank of the observability matrix, $\rho(\mathbf{V})$, is not equal to the highest order of the transfer function, $n = 5$. Intuitively it is expected that the output impedance is thus also not observable. Using a brute-force optimization algorithm such as GA, particle swarm or globalsearch may still allow accurate determination of the parameter values.

4.3.3.2. Perturbation of a Single-Phase Grid-Tied Voltage Source Inverter with an LCL filter and Output Impedance Characterization

Small-signal perturbations are produced by a PRIS perturbation source applied to the AC output side of the inverter, in parallel with the grid. Fig. 4.21 shows the perturbation arrangement. A PRBS14 is used at a clock frequency, $f_{clk} = 2.5kHz$, together with time constants $\tau_1 = 0.1 \times T_{clk}$ and $\tau_2 = 10 \times T_{clk}$.

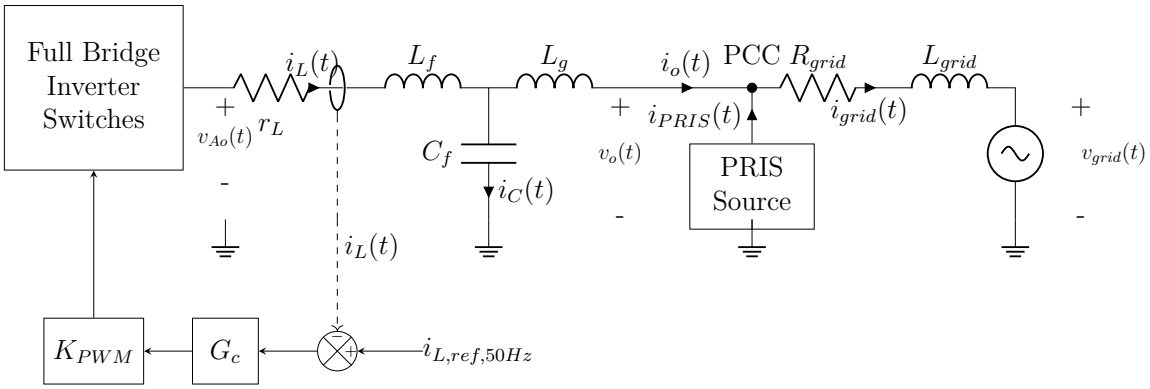

Figure 4.21: The voltage source inverter with the perturbation source connected at its output.

The equivalent output impedance frequency response, $Z_o(f)$, of the target inverter is calculated using the two-measurement approach in simulation. The inverter is operated under normal conditions, as illustrated in Fig. 4.19, as well as perturbed conditions, as illustrated in Fig. 4.21. The output voltage and current measurements are substituted in (4.21) to obtain $Z_o(f)$. The estimated output impedance frequency response is presented in Fig. 4.22. Multiple resonant points exist due to both the LCL filter, as well as the control loop.

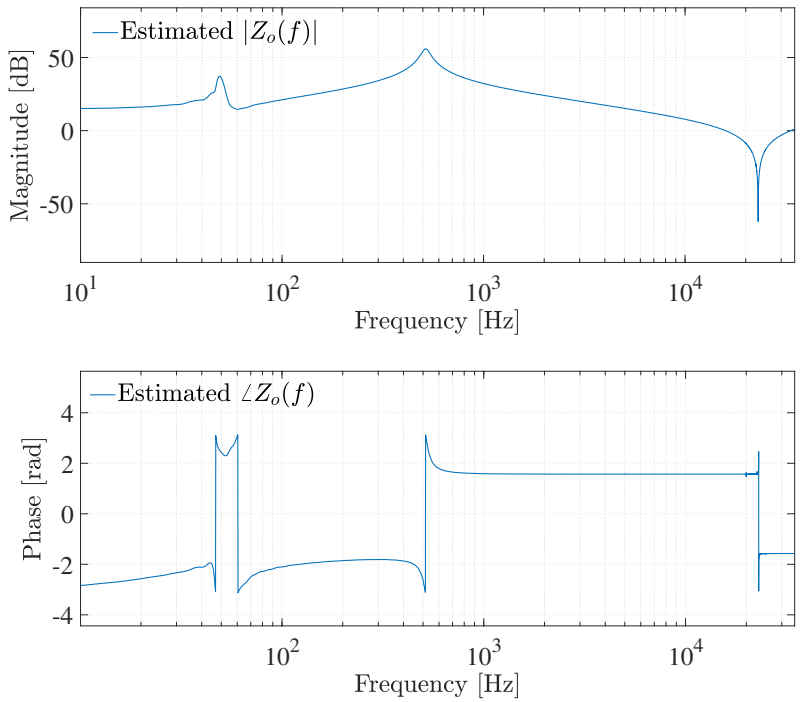

Figure 4.22: Magnitude and phase response of the estimated $Z_o(f)$ using the two-measurement approach.

4.3.3.3. Parameter Estimation of the Grid-Connected Voltage Source Inverter in Simulation

Two logarithmic frequency vectors, between 10 and 2500 Hz and 20500 and 25000 Hz respectively, with 200 and 100 frequency points each, are used during the parameter estimation process. These frequency vectors window the resonant points of the output impedance frequency response. The logarithmic frequency vectors ensure an equitable spread of information over decades. A two-step parameter estimation approach is followed where the upper bounds for the parameters are 100 times greater than the lower bounds in the first step. In the second step the bounds are 2 times higher and lower than the resultant output of the first step, θ_1.

The Genetic Algorithm (GA) is used in the first step, while the second step made use of the particle swarm optimization algorithm. In the first step, the the Mean Squared Error (MSE) between the output impedance of the model, $Z_{o,M}(f)$ and the system, $Z_{o,S}(f)$, is multiplied with the scaled correlation coefficient, $\rho_{scaled}(Z_{o,M}(f), Z_{o,S}(f))$ to obtain an objective function. The scaled correlation coefficient is defined as [131]

$$\rho_{scaled}(Z_{o,M}(f), Z_{o,S}(f)) = -\rho(Z_{o,M}(f), Z_{o,S}(f)) + 1. \tag{4.44}$$

In the second step the MSE of the output voltage and current time-domain signals of the model under perturbation, $v_{o,M,p}(t)$ and $i_{o,M,p}(t)$, and the system under perturbation, $v_{o,S,p}(t)$ and $i_{o,S,p}(t)$, are used in the objective function. Table 4.7 summarizes this process.

TABLE 4.7: The optimization algorithm, bounds and objective function used during the two-step parameter estimation process.

	Algorithm	**Lower Bound**	**Upper Bound**	**Objective Function**	**Output**
Step 1	GA	$\theta/10$	$10 \times \theta$	MSE$((Z_{o,M}(f), Z_{o,S}(f)))$ $\times\rho_{scaled}(Z_{o,M}(f), Z_{o,S}(f))$	θ_1
Step 2	Particle swarm	$\theta_1/2$	$2 \times \theta_1$	MSE$(v_{o,M,p}(t),i_{o,M,p}(t))+(v_{o,S,p}(t),i_{o,S,p}(t))$	θ_2

The resultant parameters after the first and second step can be seen in Table 4.8. After step 1 large errors still exist, although the estimated parameters are in the region of the true parameters. All parameters are estimated accurately after the second step.

TABLE 4.8: Results of Parameter Estimation of Single-Phase Grid-Tied Volt- age Source Inverter with a LCL filter.

Step	k_p	k_p **error** [%]	k_i	k_i **error** [%]	ω_{pr}	ω_{pr} **error** [%]	ω_g	ω_g **error** [%]	C_f [μF]	C_f **error** [%]	L_f [mH]	L_f **error** [%]	L_g [μH]	L_g **error** [%]
1	4.76	11.89	560.60	40.15	0.60	40.29	313.35	0.26	6.27	18.27	15.20	15.54	7.61	15.44
2	5.40	0.02	400.08	0.02	0.99	0.03	314.16	0.00	5.3	0.02	0.018	0.01	9	0.05

To validate the estimated parameters, the output impedance and output voltage of the

model, populated with the estimated parameters, and the system are compared. Fig. 4.23 shows the output voltage of the system and the model under normal operating conditions. Fig. 4.24 compares the frequency response of the output impedance of the system, $Z_{o,S}(f)$, with that of the estimated model, $Z_{o,M}(f)$. Both the frequency and time-domain responses of the estimated model are good representations of the measured system responses, as the responses lie on top of each other.

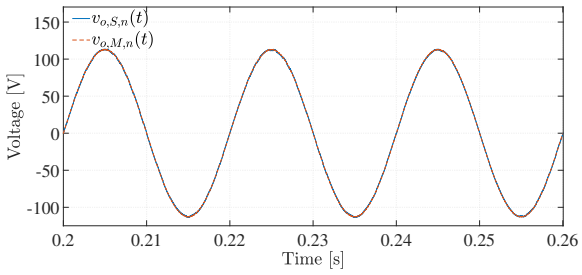

Figure 4.23: Output voltage of the model after estimation, $v_{o,M,n}(t)$, compared to the output voltage of the system, $v_{o,S,n}(t)$, under normal operating conditions.

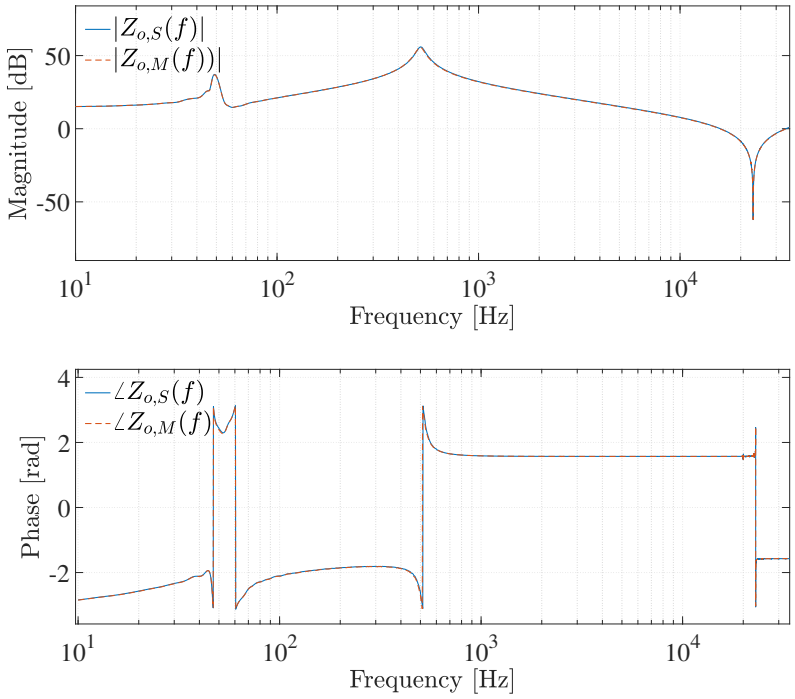

Figure 4.24: Magnitude and phase response of the output impedance of the model after parameter estimation is performed, $Z_{o,M}(f)$, compared to the system $Z_{o,S}(f)$.

Chapter 5

Parameter Estimation of a Full-Bridge Inverter using an Experimental Approach

5.1. Overview

In this chapter, the parameter estimation methodology introduced in chapter 4 using a simulation approach is implemented on a practical inverter system. A high-voltage, single-phase, full-bridge, current-controlled, solar voltage source inverter manufactured by Texas Instruments [132] is investigated. The inductor current of the inverter is controlled by a discrete controller. The inverter, therefore, supplies a constant current to a resistive load connected to the AC output side.

Similar to the methodology discussed in chapter 4, the practical inverter is perturbed at its AC output side with a PRIS source, in parallel with the load. The output voltage and current of the inverter are measured while the inverter is operating normally and while being perturbed. These measurements are used to obtain the output impedance of the inverter. Obtaining the output impedance with the use of the two-measurement approach using experimental measurements is discussed.

A Simulink model of the target system is derived. A sensitivity analysis is conducted on the output impedance frequency response of the inverter model. The experimental measurements are used to estimate accurate parameters for the Simulink model using the particle swarm optimization algorithm. The final model is validated by introducing a stepped voltage response to the system and model and comparing the time-domain output waveforms.

5.2. Practical Arrangement: Standalone Inverter System with a Resistive Load

5.2.1. High-Voltage, Single-Phase, Current-Controlled, Solar Voltage Source Inverter

5.2.1.1. Inverter Specifications

The inverter under investigation is designed as a reference inverter, allowing users more control over the inverter than commercial inverters, although the control-loop and controller parameters can not be modified. A choice was made to operate the inverter in closed-loop standalone mode as manuals for the inverter under investigation do not recommend operating the inverter in grid-connected mode [132]. The inverter has the following specifications:

- Nominal DC Input Voltage: 400 V_{DC}
- Output Power: 600 W
- Closed-loop standalone/closed-loop grid-connected ($110V_{RMS}$ or $220V_{RMS}$)/open-loop standalone operating modes
- Full-bridge switching circuit
- Unipolar-PWM
- LC low-pass filter
- Fundamental frequency of 60 Hz and a Phase Locked Loop (PLL) for grid-connected operation

The sampling frequency of the Analogue to Digital Converter (ADC), f_s, carrier frequency of the PWM generator, f_c and switching frequency, f_{sw}, of the inverter under investigation are all equal to 19.2kHz:

$$f_s = f_c = f_{sw} = 19.2kHz \tag{5.1}$$

5.2.1.2. Full-Bridge Switching Circuit

The switching circuit of the inverter under investigation consists of a full-bridge containing IRG4PC30FDPbf IGBT modules from *International Rectifier*. These IGBTs have a maximum collector-emitter voltage, $V_{CE,max}$ of $600V$, and a maximum collector current, I_c, of 17 A. The IGBT modules are optically coupled to the control signals from the discrete controller. Fig. 5.1 shows the full-bridge switching topology that contains four switches, Q1, Q2, Q3 and Q4. A DC voltage, $v_{DC}(t)$, is provided as an input to the full-bridge.

A modulation voltage, $v_{Ao}(t)$, is produced between the two legs of the switching circuit during operation.

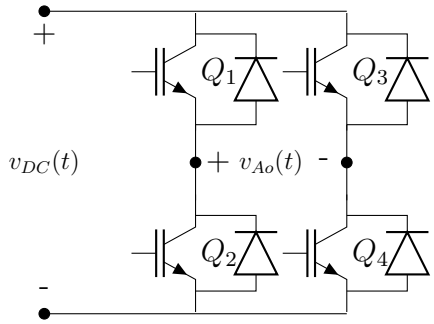

Figure 5.1: Full-bridge configuration.

5.2.1.3. Pulse-Width Modulation Scheme Implemented in the Inverter

A hybrid unipolar Pulse-Width Modulation (PWM) scheme is implemented. The modulation scheme switches one leg of the full-bridge at the grid frequency while the other leg switches at the carrier frequency. The sign of the output signal from the control-loop determines the frequency of the switching leg. Fig. 5.2 demonstrates this PWM scheme.

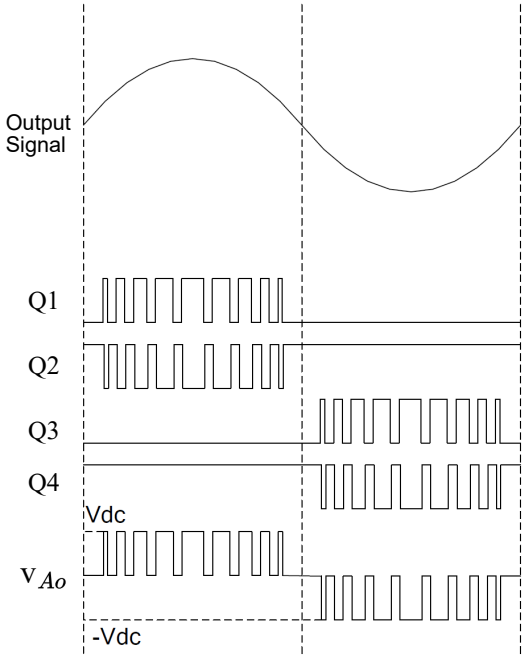

Figure 5.2: Hybrid unipolar pulse width modulation scheme implemented in the inverter under investigation [132].

While the output signal of the control-loop is greater than zero, the logic state of Q3 and Q4 remain 0 and 1 respectively, while Q1 and Q2 switch at the carrier frequency [132]. When the output signal of the control-loop is less than zero, Q1 and Q2 remain 0 and 1

respectively, while Q3 and Q4 switch at the carrier frequency to produce a modulation voltage, $v_{Ao}(t)$.

5.2.1.4. Low-Pass Output Filter

An LC-filter is used to filter the modulated voltage. The filter consists of two series $2.5mH$ inductors and a $1\mu F$ capacitor [133]. The parameter values of the LC filter are measured, as the specified values may differ from the true parameter values due to tolerances and ageing. These measured parameter values will be used during the parameter estimation study to configure an accurate model. Using a 4-wire milli-ohm meter, the two inductors used in the LC-filter are measured to have a parasitic resistance of 0.267Ω and 0.259Ω respectively. Using an LCR meter, the two filter inductors are measured as $2.514mH$ and $2.43mH$ respectively, while the capacitor is measured as $0.949\mu F$.

5.2.1.5. Voltage and Current Sensing

The output voltage of the inverter is fed back to the Analogue to Digital Converter (ADC) of the microcontroller. The output voltage is scaled down with a resistive divider and the output is passed through an operational amplifier that acts as a buffer circuit and low-pass filter. An offset of 1.65 V is added in the operational amplifier circuit. The control-loop is implemented in software that is loaded onto a microcontroller, the 1.65 V offset is accounted for in the software. The voltage sensing circuit is shown in Fig. 5.3.

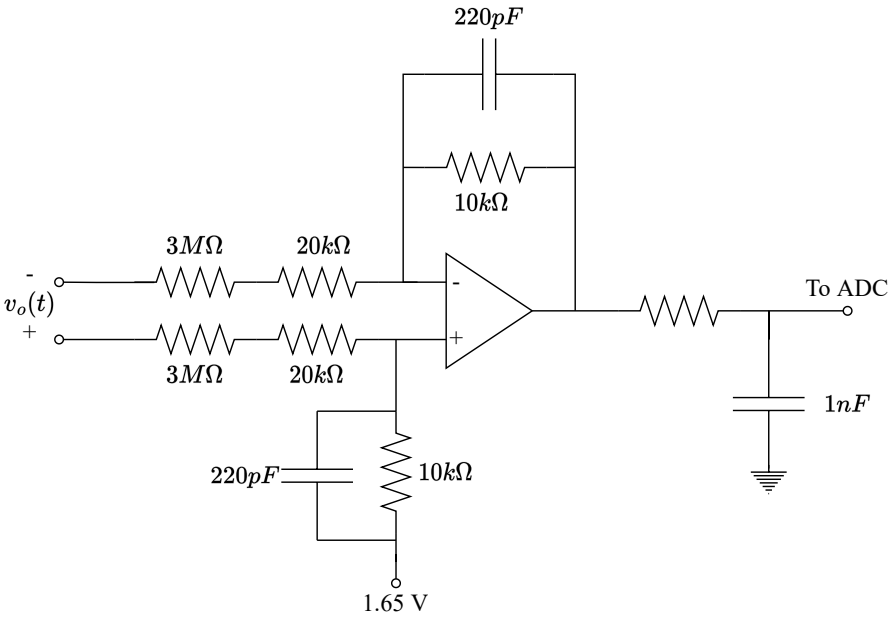

Figure 5.3: The voltage divider and buffer circuit used for voltage sensing [132].

A HNC-03SYB HNC-05SYB Hall current sensor is used to measure the inductor current.

The current measurement is converted to a voltage that is scaled with a resistive circuit and passed through a buffer circuit that also operates as a low-pass filter, also with an offset of 1.65 V.

5.2.1.6. Discrete Controller and Firmware

Fig. 5.4 displays a typical control-loop topology for a grid-connected voltage source inverter. A dual-loop control system exist with an outer DC voltage loop and inner current loop. The outer voltage loop controller, $G_v(s)$, controls the DC bus voltage. A reference voltage, $v_{DC,ref}(t)$ is provided to the control-loop. The inductor current, $i_L(t)$, is controlled by the inner current loop, $D(z)$. The reference current, $i_{ref}(t)$, is determined by the output of the outer voltage loop. A Phase Locked Loop (PLL) synchronizes the output current with the grid voltage, $v_o(t)$. The PLL of the target system consists of a zero crossing detection circuit, implemented with an operational amplifier circuit. Feedforward linearization of the output voltage, $v_o(t)$, is implemented. The transfer function, $G_o(s)$, is defined as:

$$G_o(s) = \frac{I_L(s)}{V_{Ao}(s)} \tag{5.2}$$

The current $I_L(s)$ is the Laplace-domain representation of the inductor current, $i_L(t)$, while $V_{Ao}(s)$ is the Laplace-domain representation of the modulation voltage, $v_{Ao}(t)$.

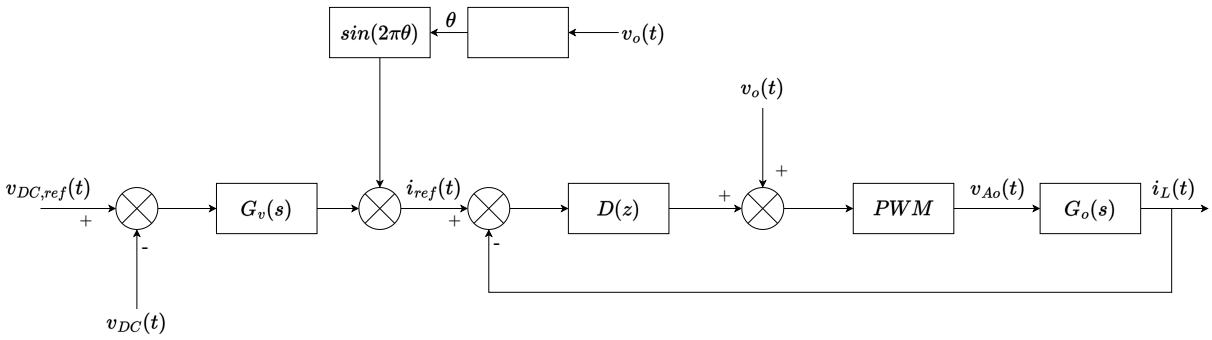

Figure 5.4: Typical control-loop topology for a grid-connected voltage source inverter adapted from [132].

The control loop, protection and modulation scheme is implemented in a Piccolo F28035 microcontroller. The microcontroller can be connected to a Graphical User Interface (GUI) to control operation, i.e. switch the inverter on and off. Two G5LA-14-DC12 relays are used to connect and disconnect the outputs of the inverter to the load or grid.

The microcontroller makes use of an 12-bit ADC to discretize the sensed signals. After sampling, the ADC triggers an interrupt. The Interrupt Service Routine (ISR) calculates the control signals of the outer voltage loop and inner current loop as well as the RMS values of the sensed signals. Similarly, the zero crossing detection circuit triggers an interrupt whenever a zero crossing is detected acting as a PLL.

Various possible control-loops exists for the different modes of operation, i.e. closed-loop grid-connected, closed-loop standalone or open-loop standalone. In this investigation the inverter is operated in standalone control-loop mode, without a MPPT connected to its input. The control topology shown in Fig. 5.4 is thus partially implemented, to exclude the outer voltage loop and PLL.

The target configuration, i.e. the closed-loop standalone voltage source inverter, consists of a current control-loop and voltage linearization. Fig. 5.5 shows a block diagram of a 2P2Z discrete controller, possibly implemented in the current control-loop, $D(z)$. It consists of two poles and two zeros, implemented as a 2^{nd} order infinite impulse response filter.

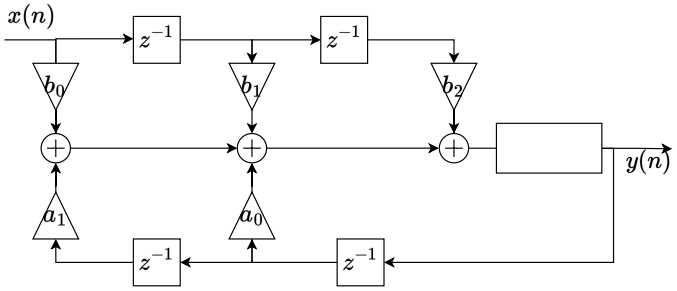

Figure 5.5: Discrete controller implemented in the Piccolo F28035 microcontroller [134].

5.2.2. DC Input Voltage Source

The inverter under investigation is a solar inverter and could be connected to photovoltaic panels through a Maximum Power Point Tracker (MPPT). During this project the inverter is supplied directly from a DC source to allow full control of all inputs to the inverter. A DC voltage of at least 380 V is required at the input of the practical solar inverter under investigation. The circuit topology that is used to supply this DC voltage is shown in Fig. 5.6. It consists of a three-phase 185 V AC voltage source connected to a three-phase variac. The output of the variac is connected to a 88:706, $Y - \Delta$ transformer. The three-phase AC voltage at the output of the transformer is rectified using a diode-rectifier. The inverter has a DC-link capacitor of $1200\mu F$.

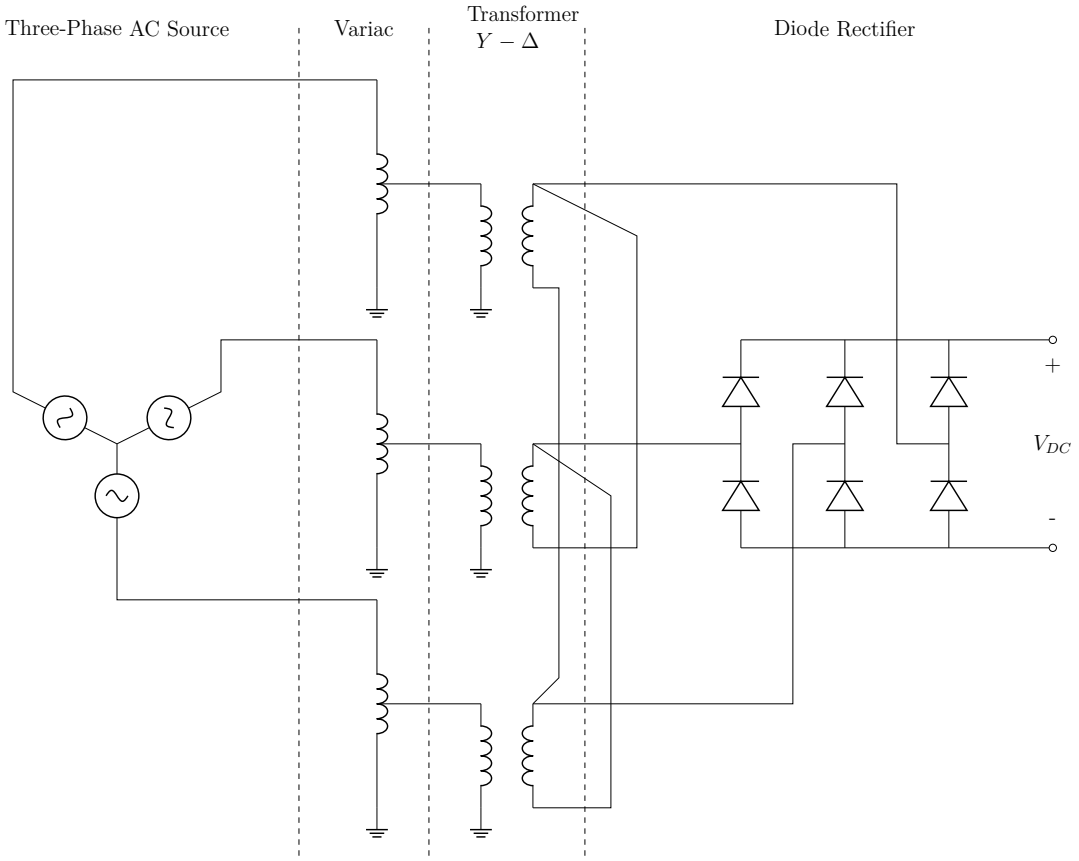

Figure 5.6: Circuit topology of the DC voltage source that is used as input to the solar inverter.

5.2.3. Load Connected to Inverter

Six wire-coiled, high-power resistors are connected in series to the inverter output, denoted by R_{load}. The resistors are expected to contain parasitic inductance, L_p. The load is thus a series RL circuit, described by the transfer function, Z_{load}, defined as

$$Z_{load}(f) = R_{load} + j2\pi f L_p. \tag{5.3}$$

The parameter values of the load will be used during the parameter estimation study and, therefore, needs to be accurate. To acquire accurate load parameters, R_{load} and L_p are first estimated using the experimental magnitude and phase responses of the practical load. The load parameters are also measured to validate these values.

The load is perturbed with a PRIS source in order to obtain the experimental impedance frequency response, $Z_{load,exp}(f)$. The frequency response, $Z_{load,exp}(f)$, is used to estimate the values R_{load} and L_p to model the load. The estimated values are 20.5Ω and $414\mu H$ respectively. These estimated values are substituted in (5.3) to obtain $Z_{load,est}(f)$.

Using a 4-wire milli-ohm meter, the load is measured to have a resistance of 20.6Ω. The parasitic inductance is measured as $361\mu H$ using a LCR meter. These measured

values are substituted in (5.3) to obtain $Z_{load,meas}(f)$.

In Fig. 5.7 the measured frequency response of the load, $Z_{load,exp}(f)$, the transfer function $Z_{load,est}(f)$ and the transfer function $Z_{load,meas}(f)$ are compared. All of the magnitude and phase responses are similar. From Fig. 5.7 it can be seen that the load is resistive between 10 Hz and 1kHz and is inductive at frequencies higher than 1kHz.

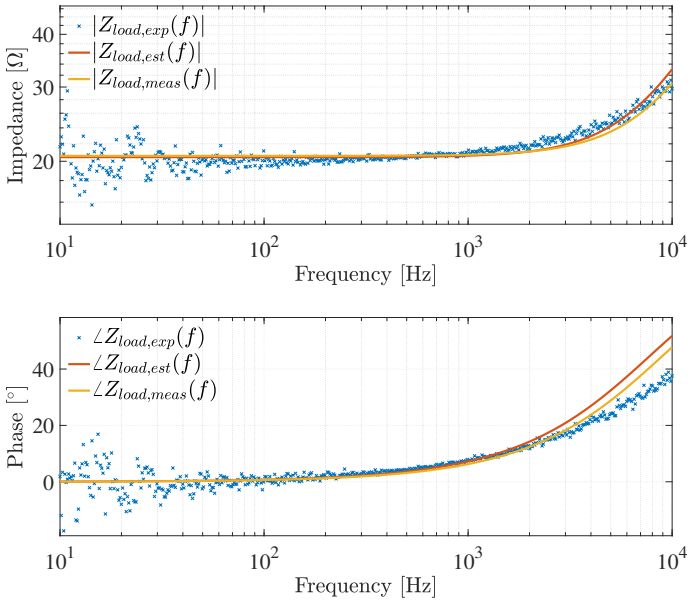

Figure 5.7: Magnitude and phase response of the experimental load, $Z_{load,exp}(f)$, estimated RL representation, $Z_{load,est}(f)$, and the measured RL representation, $Z_{load,meas}(f)$.

5.2.4. Pseudo-Random Impulse Sequence Perturbation Source

The PRIS source discussed in chapter 3 is used to perturb the practical inverter system. For each application the DC voltage, clock frequency, PRBS order and RLC values are chosen appropriately to excite the relevant frequency band of the inverter sufficiently.

5.2.5. Experimental Results under Normal Inverter Operating Conditions

The output voltage and current of the inverter arrangement is measured while the inverter is operating under normal conditions in standalone mode. The inverter system should supply the 20.6Ω resistor connected to the AC output side with a constant RMS current of 2.62 A. The expected RMS output voltage is thus 54.2 V.

The DC input voltage of the source discussed in section 5.2.2 is measured and displayed in Fig. 5.8 before and after the inverter is switched on. The input voltage is set to 380 V prior to switching on the inverter, as this is the minimum DC voltage required to switch

on the inverter. It is clear that there exists a voltage drop of approximately 40 V when the inverter is switched on, indicating that the source contains a series impedance. Switching the inverter on creates noise on the input voltage.

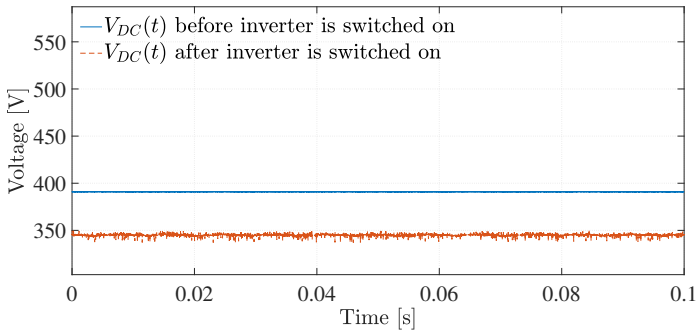

Figure 5.8: DC input voltage, $V_{DC}(t)$, under normal operating conditions before and after the inverter is switched on.

The experimental output voltage and current without perturbation whilst in normal operation, $v_{o,n}(t)$ and $i_{o,n}(t)$, are shown in Fig. 5.9. The voltage and current has a RMS value of $53.1V$ and $2.6A$ respectively, which is close to the expected voltage and current values. The voltage and current appears sinusoidal, although switching ripple is clearly present. A small amount of discontinuity is present at the zero-crossings due to deadtime.

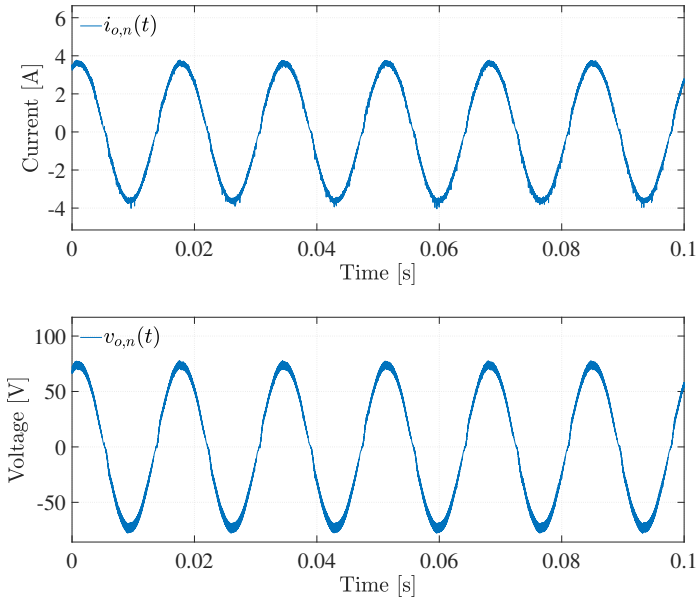

Figure 5.9: Output current, $i_{o,n}(t)$, and voltage, $v_{o,n}(t)$, of the high-voltage, current-controlled voltage source inverter under investigation under normal operating conditions.

5.3. Overview of Perturbation of a Practical Single-Phase Full-Bridge Inverter

Similar to the discussion in chapter 4, where a PRIS source is used to perturb an inverter through simulation, the PRIS source is used to perturb the practical inverter under investigation. A practical PRIS source is used, instead of an ideal PRIS source.

In the inverter under investigation no outer DC voltage loop exists. Therefore, the DC voltage is not used to determine the reference current signal. Consequently, varying the DC input voltage would not necessarily be an applicable perturbation methodology, as discussed in section 2.2.2.2. The AC output side is thus perturbed.

A high-level block digram of the perturbation arrangement is displayed in Fig. 5.10. The PRIS source is connected in parallel to the load, at the AC output side of the inverter. The output time-domain waveforms of the inverter are fed to the control-loop. Therefore, perturbing these controlled output time-domain waveforms would perturb not only the output waveforms, but also the control-loop. This makes it possible to estimate both the controller and filter parameters.

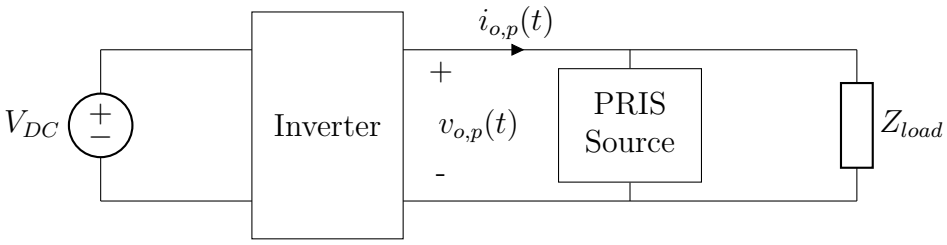

Figure 5.10: High-level block diagram of the perturbation arrangement. The PRIS source is connected to the AC output of the inverter, in parallel with the load.

The PRIS source discussed in chapter 3 is developed and used to perturb the inverter. A PRBS12 is used with a clock frequency, $f_{clk} = 12kHz$. The sampling frequency, f_s, of the discrete controller is $19.2kHz$, therefore, the discrete controller is operational at frequencies lower than $f_s/2 = 9.6kHz$. PRIS perturbation with a clock frequency of $12kHz$ allows excitation of the entire frequency band in which the discrete controller is operating. A 30 V DC voltage is supplied to the PRIS source, and the RLC filter values are 100Ω, $4.4mH$ and $10\mu F$ respectively.

The 100Ω resistor value together with the large capacitor allows for better low frequency perturbations [94]. The large inductor causes a slow change in the current, allowing the discrete current-controller to work continuously. It is observed that if the DC voltage is increased to more than 30 V that the output voltage perturbation amplitudes could become 30% - 60% of the nominal output voltage. The control-loop can cause saturation if the output voltage and current are too large. To avoid introducing non-linear inverter behaviour, the DC voltage of the PRIS source is not increased beyond 30 V to limit

perturbation amplitudes.

The perturbed output current and voltage, $i_{o,p}(t)$ and $v_{o,p}(t)$, are displayed on top of the normal operating current and voltage, $i_{o,n}(t)$ and $v_{o,n}(t)$, in Fig. 5.11. The PRIS perturbations are clearly superimposed on the output waveforms. It can be seen that even in the perturbed state, the inverter output waveforms correlate well with those from the non-perturbed inverter.

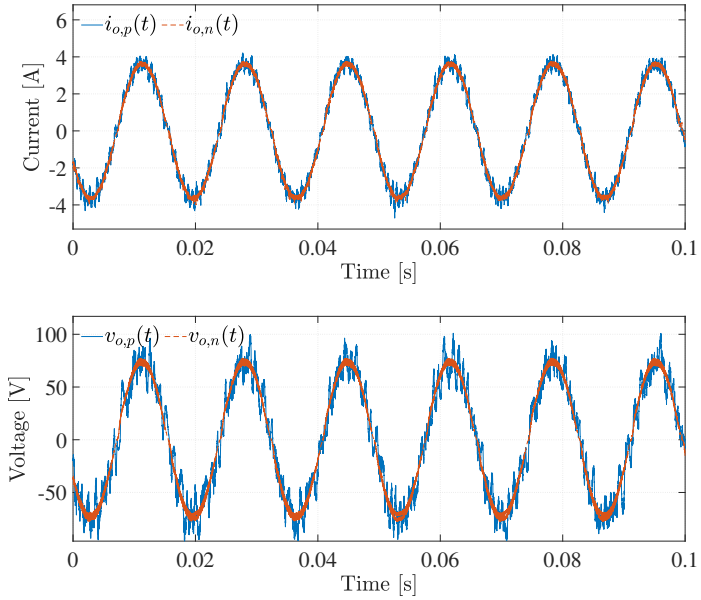

Figure 5.11: Time-domain output voltage and current under normal operating conditions, $v_{o,n}(t)$ and $i_{o,n}(t)$, as well as during perturbation, $v_{o,p}(t)$ and $i_{o,p}(t)$.

5.4. Estimation of the Output Impedance of the Inverter using Measured Output Voltage and Current Waveforms

The two-measurement approach introduced in chapter 4 is also used to estimate the output impedance of the practical inverter. The two-measurement approach assumes that the inverter can be described as a Thévenin equivalent, as illustrated in Fig. 4.3. Equation (4.21) is derived in section 4.2.4.2 and presented here as (5.4). The output current and voltage of an inverter are measured while the inverter is operating under normal operating conditions, $i_{o,n}(t)$ and $v_{o,n}(t)$, and while the inverter is perturbed with a PRIS source, $i_{o,p}(t)$ and $v_{o,p}(t)$. The frequency-domain representations of the measured time-domain signals, $I_{o,n}(f)$, $V_{o,n}(f)$, $I_{o,p}(f)$ and $V_{o,p}(f)$ are used to obtain the output impedance, $Z_o(f)$:

$$Z_o(f) = \frac{V_{o,p}(f) - V_{o,n}(f)}{I_{o,p}(f) - I_{o,n}(f)} \tag{5.4}$$

The two-measurement approach assumes that the time-domain representation of the

Thévenin source, $v_{TH}(t)$, is synchronized while the inverter is operating normally and while it is perturbed. The measured signals are recorded at random time instances and not at $t = 0$ as in simulation. Therefore, $v_{TH}(t)$ is not inherently synchronized. The voltage $v_{TH}(t)$ needs to be synchronized manually by only accessing the output voltages and currents under perturbed and normal conditions.

From chapter 4 the frequency-domain representation of $v_{TH}(t)$, $V_{TH}(f)$, contained the Laplace transform of the reference voltage, $v_{ref}(t)$, as well as a transfer function, $G(f)$, in the case of a voltage-controlled inverter. In the case of the current-controlling inverter under investigation the reference current, $i_{ref}(t)$, needs to be aligned to allow synchronization of $v_{TH}(t)$. The signal $i_{ref}(t)$ is not accessible as it is implemented in the microcontroller.

Three different methods are introduced and compared to estimate the output impedance of the inverter using measured output voltage and current waveforms of the perturbed inverter as well as the inverter under normal operating conditions. Two of these methods make use of the two-measurement approach. The methods are as follows:

- **Method 1:** This method synchronizes the time-domain Thévenin voltage source, $v_{TH}(t)$, in the perturbed and normal case by aligning the output currents. The two-measurement approach is then implemented using the aligned time-domain waveforms. This method makes use of Welch's estimate to determine (5.4) and is presented in section 5.4.1.
- **Method 2:** This method uses the Power Spectral Densities (PSDs) and Cross Power Spectral Densities (CPSDs) of the measured output voltages and currents in the two-measurement approach in such a way that no time-alignment of $v_{TH}(t)$ is needed. The PSDs and CPSDs are calculated using Welch's estimate. Method 2 is discussed in section 5.4.2.
- **Method 3:** In this method the inverter is perturbed at the DC input, in addition to the AC output perturbations as discussed in section 5.3. The input and output perturbations are used to model the inverter as a two-port network. This method does not make use of the two-measurement approach described by (5.4). Method 3 is discussed in section 5.4.3.

5.4.1. Method 1: Estimation of the Output Impedance using Time-Domain Alignment

To make use of the two-measurement approach, the Thévenin voltage, $v_{TH}(t)$, first needs to be synchronized under normal and perturbed conditions. It is first proven that the output currents, $i_{o,p}(t)$ and $i_{o,n}(t)$, are aligned when $v_{TH}(t)$ is synchronized. The methodology to

align $i_{o,p}(t)$ and $i_{o,n}(t)$ is then presented. Finally, the output impedance is obtained using this method.

To prove that $i_{o,p}(t)$ and $i_{o,n}(t)$, are aligned when $v_{TH}(t)$ is synchronized, a simulation approach is adopted. Fig. 5.12 shows the simulated output voltages and currents of the inverter under investigation while it is operating under normal and perturbed conditions. In the simulation, the reference current, $i_{ref}(t)$, and, therefore, also the Thévenin voltage, $v_{TH}(t)$, is synchronized for the two scenarios.

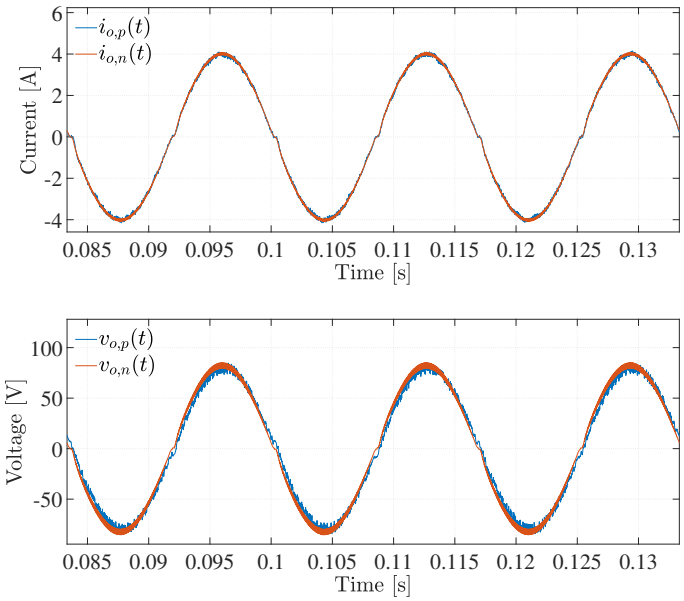

Figure 5.12: Simulated time-domain waveforms of the perturbed and non-perturbed output voltages and currents, $v_{o,p}(t)$ and $i_{o,p}(t)$ as well as $v_{o,n}(t)$ and $i_{o,n}(t)$ respectively.

Table 5.1 displays the difference in phase between the simulated output signals in Fig. 5.12. When $i_{ref}(t)$ is aligned, and thus also $v_{TH}(t)$, a negligible 0.298° phase difference occur between the fundamental frequency component of the perturbed and normal output currents, $i_{o,p}(t)$ and $i_{o,n}(t)$. This proves that the alignment of the output currents $i_{o,p}(t)$ and $i_{o,n}(t)$ synchronizes $v_{TH}(t)$. The output impedance can subsequently be calculated using (5.4).

TABLE 5.1: The phase differences between the fundamental frequency component of the simulated perturbed and normal measurements while $i_{ref}(t)$ is synchronized for the perturbed and non-perturbed case.

$v_{o,p}(t)$ and $i_{o,p}(t)$ [°]	$v_{o,n}(t)$ and $i_{o,n}(t)$ [°]	$i_{o,p}(t)$ and $i_{o,n}(t)$ [°]	$v_{o,p}(t)$ and $v_{o,n}(t)$ [°]
3.405	0.378	0.298	4.081

A methodology to align the time-domain signals, $i_{o,p}(t)$ and $i_{o,n}(t)$, is now introduced. Unlike in simulation where data can be recorded at $t = 0$, the practical data starts

recording at random time instances, as presented in Fig. 5.13, where $i_{o,p}(t)$ and $i_{o,n}(t)$ is recorded at random starting points.

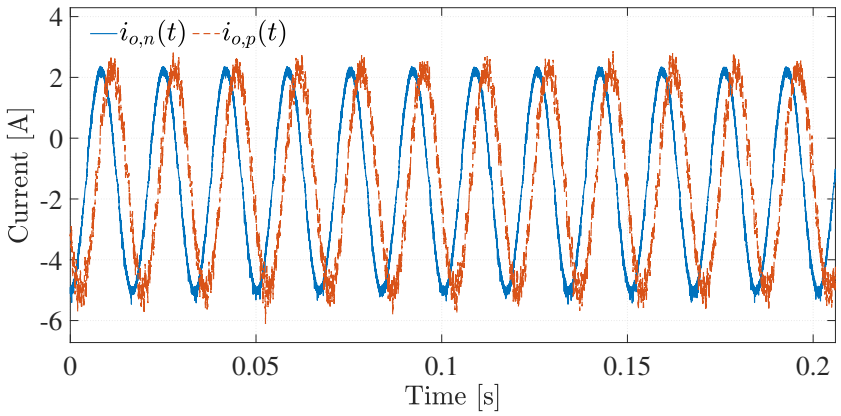

Figure 5.13: Currents $i_{o,p}(t)$ and $i_{o,n}(t)$ measured at different initial starting points.

The flow diagram in Fig. 5.14 illustrates how $i_{o,n}(t)$ and $i_{o,p}(t)$ are aligned using the measured waveforms. The current $i_{o,n}(t)$ is fixed while $i_{o,p}(t)$ is shifted over a fundamental period, $T_1 = 1/60 = 0.0167s$, in increments of the sampling period, $T_s = 1\mu s$, that is used to measure the current. At each increment, m, the Mean Squared Error (MSE) between the time-domain waveforms, $i_{o,n}(t)$ and the shifted $i_{o,p}(t)$, is determined. The number of increments, M, needed to minimize the MSE between $i_{o,n}(t)$ and the shifted $i_{o,p}(t)$ is determined.

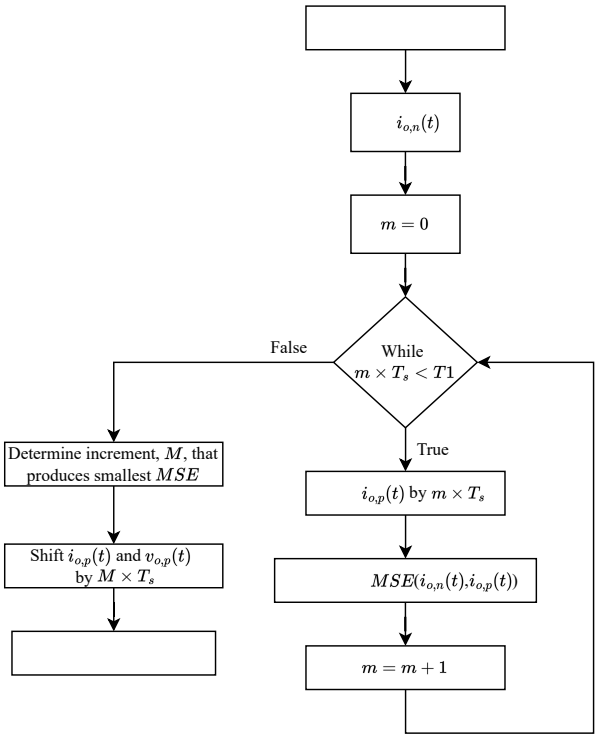

Figure 5.14: Flow-diagram explaining the synchronization of $i_{o,n}(t)$ and $i_{o,p}(t)$.

The current $i_{o,p}(t)$ is thus shifted by M sampling periods to be aligned with $i_{o,n}(t)$. The voltage $v_{o,p}(t)$ is also shifted by M sampling periods to produce the time-domain waveforms displayed in Fig. 5.16. From Fig. 5.16 it can be seen that the perturbed and non-perturbed current waveforms are synchronized.

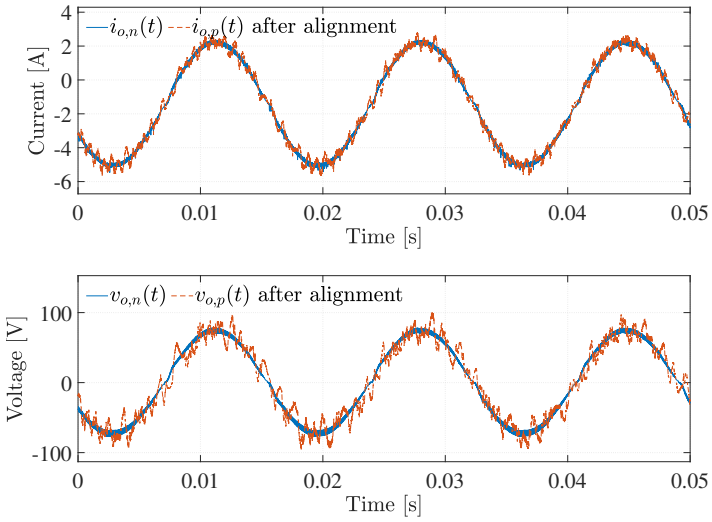

Figure 5.15: Shifted perturbed signals as well as the fixed normal measurements.

The small-signal waveforms can subsequently be obtained by taking the difference between the perturbed and normal current and voltage measurements that has been aligned. Fig. 5.16 displays the small-signal waveforms. The small-signal waveforms are not ideal PRIS signals, as the impedance of the inverter and load changes the PRIS perturbation time-constants.

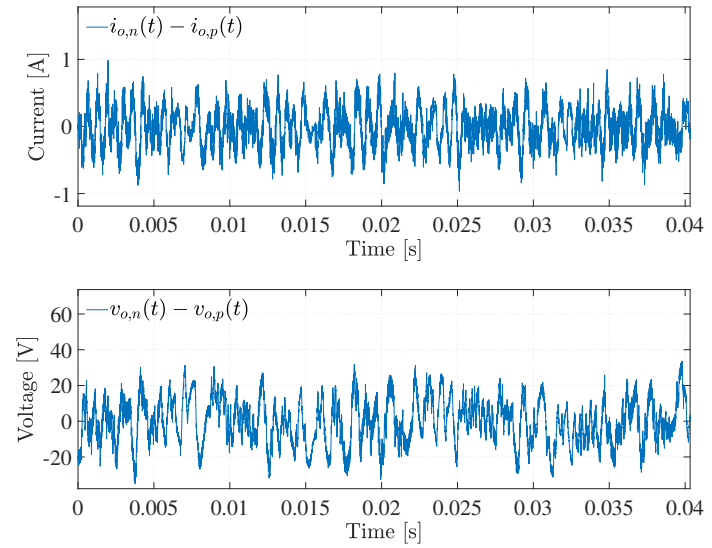

Figure 5.16: Small-signal waveforms, $i_{o,n}(t) - i_{o,p}(t)$ and $v_{o,n}(t) - v_{o,p}(t)$.

Equation (5.4) is determined using Welch's estimate of the two-measurement approach with the aligned output time-domain waveforms:

$$\begin{aligned} Z_o(f) &= \frac{V_{o,p}(f) - V_{o,n}(f)}{I_{o,p}(f) - I_{o,n}(f)} \\ &\approx Z_{o,1}(f) \approx Z_{o,2}(f) = \frac{P_{yy}(f)}{P_{xy}(f)} = \frac{P_{(v_{o,p}(t)-v_{o,n}(t)),(v_{o,p}(t)-v_{o,n}(t))}(f)}{P_{(i_{o,p}(t)-i_{o,n}(t)),(v_{o,p}(t)-v_{o,n}(t))}(f)} \end{aligned} \tag{5.5}$$

The H_1 and H_2 estimators are discussed in section 2.6.3. Although the two estimationsof the output impedance, $Z_{o,1}(f)$ and $Z_{o,2}(f)$ could be used, this project uses $Z_{o,2}(f)$ throughout, therefore, $Z_o(f) = Z_{o,2}(f)$.

The aligned time-domain waveforms of the perturbed practical inverter from Fig. 5.11 are used to obtain $Z_o(f)$ between 500 Hz and 10 kHz. Fig. 5.17 presents the output impedance frequency response, $Z_o(f)$, of the inverter. It can be seen that series and parallel resonant points are present at approximately 1.8kHz and 4kHz respectively. At frequencies beyond 4kHz the impedance is predominantly capacitive. The output impedance frequency response at frequencies lower than 500 Hz is dicussed in subsequent sections.

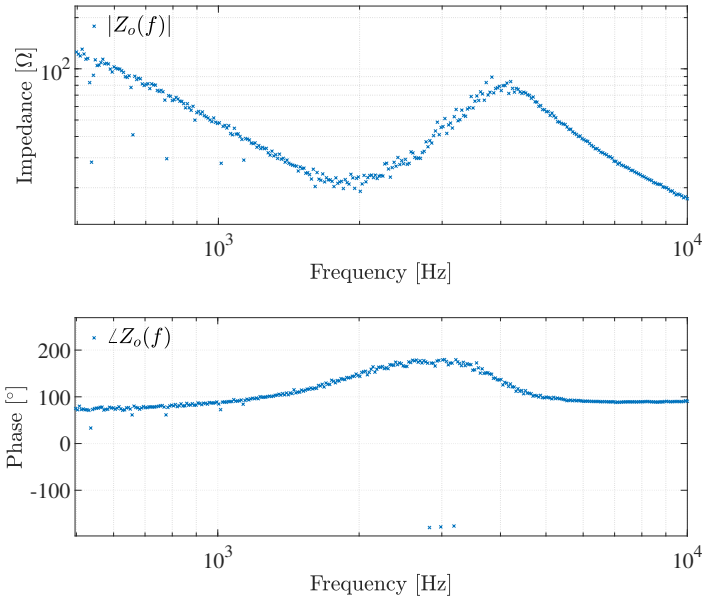

Figure 5.17: Magnitude and phase response of the output impedance, $Z_o(f)$.

5.4.2. Method 2: Estimation of the Output Impedance using Spectral Densities

A methodology to determine the output impedance without time-alignment, but instead using Power Spectral Densities (PSDs) and Cross Power Spectral Densities (CPSDs)

within the two-measurement approach is now introduced. Equation (5.4) makes use of the frequency-domain representations of the voltages and currents $V_{o,p}(f)$, $V_{o,n}(f)$, $I_{o,p}(f)$ and $I_{o,n}(f)$. If $Y(f)$ is defined as

$$Y(f) = V_{o,p}(f) - V_{o,n}(f), \tag{5.6}$$

and $X(f)$ is defined as

$$X(f) = I_{o,p}(f) - I_{o,n}(f), \tag{5.7}$$

equation (5.4) becomes

$$Z_o(f) = \frac{Y(f)}{X(f)}. \tag{5.8}$$

The time-domain representation of (5.6) and (5.7) is $y(t) = v_{o,p}(t) - v_{o,n}(t)$ and $x(t) = i_{o,p}(t) - i_{o,n}(t)$ respectively [135].

Two estimations of the transfer function $Z_o(f)$ using the CPSDs and PSDs of the time-domain signals exist [121, 122]. The first estimate uses the CPSD, $P_{yx}(f)$, of the two signals, $x(t)$ and $y(t)$, and the PSD, $P_{xx}(f)$ between the input signal, $x(t)$ [120]:

$$Z_{o,1}(f) = \frac{P_{yx}(f)}{P_{xx}(f)} \tag{5.9}$$

The transfer function could also be estimated using the CPSD, $P_{xy}(f)$, between the two signals and the PSD of the output signal, $P_{yy}(f)$ [120]:

$$Z_{o,2}(f) = \frac{P_{yy}(f)}{P_{xy}(f)} \tag{5.10}$$

Equations (5.9) and (5.10) are usually obtained using Welch's estimate. This approach uses windowing, as discussed in section 2.6.1, to reduce leakage, the influence of random noise and variance. If no windowing is used to determine (5.9) and (5.10):

$$Z_{o,1}(f) = Z_{o,2}(f) \tag{5.11}$$

Due to windowing while obtaining the PSDs and CPSDs, the two estimates, $Z_{o,1}(f)$ and $Z_{o,2}(f)$ will not be exactly the same [123], but approximations of each other:

$$Z_{o,1}(f) \approx Z_{o,2}(f) \tag{5.12}$$

Subsequent calculations in this section aim to determine $Z_{o,1}(f)$, although the exact same methodology could be used to determine $Z_{o,2}(f)$. First the mathematical representations of the PSD and CPSD are introduced. The PSD, $P_{xx}(f)$ of a signal, $x(t)$, is defined as [111]

$$P_{xx}(f) = \int_{-\infty}^{\infty} R_{xx}(\tau) e^{-j2\pi f\tau} d\tau, \tag{5.13}$$

where $R_{xx}(\tau)$ is the autocorrelation function of the signal, $x(t)$. The autocorrelation function is defined as [111]

$$R_{xx}(\tau) = \lim_{T\to\infty} \frac{1}{T} \int_{-\infty}^{\infty} x(t)x(t+\tau) d\tau, \tag{5.14}$$

or

$$R_{xx}(\tau) = \lim_{T\to\infty} \frac{1}{T} \int_{-\infty}^{\infty} x(t)x(t-\tau) d\tau. \tag{5.15}$$

The autocorrelation function is symmetrical. This implies that [111]

$$R_{xx}(\tau) = R_{xx}(-\tau). \tag{5.16}$$

Additionally, the Cross-Power Spectral Density (CPSD), $P_{xy}(f)$, between two signals, $x(t)$ and $y(t)$, is defined as [118]

$$P_{xy}(f) = \int_{-\infty}^{\infty} R_{xy}(\tau) e^{-j2\pi f\tau} d\tau, \tag{5.17}$$

where $R_{xy}(\tau)$ is the cross-correlation function. The cross-correlation function is defined as [118]

$$R_{xy}(\tau) = \lim_{T\to\infty} \frac{1}{T} \int_{-\infty}^{\infty} x(t)y(t-\tau) d\tau. \tag{5.18}$$

The cross-correlation function is not symmetrical. Therefore, [118]

$$R_{xy}(\tau) = R_{yx}(-\tau). \tag{5.19}$$

The definitions of the PSD and CPSD presented in (5.13) - (5.19) are now used to estimate the output impedance of the inverter. PSDs and CPSDs are typically obtained by applying Welch's estimate to determine (5.13) and (5.17).

The PSD, $P_{xx}(f)$, and CPSD, $P_{yx}(f)$, are required to determine (5.9). The autocorrelation function, $R_{xx}(f)$, as referenced in (5.15), is required prior to determining $P_{xx}(f)$. The autocorrelation function, $R_{xx}(f)$, of the signal $x(t) = i_{o,p}(t) - i_{o,n}(t)$ is given by

$$\begin{aligned} R_{xx}(\tau) &= \lim_{T\to\infty} \frac{1}{T} \int_{-\infty}^{\infty} x(t)x(t-\tau) d\tau \\ &= \lim_{T\to\infty} \frac{1}{T} \int_{-\infty}^{\infty} [i_{o,p}(t)i_{o,p}(t-\tau) - i_{o,p}(t)i_{o,n}(t-\tau) \\ &- i_{o,n}(t)i_{o,p}(t-\tau) + i_{o,n}(t)i_{o,n}(t-\tau)] d\tau \\ &= R_{i_{o,p}i_{o,p}}(\tau) - R_{i_{o,n}i_{o,p}}(\tau) - R_{i_{o,p}i_{o,n}}(\tau) + R_{i_{o,n}i_{o,n}}(\tau). \end{aligned} \tag{5.20}$$

In (5.20) the autocorrelation function, $R_{xx}(\tau)$, consists of the sum of two autocorrelation functions, $R_{i_{o,p}i_{o,p}}(\tau)$ and $R_{i_{o,n}i_{o,n}}(\tau)$, while two cross-correlation functions, $R_{i_{o,n}i_{o,p}}(\tau)$ and $R_{i_{o,p}i_{o,n}}(\tau)$ are subtracted. Using (5.20) and (5.13) the PSD, $P_{xx}(f)$, of the signal $x(t) = i_{o,p}(t) - i_{o,n}(t)$ is derived as

$$\begin{aligned} P_{xx}(f) &= \int_{-\infty}^{\infty} (R_{i_{o,p}i_{o,p}}(\tau) - R_{i_{o,n}i_{o,p}}(\tau) - R_{i_{o,p}i_{o,n}}(\tau) + R_{i_{o,n}i_{o,n}}(\tau)) e^{-j2\pi f\tau} d\tau \\ &= P_{i_{o,p}i_{o,p}}(f) - P_{i_{o,n}i_{o,p}}(f) - P_{i_{o,p}i_{o,n}}(f) + P_{i_{o,n}i_{o,n}}(f). \end{aligned} \tag{5.21}$$

After deriving $P_{xx}(f)$, only $P_{yx}(f)$ is required to determine $Z_{o,1}(f)$ using (5.9). The cross-correlation function, $R_{yx}(f)$ is required to determine $P_{yx}(f)$. The cross-correlation function, $R_{yx}(f)$ of the signals $y(t) = v_{o,p}(t) - v_{o,n}(t)$ and $x(t) = i_{o,p}(t) - i_{o,n}(t)$ is obtained using (5.18) and is expressed as

$$\begin{aligned} R_{yx}(\tau) &= \lim_{T\to\infty} \frac{1}{T} \int_{-\infty}^{\infty} y(t)x(t-\tau)d\tau \\ &= \lim_{T\to\infty} \frac{1}{T} \int_{-\infty}^{\infty} v_{o,p}(t)i_{o,p}(t-\tau) - v_{o,p}(t)i_{o,n}(t-\tau) \\ &\quad - v_{o,n}(t)i_{o,p}(t-\tau) + v_{o,n}(t)i_{o,n}(t-\tau)d\tau \\ &= R_{v_{o,p}i_{o,p}}(\tau) - R_{v_{o,p}i_{o,n}}(\tau) - R_{v_{o,n}i_{o,p}}(\tau) + R_{v_{o,n}i_{o,n}}(\tau). \end{aligned} \tag{5.22}$$

Using (5.17) and (5.22) the CPSD, $P_{yx}(f)$, can now be derived as

$$P_{yx}(f) = P_{v_{o,p}i_{o,p}}(f) - P_{v_{o,p}i_{o,n}}(f) - P_{v_{o,n}i_{o,p}}(f) + P_{v_{o,n}i_{o,n}}(f). \tag{5.23}$$

Finally the estimated transfer function, $Z_{o,1}(f)$, is calculated by substituting (5.23) and (5.21) into (5.9). The output impedance, $Z_{o,1}(f)$, is then expressed as

$$Z_{o,1}(f) = \frac{P_{v_{o,p}i_{o,p}}(f) - P_{v_{o,p}i_{o,n}}(f) - P_{v_{o,n}i_{o,p}}(f) + P_{v_{o,n}i_{o,n}}(f)}{P_{i_{o,p}i_{o,p}}(f) - P_{i_{o,n}i_{o,p}}(f) - P_{i_{o,p}i_{o,n}}(f) + P_{i_{o,n}i_{o,n}}(f)}. \tag{5.24}$$

The estimated transfer function, $Z_{o,1}(f)$, only consists of PSDs and CPSDs, therefore, no time-domain alignment is required. The same process can be used to calculate the estimated transfer function, $Z_{o,2}(f)$ as

$$\begin{aligned} Z_{o,2}(f) &= \frac{P_{yy}(f)}{P_{xy}(f)} \\ &= \frac{P_{v_{o,p}v_{o,p}}(f) - P_{v_{o,n}v_{o,p}}(f) - P_{v_{o,p}v_{o,n}}(f) + P_{v_{o,n}v_{o,n}}(f)}{P_{v_{o,p}i_{o,p}}(f) - P_{v_{o,p}i_{o,n}}(f) - P_{v_{o,n}i_{o,p}}(f) + P_{v_{o,n}i_{o,n}}(f)}. \end{aligned} \tag{5.25}$$

Due to windowing $Z_{o,1}(f)$ and $Z_{o,2}(f)$ are not exactly the same, but approximations of each other:

$$Z_o(f) \approx Z_{o,1}(f) \approx Z_{o,2}(f) \tag{5.26}$$

Fig. 5.18 compares the output impedance obtained using method 2 to the output impedance obtained with method 1. The two different approaches to implement the two-measurement approach produces similar results between 500 Hz and 10kHz, although method 2 produces more variation in the output impedance magnitude response. No time-domain alignment is necessary to obtain an accurate output impedance.

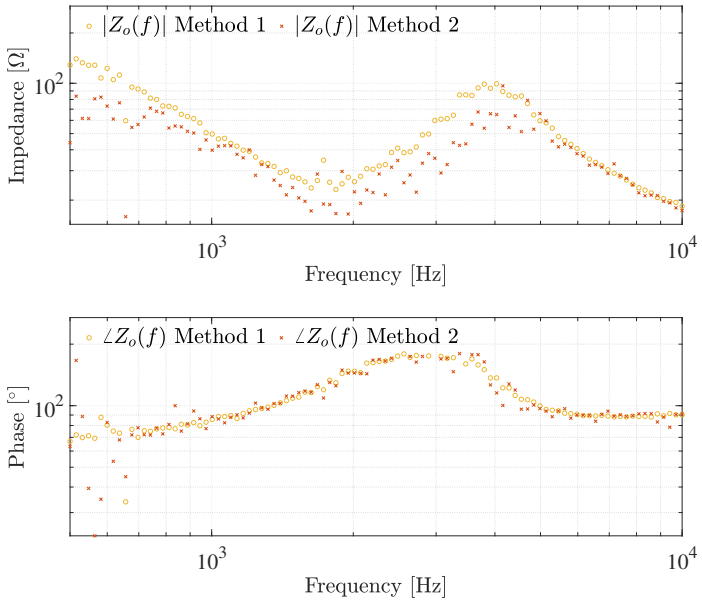

Figure 5.18: Comparison of the magnitude and phase response of the output impedance, $Z_o(f)$, obtained using method 1 and method 2.

5.4.3. Method 3: Estimation of the Output Impedance using Transfer Function Decoupling

A method to decouple transfer functions was implemented by Cvetkovic *et al.* [136] on DC-DC converters. This method has already been expanded to three-phase VSIs [93] in the DQ-axis. The approach models the inverter as a two-port network, with a DC input and AC-output. The two-measurement approach used in this project does not assume the inverter as a two-port network, but rather a Thévenin equivalent, as the source is modelled together with the inverter and not separated as in the case of a two-port network.

Similar to a single-phase DC-DC converter, the single phase inverter can be described mathematically as

$$\begin{bmatrix} V_o(f) \\ I_i(f) \end{bmatrix} = \begin{bmatrix} G_o(f) & -Z_o(f) \\ Y_i(f) & H_i(f) \end{bmatrix} \begin{bmatrix} V_i(f) \\ I_i(f) \end{bmatrix}. \tag{5.27}$$

Cvetkovic *et al.* [136] derived (5.27) as a small-signal model by subtracting the DC operating value. For the single-phase inverter case no DC offset exists, only a fundamental frequency component and the higher frequency switching harmonics.

The target system is perturbed twice, on the input and on the output side. Using the notation by Cvetkovic *et al.* [136], m denotes a measured frequency responses, a $'$ denotes measurements taken from perturbing the input side and a $''$ from perturbing the output side. The first set of frequency responses is obtained by perturbing the input side:

$$\begin{aligned} G_{om} &= \frac{V_o(f)'}{V_i(f)'} \\ Y_{im} &= \frac{I_i(f)'}{V_i(f)'}. \end{aligned} \tag{5.28}$$

Equation (5.27) can subsequently be written as

$$\begin{bmatrix} V_o(f)' \\ I_i(f)' \end{bmatrix} = \begin{bmatrix} G_o(f) & -Z_o(f) \\ Y_i(f) & H_i(f) \end{bmatrix} \begin{bmatrix} V_i(f)' \\ I_i(f)' \end{bmatrix}. \tag{5.29}$$

Equation (5.29) can be rewritten by substituting (5.28):

$$\begin{aligned} G_{om}(f) &= G_o(f) - Z_o(f)\frac{I_o(f)'}{V_i(f)'} \\ Y_{im}(f) &= Y_i(f) + H_i(f)\frac{I_o(f)'}{V_i(f)'} \end{aligned} \tag{5.30}$$

For ease of writing $T_{gm}(f)$ is defined as

$$T_{gm}(f) = \frac{I_o(f)'}{V_i(f)'}. \tag{5.31}$$

Similarly, the output side can be perturbed to obtain

$$\begin{aligned} Z_{om} &= \frac{V_o(f)''}{I_o(f)''} \\ H_{im} &= \frac{I_i(f)''}{I_o(f)''}. \end{aligned} \tag{5.32}$$

Substituting the output perturbations, (5.27) is written as

$$\begin{bmatrix} V_o(f)" \\ I_i(f)" \end{bmatrix} = \begin{bmatrix} G_o(f) & -Z_o(f) \\ Y_i(f) & H_i(f) \end{bmatrix} \begin{bmatrix} V_i(f)" \\ I_i(f)" \end{bmatrix}. \tag{5.33}$$

Equation (5.33) becomes

$$\begin{aligned} Z_{om}(f) &= G_o(f)\frac{V_i(f)"}{I_o(f)"} - Z_o(f) \\ H_{im}(f) &= Y_i(f)\frac{V_i(f)"}{I_o(f)"} + H_i(f). \end{aligned} \tag{5.34}$$

Again, for ease of use, $T_{rm}(f)$ is defined:

$$T_{rm}(f) = \frac{V_i(f)"}{I_o(f)"}. \tag{5.35}$$

Equation (5.30) and (5.34) can be written as

$$\begin{bmatrix} G_{om}(f) \\ Y_{im}(f) \\ Z_{om}(f) \\ H_{im}(f) \end{bmatrix} = \begin{bmatrix} 1 & 0 & -T_{gm}(f) & 0 \\ 0 & 1 & 0 & T_{gm}(f) \\ T_{rm}(f) & 0 & -1 & 0 \\ 0 & T_{rm}(f) & 0 & 1 \end{bmatrix} \begin{bmatrix} G_o(f) \\ Y_i(f) \\ Z_o(f) \\ H_i(f) \end{bmatrix}. \tag{5.36}$$

Using matrix algebra, the decoupled transfer functions are determined as

$$\begin{aligned} \begin{bmatrix} G_o(f) \\ Y_i(f) \\ Z_o(f) \\ H_i(f) \end{bmatrix} &= \frac{1}{1 - T_{gm}(f)T_{rm}(f)} \times \\ &\begin{bmatrix} 1 & 0 & -T_{gm}(f) & 0 \\ 0 & 1 & 0 & -T_{gm}(f) \\ T_{rm}(f) & 0 & -1 & 0 \\ 0 & -T_{rm}(f) & 0 & 1 \end{bmatrix} \begin{bmatrix} G_{om}(f) \\ Y_{im}(f) \\ Z_{om}(f) \\ H_{im}(f) \end{bmatrix}. \end{aligned} \tag{5.37}$$

While method 1 and 2 are discussed using measured data, method 3 requires perturbation of the DC input side and is explained through simulation. Perturbing the input side of the inverter would be practically difficult to execute, as a 1200 μF capacitor is used to smooth any ripple in the input. For this reason the DC voltage of the PRIS source is increased from 30 V for AC output side perturbation to 200 V for DC input side perturbation to obtain the decoupled output impedance in Fig. 5.19.

In Fig. 5.19 the output impedance, $Z_o(f)$, using method 1, and the decoupled output impedance using method 3 are compared through simulation. All of the impedances are

similar in this frequency range.

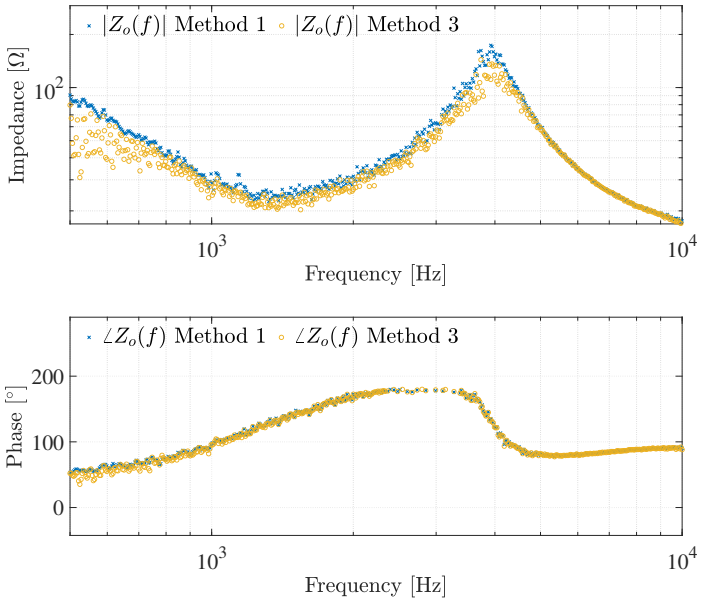

Figure 5.19: Magnitude and phase response of the output impedance using method 1 and method 3 are compared.

5.4.4. Selection of Output Impedance Estimation Methodology

Three methods are introduced to estimate the output impedance of the inverter. Method 1 align the output currents under normal and perturbed conditions to allow synchronization of $v_{TH}(t)$. Equation (5.4) is then calculated using Welch's estimate. During the rest of the project method 1 is used to estimate the output impedance of the inverter, as it is an accurate approximation and easy to implement.

Method 2 made use of PSDs and CPSDs to determine (5.4). The windowing of multiple PSDs and CPSDs are time-consuming and computationally complex to execute. The output impedance frequency response obtained using method 2 exhibits more variance than method 1. Method 3 was originally derived for DC-DC converters and does not take the fundamental frequency component of the inverter into account. Perturbation at the DC input side of the inverter is also required. For these reasons, method 1 is preferred to method 2 and 3.

5.5. Perturbation Results of a Practical Single-Phase Full-Bridge Inverter

In sections 5.3 and 5.4 a practical inverter is perturbed and the output impedance frequency response of the inverter is subsequently determined. In this section different frequency

bands of the output impedance of the inverter are investigated by varying the PRIS source parameters. The PRIS source can be controlled by varying the PRBS order, clock frequency and RLC filter values.

The PRBS order for each clock frequency is chosen such that it allows approximately equal PRBS periods, regardless of the clock frequency. The time-domain waveforms are recorded over 30 seconds. During frequency response estimation, these signals are windowed with 100 rectangular windows with no overlap. The time-domain signals are thus split into 100 sections of $0.33s$ each, allowing for a frequency resolution of $R_f = 100/30 = 3.33Hz$. These windowing parameters are used, as it is observed that it allows for a good trade off between variance and bias in the output impedance frequency response.

In this section the inverter is perturbed with multiple different PRIS source configurations and clock frequencies, as summarized in Table 5.2.

TABLE 5.2: Summary of PRIS source clock frequencies during experimental perturbations.

Section	**PRIS Clock Frequency [kHz]**
5.5.1	30
5.5.2	20
5.5.3	1
5.5.4	0.5

5.5.1. Perturbation with a 30kHz PRIS Source

The parameters of the PRIS source whilst perturbing the inverter output with a 30 kHz clock frequency are listed in Table 5.3. The RLC parameter values cause time-constants that allows equitable spread of perturbation energy over the frequency range.

TABLE 5.3: PRIS source parameters.

PRBS Order	**Clock Frequency f_{clk}**	R_{PRIS}	L_{PRIS}	C_{PRIS}	V_{DC}
15	$30kHz$	100Ω	$2.2mH$	$5\mu F$	30 V

Fig. 5.20 shows the aligned time-domain waveforms of the output voltage and current under normal and perturbed conditions, $v_{o,n}(t)$, $i_{o,n}(t)$, $v_{o,p}(t)$ and $i_{o,p}(t)$. The PRIS perturbations are clearly visible. The current perturbations are smaller than the voltage perturbations, as the current control-loop responds fast to correct any change in current. Voltage perturbation amplitudes reach approximately 30% of the fundamental frequency component of the output voltage, $v_{o,n}(t)$.

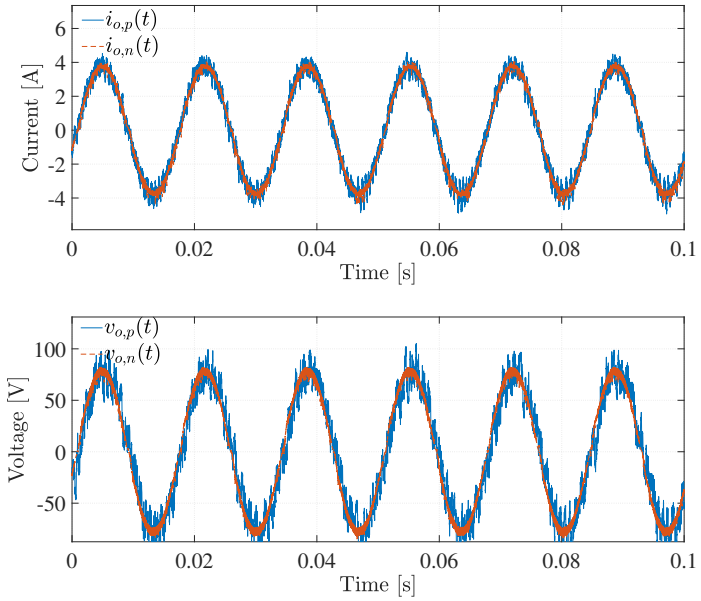

Figure 5.20: Time-domain output voltage and current under normal operating conditions, $v_{o,n}(t)$ and $i_{o,n}(t)$, as well as during perturbation, $v_{o,p}(t)$ and $i_{o,p}(t)$.

Fig. 5.21 displays the PSDs of the output currents and voltages under normal and perturbed conditions from 500 Hz to 30kHz. As the clock frequency of the PRIS source is 30 kHz, the inverter is only investigated up to 30kHz in the frequency-domain. The current, $i_{o,p}(t)$, is adequately perturbed in this frequency range as more power exist in the PSD of $i_{o,p}(t)$ than the PSD of $i_{o,n}(t)$ between 500 Hz and 30kHz. Similar to the currents, the PSD of $v_{o,p}(t)$ is greater than the PSD of $v_{o,n}(t)$ from 500 Hz to 30kHz, indicating that the voltage is adequately perturbed over this frequency range.

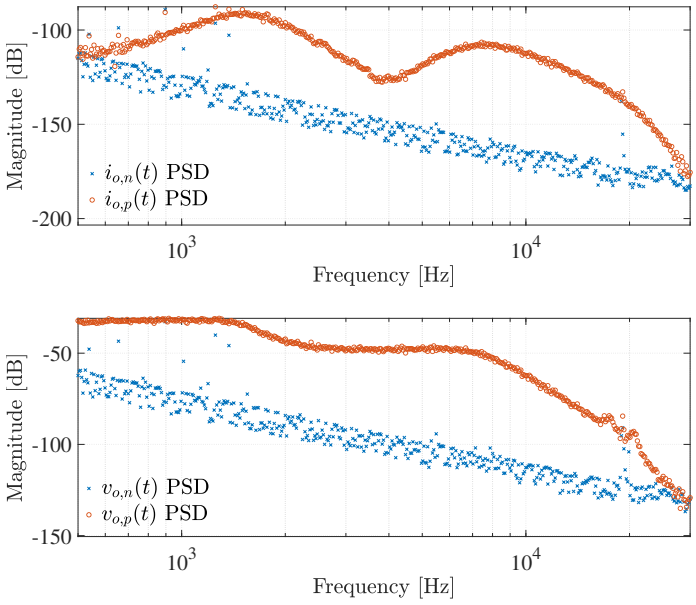

Figure 5.21: Power spectral density of the output current and voltage under normal operating conditions, $i_{o,n}(t)$ and $v_{o,n}(t)$, as well as during perturbation, $i_{o,p}(t)$ and $v_{o,p}(t)$.

Fig. 5.22 shows the frequency response of the output impedance, $Z_o(f)$, between 500 Hz and 30 kHz. The impedance is capacitive until it reaches a series resonant point at approximately 1.8 kHz. From 1.8kHz $Z_o(f)$ is inductive until a parallel resonant point is reached at 4kHz. The series and parallel resonant points are caused by the control-loop and LC filter. The output impedance is again capacitive from 4kHz. At the switching frequency, $f_{sw} = 19.2kHz$, an artefact is present.

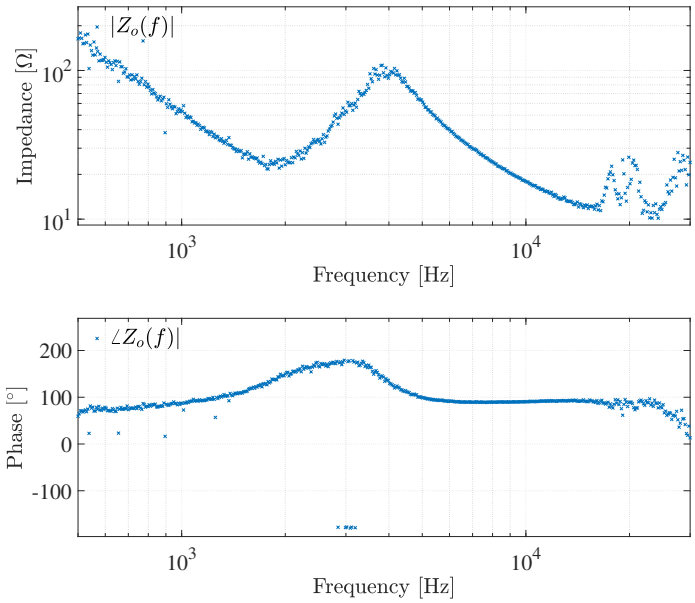

Figure 5.22: Magnitude and phase response of the experimental output impedance, $Z_o(f)$.

The two-measurement approach is not capable of removing the switching artefact completely. It does, however, reduce the artefact substantially. The two-measurement approach is derived from the average model of the inverter in chapter 4. The average model does not take the switching frequency and harmonics into account, only the fundamental frequency. It is thus expected that if the switching harmonics exhibit non-linear behaviour that the artefacts are not entirely removed by the two-measurement approach.

The discrete controller is only functional until half the sampling frequency, $f_s/2 = 9.6kHz$. As the sampling frequency is equal to the switching frequency and carrier frequency,

$$f_s = f_{sw} = f_c, \tag{5.38}$$

the switching artefact does not limit information regarding the control-loop in the output impedance, $Z_o(f)$.

5.5.2. Perturbation with a 20kHz PRIS Source

The clock frequency of the PRIS source is decreased to 20kHz, to allow more low frequency perturbations [28]. To allow a similar PRBS period to the 30kHz perturbation case, a PRBS14 is used. The inductor value is increased. The parameters of the PRIS source while perturbing the AC output of the inverter with a 20 kHz clock frequency are summarized in Table 5.4.

TABLE 5.4: PRIS source parameters.

PRBS Order	**Clock Frequency f_{clk}**	R_{PRIS}	L_{PRIS}	C_{PRIS}	V_{DC}
14	$20kHz$	100Ω	$4.4mH$	$5\mu F$	30 V

Fig. 5.23 shows the aligned time-domain waveforms of the output voltage and current under normal and perturbed conditions, $v_{o,n}(t)$, $i_{o,n}(t)$, $v_{o,p}(t)$ and $i_{o,p}(t)$. Voltage perturbation magnitudes reached approximately 34% of the fundamental frequency component of $v_{o,n}(t)$.

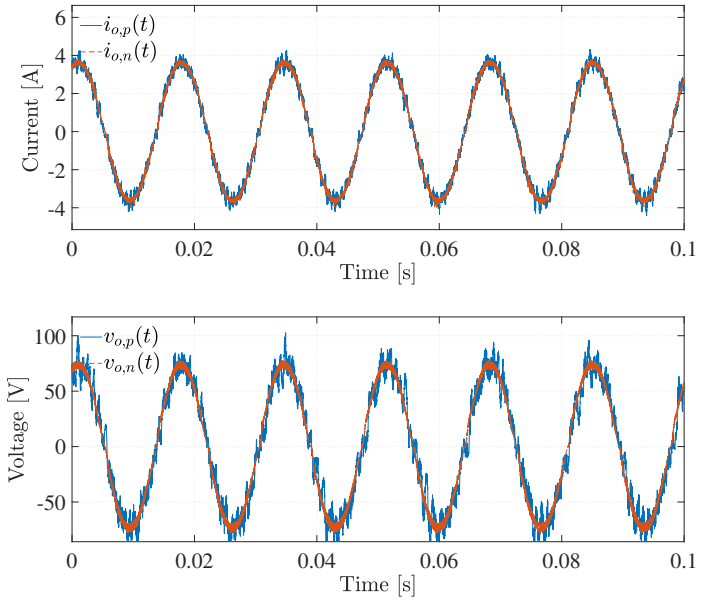

Figure 5.23: Time-domain output voltage and current under normal operating conditions, $v_{o,n}(t)$ and $i_{o,n}(t)$, as well as during perturbation, $v_{o,p}(t)$ and $i_{o,p}(t)$.

Fig. 5.24 displays the PSDs of the output currents and voltages under normal and perturbed conditions from 10 Hz to 10kHz. As the clock frequency of the PRIS source is 20 kHz, the inverter could be investigated up to 20kHz in the frequency-domain. The region between 10kHz and 30kHz is already investigated when perturbing with a 30kHz clock frequency in section 5.5.1, therefore, this section focus on lower frequencies. The

PSDs of the currents, $i_{o,n}(t)$ and $i_{o,p}(t)$, are similar up to approximately 700 Hz. This means that the PRIS source did not effect $i_{o,p}(t)$ below 700 Hz, and perturbation of the current is not adequate below 700Hz. The PSDs of the voltages, $v_{o,n}(t)$ and $v_{o,p}(t)$, are similar up to 300 Hz. The voltage $v_{o,p}(t)$ is thus not adequately perturbed at frequencies lower than approximately 300 Hz.

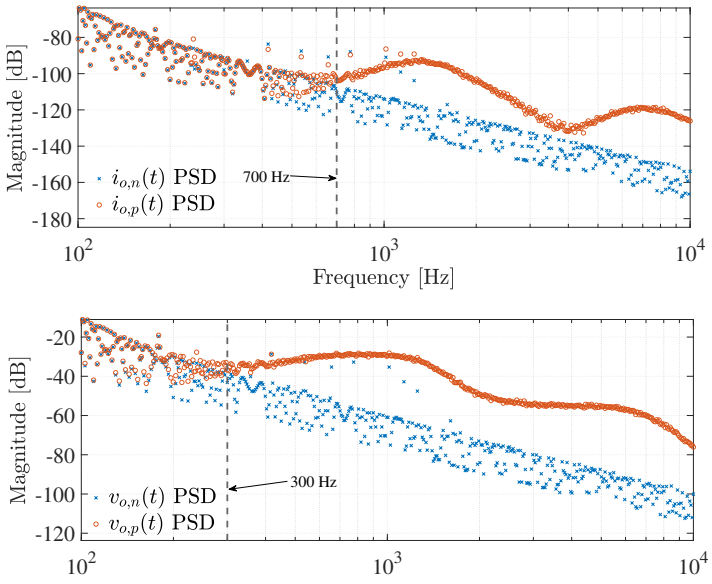

Figure 5.24: Power spectral density of the output current and voltage under normal operating conditions, $i_{o,n}(t)$ and $v_{o,n}(t)$, as well as during perturbation, $i_{o,p}(t)$ and $v_{o,p}(t)$.

Welch's estimate is used to determine the output impedance using (5.5), as discussed in section 5.4.1. To use (5.5), both the current, $i_{o,p}(t)$, and the voltage, $v_{o,p}(t)$, needs to be adequately perturbed to obtain the necessary spectral densities.

Fig. 5.25 shows the frequency response of the output impedance, $Z_o(f)$, between 700 Hz and 10kHz. Frequencies lower than 700 Hz are not presented, as perturbation is not adequate in this region. Lowering the clock frequency to 20kHz did not allow for characterization of any new frequency band of the output impedance of the inverter, compared to the 30kHz PRIS perturbation. The parallel and series frequency points seen in Fig. 5.25 are already characterized in Fig. 5.21.

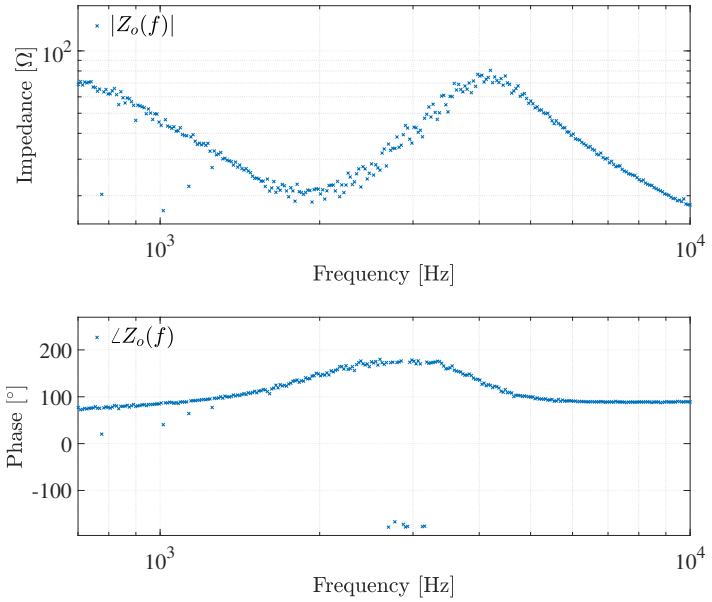

Figure 5.25: Magnitude and phase response of the experimental output impedance, $Z_o(f)$.

5.5.3. Perturbation with a 1 kHz PRIS Source

To aid perturbation of frequencies lower than 700 Hz the clock frequency is lowered to 1 kHz [94]. The PRBS order is lowered to a PRBS10, to allow comparable PRBS periods with the 30kHz and 20kHz PRIS source perturbations. The parameters of the PRIS source are listed in Table 5.5.

TABLE 5.5: PRIS source parameters.

PRBS Order	**Clock Frequency f_{clk}**	R_{PRIS}	L_{PRIS}	C_{PRIS}	V_{DC}
10	$1kHz$	100Ω	$2.2mH$	$5\mu F$	30 V

Fig. 5.26 shows the aligned time-domain waveforms of the output voltage and current under normal and perturbed conditions, $v_{o,n}(t)$, $i_{o,n}(t)$, $v_{o,p}(t)$ and $i_{o,p}(t)$. The output voltage impulse perturbations reach around 60% of the nominal output voltage magnitude. The current perturbations are quickly rectified by the current-control loop.

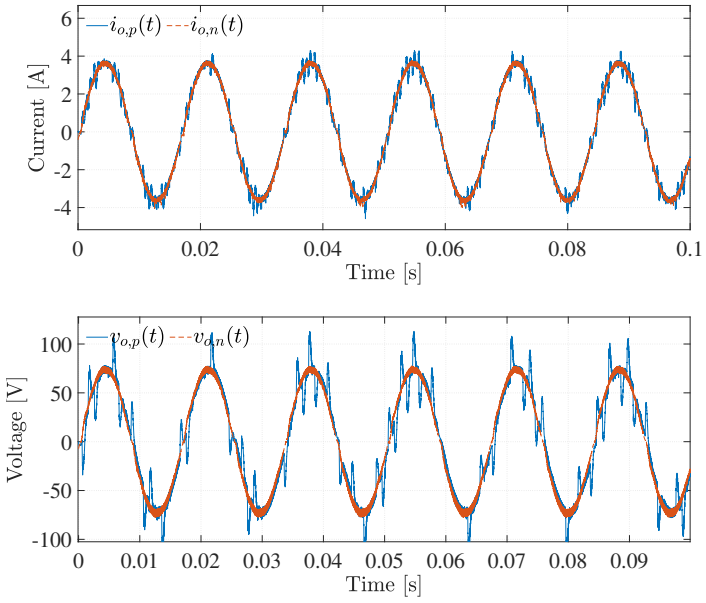

Figure 5.26: Time-domain output voltage and current under normal operating conditions, $v_{o,n}(t)$ and $i_{o,n}(t)$, as well as during perturbation, $v_{o,p}(t)$ and $i_{o,p}(t)$.

The PSDs of the output currents and voltages under normal and perturbed conditions are presented in Fig. 5.27. The PSDs are presented between 10Hz and the clock frequency, $f_{clk} = 1kHz$. The output current is not sufficiently perturbed below approximately 400 Hz. Lowering the clock frequency allowed for adequate perturbation from 400 Hz as compared to the 700 Hz in the 20kHz perturbation case. The output voltage is not perturbed adequately below approximately 200Hz.

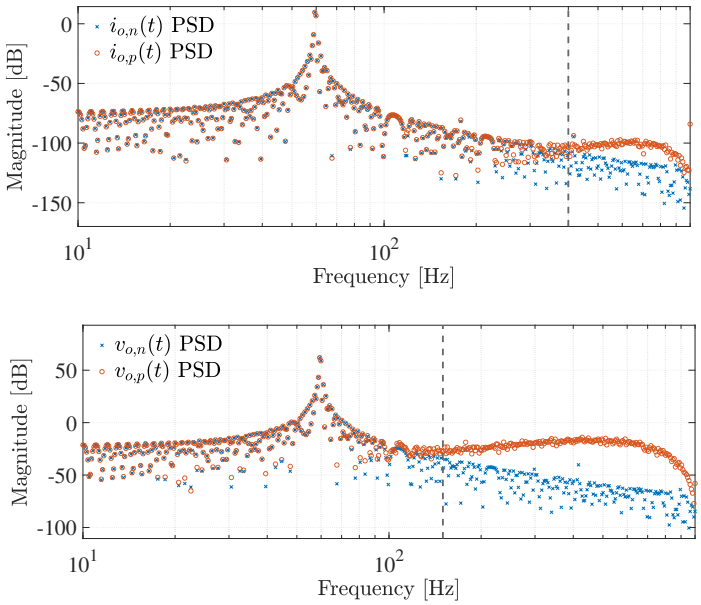

Figure 5.27: Power spectral density of the output current and voltage under normal operating conditions, $i_{o,n}(t)$ and $v_{o,n}(t)$, as well as during perturbation, $i_{o,p}(t)$ and $v_{o,p}(t)$.

Fig. 5.28 shows the frequency response of the output impedance, $Z_o(f)$, between 400 Hz and 1kHz. Frequencies lower than 400 Hz are not presented, as perturbation is not adequate in this region. This would lead to an inaccurate estimation of the output impedance below 400 Hz, as discussed in section 5.5.2. The output impedance, $Z_o(f)$, obtained is capacitive between 400 Hz and 1kHz.

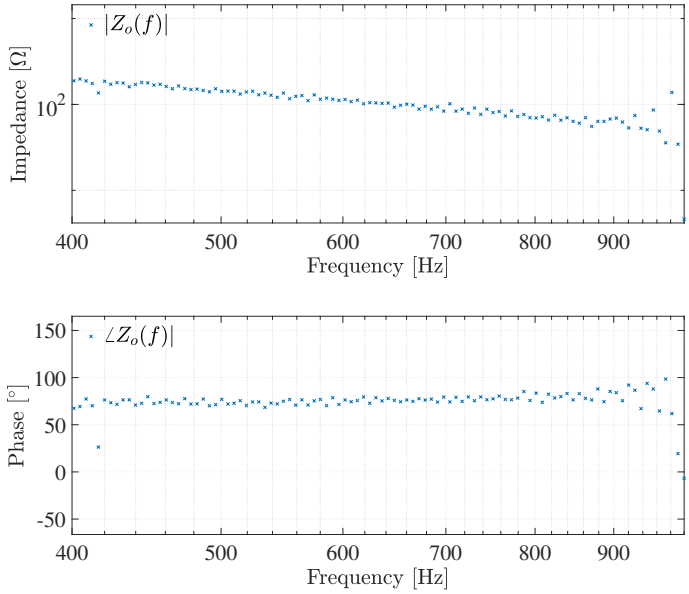

Figure 5.28: Magnitude and phase response of the experimental output impedance, $Z_o(f)$.

Lowering the clock frequency to 1kHz did allow for characterization of the output impedance frequency response from 400 Hz to 1kHz. However, this did not substantially improve perturbation of the inverter and subsequent characterization of $Z_o(f)$, as the 30kHz PRIS perturbations already perturbed frequencies as low as 500 Hz. Lower frequency perturbations are possible by decreasing the clock frequency and increasing the capacitor of the RLC source.

5.5.4. Perturbation with a 0.5 kHz PRIS Source

The parameters of the PRIS source whilst perturbing the inverter output with a 0.5 kHz clock frequency are listed in Table 5.6. The capacitor value is increased to $20\mu F$ to allow better low frequency perturbation, along with the decreasing the clock frequency. Two 100Ω resistors are used in parallel to form the 50Ω resistor, to allow the power to be divided between the two resistors. The size of the inductor is increased to allow slower time-constants and limit the current through the PRIS source. The DC voltage of the PRIS source is decreased to avoid output voltage perturbations that are too large.

TABLE 5.6: PRIS source parameters.

PRBS Order	**Clock Frequency f_{clk}**	R_{PRIS}	L_{PRIS}	C_{PRIS}	V_{DC}
9	$0.5kHz$	50 Ω	$4.4mH$	$20\mu F$	20 V

Fig. 5.29 shows aligned time-domain waveforms of the output voltage and current under normal and perturbed conditions, $v_{o,n}(t)$, $i_{o,n}(t)$, $v_{o,p}(t)$ and $i_{o,p}(t)$. It is observed that the output voltage perturbation magnitudes reach approximately 40% of the fundamental frequency component of the output voltage.

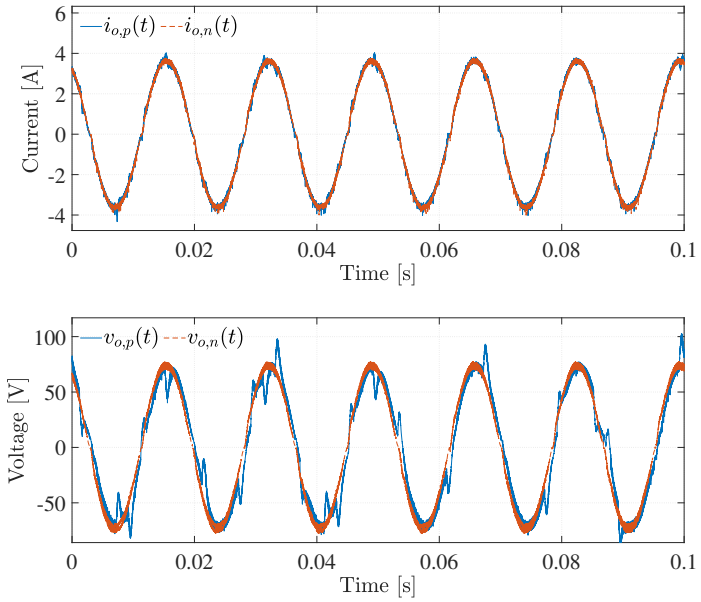

Figure 5.29: Time-domain output voltage and current under normal operating conditions, $v_{o,n}(t)$ and $i_{o,n}(t)$, as well as during perturbation, $v_{o,p}(t)$ and $i_{o,p}(t)$.

The PSDs of the output currents and voltages under normal and perturbed conditions are presented in Fig. 5.30 between 10 Hz and 500 Hz. The current $i_{o,p}(t)$ is not adequately perturbed below 200 Hz, while the voltage $v_{o,p}(t)$ is not adequately perturbed below 100 Hz. The PSD of $i_{o,p}(t)$ is also similar to the PSD of $i_{o,n}(t)$ close to the clock frequency of 500 Hz. The current, $i_{o,p}(t)$, is thus only adequately perturbed between approximately 200 Hz and 400 Hz.

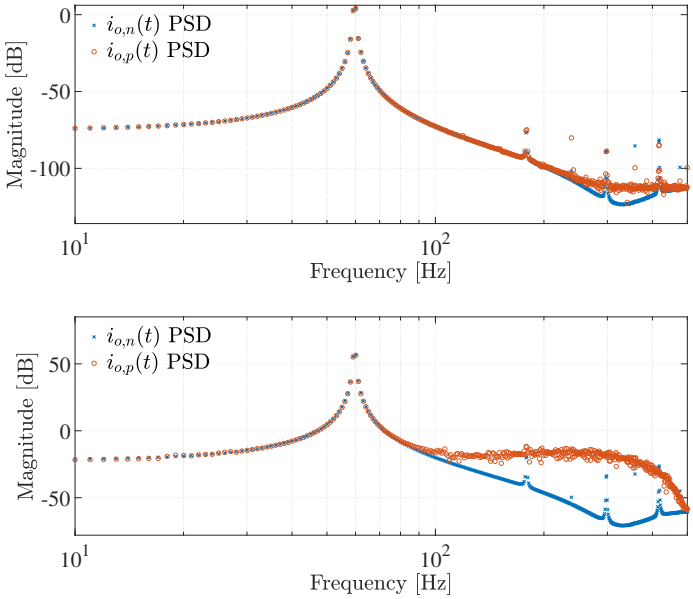

Figure 5.30: Power spectral density of the output current and voltage under normal operating conditions, $i_{o,n}(t)$ and $v_{o,n}(t)$, as well as during perturbation, $i_{o,p}(t)$ and $v_{o,p}(t)$.

Fig. 5.31 shows the frequency response of the output impedance, $Z_o(f)$, between 200 Hz and 500 Hz. The output impedance is still capacitive. Artefacts are present at odd multiples of the fundamental frequency, i.e. $60Hz \times 5 = 300Hz$ and $60Hz \times 7 = 420Hz$. These artefacts are observed as the harmonics of the inverter are not entirely removed by the two-measurement approach. The output impedance, $Z_o(f)$, decreases substantially close to 500 Hz, due to lower perturbation energy at the clock frequency, $f_{clk} = 500Hz$. The output impedance is thus not accurate between 400 Hz and 500 Hz.

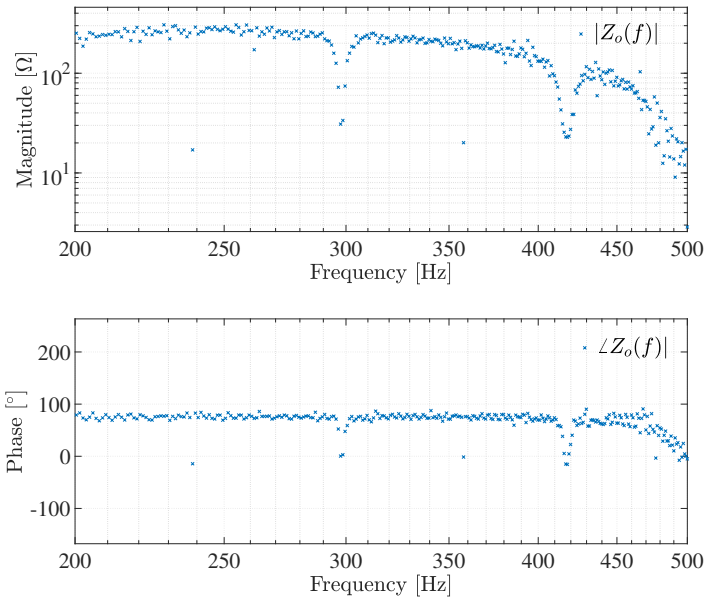

Figure 5.31: Magnitude and phase response of the experimental output impedance, $Z_o(f)$.

5.5.5. Summary and Discussion of Experimental Perturbations

Characterizing the output impedance at frequencies lower than 200 Hz requires greater perturbation power at these frequencies. In this investigation, this is not done due to the following reasons:

- To increase perturbation power, the DC voltage of the PRIS source can be increased. The output voltage perturbation magnitudes already reaches 30%-60% of the fundamental frequency component of the voltage. Therefore, increasing the DC voltage is not viable, as it may introduce non-linear inverter behaviour of the inverter.
- Increasing the capacitor would allow for lower frequency perturbation. The capacitor protects the H-bridge, resistor and inductor of the PRIS source by limiting the voltage across these components. As the capacitor value is increased, the capacitor voltage decreases, causing the power and current of the resistor and inductor used in the PRIS source to increase beyond their maximum ratings.
- Decreasing the clock frequency can increase low frequency perturbations. When the clock frequency is decreased, the RLC parameter values should change appropriately to keep the time-constants to clock period ratio similar, allowing a similar spread of energy over the frequency band covered by the clock frequency. This is not viable at frequencies lower than 200 Hz, as the power, current and voltage ratings of the RLC circuit increase beyond their maximum ratings.

The lowest frequency of the AC output of the inverter that is adequately perturbed is 200 Hz. At this frequency, the output impedance of the inverter is capacitive, until the first

series resonant point at approximately 1.8kHz. From 1.8kHz $Z_o(f)$ is inductive up to the parallel resonant point at approximately 4kHz. From 4kHz $Z_o(f)$ is once again capacitive. An artefact remains at the switching frequency, $f_{sw} = 19.2kHz$. The output impedance is thus assumed accurate between 200 Hz and 16 kHz. Fig. 5.32 shows the output impedance of the inverter in this frequency range by concatenating previous results.

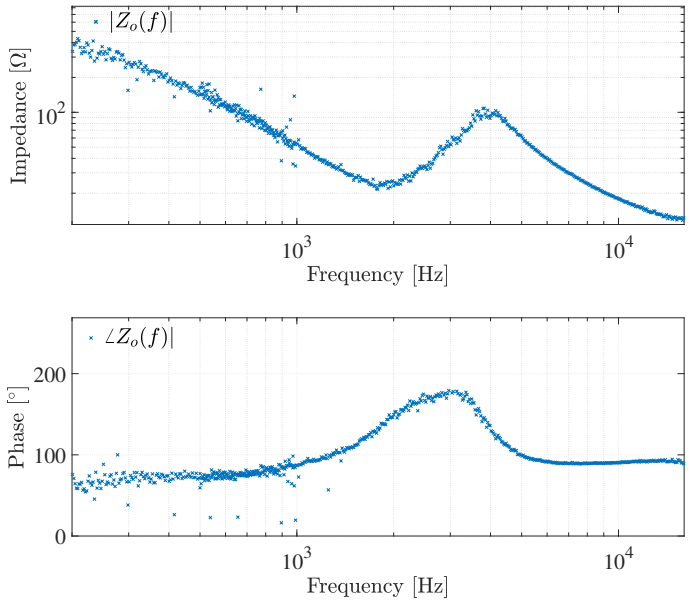

Figure 5.32: The magnitude and phase responses of $Z_o(f)$ over the frequency band that is assumed to be accurately estimated.

5.6. Modelling of the Practical Inverter System

The practical inverter system is modelled in Simulink. Practical measurements will be used to estimate the parameters of the model during a parameter estimation study in later sections. To perform an applicable parameter estimation study the model topology that will be populated is required to be as accurate as possible.

5.6.1. Modelling the Practical Inverter in Simulink

Fig. 5.33 shows the model topology of the inverter under investigation. This inverter is simulated in Simulink. The inverter consists of a full-bridge switching circuit with a LC low-pass filter connected to the output of the switching circuit. The filtered output current and voltage, $i_o(t)$ and $v_o(t)$, supplies a load. The inductor current, $i_L(t)$, is scaled by the gain, k_i, and subsequently passed to a 2P2Z current controller, $D(z)$. The output voltage is scaled by the gain, k_v, before it is used to implement feedforward linearization. A gain, k_{PWM}, is multiplied to the output of the control-loop, before a hybrid unipolar PWM scheme is used to control the switches.

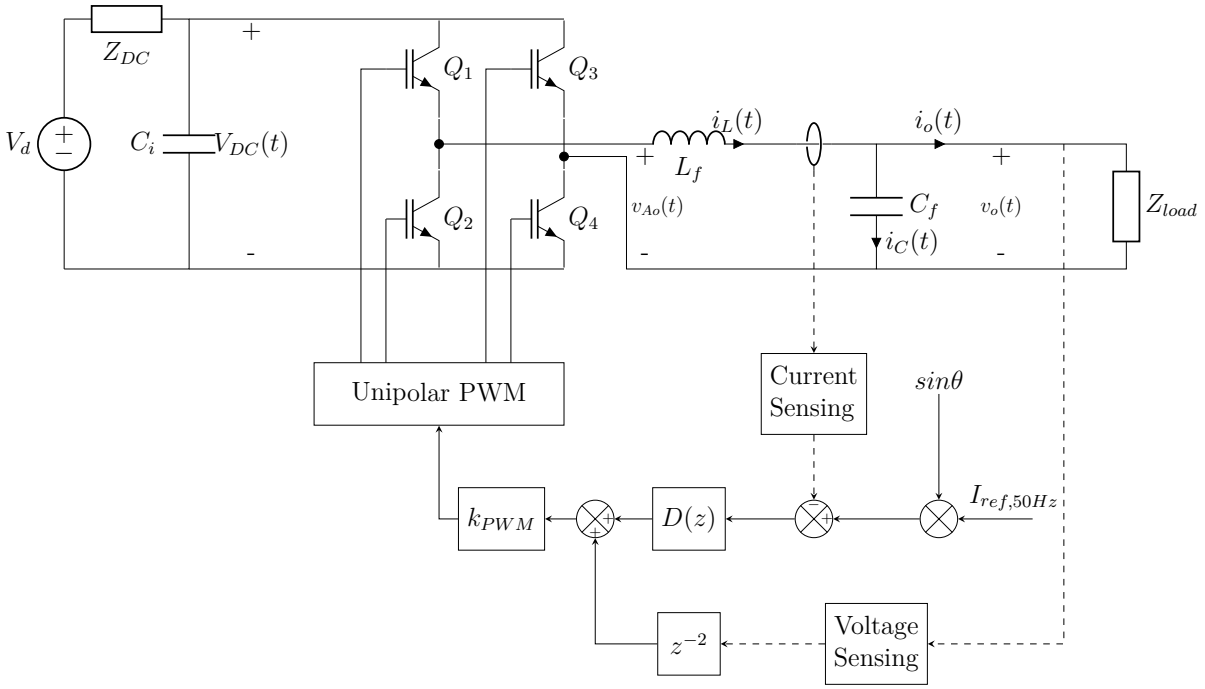

Figure 5.33: Final high-voltage, single-phase, full-bridge, current-controlled, solar voltage source inverter topology.

5.6.1.1. Modelling the Discrete Current Controller

As discussed in section 5.2.1.6, a 2P2Z controller is implemented in the Piccolo microcontroller. The equivalent discrete-domain transfer function is

$$D(z) = \frac{Y(z)}{X(z)} = \frac{b_2 z^{-2} + b_1 z^{-1} + b_0}{1 + a_0 z^{-1} + a_1 z^{-2}} = \frac{b_0 z^2 + b_1 z^1 + b_2}{z^2 + a_0 z + a_1}. \tag{5.39}$$

This transfer function neglects the saturation block in the feedback path of the 2P2Z controller. The current controller is thus modelled in Simulink to include this saturation block, as shown in Fig. 5.34. The parameter values of the discrete controller are listed in Table 5.7 as obtained from example code for a grid-connected inverter [132] whereas the inverter under investigation is a standalone inverter.

TABLE 5.7: Parameter values for the discrete controller, $D(z)$.

b_0	b_1	b_2	a_0	a_1	T_s [μs]
0.5253	0.1314	-0.3938	-1.01	0.01	52

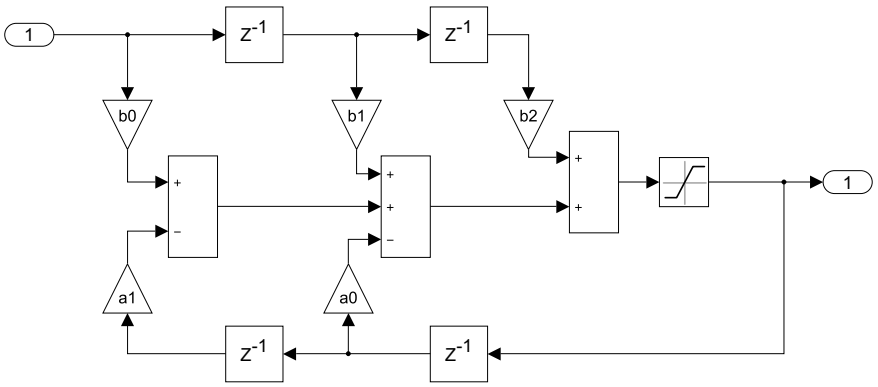

Figure 5.34: Model of the discrete controller in Simulink.

The discrete controller, $D(z)$, can be plotted in the frequency-domain up to $\frac{f_s}{2} = 9.6kHz$ to adhere to the Nyquist theorem. The equivalent frequency-domain transfer function can be determined by substituting $z = e^{-j2\pi f}$ in (5.39) to produce

$$D(f) = \frac{b_0(e^{-j2\pi f})^2 + b_1 e^{-j2\pi f} + b_2}{(e^{-j2\pi f})^2 + a_0 e^{-j2\pi f} + a_1}. \tag{5.40}$$

Fig. 5.35 shows the discrete controller, $D(z)$, and the frequency-domain representation, $D(f)$. The frequency-domain transfer function, $D(f)$, is an accurate approximation of $D(z)$, as $D(f)$ lies on top of $D(z)$.

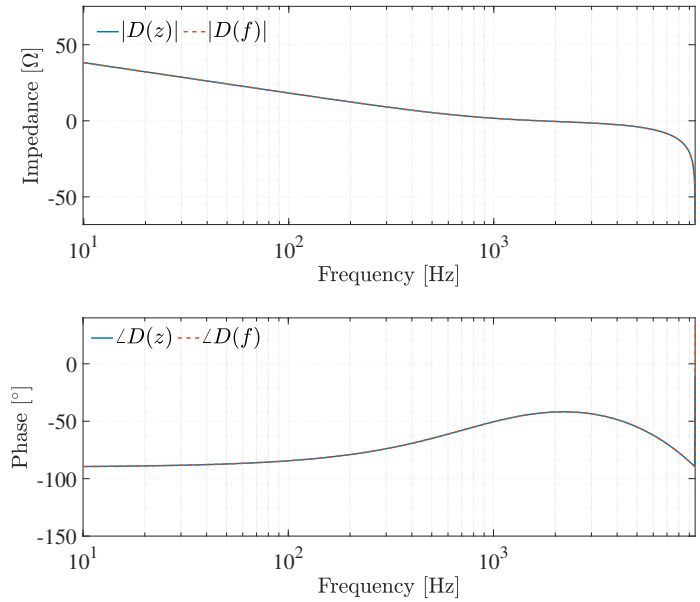

Figure 5.35: Magnitude and phase response of the discrete controller, $D(z)$, and the frequency-domain approximation, $D(f)$, of $D(z)$.

The state-space matrices for the discrete controller, $D(z)$, can be used to determine the observability of $D(z)$. The state matrix, $\mathbf{A}$, is equal to

$$\mathbf{A} = \begin{bmatrix} -0.01 & 1.01 \\ 1 & 0 \end{bmatrix}. \tag{5.41}$$

The input vector, $\mathbf{b}$, is

$$\mathbf{b} = \begin{bmatrix} 1 \\ 0 \end{bmatrix}. \tag{5.42}$$

The output vector, $\mathbf{c}$, is

$$\mathbf{c} = \begin{bmatrix} 0.1261 & 0.1368 \end{bmatrix}, \tag{5.43}$$

and the feedthrough constant, d, is

$$d = 0.5253. \tag{5.44}$$

The observability matrix, $\mathbf{V}$, for this state-space model can be calculated as

$$\mathbf{V} = \begin{bmatrix} 0.1261 & 0.1368 \\ 0.1355 & 0.1274 \end{bmatrix}. \tag{5.45}$$

The rank, ρ, of the observability matrix, $\mathbf{V}$, can be determined as

$$\rho(\mathbf{V}) = 2, \tag{5.46}$$

and is equal to the order, n, of the state-space model, therefore, the system is observable. It is important to note that this implies that the discrete controller, $D(z)$, is observable from its input and output signals. This does not imply that it is observable from the output impedance of the voltage source inverter, $Z_o(f)$, which will be available from the experimental results to use in parameter estimation.

A sensitivity analysis is conducted on the frequency-domain transfer function of the discrete controller, $D(f)$. The true value of coefficient, i.e. a_0, a_1, b_0, b_1 and b_2, are doubled and halved to determine the effect it has in the frequency-domain. Figure 5.36 displays the effect of these coefficients of the frequency response on the discrete controller, $D(f)$.

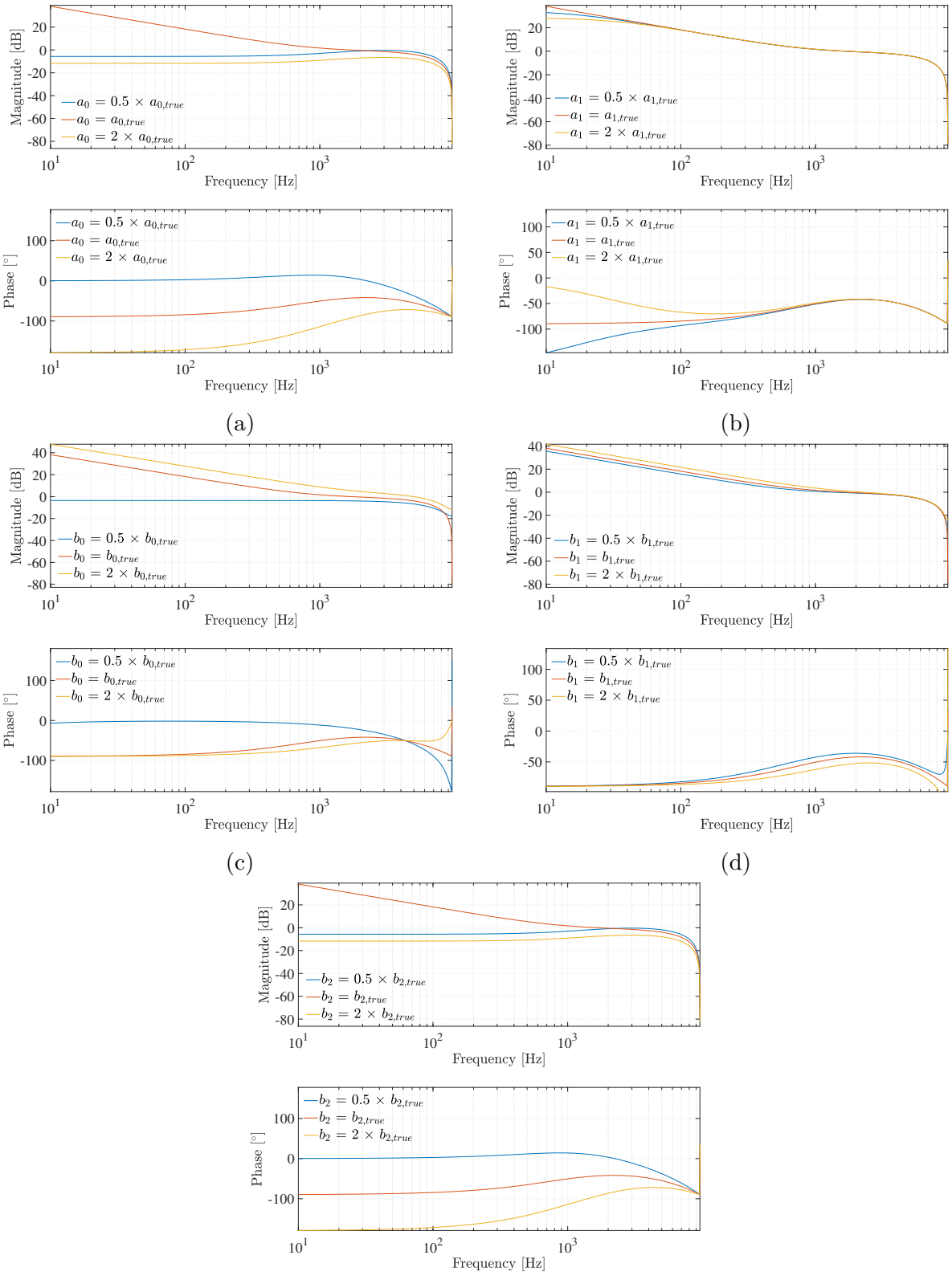

Figure 5.36: (a) Magnitude and phase response of $D(f)$ as a function of a_0. (b) Magnitude and phase response of $D(f)$ as a function of a_1. (c) Magnitude and phase response of $D(f)$ as a function of b_0. (d) Magnitude and phase response of $D(f)$ as a function of b_1. (e) Magnitude and phase response of $D(f)$ as a function of b_2.

All of the controller coefficients have an effect on the damping of the frequency response of $D(f)$. The coefficients a_1 and b_1 have the smallest influence on the frequency response and a_1 specifically only at frequencies lower than 100 Hz. The coefficients a_0, b_0 and b_2 have a damping effect from 10 Hz all the way up until $\frac{f_s}{2}$ Hz.

5.6.1.2. Modelling of the Voltage and Current Sensing Circuits

The voltage and current sensing circuits as well as the ADC are discussed in sections 5.2.1.5 and 5.2.1.6. Fig. 5.37 shows how the current sensing circuit is modelled in Simulink [137]. The high magnitude resistive divider and hall sensor ratio used during current sensing are modelled as a combined gain, $k_i = 0.15974$. The inductor current is measured with a current sensor in Simulink with a sampling frequency, $f_s = 19.2kHz$, before it is multiplied with the gain, k_i. The buffer circuit that adds a 1.65 V offset is modelled as a summing block. The 12-bit ADC is modelled by multiplying the output value of the buffer circuit by $2^{12} - 1 = 4095$. The maximum input to the ADC pin is 3.3 V, therefore, the signal is divided by 3.3. The value is saved as an 16-bit integer, before it is shifted to produce a 32-bit integer, as in the software. The 1.65 V offset is accounted for in the software by subtracting 0.5, as the 1.65V is approximately half of the 3.3 V that the ADC pin can read. The voltage sensing circuit is modelled similarly to the current sensing circuit and ADC, with the resistive gain, $k_v = 0.00311$, being the only difference.

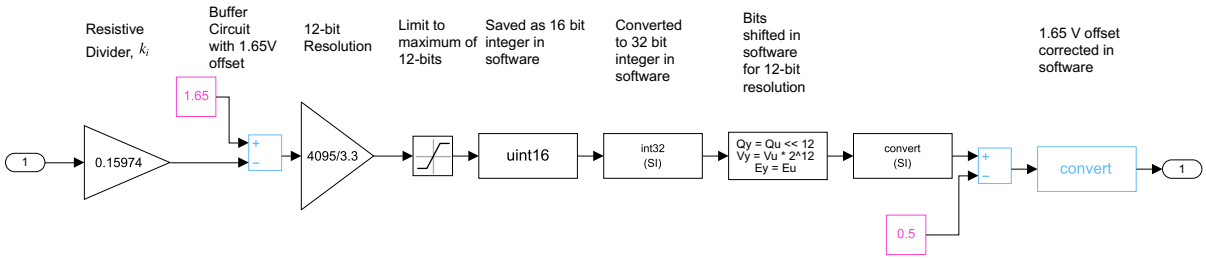

Figure 5.37: Modelling the current sensing circuit and ADC in Simulink [137].

5.6.1.3. Modelling the Unipolar Pulse Width Modulation Scheme

The PWM scheme implemented in the inverter is discussed in section 5.2.1.3. Fig. 5.38 shows how the hybrid unipolar PWM is implemented in Simulink [137]. The output signal of the control-loop is multiplied with a gain, $K_{PWM} = \frac{1000}{V_{DC}}$. The sign of this scaled output signal of the control-loop is obtained by comparing it to zero to determine which switching leg is switching at the carrier frequency. The other switching leg switches at the grid frequency. The scaled output signal of the control-loop controls a PWM generator that, in turn, controls the switching leg that is switching at the carrier frequency. The IGBTs of the remaining switching leg are provided with a logical high and low. Deadtime is added to the logical signals passed to the switches.

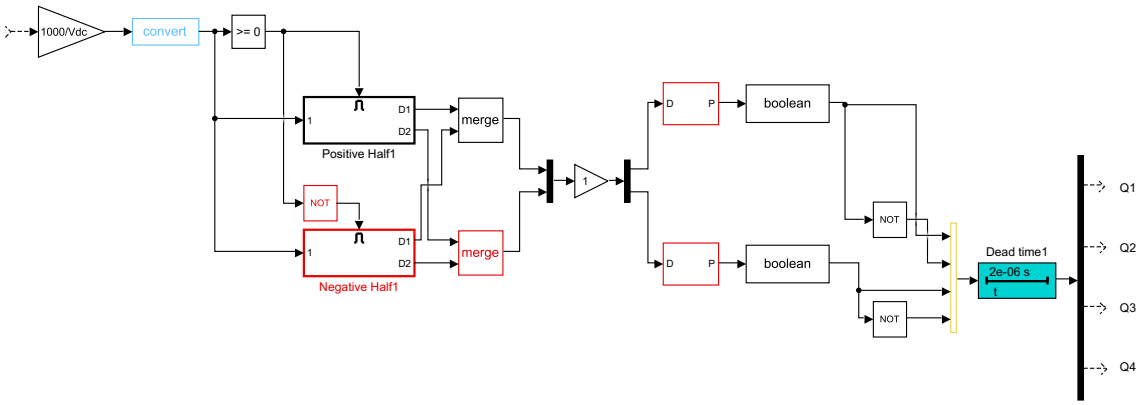

Figure 5.38: Modelling the hybrid unipolar PWM in Simulink [137].

Fig. 5.39 shows the corresponding simulated PWM signals that drive the switches, Q_1, Q_2, Q_3 and Q_4 of the full-bridge switching circuit used in Fig. 5.33. The switches Q_1 and Q_2 operate complimentary, as well as Q_3 and Q_4.

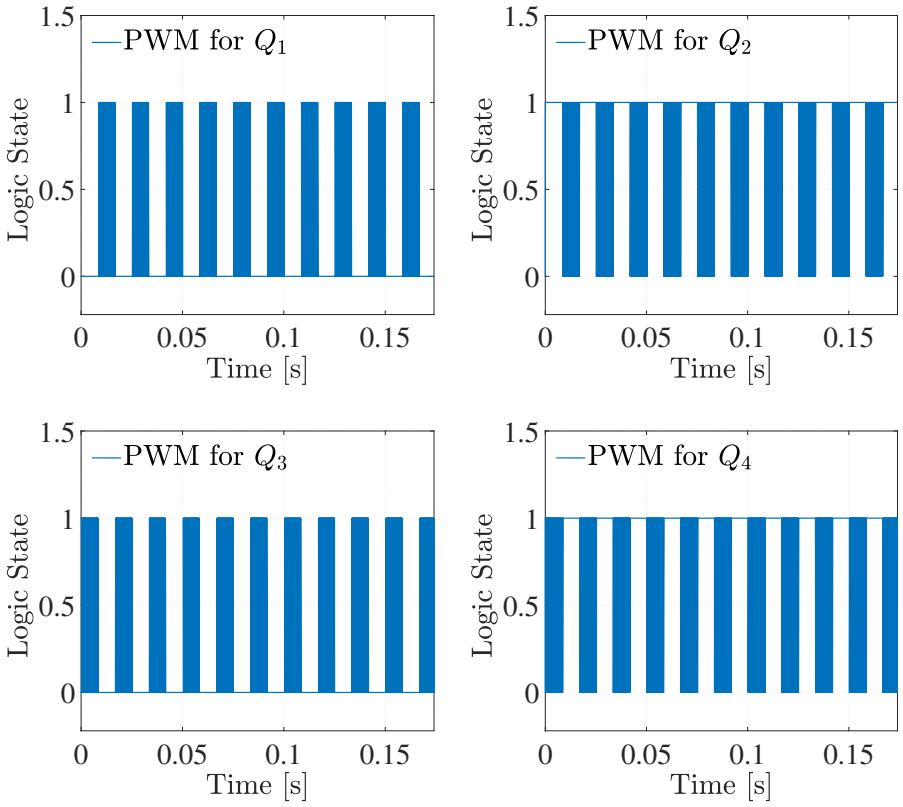

Figure 5.39: Simulated PWM logic state output signals to switches, Q_1, Q_2, Q_3 and Q_4.

5.6.1.4. Modelling Full-Bridge Switching Circuit

The full-bridge switching circuit in Fig. 5.33 is modelled with four IGBTs, each with an "on" resistance of 0.01 Ω, and "off" resistance of 10 $k\Omega$, a forward voltage drop, $V_f = 1.59V$ and a feedback diode with a forward voltage drop of 1.4 V.

5.6.2. Modelling the DC Voltage Source

The 400V DC voltage source in Fig. 5.6 consists of a three-phase diode rectifier circuit supplied with a three-phase transformer as explained in section 5.2.2. It is not possible to model this DC source topology accurately in Simulink, due to the variablity introduced with the use of the variac. In this section it is shown that the magnitude of the DC voltage supplied to the inverter is required to model the inverter accurately, but the impedance of the DC source is not important.

Fig. 5.40 shows the simulated output impedance of the inverter as a function of the DC input voltage magnitude, V_{DC}. As the DC input voltage magnitude, V_{DC}, increases, the resonant points of the simulated output impedance of the inverter shifts to higher frequencies. The DC voltage magnitude has a significant impact on the simulated output impedance frequency response of the inverter. It is, therefore, important to accurately define the input voltage, V_{DC}, in order to simulate the inverter.

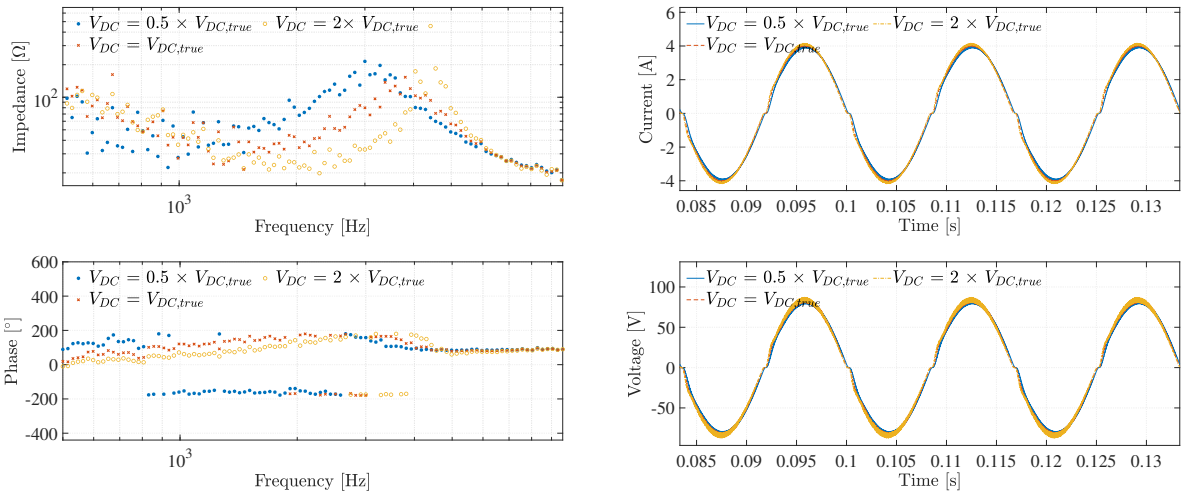

(a) (b)

Figure 5.40: (a) Magnitude and phase response of the inverter output impedance, $Z_o(f)$, as a function of V_{DC} obtained through simulation. (b) Output current, $i_o(t)$, and voltage, $v_o(t)$ as a function of V_{DC}.

To validate the results in Fig. 5.40, the influence of the DC input voltage on the practical inverter is investigated. Fig. 5.41 shows the frequency response of the output impedance of the inverter when the DC voltage of the practical inverter is set to $V_{DC} = 336V$ and

$V_{DC} = 401V$ respectively. Similar to the simulated results, the resonant points of the frequency response of the output impedance shift towards higher frequencies as V_{DC} is increased.

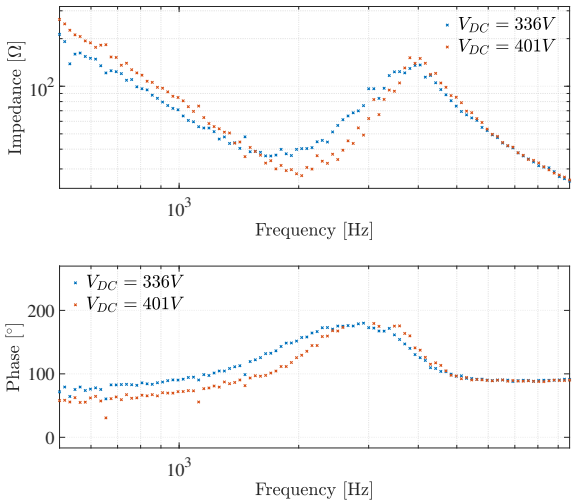

Figure 5.41: Magnitude and phase response of the experimental output impedance, $Z_o(f)$, as a function of V_{DC}.

The influence of the DC voltage magnitude, V_{DC}, on the output impedance frequency response is explained by examining the relationship between the fundamental frequency component of the modulated voltage, $\hat{V}_{Ao}^1$, and the DC input voltage, V_{DC}. The fundamental frequency component of the modulated voltage, $\hat{V}_{Ao}^1$, and the DC input voltage, V_{DC}, are related by the modulation index, m_a:

$$\hat{V}_{Ao}^1 = m_a V_{DC} \tag{5.47}$$

Equation (5.47) shows that when V_{DC} is lowered, m_a increases to keep $\hat{V}_{Ao}^1$ constant. Similarly, when V_{DC} is increased, m_a needs to decrease to keep $\hat{V}_{Ao}^1$ constant. This is done by the controller. Therefore, varying the DC voltage has the same effect as changing a gain at the output of the control-loop.

From the voltage drop present in Fig 5.8 it is clear that a series impedance exists in the source. It is now shown that this impedance can be neglected when deriving a model for the inverter. It is assumed that this series impedance can be modelled as a inductor, L_{DC}, in series with a resistor, R_{DC}. Figures 5.42 and 5.43 show the simulated output impedance of the inverter as a function of possible values for R_{DC} and L_{DC} respectively. Changing the series $R_{DC}L_{DC}$ impedance of the source has a negligible impact on the output voltage, current and impedance frequency response of the voltage source inverter, as long as the DC source impedance does not change the DC voltage substantially.

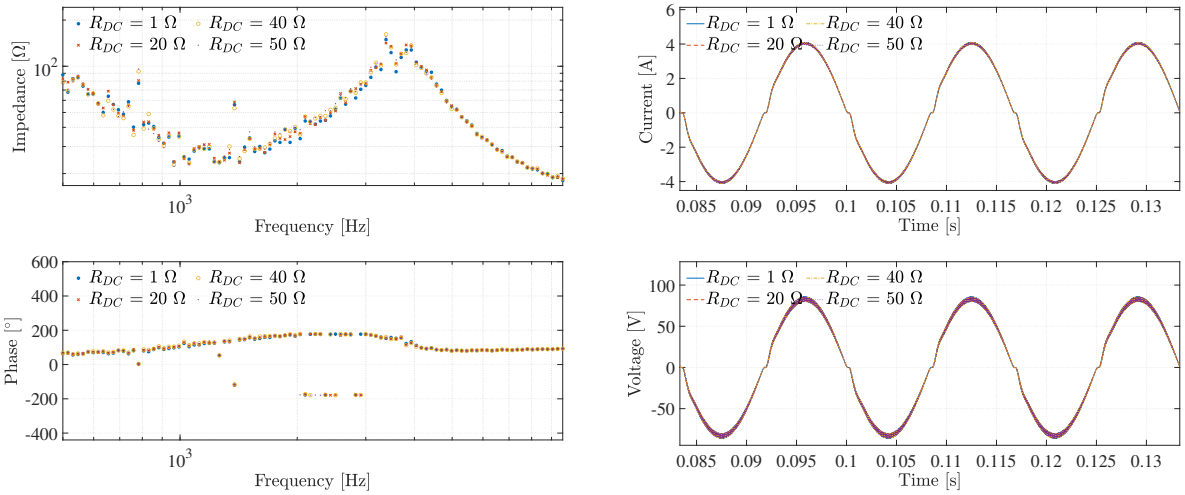

(a) (b)

Figure 5.42: (a) Magnitude and phase response of the output impedance, $Z_o(f)$, as a function of R_{DC}. (b) Output current, $i_o(t)$, and voltage, $v_o(t)$ as a function of R_{DC}.

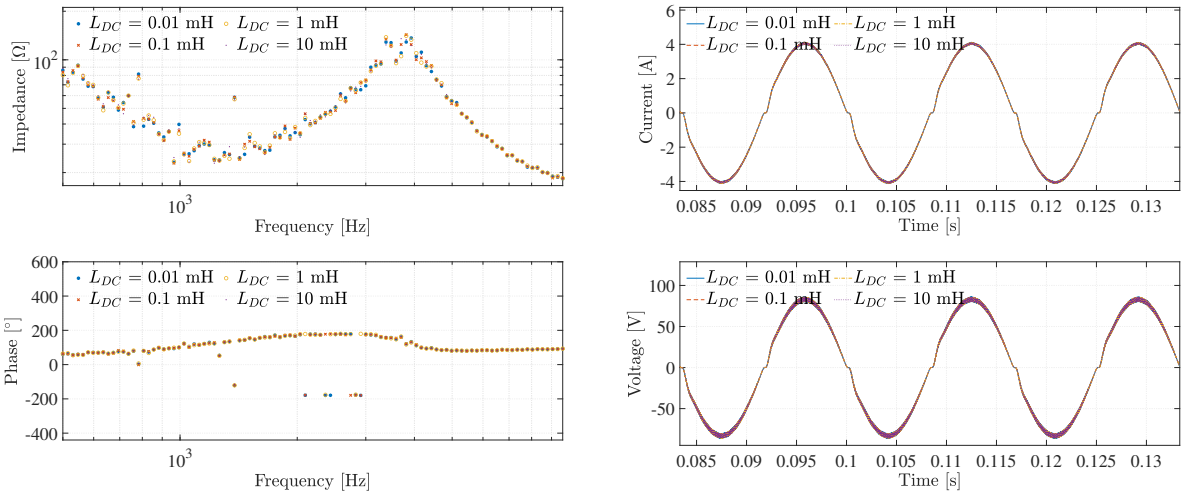

(a) (b)

Figure 5.43: (a) Magnitude and phase response of the output impedance, $Z_o(f)$, as a function of L_{DC}. (b) Output current, $i_o(t)$, and voltage, $v_o(t)$ as a function of L_{DC}.

As the DC voltage magnitude has a greater influence on the output impedance, voltage and current of the inverter than the impedance of the DC source, the DC voltage source is not modelled as a Thévenin equivalent, but as an ideal voltage source with a DC magnitude equal to the measured DC voltage magnitude after the voltage drop occurs, as displayed in Fig. 5.44. The DC voltage supplied to the input of the inverter is all that is required for an accurate model of the inverter.

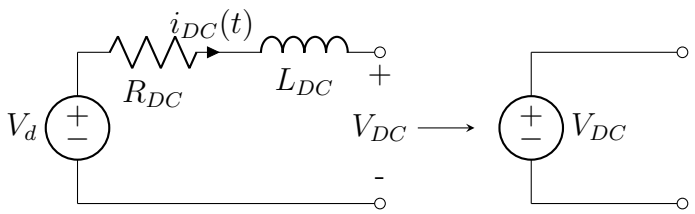

Figure 5.44: Modelling the DC voltage source as an ideal voltage source rather than a Thévenin equivalent.

5.6.3. Final Model of Practical Inverter System

The parameters used to populate the final model topology of the inverter system are presented in Table. 5.8. The filter and other circuit parameter values are measured in section 5.2.1. The parameters for the digital controller are found in example code for the Piccolo microcontroller provided by Texas Instruments of a possible grid-connected configuration, while the inverter under investigation operates in standalone mode.

TABLE 5.8: Parameter values.

Parameter	b_0	b_1	b_2	a_0	a_1	T_s $[\mu s]$	L_f $[mH]$	C_f $[\mu F]$	r_{L_f} $[\Omega]$	C_i $[\mu F]$
Value	0.5253	0.1314	-0.3938	-1.01	0.01	52	4.944	9.49	0.526	1200

The final model used in simulation is compared to the practical inverter. Fig. 5.45a shows the practical output impedance of the measured target system, $Z_{o,S}(f)$, as well as the simulated output impedance of the model, $Z_{o,M}(f)$, populated with the parameters in Table 5.8. Fig. 5.45b shows the simulated output voltage and current of the model under normal operating conditions, $v_{o,M,n}(t)$ and $i_{o,M,n}(t)$, as well as the measured output voltage and current of the system under normal operating conditions, $v_{o,S,n}(t)$ and $i_{o,S,n}(t)$. Although the magnitudes of the frequency responses and the amplitudes of the time-domain output waveforms of the system and model are not exactly the same, characteristics of the frequency- and time-domain outputs are comparable. From Fig. 5.45 it is clear that model exhibits the same amount of modes as the system. Therefore, even if the model presented is not the exact complete model, it is a good representation of the inverter.

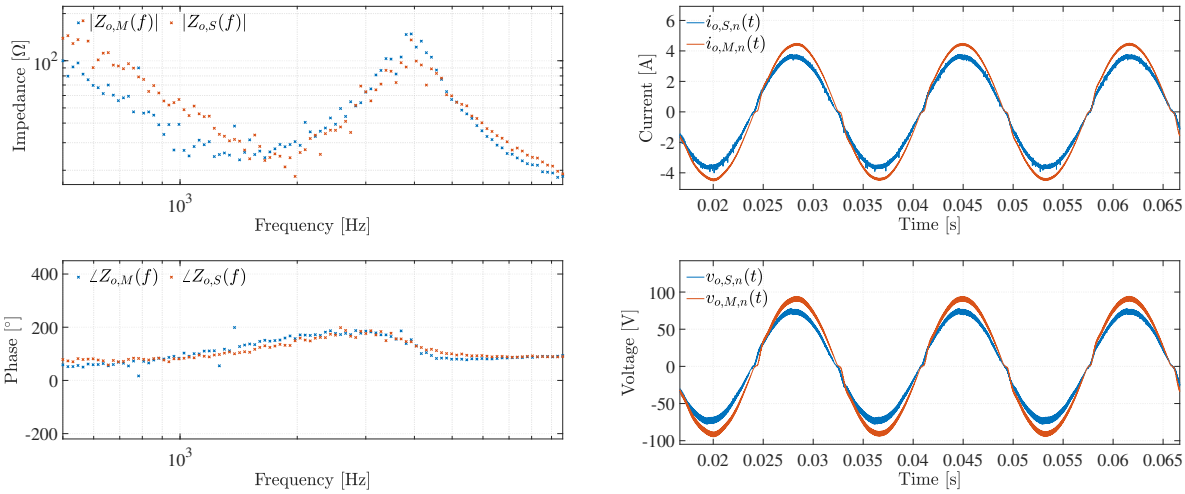

(a) (b)

Figure 5.45: (a) Comparison of the magnitude and phase response of the output impedance of the system, $Z_{o,S}(f)$, and the simulated model, $Z_{o,M}(f)$. (b) Output current and voltage of the target system, $i_{o,S,n}(t)$ and $v_{o,S,n}(t)$, as well as the model, $i_{o,M,n}(t)$ and $v_{o,M,n}(t)$.

The differences between the model and system could be due to the following reasons:

- As there are some uncertainty on how the software is implemented, the controller parameter values in Table 5.8 which are used to populate the model could be inaccurate. It is unknown whether the controller parameters used in the model are the correct values.
- The circuit and control topologies of the inverter are determined by inspection, investigating all available datasheets, user manuals, software and schematics. The exact model is not provided by Texas Instruments. It is possible that the model neglects a part of the real inverter.
- The practical inverter circuit can contain parasitic inductance and resistances that are not accounted for.

Parameter estimation can be performed to obtain more accurate model parameters.

5.6.4. Sensitivity Analysis of Controller and Filter Parameters on the Inverter Output Impedance

A simulated sensitivity analysis is performed to determine the effect of the various filter and controller parameters on the output impedance frequency response of the inverter and the output voltage and current in the time-domain. Each parameter, a_0, a_1, b_0, b_1, b_2, C_f and L_f, are halved and doubled from its true values in simulation to study its effect in the time- and frequency-domain.

Fig. 5.46 shows the simulated output impedance of the inverter, as well as the simulated output voltage and current under normal operating conditions as a function of the controller coefficient, a_0. Halving the coefficient a_0 damps the resonant points of $Z_o(f)$. The current and voltage amplitudes are decreased. Doubling a_0 causes the inverter to become unstable, therefore, only the LC filter resonance is observed in the frequency response and no time-domain waveforms are presented.

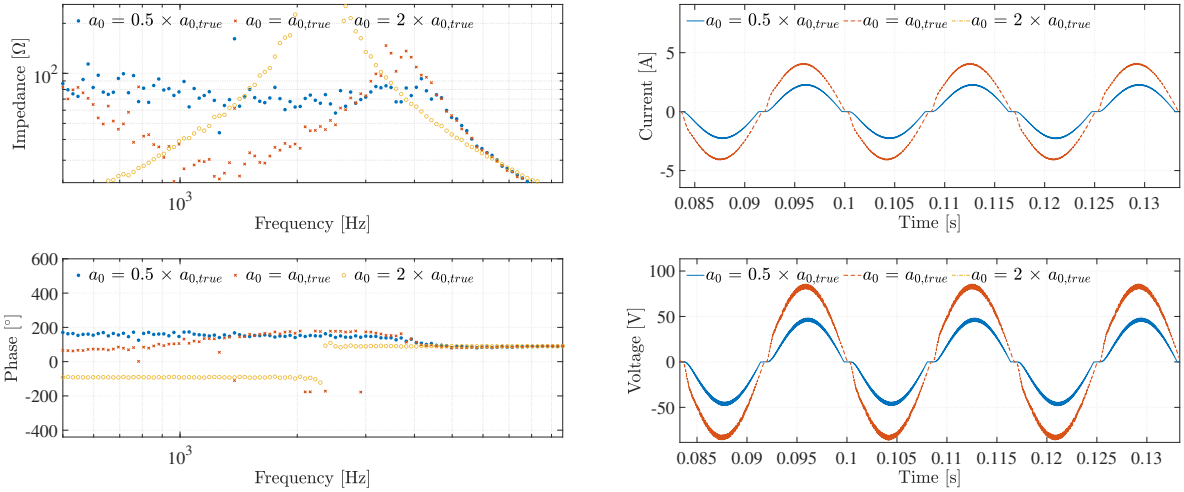

(a) (b)

Figure 5.46: (a) Magnitude and phase response of the output impedance, $Z_o(f)$, as a function of a_0. (b) Output current, $i_o(t)$, and voltage, $v_o(t)$ as a function of a_0.

Fig. 5.47 shows the simulated output impedance of the inverter, as well as the simulated output voltage and current under normal operating conditions as a function of the controller coefficient, a_1. The coefficient a_1 has very little effect on both the time- and frequency domain outputs of the inverter. Recall from section 5.6.1.1 that a_1 only affects frequencies lower than 50 Hz of the discrete controller. The coefficient a_1 has a limited effect on the amplitudes of the current and voltage outputs.

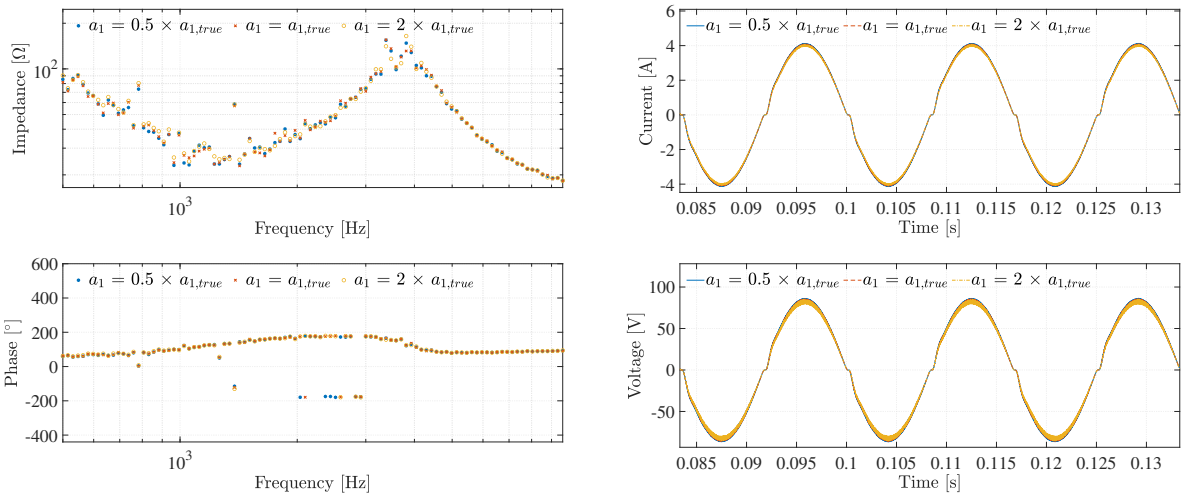

(a) (b)

Figure 5.47: (a) Magnitude and phase response of the output impedance, $Z_o(f)$ as a function of a_1. (b) Output current, $i_o(t)$, and voltage, $v_o(t)$ as a function of a_1.

Fig. 5.48 shows the simulated output impedance of the inverter, as well as the simulated output voltage and current under normal operating conditions as a function of the controller coefficient, b_0. The coefficient b_0 has an effect on the damping and location of the first resonant point and an effect on the damping of the second resonant point. When b_0 is halved the output current amplitude decreases. When b_0 is doubled the time-domain output current and voltage are similar to that of the true value of b_0.

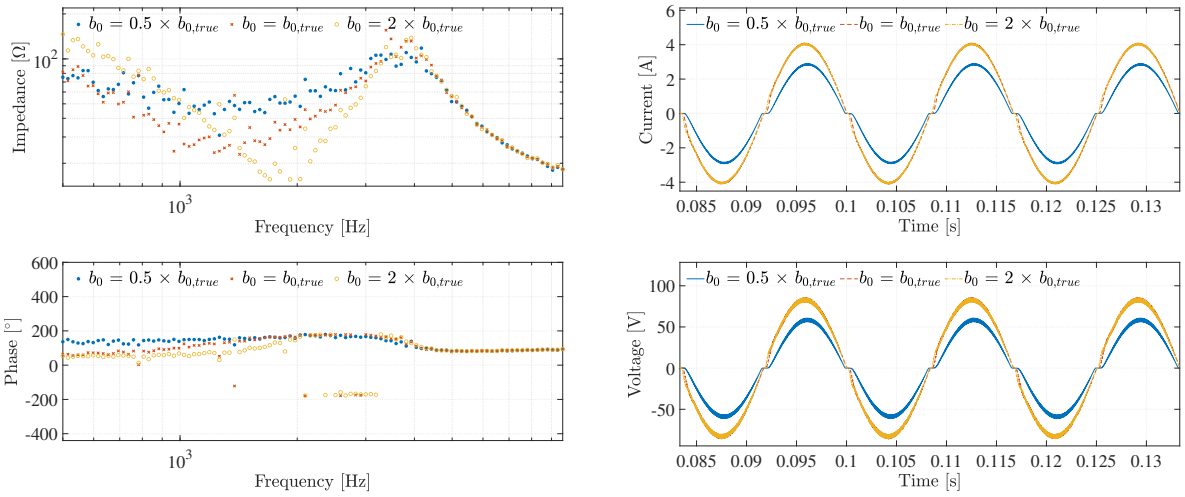

(a) (b)

Figure 5.48: (a) Magnitude and phase response of the output impedance, $Z_o(f)$, as a function of b_0. (b) Output current, $i_o(t)$, and voltage, $v_o(t)$ as a function of b_0.

Fig. 5.49 shows the simulated output impedance of the inverter, as well as the simulated output voltage and current under normal operating conditions as a function of the controller

coefficient, b_1. The effect of b_1 is only observed by the damping of the first resonant point of the output impedance. The effect on the output current and voltage is negligible.

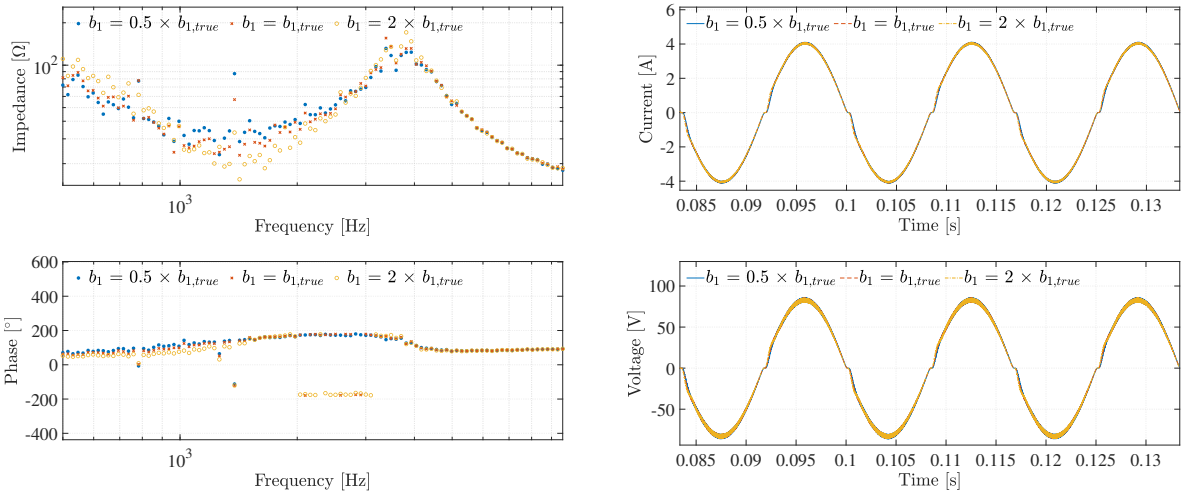

(a) (b)

Figure 5.49: (a) Magnitude and phase response of the output impedance, $Z_o(f)$, as a function of b_1. (b) Output current, $i_o(t)$, and voltage, $v_o(t)$ as a function of b_1.

Fig. 5.50 shows the simulated output impedance of the inverter, as well as the simulated output voltage and current under normal operating conditions as a function of the controller coefficient, b_2. The effect on the output current and voltage is negligible. The coefficient b_2 mainly impacts the damping of the first resonant point of the output impedance. When b_2 is doubled, the inverter becomes unstable, similar to doubling a_0.

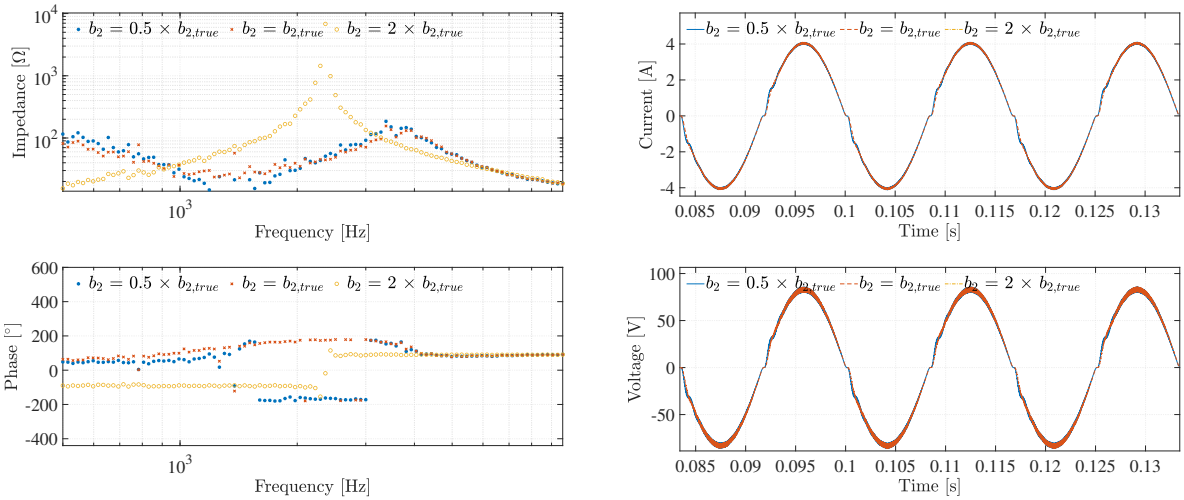

(a) (b)

Figure 5.50: (a) Magnitude and phase response of the output impedance, $Z_o(f)$, as a function of b_2. (b) Output current, $i_o(t)$, and voltage, $v_o(t)$ as a function of b_2.

Figures 5.51 and 5.52 show the simulated output impedance of the inverter, as well as the simulated output voltage and current under normal operating conditions as a function of the filter parameters, L_f and C_f, respectively. Both the inductor and capacitor used in the low-pass filter influence the location and magnitude of the second resonant point of the output impedance frequency response as presented in figures 5.51a and 5.52a. The inductor and capacitor also influence the ripple contained in the time-domain waveforms. The inductor L_f influences the amplitude of the output current and voltage waveforms.

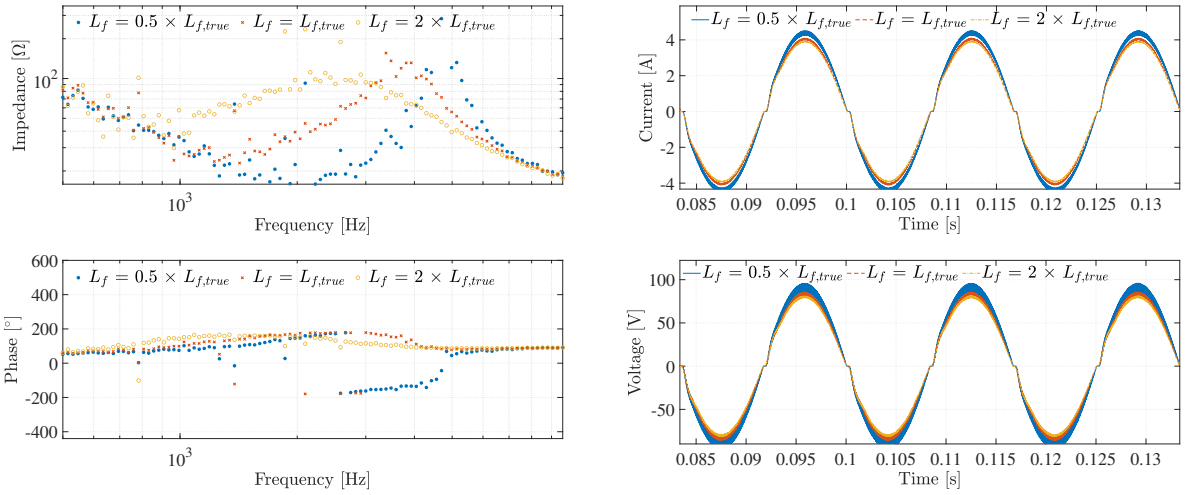

(a) (b)

Figure 5.51: (a) Magnitude and phase response of the output impedance, $Z_o(f)$, as a function of L_f. (b) Output current, $i_o(t)$, and voltage, $v_o(t)$ as a function of L_f.

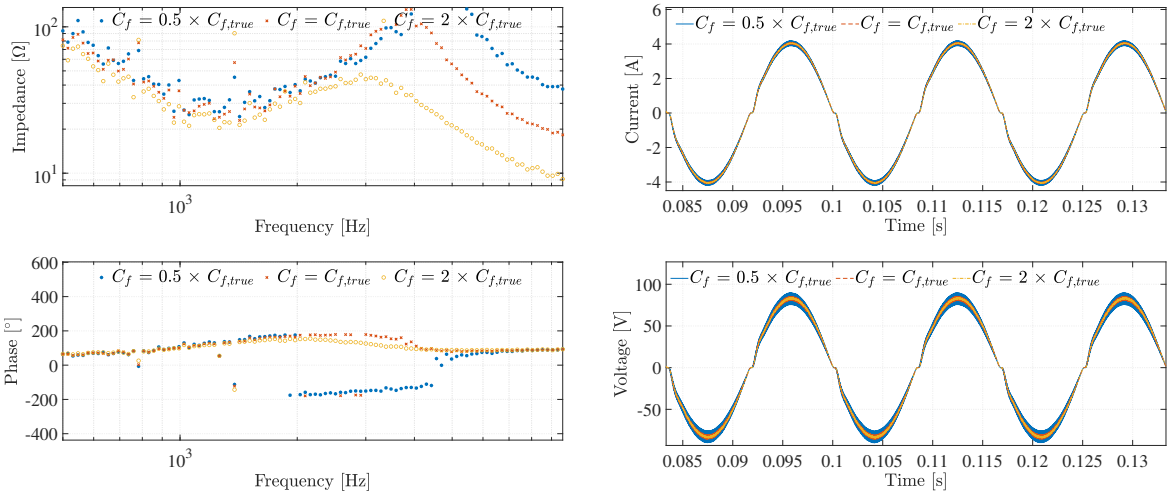

(a) (b)

Figure 5.52: (a) Magnitude and phase response of the output impedance, $Z_o(f)$, as a function of C_f. (b) Output current, $i_o(t)$, and voltage, $v_o(t)$ as a function of C_f.

5.7. Parameter Estimation of Controller Parameters of the Inverter

Parameter estimation studies aim to populate a model of a target system with parameters to enable accurate modelling of the target system. The aim of applying parameter estimation in this chapter is to populate an Electromagnetic Transient (EMT) model of the inverter in Simulink with estimated controller parameters using the measured data of the practical inverter system. The Simulink model of the target inverter is discussed in section 5.6 and the practical inverter measurements in sections 5.3 - 5.5.

Before parameter estimation is conducted on the practical inverter, parameter estimation of the transfer function of the discrete controller and the Simulink model of the inverter are investigated. The parameter estimation studies conducted in this section are summarized in Table 5.9.

TABLE 5.9: Summary of the parameter estimation studies conducted in this section.

Section	**Parameters Estimated**	**Model Used during Parameter Estimation**	**Target System**	**Time- and Frequency-Domain Responses Used in Objective Function**
5.7.1	a_0, a_1, b_0, b_1, b_2	Analytical transfer function of discrete controller as discussed in section 5.6.1.1	Analytical transfer function of discrete controller populated with true parameter values	Transfer function of D(z)
5.7.2	a_0, a_1, b_0, b_1, b_2	EMT model of inverter as presented in section 5.6.	EMT model populated with parameter values of final model as presented in section 5.6.3	Estimation of $Zo(f)$ using method 1, $v_o(t)$, $i_o(t)$
5.7.3	a_0, a_1, b_0, b_1, b_2	EMT model of inverter as presented in section 5.6	Measured values of practical inverter as discussed in sections 5.3 to 5.5	Estimation of $Zo(f)$ using method 1, $v_o(t)$, $i_o(t)$

5.7.1. Parameter Estimation of the Coefficients of the Discrete Controller using an Analytical Approach

As discussed in sections 5.2.1.6 and 5.6.1.1 a discrete controller, $D(z)$, is implemented in the current control loop. In this section the analytical Laplace-domain transfer function of this current controller, $D(z)$, is used to estimate the coefficients of the controller. As the analytical transfer function is available, various case studies of parameter estimation can be applied with relative ease and low computational complexity, as compared to using the Simulink model in a parameter estimation study. These case studies are summarized in Table 5.10.

TABLE 5.10: Parameter estimation results of discrete controller using analytical transfer function.

				Errors (%)				
Case	**Frequency Vector**	**Parameters Estimated**	**Final Objective Function Value**	b_0	b_1	b_2	a_0	a_1
1	Logarithmic frequency vector between 1 and $f_s/2$ Hz containing 1000 points	b_0, b_1, b_2, a_0, a_1	0.008223	1.35	3.69	0.52	3.50	353.41
2	Logarithmic frequency vector between 1 and $f_s/2$ Hz containing 1000 points	b_0, b_1, b_2, a_0 Fix $a_1 = 0$ system and $a_1 = 0$ in model	0.0001887	0.28	0.09	0.34	0.00	N/A
3	Logarithmic frequency vector between 1 and $f_s/2$ Hz containing 1000 points	b_0, b_1, b_2, a_0 Fix $a_1 = 0.01$ system and $a_1 = 0$ in model	0.00067	0.28	1.08	0.01	0.99	N/A
4	Logarithmic frequency vector between 10 and $f_s/2$ Hz containing 1000 points	b_0, b_1, b_2, a_0 Fix $a_1 = 0.01$ system and $a_1 = 0$ in model	0.0008277	0.26	1.23	0.01	0.96	N/A
5	Logarithmic frequency vector between 500 and $f_s/2$ Hz containing 1000 points	b_0, b_1, b_2, a_0 Fix $a_1 = 0.01$ system and $a_1 = 0$ in model	0.001217	1.49	4.00	0.65	1.32	N/A

The aim of performing parameter estimation on the transfer function is to gain a better understanding of the controller and the difficulties that might arise when using the Simulink simulations to perform parameter estimation on measured data. Case 1 is used as a baseline and all the case studies that follow are iterations of case 1. The differences between and significance of the case studies that are summarized in Table 5.10 are listed as follows:

- **Case 1**: A parameter estimation procedure is applied to estimate all 5 parameters of the discrete controller. The frequency vector is logarithmicly spaced between 1 Hz and $f_s/2 = 9.6kHz$ Hz, where f_s is the sampling frequency of the discrete controller. The particle swarm optimization algorithm is used. The MSE of the analytical transfer function of the discrete controller in the Laplace domain is used in the objective function. A 353% error exist in a_1. Errors can be seen in the rest of the parameters, but all within 4%.

- **Case 2**: It is known that a_1 influences frequencies below 100 Hz, based on the sensitivity analysis conducted in section 5.6.1.1. Therefore, the effect of a_1 will be observed in the fundamental frequency component, i.e. when looking at the time-domain, which is unavailable when using only the Laplace-domain transfer function of the discrete controller. Therefore, a_1 is fixed to $a_1 = 0.01$ and the other four parameters are estimated with the idea that a two-step verification could be used in the future, i.e. step 1: estimate four parameters from frequency domain where a_1 has negligible effect, step 2: estimate a_1 from time-domain information. The remaining four parameters are estimated successfully when using the Laplace-domain transfer function of the discrete controller.

- **Case 3**: The coefficient a_1 is fixed in the model, $a_1 = 0$, but $a_1 = 0.01$ in the system. Four parameters are estimated successfully.

- **Case 4**: The initial frequency of the frequency vector is increased from 1 Hz to 10 Hz. Four parameters are estimated successfully.
- **Case 5**: The initial frequency of the frequency vector is increased from 10 Hz to 500 Hz. Four parameters are estimated successfully.

In the parameter estimation methodologies applied to the discrete transfer function of the controller, the coefficient, a_1, is not estimated accurately. Recall from the sensitivity analysis conducted on the discrete controller in section 5.6.1.1, that a_1 only affects low frequencies. These low frequencies are also influenced by most of the other coefficients of the discrete transfer function.

From cases 1-5 it is clear that assuming $a_1 = 0$ still allows for accurate estimation of the other four parameters. It might be possible to estimate a_1 using the time-domain output waveforms, which was not possible when investigating the transfer function of the discrete controller. It might also be possible that a sufficiently accurate model of the inverter is obtainable when assuming $a_1 = 0.01 \approx 0$.

5.7.2. Parameter Estimation of the Coefficients of the Discrete Controller through a Simulation Approach

The analytical transfer function is used to estimate up to four out of the five controller coefficients accurately in the previous subsection. However, in practice, the only readily accessible part of the inverter is assumed to be the AC output, i.e. the output voltage and current from which the output impedance can be estimated. The focus of the investigation, therefore, shifts to using these signals to perform parameter estimation with the aim of obtaining the controller parameters.

The Simulink model discussed in section 5.6 is used as model, while the target system is the Simulink model populated with the final model parameters, as discussed in section 5.6.3. The same PRIS source parameters is used as discussed in section 5.3, as summarized in Table 5.11.

TABLE 5.11: PRIS source parameters.

PRBS Order	**Clock Frequency f_{clk}**	R_{PRIS}	L_{PRIS}	C_{PRIS}	V_{DC}
12	$12kHz$	100 Ω	$4.4mH$	$10\mu F$	20 V

The output impedance of the model, $Z_{o,M}(f)$, and the system, $Z_{o,S}(f)$, are determined between 100 Hz and 10 kHz with 100 frequency points logarithmically spaced. The particle swarm optimization algorithm is used throughout. A multi-step parameter estimation approach is adopted:

- **Step 1:** The output impedance of the model, $Z_{o,M}(f)$, and the system, $Z_{o,S}(f)$, of the inverter are estimated between 100 Hz and 10 kHz. Particle swarm optimization is used to estimate four of the five controller parameters using a MSE objective function of the output impedance. The effect of a_1 on the frequency response of the output impedance of the inverter is assumed to be negligible, as shown in the sensitivity analysis performed in section 5.6.1.1. The coefficient a_1 is thus fixed to $a_1 = 0$ in the model, but the true value $a_1 = 0.01$ is used in the system. The four parameters, b_0, b_1, b_2, a_0 are readily estimated within a 1% error. The output impedance of the model, $Z_{o,M}(f)$, and the system, $Z_{o,S}(f)$, as well as the output current and voltage of the estimated model and system under normal operating conditions, $i_{o,M,n}(t)$, $i_{o,S,n}(t)$, $v_{o,M,n}(t)$ and $v_{o,S,n}(t)$, are compared in Fig. 5.53. These outputs correspond well while assuming $a_1 \approx 0$, as the frequency- and time-domain responses lie on top of each other. This might be a sufficient model of the system, but another two steps are incorporated to estimate a_1 as well.

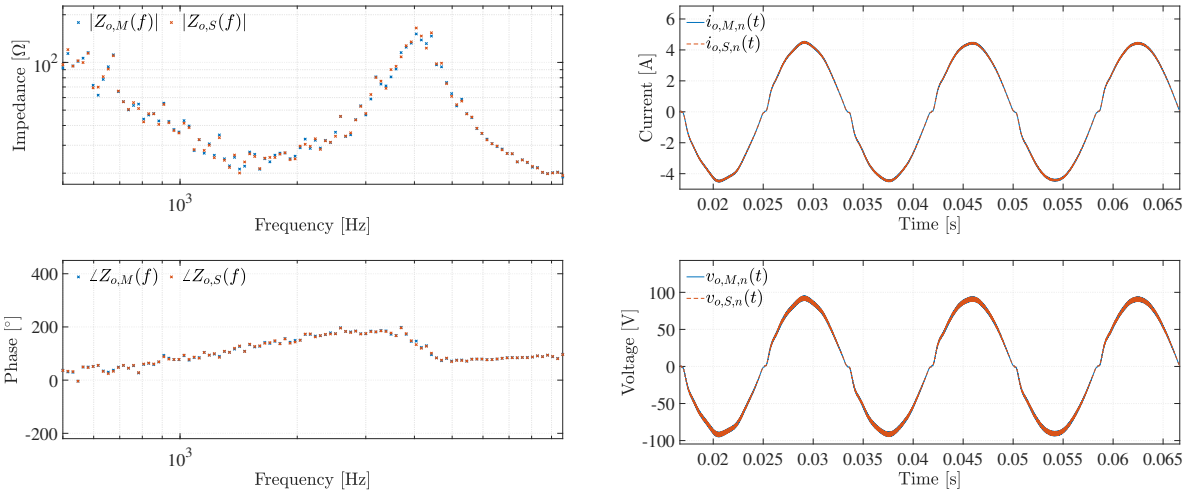

(a) (b)

Figure 5.53: (a) Magnitude and phase response of the output impedance of the estimated model, $Z_{o,M}(f)$, and the system, $Z_{o,S}(f)$, after step 1. (b) Time-domain waveforms of the output currents and voltages of the estimated model and the system under normal conditions, $i_{o,M,n}(t)$, $i_{o,S,n}(t)$, $v_{o,M,n}(t)$ and $v_{o,S,n}(t)$, after step 1.

- **Step 2:** From the sensitivity analysis performed on the analytical transfer function of the discrete controller in section 5.6.1.1, it is clear that a_1 has an influence at frequencies lower than 100 Hz. The parameter a_1 has an influence at the fundamental frequency. In step 1, four parameters are estimated within 1% error. During step 2 b_0 and b_2 are fixed to the estimated values in step 1. The remaining three parameters, including a_1, are estimated using the RMS value of the current and the fundamental

voltage component in an absolute error objective function, as it is known that a_1 influence the fundamental frequency component. Fig. 5.54 compares the output impedance of the model, $Z_{o,M}(f)$, and the system, $Z_{o,S}(f)$, as well as the output current and voltage of the estimated model and system under normal operating conditions, $i_{o,M,n}(t)$, $i_{o,S,n}(t)$, $v_{o,M,n}(t)$ and $v_{o,S,n}(t)$ after step 2. The time-domain signals and frequency-domain responses remain on top of each other. The estimated parameter a_1 still has a 16.58% error after step 2.

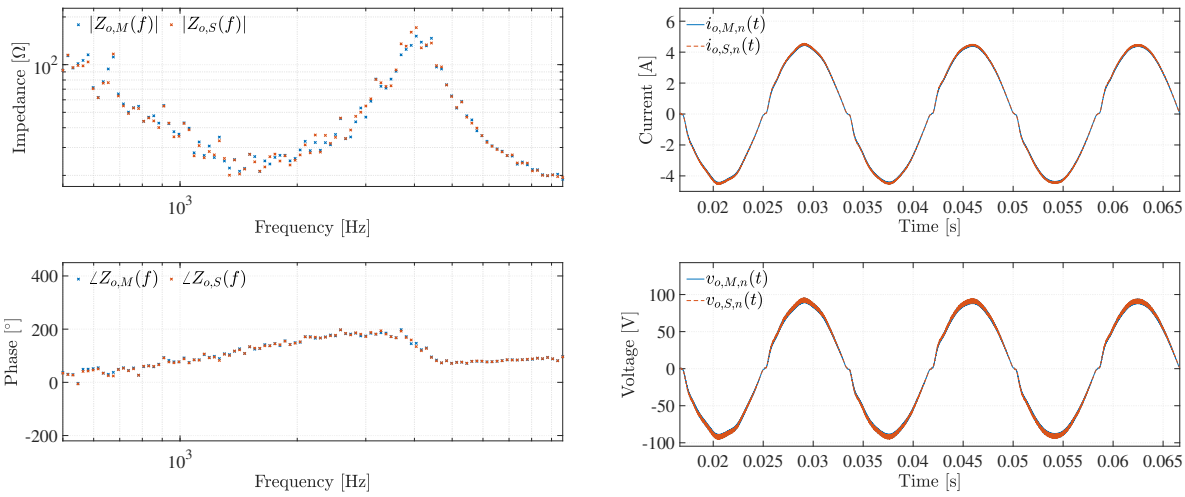

(a) (b)

Figure 5.54: (a) Magnitude and phase response of the output impedance of the estimated model, $Z_{o,M}(f)$, and the system, $Z_{o,S}(f)$, after step 2. (b) Time-domain waveforms of the output currents and voltages of the estimated model and the system under normal conditions, $i_{o,M,n}(t)$, $i_{o,S,n}(t)$, $v_{o,M,n}(t)$ and $v_{o,S,n}(t)$, after step 2.

- **Step 3 :** To refine the estimated parameters, all five parameters are estimated in step 3 using the RMS value of the current in an absolute error objective function. The initial starting point of the optimization is the estimated parameter values after step 2. Fig. 5.55 compares the output impedance of the model, $Z_{o,M}(f)$, and the system, $Z_{o,S}(f)$, as well as the output current and voltage of the estimated model and system under normal operating conditions, $i_{o,M,n}(t)$, $i_{o,S,n}(t)$, $v_{o,M,n}(t)$ and $v_{o,S,n}(t)$ after step 3. The output voltage, current and impedance of the system and model are similar, as the responses lie on top of each other.

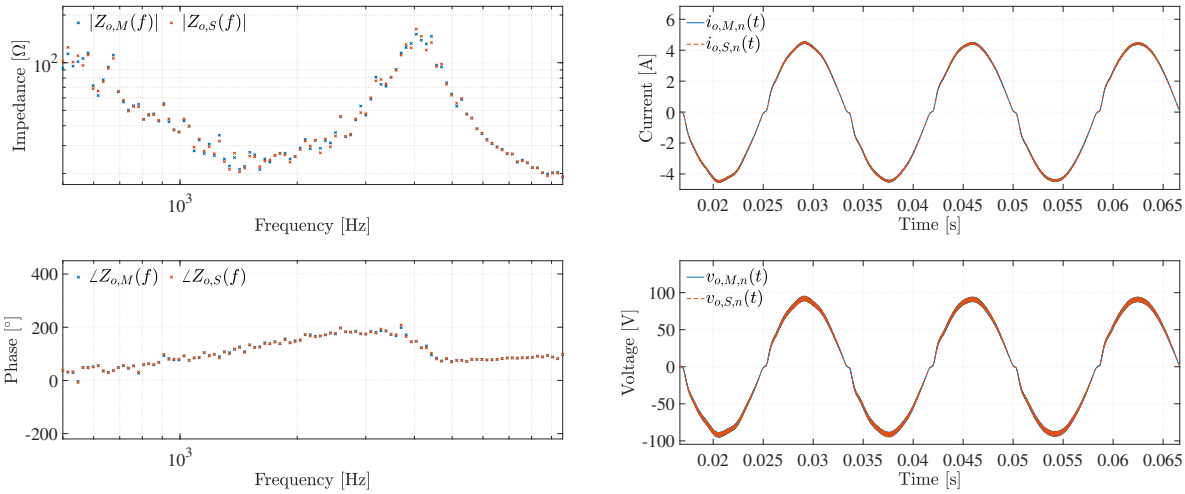

(a) (b)

Figure 5.55: (a) Magnitude and phase response of the output impedance of the estimated model, $Z_{o,M}(f)$, and the system, $Z_{o,S}(f)$, after step 3. (b) Time-domain waveforms of the output currents and voltages of the estimated model and the system under normal conditions, $i_{o,M,n}(t)$, $i_{o,S,n}(t)$, $v_{o,M,n}(t)$ and $v_{o,S,n}(t)$, after step 3.

The three-step parameter estimation process used in this section is summarized in Fig. 5.56.

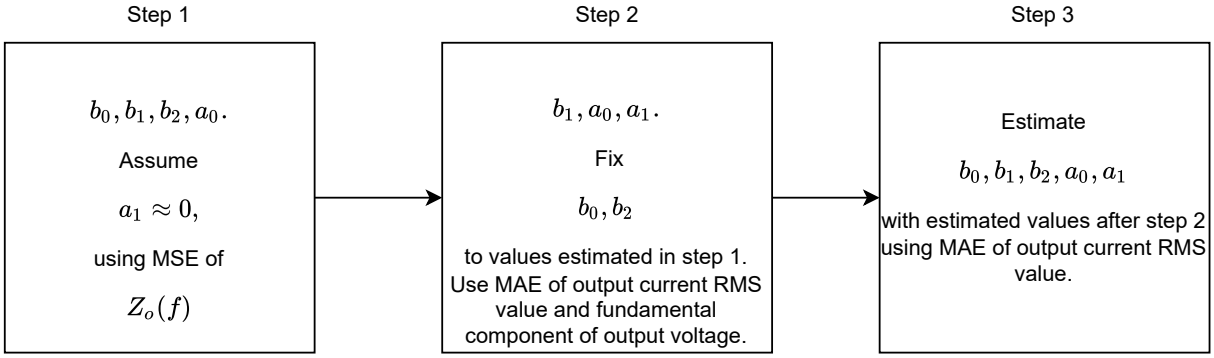

Figure 5.56: Parameter estimation process.

The resultant parameters after each step, as well as their errors, are presented in Table 5.12. All 5 controller parameters of the simulated inverter are estimated accurately using the three-step approach in simulation. In step 1, four parameters are estimated within 1% error. After step 3 a_1 is also estimated within 4%. It is unclear whether it is necessary to obtain the correct value of coefficient a_1, as it has a negligible effect on the outputs of the inverter and does not influence the model accuracy significantly if the output current, voltage and impedance are compared.

TABLE 5.12: Resultant parameters after each step of parameter estimation.

	b_0		b_1		b_2		a_0		a_1	
Step	**Value**	**Error** [%]	**Value**	**Error** [%]	**Value**	**Error** [%]	**Value**	**Error** [%]	**Value**	**Error** [%]
1	0.528	0.501	0.132	0.704	-0.395	0.213	-1	0.985	N/A	N/A
2	N/A	N/A	0.132832	1.0907	N/A	N/A	-1.008	0.165	0.00834	16.58
3	0.530	0.852	0.132	0.159	-0.39597	0.554	-1.009	0.0425	0.00961	3.939

5.7.3. Parameter Estimation of the Coefficients of the Discrete Controller through an Experimental Approach

In this section the measurements of the practical inverter, the target system, as presented in sections 5.3 - 5.5 are used to estimate parameters for the Simulink model. A parameter estimation process similar to the one discussed in section 5.7.2 is implemented. Different frequency- and time-domain responses are used in the objective function in steps 2 and 3.

The same PRIS source parameters are used as discussed in section 5.3, as summarized in Table 5.13.

TABLE 5.13: PRIS source parameters.

PRBS Order	**Clock Frequency** f_{clk}	R_{PRIS}	L_{PRIS}	C_{PRIS}	V_{DC}
12	$12kHz$	100 Ω	$4.4mH$	$10\mu F$	20 V

The output impedance is determined between 500 Hz and 10 kHz with 100 frequency points spaced logarithmicly. Particle swarm optimization is used throughout. The three steps of the parameter estimation approach are described as follows:

- **Step 1:** In step 1, a_1 is assumed $a_1 = 0$. The other four controller parameters are estimated using $Z_{o,M}(f)$ and $Z_{o,S}(f)$ in a MSE objective function. Fig. 5.57 compares the output impedance of the model, $Z_{o,M}(f)$, and the system, $Z_{o,S}(f)$, as well as the output current and voltage of the estimated model and system under normal operating conditions, $i_{o,M,n}(t)$, $i_{o,S,n}(t)$, $v_{o,M,n}(t)$ and $v_{o,S,n}(t)$ after step 1. The responses are similar, as the frequency- and time-domain responses lie on top of each other.

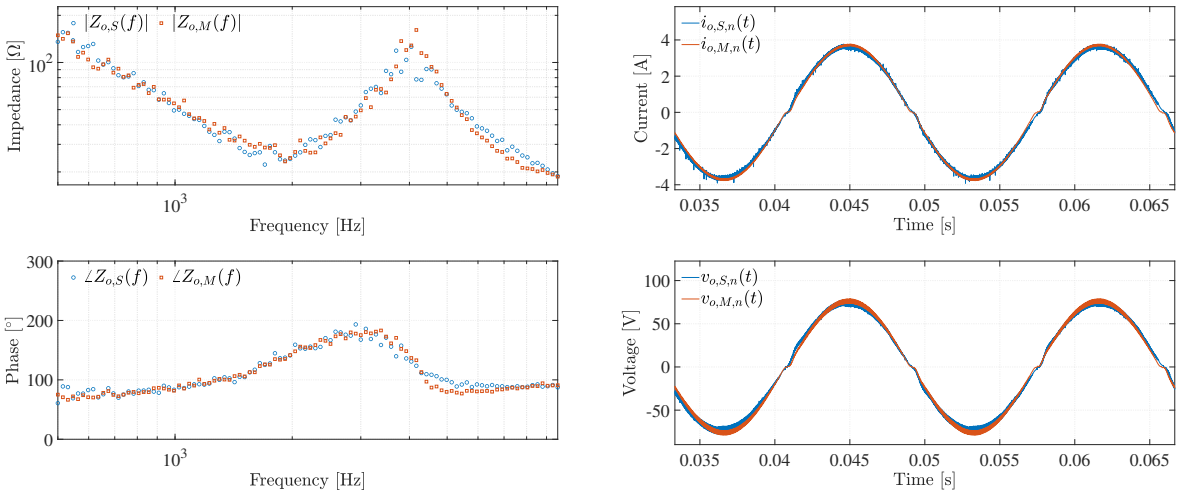

(a) (b)

Figure 5.57: (a) Magnitude and phase response of the output impedance of the estimated model, $Z_{o,M}(f)$, and the system, $Z_{o,S}(f)$, after step 1. (b) Time-domain waveforms of the output currents and voltages of the estimated model and the system under normal conditions, $i_{o,M,n}(t)$, $i_{o,S,n}(t)$, $v_{o,M,n}(t)$ and $v_{o,S,n}(t)$, after step 1.

- **Step 2:** In step 2 b_0 and b_2 are fixed to its estimated parameters of step 1 whilst the other three coefficients, including a_1, are estimated. The absolute error of the output current magnitude at the fundamental frequency, the absolute error of the output current RMS value, as well as the MSE of $Z_o(f)$ are used in the objective function. Fig. 5.58 compares the output impedance of the model, $Z_{o,M}(f)$, and the system, $Z_{o,S}(f)$, as well as the output current and voltage of the estimated model and system under normal operating conditions, $i_{o,M,n}(t)$, $i_{o,S,n}(t)$, $v_{o,M,n}(t)$ and $v_{o,S,n}(t)$ after step 2. The output voltage, current and impedance frequency responses of the system and the model remain sufficiently similar.

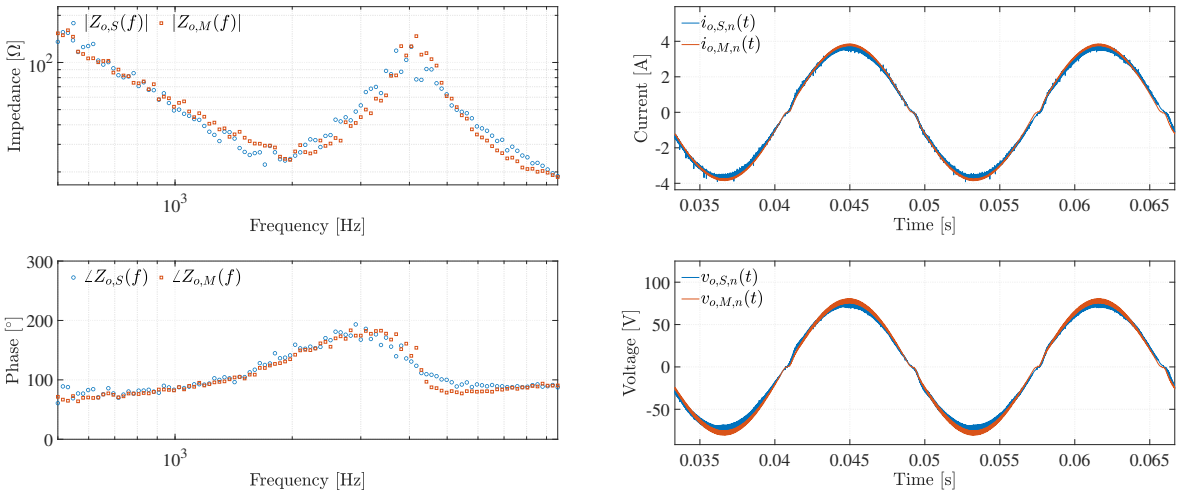

(a) (b)

Figure 5.58: (a) Magnitude and phase response of the output impedance of the estimated model, $Z_{o,M}(f)$, and the system, $Z_{o,S}(f)$, after step 2. (b) Time-domain waveforms of the output currents and voltages of the estimated model and the system under normal conditions, $i_{o,M,n}(t)$, $i_{o,S,n}(t)$, $v_{o,M,n}(t)$ and $v_{o,S,n}(t)$, after step 2.

- **Step 3:** In the final step of the parameter estimation process all five parameters are estimated. The absolute error of the output current magnitude at the fundamental frequency as well as the MSE of $Z_o(f)$ are used in the objective function. Fig. 5.59 compares the output impedance of the model, $Z_{o,M}(f)$, and the system, $Z_{o,S}(f)$, as well as the output current and voltage of the estimated model and system under normal operating conditions, $i_{o,M,n}(t)$, $i_{o,S,n}(t)$, $v_{o,M,n}(t)$ and $v_{o,S,n}(t)$ after step 3. The output voltage, current and impedance frequency response remain sufficiently similar.

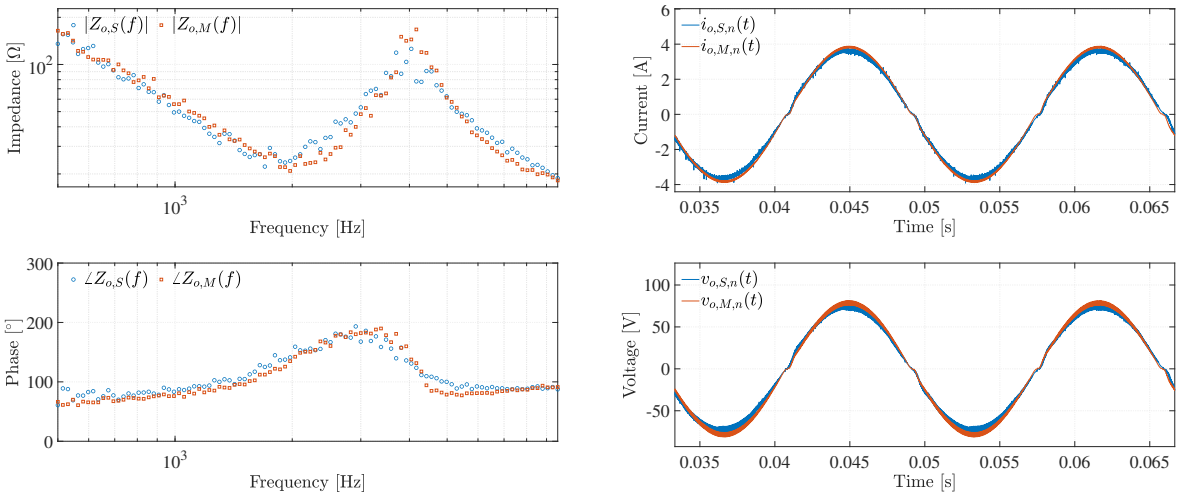

(a) (b)

Figure 5.59: (a) Magnitude and phase response of the output impedance of the estimated model, $Z_{o,M}(f)$, and the system, $Z_{o,S}(f)$, after step 3. (b) Time-domain waveforms of the output currents and voltages of the estimated model and the system under normal conditions, $i_{o,M,n}(t)$, $i_{o,S,n}(t)$, $v_{o,M,n}(t)$ and $v_{o,S,n}(t)$, after step 3.

The estimated parameters after each step are presented in Table 5.14. After step 1, only the coefficient b_1 changes substantially. The other parameters are refined in step 2 and 3, but do not change substantially. The output time-domain waveforms and output impedance frequency response of the system and model of the inverter after the first step are sufficiently similar to suggest that the estimated model after step 1 is a sufficient representation of the system.

TABLE 5.14: Results for each step of the parameter estimation process.

Step	b_0	b_1	b_2	a_0	a_1
1	0.7393	0.0776	-0.3096	-0.8521	N/A
2	N/A	0.1001	N/A	-0.8810	0.0131
3	0.7901	0.1472	-0.3088	-0.8578	0.0139

To validate the estimated parameters, a step response in the output voltage is investigated. The resistive load is reduced from 20.6 Ω to 10.39 Ω by short circuiting a resistor. As the inverter is controlling the output current, the voltage supplied at its output would drop with a decrease in the resistive load, while the current will be restored by the current-controller. Figures 5.60a and 5.60b displays the step change in the voltage of the measured system compared to the simulated model. The response of the model is less damped than the measured system, but the time constants of the steps response seem similar.

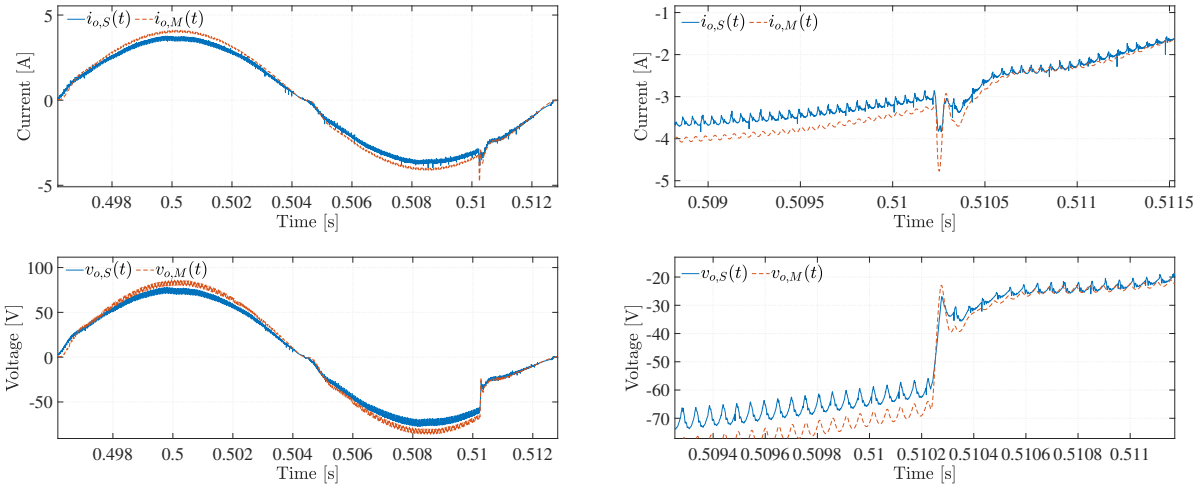

(a) (b)

Figure 5.60: (a) Output current, $i_o(t)$, and voltage, $v_o(t)$, of the system and model over a fundamental period while a resistive load reduction occurs to introduce a step in the output voltage. (b) The output current, $i_o(t)$, and voltage, $v_o(t)$, of the system and model at the time of the step.

By making use of a high-pass filter, all frequencies below 500 Hz are filtered to remove the fundamental 60 Hz component of the current to measure the time-specifications of the current during the step-response, as presented in Fig. 5.61. The current is investigated instead of the voltage, as the inverter is controlling the current.

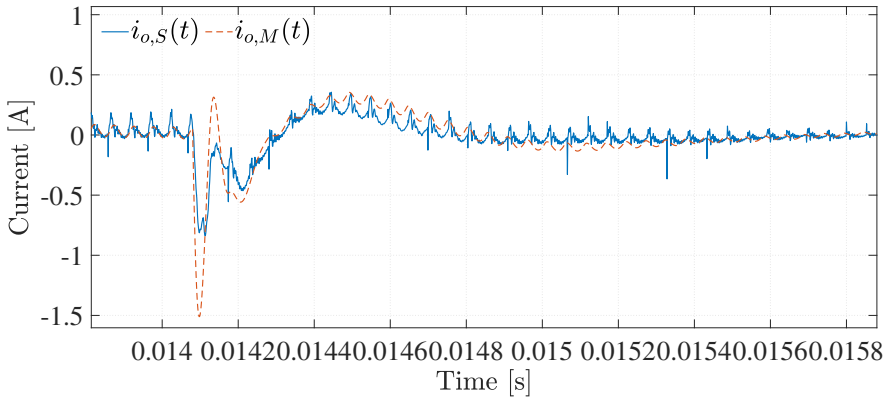

Figure 5.61: Filtered step response of the output current, $i_o(t)$, of the system and the model.

The time-specifications of the step-response is summarized in Table 5.15. The step-response of the experimental system and estimated model are sufficiently similar to suggest that an accurate model is obtained.

TABLE 5.15: Time specifications of the step response produced in the system and model.

	Peak Time [s]	**5 % Settling Time** [s]	**Overshoot Amplitude**
System	19.9 $\times 10^{-6}$	0.00146	1.0112
Model	19.9 $\times 10^{-6}$	0.00148	1.56434

Chapter 6

Conclusions and Future Work

6.1. Overview

This chapter summarizes the results obtained during this project and presents conclusions. A list of possible future work and limitations in this project are discussed.

6.2. Research Conclusions

6.2.1. Investigation of the use of a Customizable Pseudo-Random Impulse Sequence Excitation Source for *In Situ* Perturbation of an Inverter

Excitation signals are used during system identification studies to perturb a target system. During this project a Pseudo-Random Impulse Sequence (PRIS) source is used to perturb an inverter *in situ* at its AC output side. Careful consideration of the PRIS perturbation arrangement for an inverter are required, as the inverter is not a passive element, but rather produces a voltage and current at the fundamental frequency as well as at higher frequency harmonics, inter-harmonics and supra-harmonics.

In this project a practical PRIS source is built and tested. A PRBS generator is constructed using a FPGA, to control the gating signals of the H-bridge of the PRIS source. The PRBS generator allows the order, clock frequency and length of the PRBS gating signal to be configured by the user to control the time- and frequency-domain characteristics of the PRIS source. The RLC filter values of the PRIS source can also be changed to control the time- and frequency-domain characteristics of the PRIS source. The DC voltage that supplies the PRIS source can be varied to increase or decrease perturbation energy. The PRIS source has a maximum voltage of approximately 1.6 kV at its PCC and can withstand a maximum current of 25 A and is, thus, suitable for use in high power environments, such as inverter systems. It is shown that the PRBS generator and PRIS source operate as expected through experimental verification.

Before applying the PRIS source to a practical inverter, two idealized inverter topologies are perturbed using an ideal PRIS signal through simulation. The idealized PRIS source

is applied *in situ* at the AC output side of the simulated inverters. It is shown that the inverters are perturbed over a wide frequency band, from as low as 10 Hz to as high as 40 kHz. The inverters are able to operate at nominal current and voltage ratings while being perturbed by the PRIS source.

The PRIS source is subsequently applied *in situ* to a practical inverter that supplies 54.2 V_{RMS} and 2.62 A_{RMS} to a load. It is shown that by changing the clock frequency, PRBS order, DC voltage magnitude and RLC values of the PRIS source, different frequency bands of the inverter are excited. It is observed that the PRIS source is able to excite the inverter from 200 Hz up to 30 kHz. The inverter does not display non-linear behaviour due to perturbation, but continues operating at nominal voltage and current ratings.

The PRIS source is also applied to a practical open-loop half-bridge inverter in appendix A. It is observed that a 500 Hz clock frequency for the PRIS source, together with suitable RLC values allow for excitation of the half-bridge inverter at frequencies between 10 Hz and 150 Hz.

6.2.2. Characterization of Inverter Output Impedance Frequency Response

In this project, the wideband, small-signal perturbations introduced by the PRIS source are used to characterize the frequency response of the output impedance of the inverter. The output impedance of inverters will be used during parameter estimation to estimate filter and controller parameters, as it is a function of the filter and controller parameters of the inverter.

The analytical output impedance transfer function, $Z_o(f)$, of two different inverter topologies are derived. The analytical investigation in section 4.2.4.2 indicates that the measured output impedance, $Z_{om}(f)$, contains a harmonic artefact at the fundamental frequency. A linear approximation of the output impedance, $Z_o(f)$, is subsequently estimated using a two-measurement approach. The estimated output impedance is obtained through simulation using perturbed and normal measurements of the inverter. It is shown that the estimated output impedance corresponds well with the analytical transfer function and is thus successfully characterized.

The output impedance frequency response of a practical single-phase feedback-controlled inverter is investigated. It is observed that the experimental measurements of the feedback-controlled inverter require alignment of the output currents to adhere to the assumptions made in the two-measurement approach to obtain the output impedance frequency response of the inverter. A methodology that uses spectral densities to obtain the output impedance frequency response is introduced. This method would be beneficial in cases where it is not known which output is continuously compared to a reference signal. It is shown that the output impedance of the practical inverter can be characterized between 200 Hz and 16

kHz using PRIS perturbations and the two-measurement approach.

The output impedance of a half-bridge inverter is discussed in appendix A. Obtaining the experimental output impedance of a half-bridge inverter requires alignment of the Thévenin voltage source. It is shown that aligning the PWM signals of an open-loop inverter allowed successful estimation of the output impedance using the two-measurement approach.

6.2.3. Modelling of a Single-Phase Feedback-Controlled Inverter

An increase in inverter-based generation, due to higher penetration of renewable energy sources in the grid, gives rise in the need for inverter modelling. Inverter modelling is essential for grid analysis, design and integration [64–67]. Using electromagnetic transients models allow for accurate modelling of inverters.

In this project, a electromagnetic transient model of a practical inverter manufactured by Texas Instruments is obtained. The standalone inverter topology incorporated a current-controlled loop as well as voltage linearization. All components or subsystems that the inverter consists of, including the PWM scheme, ADC, control-loop and filter, are modelled in Simulink. All subsystems are identified through inspection and examining applicable datasheets and user manuals.

It is shown that although the simulated model of the practical inverter system does not have the exact same output voltage and current as that of the practical inverter system, the model and system have a similar number of modes. It is concluded that the differences between the model and system could be due to inaccurate model parameters or model topology differences.

6.2.4. System Identification and Parameter Estimation of a Single-Phase Voltage Source Inverter

To model inverters, the model parameters are required. These model parameters can be determined using parameter estimation methodologies. During this project the filter and controller parameters of voltage source inverters are estimated. The output impedance, characterized by making use of PRIS perturbations, as well as the output current and voltage of the system and model are compared as a measure of the accuracy of the model.

Parameter estimation of two idealized inverter topologies are investigated through simulation. Parameters of a standalone dual-loop inverter with three controller gains and two filter parameters are accurately estimated within 5.23% accuracy using the grey-wolf optimization algorithm in a three-step optimization approach. As a second case study, parameter estimation is applied to a grid-connected inverter with an LCL filter. It is shown that three filter parameters and four controller parameters are determined using the particle swarm optimization algorithm in a two-step approach within 0.05% accuracy.

The output impedance of a practical inverter, that is characterized using PRIS perturbations, are used to estimate parameters for the Simulink model of the practical inverter. The parameter estimation study aims to determine five coefficients used in a discrete current controller. It is observed that obtaining four of these five parameters allows for an accurate model, but using a multi-step approach the final parameter is also estimated to obtain an accurate model. The estimated parameters are validated using a step response of the output voltage.

6.3. Limitations of this Project and Possible Future Work

Some of the limitations of this project and possible future work to address these limitations are:

- **Low frequency perturbations**: One of the PRIS's characteristics is the lack of low frequency excitation, this is affected by the PRIS source configuration, but occurs, in this project, generally at frequencies lower than 500 Hz. The PRBS produces power at low frequencies, but the RLC filter used in the PRIS source filters the power at these frequencies. Inverters produce a voltage and current component at the fundamental frequency, i.e. 50 Hz or 60 Hz. Therefore, the control-loop and filter are active at the fundamental frequency. However, at these low frequencies the PRIS source does not always perturb the inverter sufficiently. This could be beneficial, as the PRIS source has negligible influence on the normal operation of the inverter at the fundamental frequency. However, this means the PRIS perturbation does not allow the extraction of all the information of the inverter, for example the output impedance at the fundamental frequency, which would be helpful during parameter estimation. If the parameters of the inverter have an influence at high frequencies this problem is mitigated. In this project, controller gains that predominantly operate at low frequencies were challenging to estimate.

- **Perturbation amplitudes**: Various saturation blocks are implemented in a practical inverter to ensure that maximum current and voltage ratings are not exceeded, or to comply with the network requirements. Care must be taken that perturbations do not exceed these limits to ensure that this will not introduce non-linearities. Furthermore, perturbation magnitudes are important when perturbing the inverter for adequate signal-to-noise ratios. The *in situ* perturbation magnitudes required to produce adequate signal-to-noise ratios could be investigated, similarly to Alenius *et al.* [138].

- **Inverter modelling**: Obtaining and using the correct inverter model is vital for parameter estimation as well as the applicability of results. Practical inverters make

use of digital control. These controllers are normally programmed in C or C++ programming languages. It is possible to model software in Simulink as an S-function model. If a microcontroller of a practical inverter can be modelled as an S-function in Simulink the accuracy of the model would be greatly improved.

- **Single-phase DQ representation**: A single-phase DQ representation is possible if an orthogonal waveform is generated. A DQ representation of the output current and voltage waveforms of the inverter investigated in chapter 5 were implemented, but not documented, as the DQ representation had too much noise to be of any use. Investigating the single-phase DQ-representation can be beneficial when the inverter is perturbed, as the small-signal model would be easier to obtain.

- **Black-box model**: Inverters are commonly modelled as a black-box due to the difficulty of obtaining its circuit and control topologies. The use of PRIS perturbation to obtain a black-box model during system identification studies can be the subject of future work.

- **Simulation speed**: Electromagnetic transient models are computationally complex to execute. Care can be taken to increase the simulation speed to make parameter estimation more viable.

- **Non-linearities**: An inverter response exhibits non-linearities. In this project the average system models of the inverter were obtained. It is unknown to what extent these dynamic models represent the inverter accurately.

- **Accurate source and load modelling** - When an inverter is modelled, the DC voltage source, its impedance, and the load or grid are included in the simulation. Accurate modelling of the DC source was challenging in this project. However, it was discovered that the impedance of the source did not greatly influence the accuracy of the inverter model. This might not always be the case and accurate source modelling should be investigated. Furthermore, the load or grid to which the inverter dispatches power has a large impact on the operation of the inverter. Although the load or grid does not change the inverter, the control-loop reacts to the output voltage and current that is also dependant on the load or grid's voltage, current and phase angle. This necessitates accurate modelling of the load or grid. If the load or grid could be modelled accurately over a frequency range, then the parameters of the inverter could likely be estimated more accurately.

- **DC-link capacitor ripple**: Various mathematical models of inverters assume a stiff DC voltage and, therefore, neglect the DC-link capacitor. The voltage across the DC-link capacitor could contain ripple. This ripple is also dependent on the

modulation index of the inverter. The true influence of the DC-link capacitor and the amount of voltage ripple on the output impedance is unknown.

- **Three-phase inverter**: Only single-phase inverters were investigated in this project. Single-phase inverters are typically used in residential applications while three-phase inverters would rather be used on power plants. Extending this investigation to three-phase inverters could be subject to future work. This adds complexity of perturbing a three-phase system. Investigating three-phase systems will have a benefit, in that the DQ representation of the inverters can be investigated that would greatly reduce the complexity of the small-signal model.

- **Generic parameter estimation approaches**: During this project, parameter estimation was conducted on several inverter topologies and control structures. Each of these inverter topologies required a different parameter estimation approach based on the sensitivity analysis conducted before parameter estimation is applied. Future work might investigate a generic parameter estimation process that is capable of estimating parameters of different topologies.

- **Synchronization of time-domain perturbation measurements**: When the inverter AC output side is perturbed in this project, a pseudo-random signal is superimposed onto a sine wave. The practical inverter investigated displayed small variations in its fundamental frequency when in operation. Due to this frequency changing constantly, it is difficult to compare the experimental measurements with simulation. Synchronization of time-domain waveforms of the experimental system and model is increasingly difficult if the perturbed output waveforms are compared. Starting perturbation at the same time in both the model and the system is possible, but will require the use of hardware, such as zero-crossing detection circuits, to control the time instance perturbation is applied.

Bibliography

[1] J. A. Taylor, S. V. Dhople, and D. S. Callaway, "Power systems without fuel," *Renewable and Sustainable Energy Reviews*, vol. 57, pp. 1322–1336, 2016.

[2] C. Yoon, R. N. Beres, and C. L. Bak, "Harmonic stability assessment for multi-paralleled, grid-connected inverters," *IEEE Trans. Sust. Energ.*, vol. 7, no. 4, pp. 1388–1397, 2016.

[3] J. Enslin and P. Heskes, "Harmonic interaction between a large number of distributed power inverters and the distribution network," *IEEE Transactions on Power Electronics*, vol. 19, no. 6, pp. 1586–1593, 2004.

[4] A. Bhowmik, A. Maitra, S. Halpin, and J. Schatz, "Determination of allowable penetration levels of distributed generation resources based on harmonic limit considerations," *IEEE Transactions on Power Delivery*, vol. 18, no. 2, pp. 619–624, 2003.

[5] G. Wang, Z. Xu, and W. Hua, "Analysis on impact of baihetan inverter connection modes on stability of zhejiang power grid," in *2019 IEEE Innovative Smart Grid Technologies - Asia (ISGT Asia)*, 2019, pp. 1075–1079.

[6] S. Operator, "Amendments on the renewable grid code appendix 13," Eskom Transmission Division, Germiston, RSA, Tech. Rep., 2020.

[7] NERSA, "Nrs 048: Electricity supply - quality of supply," Tech. Rep., 2009. [Online]. Available: http://www.nrs.eskom.co.za/

[8] S. Operator, "Grid connection code for renewable power plants connected to the electricity transmission system or the distribution system in south africa," Eskom Transmission Division, Germiston, RSA, Tech. Rep., 2020.

[9] H. Shehadeh, V. Boscaino, S. Favuzza, and E. R. Sanseverino, "Mathematical modelling of an inverter-based distributed generator," in *2016 IEEE 16th International Conference on Environment and Electrical Engineering (EEEIC)*, 2016, pp. 1–6.

[10] B. Matthias, S. Eberlein, and R. Krzysztof, "Design of an inverter model according to the network code requirements for low-voltage grids," in *2019 Modern Electric Power Systems (MEPS)*, 2019, pp. 1–6.

[11] I. S. Stoyanov, T. B. Iliev, G. Y. Mihaylov, and B. I. Evstatiev, "Modelling of power inverters used in pv systems," in *2017 IEEE 23rd International Symposium for Design and Technology in Electronic Packaging (SIITME)*, 2017, pp. 263–266.

[12] N. Guruwacharya, N. Bhujel, T. M. Hansen, S. Suryanarayanan, R. Tonkoski, U. Tamrakar, and F. Wilches-Bernal, "Modeling inverters with grid support functions for power system dynamics studies," in *2021 IEEE Power Energy Society Innovative Smart Grid Technologies Conference (ISGT)*, 2021, pp. 1–5.

[13] K. Sano, S. Horiuchi, and T. Noda, "Comparison and selection of grid-tied inverter models for accurate and efficient emt simulations," *IEEE Transactions on Power Electronics*, vol. 37, no. 3, pp. 3462–3472, 2022.

[14] N. Guruwacharya, N. Bhujel, U. Tamrakar, M. Rauniyar, S. Subedi, S. Berg, T. Hansen, and R. Tonkoski, "Data-driven power electronic converter modeling for low inertia power sytem dynamic studies," in *2020 IEEE Power Energy Society General Meeting (PESGM)*, 2020, pp. 589–592.

[15] N. Patcharaprakiti, K. Kirtikara, D. Chenvidhya, V. Monyakul, and B. Muenpinij, "Modeling of single phase inverter of photovoltaic system using system identification," in *2010 Second International Conference on Computer and Network Technology*, 2010, pp. 462–466.

[16] B. Hoff and W. Sulkowski, "Comprehensive modeling and practical verification of grid connected vsi with lcl filter," in *2012 15th International Power Electronics and Motion Control Conference (EPE/PEMC)*, 2012, pp. DS3f.7–1–DS3f.7–7.

[17] L. Harnefors, "Modeling of three-phase dynamic systems using complex transfer functions and transfer matrices," *IEEE Transactions on Industrial Electronics*, vol. 54, no. 4, pp. 2239–2248, 2007.

[18] R. D. Middlebrook and S. Cuk, "A general unified approach to modelling switching-converter power stages," in *1976 IEEE Power Electronics Specialists Conference*, 1976, pp. 18–34.

[19] L. Rese, A. S. Costa, and A. S. e Silva, "Enhanced modeling and control of vsis in microgrids operating in grid-connected mode," in *2012 IEEE PES Innovative Smart Grid Technologies (ISGT)*, 2012, pp. 1–8.

[20] K. Yamashita, H. Renner, S. Martinez Villanueva, K. Vennemann, J. Martins, P. Aristidou, T. Van Cutsem, Z. Song, G. Lammert, L. Pabon Ospina, L. Zhu, I. Green, G. Irwin, D. Geibel, S. Jankovic, C. Zhan, F. Ciausiu, K. Karoui, K. Chan, and M. Steurer, "Modelling of inverter-based generation for power system dynamic studies," pp. 81 – 87, 06 2018.

[21] V. Valdivia, A. Lazaro, A. Barrado, P. Zumel, C. Fernandez, and M. Sanz, "Black-box modeling of three-phase voltage source inverters for system-level analysis," *IEEE Transactions on Industrial Electronics*, vol. 59, no. 9, pp. 3648–3662, 2012.

[22] M. Stender, O. Wallscheid, and J. Böcker, "Development of a black-box two-level igbt three-phase inverter compensation scheme for electrical drives," in *2019 IEEE 28th International Symposium on Industrial Electronics (ISIE)*, 2019, pp. 296–301.

[23] A. S. Abdelsamad, M. Johanna Myrzik, E. Kaufhold, J. Meyer, and P. Schegner, "Nonlinear identification approach for black-box modeling of voltage source converter harmonic characteristics," in *2020 IEEE Electric Power and Energy Conference (EPEC)*, 2020, pp. 1–5.

[24] I. Maio, I. Stievano, and F. Canavero, "Narx approach to black-box modeling of circuit elements," in *1998 IEEE International Symposium on Circuits and Systems (ISCAS)*, 1998, pp. 411–414.

[25] V. Valdivia, A. Lázaro, A. Barrado, P. Zumel, C. Fernández, and M. Sanz, "Black-box modeling of three phase voltage source inverters based on transient response analysis," in *2010 Twenty-Fifth Annual IEEE Applied Power Electronics Conference and Exposition (APEC)*, 2010, pp. 1279–1286.

[26] G. Guarderas, A. Francés, R. Asensi, and J. Uceda, "Large-signal black-box behavioral modeling of grid-supporting power converters in ac microgrids," in *2017 IEEE 6th International Conference on Renewable Energy Research and Applications (ICRERA)*, 2017, pp. 153–158.

[27] G. Ala, A. Spagnuolo, and F. Viola, "A local linear black-box identification technique for power converters modeling," in *2009 IEEE Vehicle Power and Propulsion Conference*, 2009, pp. 257–264.

[28] F. M. Mwaniki, "Modelling and performance evaluation of a pseudo-random impulse sequence for in situ parameter estimation in energy applications," Ph.D. dissertation, Stellenbosch University, Stellenbosch, RSA, 2020.

[29] J. van Rooijen and H. Vermeulen, "A perturbation source for in situ parameter estimation applications," in *Proceedings of IECON'94 - 20th Annual Conference of IEEE Industrial Electronics*, vol. 3, 1994, pp. 1819–1823 vol.3.

[30] J. W. Pierre, D. Trudnowski, M. Donnelly, N. Zhou, F. K. Tuffner, and L. Dosiek, "Overview of system identification for power systems from measured responses1," *IFAC Proceedings Volumes*, vol. 45, no. 16, pp. 989–1000, 2012, 16th IFAC Symposium on System Identification.

[31] T. A. Papadopoulos, E. O. Kontis, P. N. Papadopoulos, and G. K. Papagiannis, "System identification techniques for power systems analysis using distorted data," in *MedPower 2014*, 2014, pp. 1–7.

[32] H. Vermeulen, J. Strauss, and V. Shikoana, "On-line estimation of synchronous generator parameters using prbs perturbations," in *2003 IEEE Power Engineering Society General Meeting (IEEE Cat. No.03CH37491)*, vol. 4, 2003, pp. 2398–2398.

[33] O. Turkay and A. Ulsoy, "Frequency versus time domain parameter estimation: Application to a slot milling operation," *Mechanical Systems and Signal Processing*, vol. 2, no. 3, pp. 265–277, 1988.

[34] L. Chang, X. Jiang, M. Mao, and H. Zhang, "Parameter identification of controller for photovoltaic inverter based on l-m method," in *2018 IEEE International Power Electronics and Application Conference and Exposition (PEAC)*, 2018, pp. 1–6.

[35] L. Zhongqian, H. Wu, W. Jin, B. Xu, Y. Ji, and M. Wu, "Two-step method for identifying photovoltaic grid-connected inverter controller parameters based on the adaptive differential evolution algorithm," *Iet Generation Transmission & Distribution*, vol. 11, pp. 4282–4290, 2017.

[36] X. Shen, J. Zheng, S. Zhu, and L. Shu, "d-q axis decoupling parameter identification strategy for the grid-connected inverter of photovoltaic generation system," in *2012 China International Conference on Electricity Distribution*, 2012, pp. 1–4.

[37] K. Dong, J. Yan, W. Shen, S. Li, X. Ma, and R. Jia, "Parameter identification of grid-connected photovoltaic inverter based on adaptive - improved gpso algorithm," in *2019 IEEE 8th International Conference on Advanced Power System Automation and Protection (APAP)*, 2019, pp. 1536–1540.

[38] R. Jiayu, L. Chunlai, T. Yun, Y. Xia, and Y. Shengpeng, "Modeling of photovoltaic grid connected generation system based on parameter identification method," in *2016 International Conference on Smart City and Systems Engineering (ICSCSE)*, 2016, pp. 378–381.

[39] L. Arnedo, D. Boroyevich, R. Burgos, and F. Wang, "Un-terminated frequency response measurements and model order reduction for black-box terminal characterization models," in *2008 Twenty-Third Annual IEEE Applied Power Electronics Conference and Exposition*, 2008, pp. 1054–1060.

[40] L. Arnedo, R. Burgos, D. Boroyevich, and F. Wang, "System-level black-box dc-to-dc converter models," in *2009 Twenty-Fourth Annual IEEE Applied Power Electronics Conference and Exposition*, 2009, pp. 1476–1481.

[41] J. A. Oliver, R. Prieto, J. A. Cobos, O. Garcia, and P. Alou, "Hybrid wiener-hammerstein structure for grey-box modeling of dc-dc converters," in *2009 Twenty-Fourth Annual IEEE Applied Power Electronics Conference and Exposition*, 2009, pp. 280–285.

[42] V. Valdivia, A. Barrado, A. LÁzaro, P. Zumel, C. Raga, and C. FernÁndez, "Simple modeling and identification procedures for "black-box" behavioral modeling of power converters based on transient response analysis," *IEEE Transactions on Power Electronics*, vol. 24, no. 12, pp. 2776–2790, 2009.

[43] N. Patcharaprakiti, K. Kirtikara, D. Chenvidhya, V. Monyakul, and B. Muenpinij, "Modeling of single phase inverter of photovoltaic system using system identification," in *2010 Second International Conference on Computer and Network Technology*, 2010, pp. 462–466.

[44] S. Saha, "2 - basic principles of control systems in textile manufacturing," in *Process Control in Textile Manufacturing*, ser. Woodhead Publishing Series in Textiles, A. Majumdar, A. Das, R. Alagirusamy, and V. Kothari, Eds. Woodhead Publishing, 2013, pp. 14–40.

[45] T. Bogodorova, "Modeling, model validation and uncertainty identification for power system analysis," Ph.D. dissertation, KTH Royal Institute of Technology, 2017.

[46] H. Le-Huy and G. Sybille, "Matlab/simulink and pspice as modelling tools for power systems and power electronics," in *2000 Power Engineering Society Summer Meeting (Cat. No.00CH37134)*, vol. 2, 2000, pp. 766–767 vol. 2.

[47] S. Chiniforoosh, J. Jatskevich, A. Yazdani, V. Sood, V. Dinavahi, J. A. Martinez, and A. Ramirez, "Definitions and applications of dynamic average models for analysis of power systems," *IEEE Transactions on Power Delivery*, vol. 25, no. 4, pp. 2655–2669, 2010.

[48] A. Guha and G. Narayanan, "Average modelling of a voltage source inverter with dead-time in a synchronous reference frame," in *2013 IEEE Innovative Smart Grid Technologies-Asia (ISGT Asia)*, 2013, pp. 1–6.

[49] S. Rogalla, F. Ackermann, N. Bihler, H. Moghadam, and O. Stalter, "Source-driven and resonance-driven harmonic interaction between pv inverters and the grid," in *2016 IEEE 43rd Photovoltaic Specialists Conference (PVSC)*, 2016, pp. 1399–1404.

[50] A. Raghami, G. Ledwich, and Y. Mishra, "Improved reactive power sharing among customers' inverters using online thévenin estimates," *IEEE Transactions on Power Systems*, vol. 34, no. 6, pp. 4168–4176, 2019.

[51] G. Y. Yang, M. Mattesen, S. B. Kjær, R. D. Lazar, A. Constantin, J. Østergaard, and C. Stephansen, "Analysis of thevenin equivalent network of a distribution system for solar integration studies," in *2012 3rd IEEE PES Innovative Smart Grid Technologies Europe (ISGT Europe)*, 2012, pp. 1–5.

[52] H. J. Bahirat, H. K. Høidalen, and B. A. Mork, "Thévenin equivalent of voltage-source converters for dc fault studies," *IEEE Transactions on Power Delivery*, vol. 31, no. 2, pp. 503–512, 2016.

[53] M. Naderi, Y. Khayat, Q. Shafiee, and H. Bevrani, "Modeling of voltage source converters in microgrids using equivalent thevenin circuit," in *2018 9th Annual Power Electronics, Drives Systems and Technologies Conference (PEDSTC)*, 2018, pp. 510–515.

[54] S. M. Kotian and K. N. Shubhanga, "Dynamic phasor modelling and simulation," in *2015 Annual IEEE India Conference (INDICON)*, 2015, pp. 1–6.

[55] A. Nagarajan and R. Ayyanar, "Dynamic phasor model of single-phase inverters for analysis and simulation of large power distribution systems," in *2013 4th IEEE International Symposium on Power Electronics for Distributed Generation Systems (PEDG)*, 2013, pp. 1–6.

[56] S. R. Deore, P. B. Darji, and A. M. Kulkarni, "Dynamic phasor modeling of modular multi-level converters," in *2012 IEEE 7th International Conference on Industrial and Information Systems (ICIIS)*, 2012, pp. 1–6.

[57] A. Nazari, Y. Xue, J. K. Motwani, I. Cvetkovic, D. Dong, and D. Boroyevich, "Dynamic phasor modeling of multi-converter systems," in *2021 IEEE Energy Conversion Congress and Exposition (ECCE)*, 2021, pp. 2716–2721.

[58] U. C. Nwaneto and A. M. Knight, "Dynamic phasor-based modeling and simulation of a reduced-order single-phase inverter in voltage-controlled and current-controlled modes," in *2020 IEEE Texas Power and Energy Conference (TPEC)*, 2020, pp. 1–6.

[59] T. Itkonen and J. Luukko, "Switching-function-based simulation model for three-phase voltage source inverter taking dead-time effects into account," in *2008 34th Annual Conference of IEEE Industrial Electronics*, 2008, pp. 992–997.

[60] S. M. Fazeli, W. Hew, N. Rahim, and B. Ooi, "Switching functions model of a three-phase voltage source converter (vsc)," *Journal of Power Electronics*, vol. 17, pp. 422–431, 03 2017.

[61] L. Qi, J. Pan, Z. Wang, and J. Daniel, "Functional simulation models for three-level converters using average and switching function concepts," 07 2009, pp. 121–127.

[62] Y. Panov and M. Jovanovic, "Practical issues of input/output impedance measurements in switching power supplies and application of measured data to stability analysis," in *Twentieth Annual IEEE Applied Power Electronics Conference and Exposition, 2005. APEC 2005.*, vol. 2, 2005, pp. 1339–1345 Vol. 2.

[63] J. Sun, "Impedance-based stability criterion for grid-connected inverters," *IEEE Transactions on Power Electronics*, vol. 26, no. 11, pp. 3075–3078, 2011.

[64] C. Yoon, H. Bai, R. N. Beres, X. Wang, C. L. Bak, and F. Blaabjerg, "Harmonic stability assessment for multiparalleled, grid-connected inverters," *IEEE Transactions on Sustainable Energy*, vol. 7, no. 4, pp. 1388–1397, 2016.

[65] X. Wang, L. Harnefors, and F. Blaabjerg, "Unified impedance model of grid-connected voltage-source converters," *IEEE Transactions on Power Electronics*, vol. 33, no. 2, pp. 1775–1787, 2018.

[66] Z. Liu, J. Liu, X. Hou, Q. Dou, D. Xue, and T. Liu, "Output impedance modeling and stability prediction of three-phase paralleled inverters with master–slave sharing scheme based on terminal characteristics of individual inverters," *IEEE Transactions on Power Electronics*, vol. 31, no. 7, pp. 5306–5320, 2016.

[67] M. Cespedes and J. Sun, "Impedance modeling and analysis of grid-connected voltage-source converters," *IEEE Transactions on Power Electronics*, vol. 29, no. 3, pp. 1254–1261, 2014.

[68] J. Jiao and R. Nelms, "Adjusting output impedance using a pi controller to improve the stability of a single-phase inverter under weak grid," *Transactions on Environment and Electrical Engineering*, vol. 1, no. 4, 2016.

[69] B. Peterson, J. Rens, M. G. Botha, and J. Desmet, "On harmonic emission assessment: A discriminative approach," *SAIEE Africa Research Journal*, vol. 108, 12 2017.

[70] S. Rogalla, S. Kaiser, B. Burger, and B. Engel, "Determination of the frequency dependent thévenin equivalent of inverters using differential impedance spectroscopy," in *2020 IEEE 11th International Symposium on Power Electronics for Distributed Generation Systems (PEDG)*, 2020, pp. 181–186.

[71] I. Hiskens and A. Koeman, "Power system parameter estimation," *Journal of Electrical and Electronic Engineering*, vol. 19, no. 1, pp. 1–8, 1999.

[72] I. P. Gerber, F. M. Mwaniki, and H. J. Vermeulen, "Parameter estimation of a ferroresonance damping circuit using pseudo-random impulse sequence perturbations," in *2021 56th International Universities Power Engineering Conference (UPEC)*, 2021, pp. 1–6.

[73] V. Kotu and B. Deshpande, "Chapter 4 - classification," in *Data Science (Second Edition)*, second edition ed., V. Kotu and B. Deshpande, Eds. Morgan Kaufmann, 2019, pp. 65–163.

[74] A. Garcia Asuero, A. Sayago, and G. González, "The correlation coefficient: An overview," *Critical Reviews in Analytical Chemistry - CRIT REV ANAL CHEM*, vol. 36, pp. 41–59, 01 2006.

[75] D. Freedman, R. Pisani, and R. Purves, "Statistics (international student edition)," *Pisani, R. Purves, 4th edn. WW Norton & Company, New York*, 2007.

[76] C. J. Willmott and K. Matsuura, "Advantages of the mean absolute error (mae) over the root mean square error (rmse) in assessing average model performance," *Climate Research*, vol. 30, no. 1, pp. 79–82, 2005.

[77] S. Bermejo and J. Cabestany, "Oriented principal component analysis for large margin classifiers," *Neural Networks*, vol. 14, no. 10, pp. 1447–1461, 2001.

[78] S. P. Neill and M. R. Hashemi, "Chapter 8 - ocean modelling for resource characterization," in *Fundamentals of Ocean Renewable Energy*, ser. E-Business Solutions, S. P. Neill and M. R. Hashemi, Eds. Academic Press, 2018, pp. 193–235.

[79] P. Niu, S. Niu, N. liu, and L. Chang, "The defect of the grey wolf optimization algorithm and its verification method," *Knowledge-Based Systems*, vol. 171, pp. 37–43, 2019.

[80] S. Mirjalili, S. M. Mirjalili, and A. Lewis, "Grey wolf optimizer," *Advances in Engineering Software*, vol. 69, pp. 46–61, 2014.

[81] F. Güneş and F. Tokan, "Pattern search optimization with applications on synthesis of linear antenna arrays," *Expert Systems with Applications*, vol. 37, no. 6, pp. 4698–4705, 2010.

[82] V. Gardeux, M. Omran, R. Chelouah, P. Siarry, and F. Glover, "Adaptive pattern search for large-scale optimization," *Applied Intelligence*, vol. 45, 09 2017.

[83] N. V. Queipo, R. T. Haftka, W. Shyy, T. Goel, R. Vaidyanathan, and P. Kevin Tucker, "Surrogate-based analysis and optimization," *Progress in Aerospace Sciences*, vol. 41, no. 1, pp. 1–28, 2005.

[84] J. D. Jakeman, D. P. Kouri, and J. G. Huerta, "Surrogate modeling for efficiently, accurately and conservatively estimating measures of risk," *Reliability Engineering System Safety*, vol. 221, p. 108280, 2022.

[85] X.-S. Yang, "Chapter 6 - genetic algorithms," in *Nature-Inspired Optimization Algorithms (Second Edition)*, second edition ed., X.-S. Yang, Ed. Academic Press, 2021, pp. 91–100.

[86] I. G. Tsoulos, "Solving constrained optimization problems using a novel genetic algorithm," *Applied Mathematics and Computation*, vol. 208, no. 1, pp. 273–283, 2009.

[87] "Matlab optimization toolbox," R2020b, the MathWorks, Natick, MA, USA.

[88] X.-S. Yang, "Chapter 8 - particle swarm optimization," in *Nature-Inspired Optimization Algorithms (Second Edition)*, second edition ed., X.-S. Yang, Ed. Academic Press, 2021, pp. 111–121.

[89] R. Ceylan and H. Koyuncu, "Chapter 7 - scpso-based multithresholding modalities for suspicious region detection on mammograms," in *Soft Computing Based Medical Image Analysis*, N. Dey, A. S. Ashour, F. Shi, and V. E. Balas, Eds. Academic Press, 2018, pp. 109–135.

[90] M. S. Mahmoud, "Chapter 1 - introduction," in *Advanced Control Design with Application to Electromechanical Systems*, M. S. Mahmoud, Ed. Butterworth-Heinemann, 2018, pp. 1–41.

[91] R. Pintelon, G. Vandersteen, J. Schoukens, and Y. Rolain, "Improved (non-)parametric identification of dynamic systems excited by periodic signals—the multivariate case," *Mechanical Systems and Signal Processing*, vol. 25, pp. 2892–2922, 11 2011.

[92] W. Doorsamy and W. Cronje, "Conceptual design of an online estimation system for stigmergic collaboration and nodal intelligence on distributed dc systems," *Advances in Electrical and Computer Engineering*, vol. 17, pp. 47–54, 05 2017.

[93] V. Valdivia, A. Lazaro, A. Barrado, P. Zumel, C. Fernandez, and M. Sanz, "Black-box modeling of three-phase voltage source inverters for system-level analysis," *IEEE Transactions on Industrial Electronics*, vol. 59, no. 9, pp. 3648–3662, 2012.

[94] F. M. Mwaniki and H. J. Vermeulen, "Characterization and application of a pseudo-random impulse sequence for parameter estimation applications," *IEEE Transactions on Instrumentation and Measurement*, vol. 69, no. 6, pp. 3917–3927, 2020.

[95] A. H. Tan and K. R. Godfrey, "A guide to the design and selection of perturbation signals," in *Proceedings of the 48h IEEE Conference on Decision and Control (CDC) held jointly with 2009 28th Chinese Control Conference*, 2009, pp. 464–469.

[96] X. Wang and F. Blaabjerg, "Harmonic stability in power electronic-based power systems: Concept, modeling, and analysis," *IEEE Transactions on Smart Grid*, vol. 10, no. 3, pp. 2858–2870, 2019.

[97] C. Brozio and H. J. Vermeulen, "Wideband equivalent circuit modelling and parameter estimation methodology for two-winding transformers," 2003.

[98] A. Solomon, F. Mwaniki, and H. Vermeulen, "Application of pseudo-random impulse perturbation for characterizing capacitor voltage transformer frequency responses," in *2020 6th IEEE International Energy Conference (ENERGYCon)*, 2020, pp. 744–748.

[99] F. Mwaniki and A. Sayyid, "Characterizing power transformer frequency responses using bipolar pseudo-random current impulses," *International Journal of Power Electronics and Drive Systems (IJPEDS)*, vol. 12, p. 2423, 12 2021.

[100] D. M. Banks, J. Cornelius Bekker, and H. J. Vermeulen, "Parameter estimation of a two-section transformer winding model using pseudo-random impulse sequence perturbation," in *2021 56th International Universities Power Engineering Conference (UPEC)*, 2021, pp. 1–6.

[101] O. Turkay and A. Ulsoy, "Frequency versus time domain parameter estimation: Application to a slot milling operation," *Mechanical Systems and Signal Processing*, vol. 2, no. 3, pp. 265–277, 1988.

[102] A. Novak, L. Simon, F. Kadlec, and P. Lotton, "Nonlinear system identification using exponential swept-sine signal," *IEEE Transactions on Instrumentation and Measurement*, vol. 59, no. 8, pp. 2220–2229, 2010.

[103] T. Roinila, H. Abdollahi, and E. Santi, "Frequency-domain identification based on pseudorandom sequences in analysis and control of dc power distribution systems: A review," *IEEE Transactions on Power Electronics*, vol. 36, no. 4, pp. 3744–3756, 2021.

[104] F. Shen and R.-m. He, "A feasibility study of excitation system parameters identification based on measured perturbation," in *2007 International Power Engineering Conference (IPEC 2007)*, 2007, pp. 904–909.

[105] H. M. Shariff, M. H. Fazalul Rahiman, and M. Tajjudin, "Nonlinear system identification: Comparison between prbs and random gaussian perturbation on steam distillation pilot plant," in *2013 IEEE 3rd International Conference on System Engineering and Technology*, 2013, pp. 269–274.

[106] M. Singh, M. Sakare, and S. Gupta, "Testing of high-speed dacs using prbs generation with "alternate-bit-tapping"," *2011 Design, Automation Test in Europe*, pp. 1–6, 2011.

[107] L. Yan, C. Bingham, S. Cruz-Manzo, D. Cui, and Y. Lv, "Battery impedance measurement using pseudo random binary sequences," in *2020 IEEE 3rd Student Conference on Electrical Machines and Systems (SCEMS)*, 2020, pp. 686–691.

[108] T. Roinila, H. Abdollahi, and E. Santi, "Frequency-domain identification based on pseudorandom sequences in analysis and control of dc power distribution systems: A review," *IEEE Transactions on Power Electronics*, vol. 36, no. 4, pp. 3744–3756, 2021.

[109] H. Vermeulen and J. Strauss, "Off-line identification of an open-loop automatic voltage regulator using pseudo-random binary sequence perturbations," in *1999 IEEE Africon. 5th Africon Conference in Africa (Cat. No.99CH36342)*, vol. 2, 1999, pp. 799–802 vol.2.

[110] F. M. Mwaniki and H. J. Vermeulen, "Grid impedance frequency response measurements using pseudo-random impulse sequence perturbation," in *2019 9th International Conference on Power and Energy Systems (ICPES)*, 2019, pp. 1–6.

[111] J. DEMPSTER, "Chapter six - signal analysis and measurement," in *The Laboratory Computer*, ser. Biological Techniques Series, J. DEMPSTER, Ed. London: Academic Press, 2001, pp. 136–171.

[112] S. L. Miller and D. Childers, "10 - power spectral density," in *Probability and Random Processes*, S. L. Miller and D. Childers, Eds. Burlington: Academic Press, 2004, pp. 369–411.

[113] J. J. Benedetto, "Harmonic analysis and spectral estimation," *Journal of Mathematical Analysis and Applications*, vol. 91, no. 2, pp. 444–509, 1983.

[114] G. S. Gupta, M. Bhatnagar, D. K. Mohanta, and R. K. Sinha, "Chapter 1 - prototype algorithm for three-class motor imagery data classification: a step toward development of human–computer interaction-based neuro-aid," in *Smart Biosensors in Medical Care*, ser. Advances in ubiquitous sensing applications for healthcare, J. Chaki, N. Dey, and D. De, Eds. Academic Press, 2020, pp. 1–28.

[115] F. Attivissimo, M. Savino, and A. Trotta, "Flat-top smoothing of periodograms and frequency averagings to increase the accuracy in estimating power spectral density," *Measurement*, vol. 15, no. 1, pp. 15–24, 1995.

[116] S. Braun, "Windows," in *Encyclopedia of Vibration*, S. Braun, Ed. Oxford: Elsevier, 2001, pp. 1587–1595.

[117] F. J. HARRIS, "Chapter 3 - multirate fir filters for interpolating and desampling," in *Handbook of Digital Signal Processing*, D. F. Elliott, Ed. San Diego: Academic Press, 1987, pp. 173–287.

[118] K. Kanazawa and K. Hirata, "Parametric estimation of the cross-power spectral density," *Journal of Sound and Vibration*, vol. 282, pp. 1–35, 04 2005.

[119] M. Jannoun, Y. Aoues, E. Pagnacco, A. El Hami, and P. Pougnet, "9 - estimation of fatigue damage of a control board subjected to random vibration," in *Reliability of High-Power Mechatronic Systems 1*, A. El Hami, D. Delaux, and H. Grzeskowiak, Eds. Elsevier, 2017, pp. 187–211.

[120] W. R. Perkins, "15 - feedback control systems," in *Reference Data for Engineers (Ninth Edition)*, ninth edition ed., W. M. Middleton and M. E. Van Valkenburg, Eds. Woburn: Newnes, 2002, pp. 15–1–15–33.

[121] L. Ljung, "On the estimation of transfer functions," *IFAC Proceedings Volumes*, vol. 18, no. 5, pp. 1653–1657, 1985, 7th IFAC/IFORS Symposium on Identification and System Parameter Estimation, York, UK, 3-7 July.

[122] MATLAB, "Signal processing toolbox," Mathworks, 2022 [Online]. [Online]. Available: https://www.mathworks.com/help/pdf_doc/signal/signal.pdf

[123] F. Amini, "Effect of confining pressure on dynamic soil properties using improved transfer function estimators," *Soil Dynamics and Earthquake Engineering*, vol. 12, no. 3, pp. 145–147, 1993.

[124] G. Lindstrom, "Programming with python," *IT Professional*, vol. 7, no. 5, pp. 10–16, 2005.

[125] F. Lundh, "An introduction to tkinter," *URL: www. pythonware. com/library/tkinter/introduction/index. htm*, 1999.

[126] [Online]. Available: https://www.eecg.utoronto.ca/~vaughn/challenge/fpga_arch.html

[127] "Introduction to the quartus® ii software," Altera Corporation, Tech. Rep. [Online]. Available: https://www.intel.com/content/dam/www/programmable/us/en/pdfs/literature/manual/intro_to_quartus2.pdf

[128] I. P. Gerber, F. M. Mwaniki, and H. J. Vermeulen, "Parameter estimation of a single-phase voltage source inverter using pseudo-random impulse sequence perturbation," in *2022 IEEE International Conference on Environment and Electrical Engineering and 2022 IEEE Industrial and Commercial Power Systems Europe (EEEIC / ICPS Europe)*, 2022, pp. 1–6.

[129] S. Xu and J. Xu, "Parallel control strategy of single-phase inverter based on virtual impedance," in *2010 International Conference on Communications, Circuits and Systems (ICCCAS)*, 2010, pp. 589–592.

[130] M. Gopal, *Modern Control System Theory*. USA: Halsted Press, 1984.

[131] D. M. Banks, J. C. Bekker, and H. J. Vermeulen, "Parameter estimation of a three-section winding model using intrinsic mode functions," in *2022 IEEE International Conference on Environment and Electrical Engineering and 2022 IEEE Industrial and Commercial Power Systems Europe (EEEIC / ICPS Europe)*, 2022, pp. 1–6.

[132] T. Instruments, "High-voltage solar inverter dc-ac kit," Texas Instruments, Tech. Rep., 2013.

[133] M. Bhardwaj and B. Subharmanya, "Solar explorer kit hardware and control reference guide," Texas Instruments, Tech. Rep. 1.1, 2016.

[134] T. I. Inc., "C28x digital power library," Texas Instruments, Tech. Rep. 3.5, 2015.

[135] J. Stewart, *Calculus*, 8th ed. USA: Cengage, 2015.

[136] I. Cvetkovic, D. Boroyevich, P. Mattavelli, F. C. Lee, and D. Dong, "Unterminated small-signal behavioral model of dc–dc converters," *IEEE Transactions on Power Electronics*, vol. 28, no. 4, pp. 1870–1879, 2013.

[137] T. Instruments, *Photovoltaic Inverter with MPPT Using Solar Explorer Kit*. Natick, Massachusetts: The MathWorks Inc., 2022. [Online]. Available: https://www.mathworks.com/help/supportpkg/texasinstrumentsc2000/ug/photovoltaic-inverter-mppt-solar-explorer-kit.html#d123e13760

[138] H. Alenius, R. Luhtala, and T. Roinila, "Amplitude design of perturbation signal in frequency-domain analysis of grid-connected systems," *IFAC-PapersOnLine*, vol. 53, no. 2, pp. 13 161–13 166, 2020, 21st IFAC World Congress.

[139] H. Mouton, P. Petzer, and F. Combrink, *Isolated IGBT Half-Bridge Converter*, ver. 1, Stellenbosch, WC, SA, 1999.

Appendix A

Output Impedance Frequency Response of a Practical Half-Bridge Inverter

A.1. Overview

A half-bridge inverter is investigated in this chapter. A practical open-loop half-bridge inverter is implemented, whereafter its output impedance is determined. Non-linearities present in the output impedance are investigated.

The practical open-loop half-bridge presented in this chapter operates at output voltages lower than $30V_{p-p}$ and produces less than $2W$ of power. Investigating the output impedance of the half-bridge provides valuable information as it contains similar characteristics to less accessible more sophisticated inverters.

A single-phase half-bridge inverter consists of one switching leg containing two switches, as shown in Fig. A.1. Two identical DC-link capacitors are used to divide the DC voltage, V_d. The modulated voltage, $v_{Ao}(t)$, therefore, varies between $\frac{V_d}{2}$ and $\frac{-V_d}{2}$. An LC filter is used to filter high-frequency harmonics from $v_{Ao}(t)$ to produce a sinusoidal output voltage, $v_o(t)$.

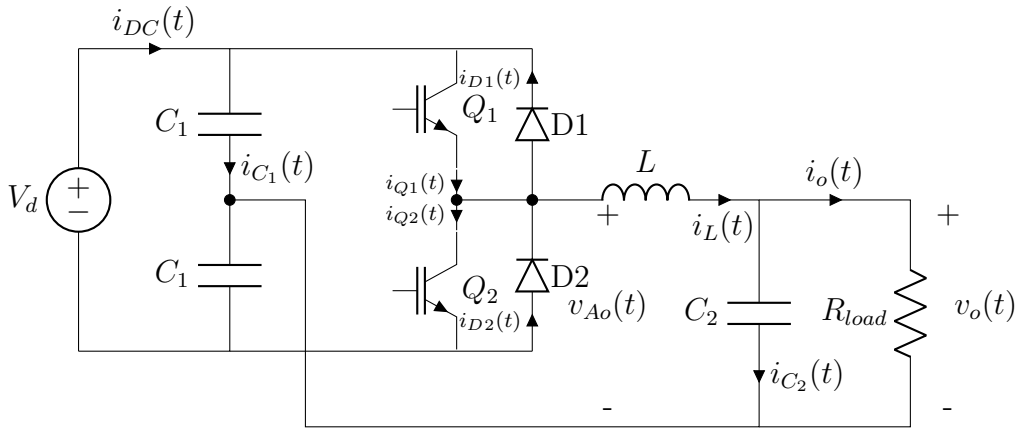

Figure A.1: Circuit configuration of a half-bridge inverter.

A.2. Practical Arrangement

A.2.1. System Overview

A practical open-loop half-bridge is constructed using an isolated IGBT half-bridge converter phase-arm [139]. An LC filter is used to filter higher order harmonics. A DC power supply with a maximum of 50 V is used as the DC source to the half-bridge inverter. A 100Ω resistor is used as load.

A.2.2. Pulse Width Modulation Generation

Sinusoidal Pulse-Width Modulation (SPWM) is implemented in the half-bridge inverter. The maximum carrier frequency, f_c, of the phase arm is 5kHz. A triangular carrier wave of 1kHz is thus used. Deadtime of $10\mu s$ is added to the PWM signal, which is 1% of the carrier period, $T_c = 1/f_c$, to protect the IGBTs from a short-circuit. The inverter operates as an open-loop system. A FPGA is used to implement the SPWM in VHDL code and provides the PWM gating signals to the phase arm.

A.2.3. LC Low-Pass Filter

A LC filter with values of approximately $L = 2mH$ and $C = 1000\mu F$ is implemented, with a cut-off frequency, f_{cut}, of

$$f_{cut} = \frac{1}{2\pi\sqrt{LC}} = 112.24Hz. \tag{A.1}$$

The transfer function, $Z_f(f)$, is the impedance of the LC filter if the modulated voltage, $v_{Ao}(t)$, is approximated as a constant voltage source and is expressed as

$$Z_f(f) = \frac{sL}{s^2LC + 1}. \tag{A.2}$$

The impedance, $Z_f(f)$, is obtained experimentally with PRIS perturbations. Fig. A.2 compares the experimental, simulated and analytical $Z_f(f)$. The analytical and simulated $Z_f(f)$ are very similar. The experimental $Z_f(f)$ has a similar shape, but is shifted slightly to higher frequencies. The difference between these results could be due to the experimental LC filter parameters being a little bit different from the parameters used in the analytical and simulated $Z_f(f)$.

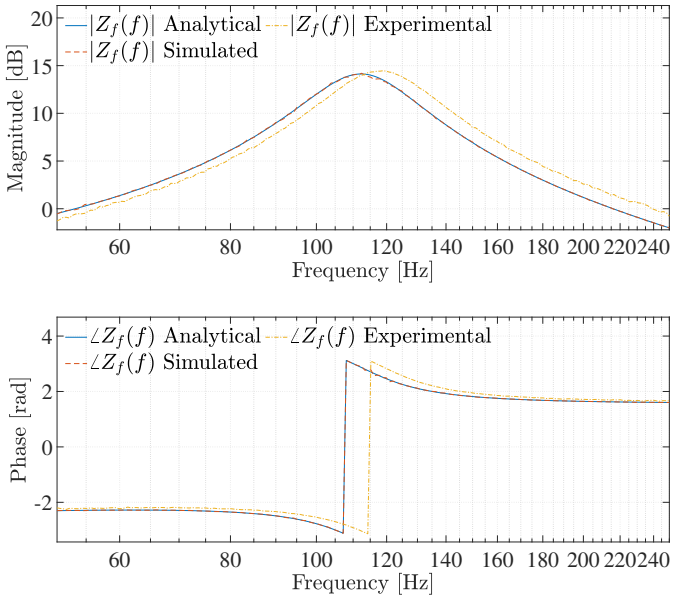

Figure A.2: Magnitude and phase response of the analytical, experimental and simulated filter impedance, $Z_f(f)$.

A.2.4. Half-Bridge Switching Circuit

A half-bridge phase arm [139] is utilized in constructing the half-bridge inverter. It is controlled by a FPGA. The phase arm consists of two 2200 μF DC-link capacitors to split the DC voltage. Two high-valued resistors are used to aid the equal division of the DC voltage. Two 1MBH60D-090A IGBTs are driven by a MC33153 IGBT driver. Fig. A.3 displays the circuit topology of the phase-arm.

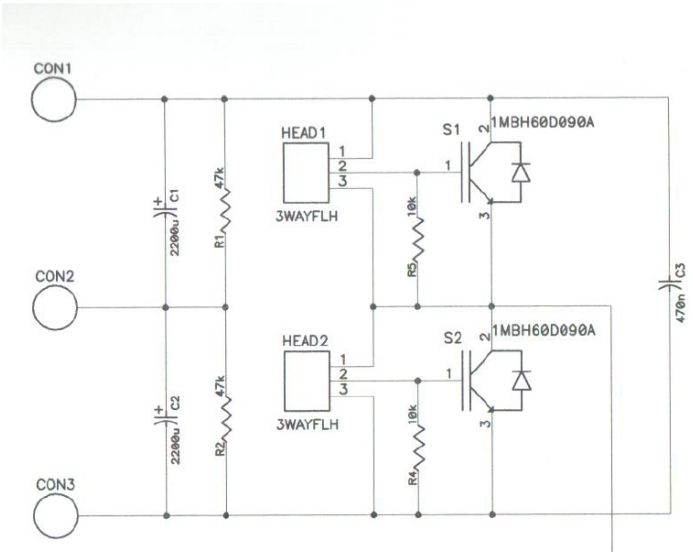

Figure A.3: Circuit topology of the half-bridge used to construct the inverter [139].

A.2.5. PRIS source

The PRIS source discussed in chapter 3 is used as perturbation source.

A.2.6. Experimental Results

The practical setup has a DC voltage of 30 V, a carrier frequency of 1kHz, a load of 100 Ω and a modulation index $m_a = 0.8$. The measured PWM signal that drives the top IGBT is displayed in Fig. A.4. The PWM signal is periodic with a period $T = 0.02s$. The measured signal contains a lot of noise.

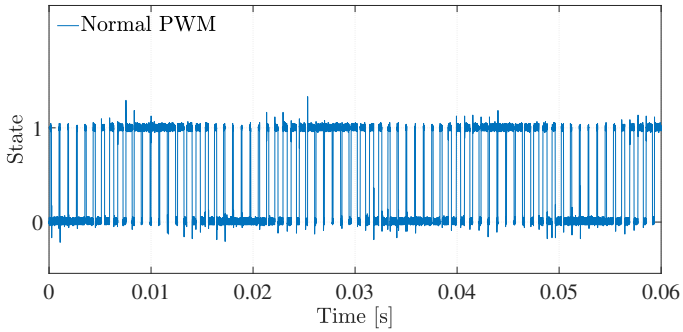

Figure A.4: Measured PWM gating signal supplied to the top switch of the phase-arm.

The measured output voltage, $v_{o,n}(t)$, and current, $i_{o,n}(t)$, for the half-bridge inverter arrangement under normal operating conditions are displayed in Fig. A.5. The expected output voltage is $V_d \times m_a/2 = 30 \times 0.8/2 = 12V$ while the measured output voltage is a bit less due to a voltage loss in the non-ideal LC filter. Both $v_{o,n}(t)$ and $i_{o,n}(t)$ are almost sinusoidal.

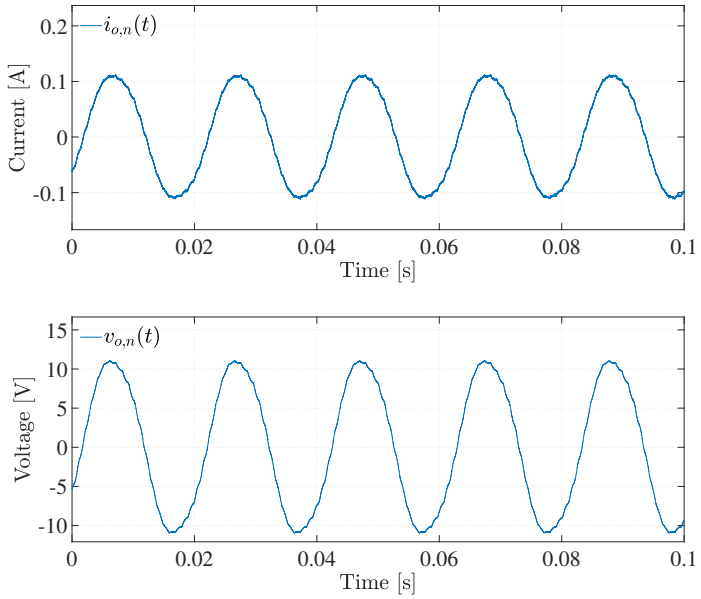

Figure A.5: Measured output current, $i_{o,n}(t)$, and voltage, $v_{o,n}(t)$, of the half-bridge inverter arrangement.

A.3. Analytical Impedance Transfer Function of the Half-Bridge Inverter Circuit

The equivalent cicruit while the top switch is conducting and the bottom switch is open, assuming no resistance in the conducting switch is shown in Fig. A.6.

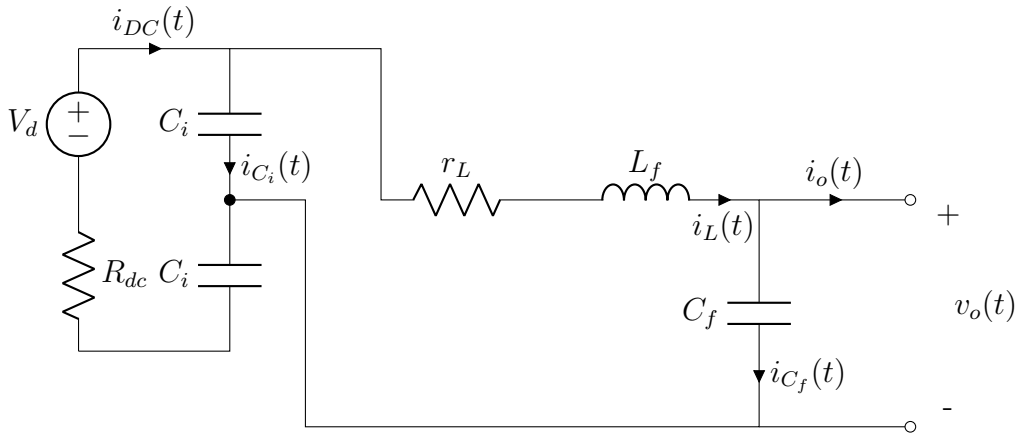

Figure A.6: Circuit configuration of a half-bridge inverter.

The output impedance of the above circuit can be calculated as

$$
\begin{aligned}
&Z_{o,analytical}(s) \\
&= \left(\frac{1}{\left(\frac{1}{R_{dc}+\frac{1}{sC_i}} + sC_i\right)^{-1} + r_L + sL_f} + sC_f\right)^{-1} \\
&= \left(\frac{1}{\frac{sR_{dc}C_i+1}{s^2R_{dc}{C_i}^2+2sC_i} + r_L + sL_f} + sC_f\right)^{-1} \\
&= \left(\frac{s^2R_{dc}{C_i}^2 + 2sC_i}{s^3R_{dc}{C_i}^2L_f + s^2R_{dc}{C_i}^2r_L + 2s^2C_iL_f + 2sC_ir_L + 1} + sC_f\right)^{-1} \\
&= \frac{s^3R_{dc}{C_i}^2L_f + s^2R_{dc}{C_i}^2r_L + 2s^2C_iL_f + 2sC_ir_L + 1}{s^4R_{dc}{C_i}^2L_fC_f + s^3R_{dc}{C_i}^2r_LC_f + 2s^3C_iL_fC_f + 2s^2C_ir_LC_f + sC_f + s^2R_{dc}{C_i}^2 + 2sC_i}.
\end{aligned}
\tag{A.3}
$$

Equation (A.3) is not the exact analytical output impedance of the average model of the inverter. It does not take the modulation index that control the switching into account. An average model would normally assume a stiff DC voltage and therefore neglect the DC-capacitors. Equation (A.3) is therefore simply the output impedance of the equivalent circuit of the setup when the top switch is closed and the bottom switch is open. When the bottom switch is closed and the top switch open, the output impedance of the equivalent circuit will also be described by (A.3). The magnitude and phase responses of the impedance, $Z_{o,analytical}(s)$, is shown in Fig. A.7. A series and a parallel resonant point exist, with lower and higher frequencies exhibiting capacitive characteristics.

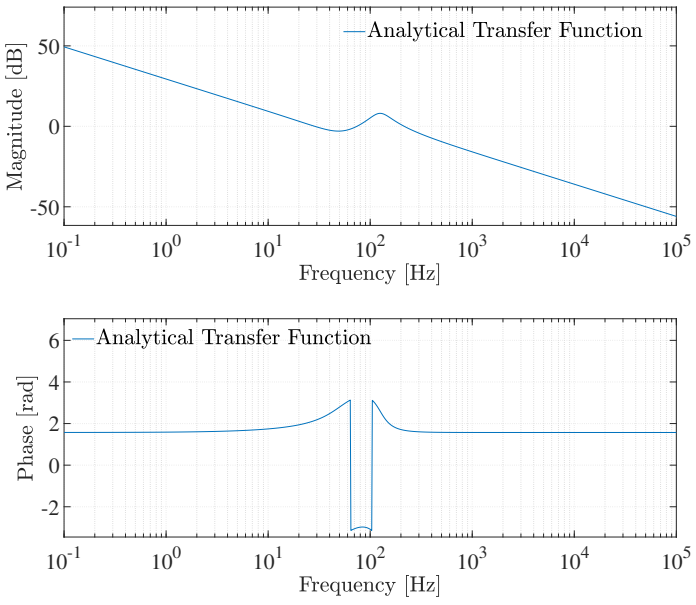

Figure A.7: The magnitude and phase response of the analytical transfer function, $Z_{o,analytical}(s)$.

A.4. Output Impedance Frequency Response of a Practical Half-Bridge Inverter

A.4.1. Output Perturbation of the Half-Bridge Inverter

The half-bridge inverter is experimentally perturbed with a PRIS source in parallel with the load. The PRIS source is constructed using a PRBS10, a clock frequency, $f_{clk} = 500Hz$ and a RLC filter of $1k\Omega$, $47\mu H$ and $4\mu F$ respectively. These RLC values allow for suitable time-constants. A sampling frequency of $f_s = 1MHz$ is used to record the voltage and current signals for 30 seconds.

Perturbation is applied to the output of the half-bridge inverter, in parallel with the load. Fig. A.8 presents the measured current and voltage waveforms of the normal and perturbed arrangement. The current perturbation can clearly be seen superimposed on the perturbed output current, $i_{o,p}(t)$. The perturbed voltage waveform, $v_{o,p}(t)$, does not exhibit clear perturbations.

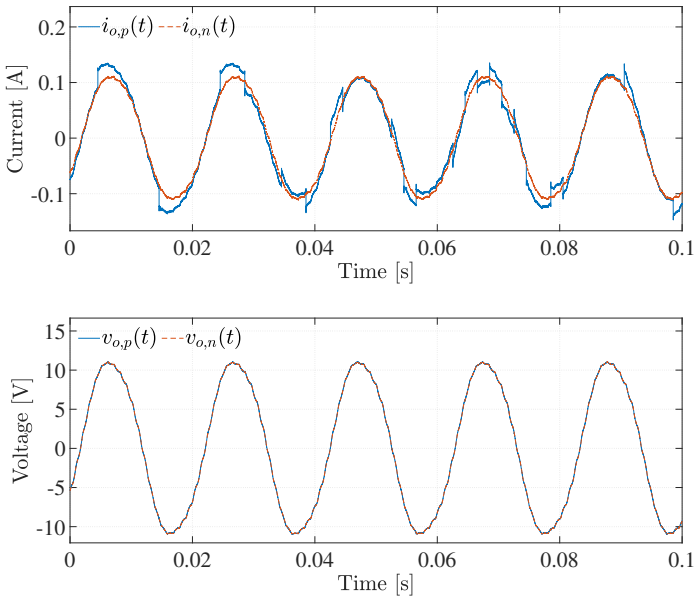

Figure A.8: The experimental output current and voltage under normal operating conditions, $i_{o,n}(t)$ and $v_{o,n}(t)$, as well as during perturbation, $i_{o,p}(t)$ and $v_{o,p}(t)$.

A.4.2. Calculating the Output Impedance of the Half-Bridge Inverter

The two measurement approached as discussed in chapter 4 is utilized to determine the output impedance of the half-bridge inverter. The two measurement approach cancels out $V_{TH}(f)$ of the inverter. To do this with experimental measurements of an open-loop half-bridge inverter, the reference signal of the inverter needs to be aligned for the normal

and perturbed measurements. As the PWM controlled switches are the actuator of the reference signal in the open-loop inverter, the two measurements need to be aligned by aligning the PWM gating signals. The PWM signals measured under normal and perturbed conditions are aligned in Fig. A.9. Although the measured PWM signals contain random noise, the signals are able to be aligned.

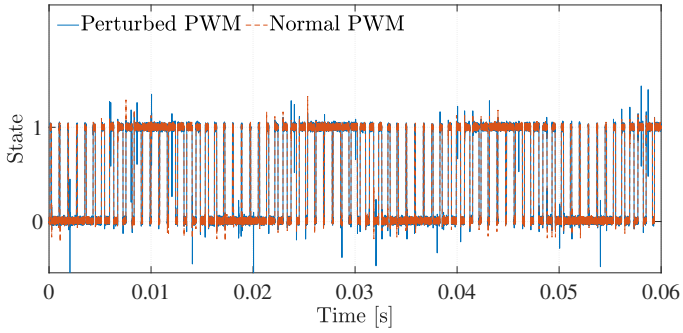

Figure A.9: The aligned PWM signals measured under normal and perturbed operating conditions.

After the output signals are aligned accordingly, the small-signal PRIS perturbations can be witnessed by subtracting the normal and perturbed measurements, as shown in Fig. A.10. The small-signal current perturbations have impulse waveforms, while the small-signal voltage perturbations exhibit more noise.

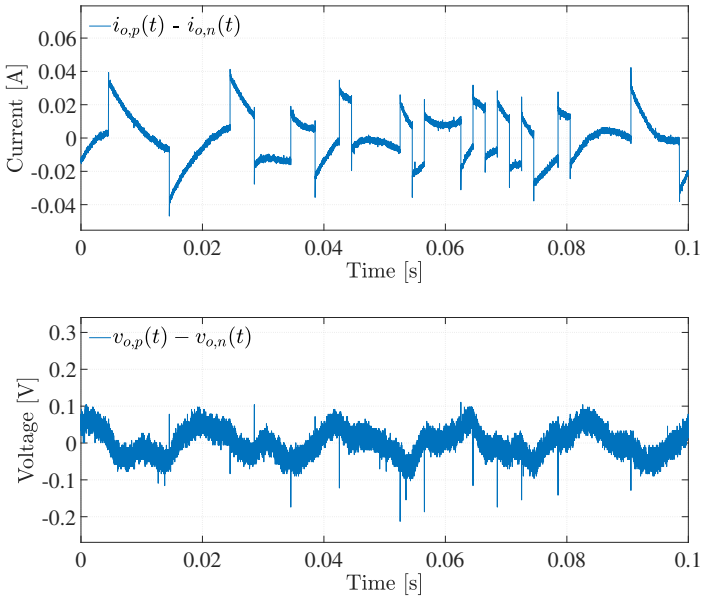

Figure A.10: The small-signal PRIS perturbations observed on the inverter output current, $i_{o,p}(t)$ - $i_{o,n}(t)$, and voltage, $v_{o,p}(t)$ - $v_{o,n}(t)$.

Fig. A.11 shows the output impedance frequency response obtained experimentally for the half-bridge inverter using the two-measurement approach, compared to the analytical

transfer function as discussed in subsection A.3. These two frequency responses have the same amount of resonant points. The parallel resonant point is due to the the LC filter, while the series resonant is due to the inductor of the LC filter and the DC link capacitors.

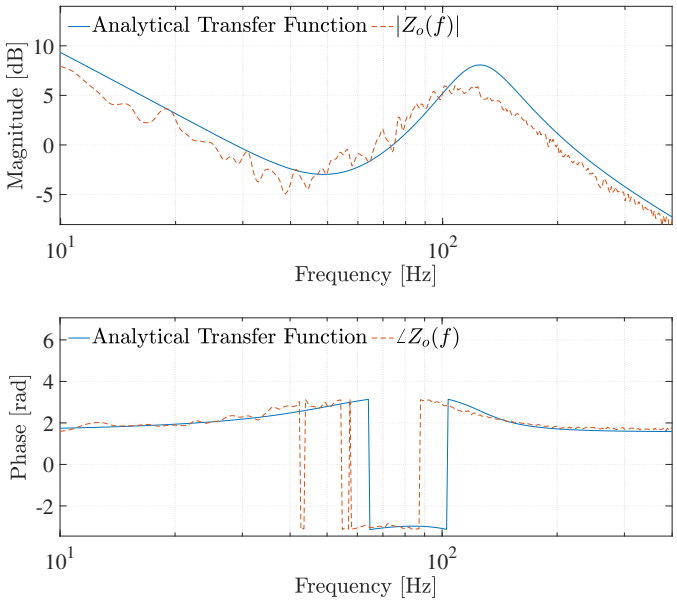

Figure A.11: The output impedance, $Z_o(f)$, of the experimental half-bridge inverter compared to the analytical transfer function of the impedance while one switch is closed and the other open.

A.5. Effects on the Experimental Output Impedance

A dedicated half-bridge inverter was constructed for this investigation, allowing complete control of its operation. Various influences on the output impedance can therefore be investigated. Different aspects of the experimental arrangement is varied to witness the effect of these changes on the output impedance of the inverter.

A.5.1. Effect of the Deadtime

The deadtime implemented to protect the switches from short-circuiting is varied to see the effect on the output impedance in Fig. A.12. The deadtime applied is varied between $10\mu s$, $20\mu s$ and 30 μs. From the results in Fig. A.12 it is shown that the deadtime does not influence the location or damping of resonant frequency points of the output impedance frequency response.

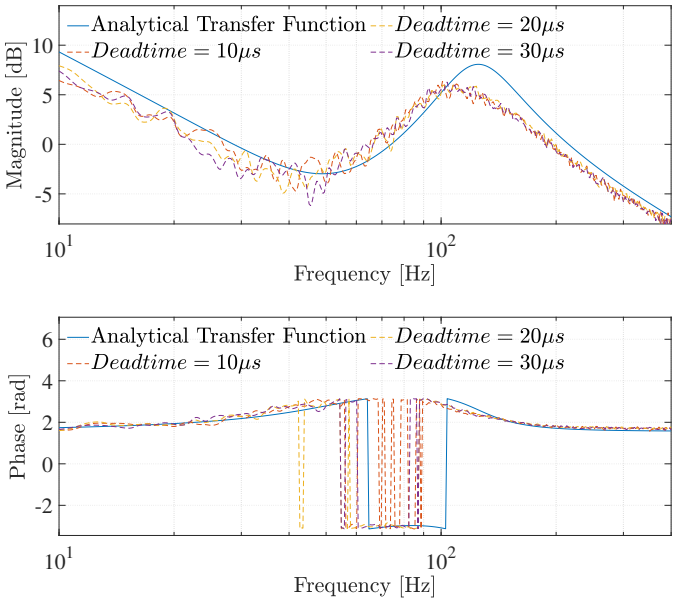

Figure A.12: Magnitude and phase response of the output impedance, $Z_o(f)$, whilst varying the deadtime of the half-bridge inverter.

A.5.2. Effect of the Carrier Frequency

The frequency of the carrier signal, f_c, is varied in Fig. A.13. Varying the carrier frequency influence the magnitude of the second resonant point. When $f_c = 1kHz$, the second resonant is more damped than at the other carrier frequencies.

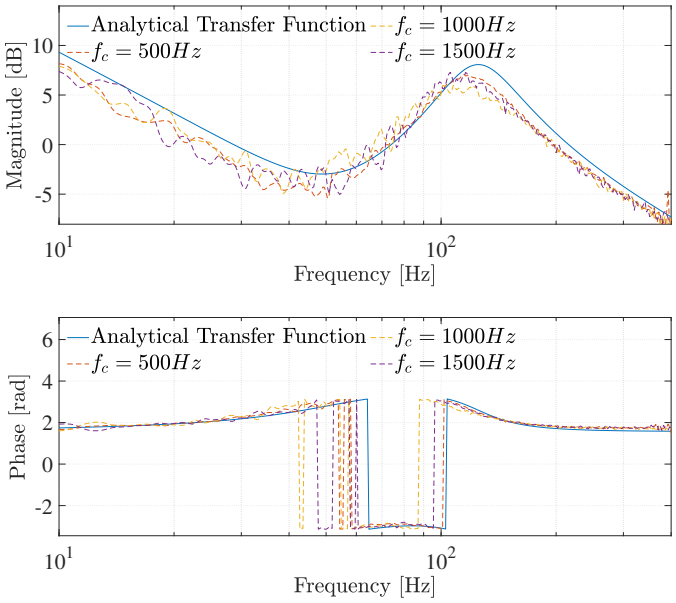

Figure A.13: Magnitude and phase response of the output impedance, $Z_o(f)$, whilst varying the switching frequency of the half-bridge inverter.

A.5.3. Effect of the Modulation Index

The modulation index, m_a, is varied experimentally in Fig. A.14. Varying the modulation index have some effect on the damping of the resonant points of the output impedance of the half-bridge inverter.

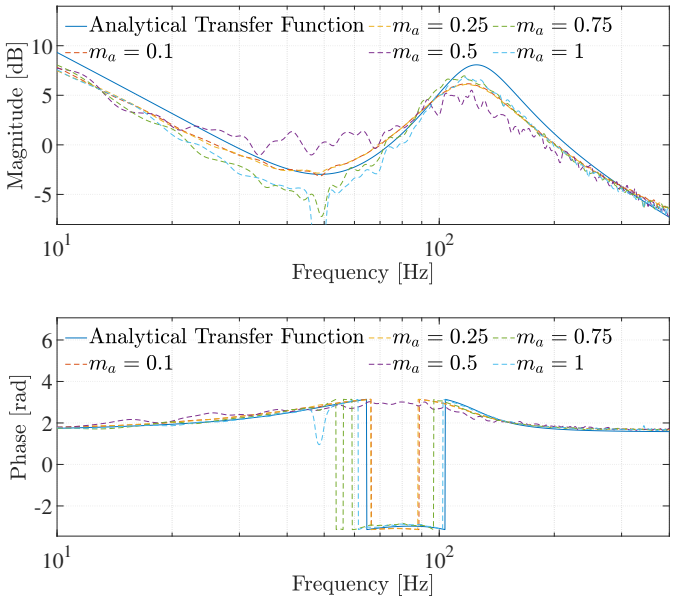

Figure A.14: Magnitude and phase response of the output impedance, $Z_o(f)$, whilst varying the modulation index of the half-bridge inverter.

A.5.4. Effect of the DC Voltage Magnitude

The DC voltage magnitude, V_d, is varied experimentally to witness the effect on the output impedance of the open-loop half-bridge inverter in Fig. A.15. The DC voltage effects the output impedance frequency response, especially in the region between the two resonant frequencies.

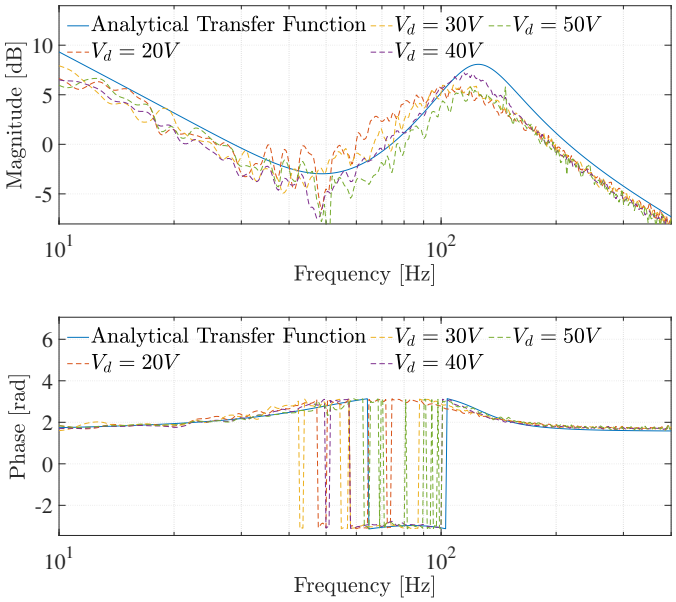

Figure A.15: Magnitude and phase response of the output impedance, $Z_o(f)$, whilst varying the DC voltage of the half-bridge inverter.

Appendix B

Graphical User Interface

A Graphical User Interface (GUI) is developed to obtain user inputs to the PRBS generator. A screenshot of this GUI is presented in Fig. B.1.

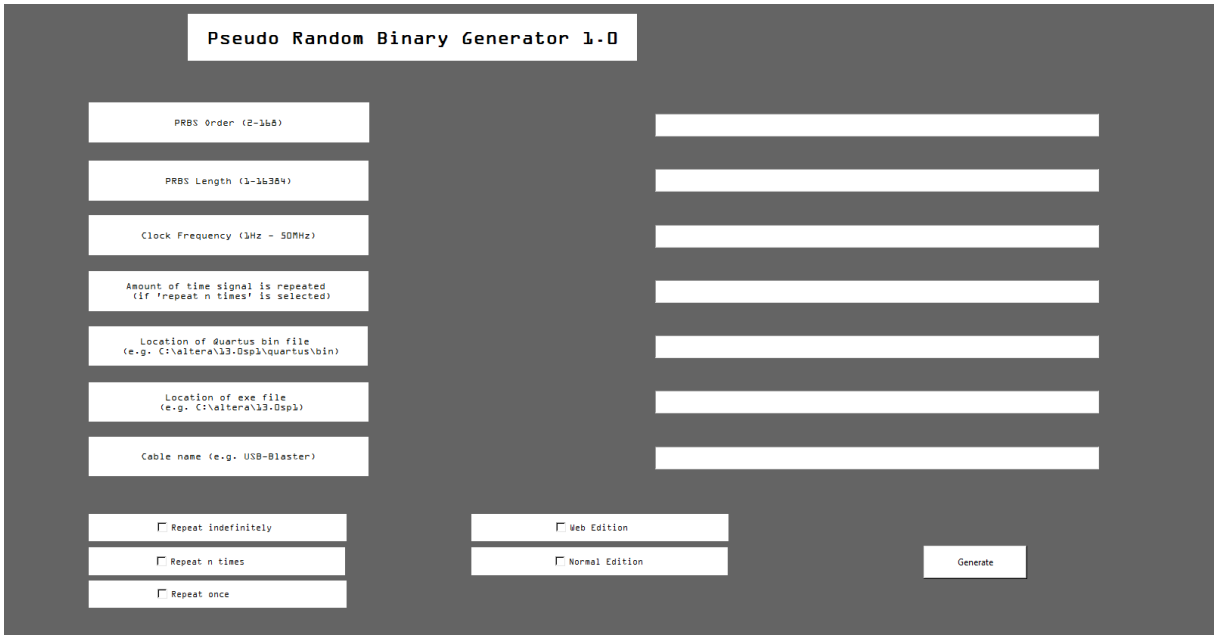

Figure B.1: A screenshot of the GUI interface.

Appendix C

Programming of the PRBS

TCL commands are used by running a batch file from Python. The TCL commands synthesize and build the VHDL code on the FPGA. All command line commands starting with *"quartus_"* are TCL commands inherit to the Quartus software. The contents of the batch file are as follows:

```
cd C:\altera\13.0sp1
PATH=%PATH%;C:\altera\13.0sp1\quartus\bin
quartus_map prbsgen
quartus_fit prbsgen
quartus_asm prbsgen
quartus_sh --flow compile prbsgen
quartus_pgm -c USB-Blaster -a
cd C:\altera\13.0sp1\output_files
quartus_cpf -c prbsgen.sof prbsgen.jic -d EPCS64 -s EP4CE22
quartus_pgm -m JTAG -o ip;prbsgen.jic@1
rem pause
```

VHDL coding is used to control the FPGA and output a PRBS sequence. The code below is uploaded to the FPGA:

```
library IEEE;
use IEEE.STD_LOGIC_1164.ALL;
use IEEE.STD_LOGIC_UNSIGNED.ALL;

entity prbsgen is
    Port (      CLK : in  STD_LOGIC;
                button : in  STD_LOGIC; -- Starting Button
                PRBS    : out  STD_LOGIC; -- Must be rooted to GPIO later, this is my PRBS
                D1_SO1    : in  STD_LOGIC; -- Driver 1, Fault 1
                D1_SO2    : in  STD_LOGIC; -- Driver 1, Fault 2
                D2_SO1    : in  STD_LOGIC; -- Driver 2, Fault 1
                D2_SO2    : in  STD_LOGIC; -- Driver 2, Fault 2
                LED8    : out  STD_LOGIC; -- NOT PRBS
                LED7    : out  STD_LOGIC; -- D2_SO2
                LED6    : out  STD_LOGIC; -- D2_SO1
                LED5    : out  STD_LOGIC; -- D1_SO2
                LED4    : out  STD_LOGIC; -- D1_SO1
                LED3    : out  STD_LOGIC; -- Enable line
                LED2    : out  STD_LOGIC; -- Gating signal
                LED1    : out  STD_LOGIC; -- Output of PRBS
                GATE_Start_Stop    : out  STD_LOGIC; -- Gating signal
                NOT_PRBS    : out  STD_LOGIC; -- NOT prbs
                ENABLE    : out  STD_LOGIC; -- Enable line
                D1_SO1_STATE    : out  STD_LOGIC;
                D1_SO2_STATE    : out  STD_LOGIC;
                D2_SO1_STATE    : out  STD_LOGIC;
                D2_SO2_STATE    : out  STD_LOGIC;
                D1_EN : out  STD_LOGIC; --1
                D2_EN : out  STD_LOGIC; --2
                D1_PRBS : out  STD_LOGIC; --3
                D2_PRBS : out  STD_LOGIC; --4
                GPIO1 : out  STD_LOGIC; --1.1
                GPIO2 : out  STD_LOGIC; --1.2
                GPIO3 : out  STD_LOGIC;--1.3
                GPIO4 : out  STD_LOGIC;--1.4
                GPIO5 : out  STD_LOGIC);--1.5

end prbsgen;
```

```
architecture Behavioral of prbsgen is
        constant N : integer := 254; --Change this line for length
        signal input : STD_LOGIC_VECTOR(0 to N) := "111111110000";
        signal count: integer range 0 to 50000000 := 0; --Change this line? Not entirely necessary
        signal max_counter : integer := 500000; --Change this line with max counter
        signal ctr: integer range 0 to N := 0;
        signal repeat : STD_LOGIC := '0'; --Change this line for repeat, 0 for repeat inf, 1 for
            repeat x times
        signal repeat_true : STD_LOGIC := '0'; --Change this line for repeat, 0 for repeat inf, 1 for
            repeat x times --18
        signal repeat_ctr : integer range 0 to 2 := 0; --Change this for amount of repeats
        constant repeat_target : integer  := 1;
        signal loop_ctr : integer := 9999;
        signal output_temp : STD_LOGIC;
        signal gate : integer := 1;
        signal start : STD_LOGIC := '0';
        signal first_start : STD_LOGIC := '0';

        begin
    process (button, CLK)

    begin

                GPIO1 <= '0';
                GPIO2 <= '0';
                GPIO3 <= '0';
                GPIO4 <= '0';
                GPIO5 <= '0';

                if (CLK'event and CLK = '1') then
                                        if (button = '0') then
                                                start <= '1';
                                                PRBS <= '0';
                                                D1_PRBS <= '0'; --1
                                                LED1 <= '0';
                                                LED8 <= '0';
                                                NOT_PRBS  <= '0';
                                                D2_PRBS <= '0'; --2
                                                LED3 <= '0';
                                                ENABLE <= '0';
                                                D1_EN <= '0'; --3
                                                D2_EN <= '0'; --4
                                                repeat_ctr <= 0;
                                                ctr <= 0;
                                                gate <= 1;
                                        end if;
                                        if (count = max_counter and start = '1' and (button = '1'))
                                             then
                                                if (repeat = '0') then
                                                        count <= 0;
                                                        gate <= 0;
                                                        PRBS <= input(ctr);
                                                        D1_PRBS <= not(input(ctr)); --8 --I switched
                                                             this
                                                        LED3 <= '1';
                                                        ENABLE <= '1';
                                                        D1_EN <= '1'; --6
                                                        D2_EN <= '1'; --7
                                                        LED1 <= input(ctr);
                                                        LED8 <= not(input(ctr));
                                                        NOT_PRBS  <= not(input(ctr));
                                                        D2_PRBS <= input(ctr); --5 --I switched this
                                                        ctr <= ctr + 1;
                                                        if (ctr = 0) then
                                                                LED2 <= '1';
                                                                GATE_Start_Stop <= '1';
                                                        else
                                                                LED2 <= '0';
                                                                GATE_Start_Stop <= '0';

                                                                END IF;
                                                                if ctr = N then
                                                                        ctr <= 0;


                                                                if (repeat_true = '1') then
                                                                        repeat_ctr <=
                                                                             repeat_ctr + 1;
                                                                        if (repeat_ctr >=
```

```
                                                                repeat_target)
                                                                then
                                                                    repeat <= '1';
                                                            end if;
                                                        end if;
                                                    end if;
                                                else
                                                        PRBS <= '0';
                                                        D1_PRBS <= '0'; --9
                                                        LED1 <= '0';
                                                        LED8 <= '0';
                                                        NOT_PRBS <= '0';
                                                        D2_PRBS <= '0'; --10
                                                        LED3 <= '0';
                                                        ENABLE <= '0';
                                                        D1_EN  <= '0'; --11
                                                        D2_EN  <= '0'; --12
                                                        start <= '0';
                                                        repeat_ctr <= 0;
                                                        repeat <= '0';
                                                        ctr <= 0;
                                                end if;
                                            else
                                                    count <= count + 1;
                                            end if;
                    end if;
                --end if;
            end process;
    -- Root led's to faults states
    LED4 <= NOT(D1_SO1);
    LED5 <= NOT(D1_SO2);
    LED6 <= NOT(D2_SO1);
    LED7 <= NOT(D2_SO2);

    -- Root GPIO pins to faults states
    D1_SO1_state <= NOT(D1_SO1);
    D1_SO2_STATE <= NOT(D1_SO2);
    D2_SO1_STATE <= NOT(D2_SO1);
    D2_SO2_STATE <= NOT(D2_SO2);

    end Behavioral;
```

Appendix D

Practical Equipment

The PRIS source that is designed and built to use for experimental perturbations during this project is displayed in Fig. D.1.

Figure D.1: The practical pseudo-random impulse sequence source.

Appendix E

Sensitivity Analysis

E.1. Time-Domain Sensitivity Analysis

Similar to the frequency-domain sensitivity analysis in chapter 4, the influence of the parameters on the simulated time-domain output voltage, $v_o(t)$, is investigated by varying each parameter between its true value and values 10 times higher and lower than its true value. The effect of varying parameters in the time-domain is less significant compared to the effect in the frequency-domain. Parameters k_{P_i} and k_{pv} influence the amplitudes of $v_o(t)$ significantly. The parameter k_{iv} has a small effect on the amplitude and phase of $v_o(t)$, while the filter parameters, L_f and C_f only influences the ripple in $v_o(t)$.

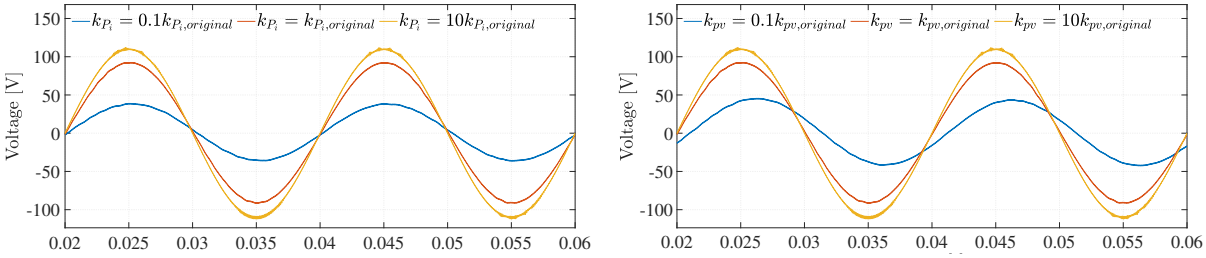

(a) (b)

Figure E.1: (a) The output voltage $v_o(t)$ as a function of k_{P_i}. (b) The output voltage $v_o(t)$ as a function of k_{pv}.

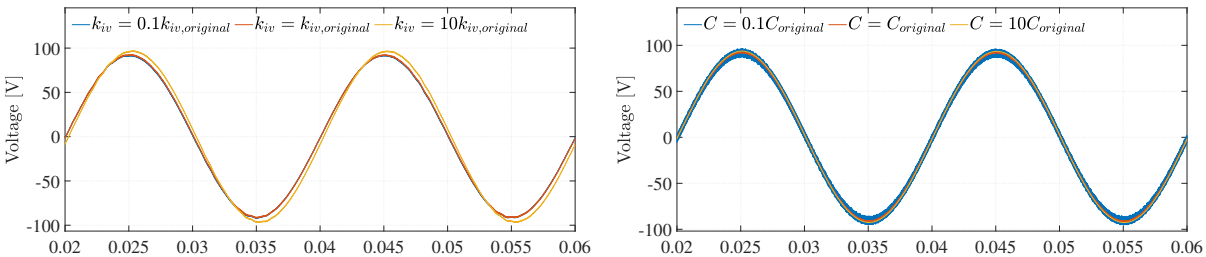

(a) (b)

Figure E.2: (a) The output voltage $v_o(t)$ as a function of k_{iv}. (b) The output voltage $v_o(t)$ as a function of C_f.

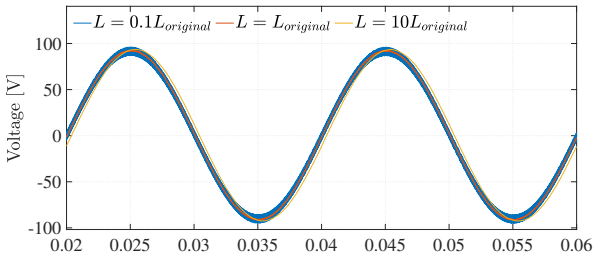

Figure E.3: The output voltage $v_o(t)$ as a function of L_f.

Compared to the frequency-domain sensitivity analysis, the effect of varying parameters does not have a significant effect in the time-domain. The frequency-domain information is therefore a more appropriate option to use during the parameter estimation process.

Appendix F

Arrangement of Practical Inverter System

The practical arrangement used in chapter 5 is shown in Fig. F.1. It consists of a DC voltage source supplying an inverter. The inverter controls the current through a resistive load. A PRIS perturbation source is used.

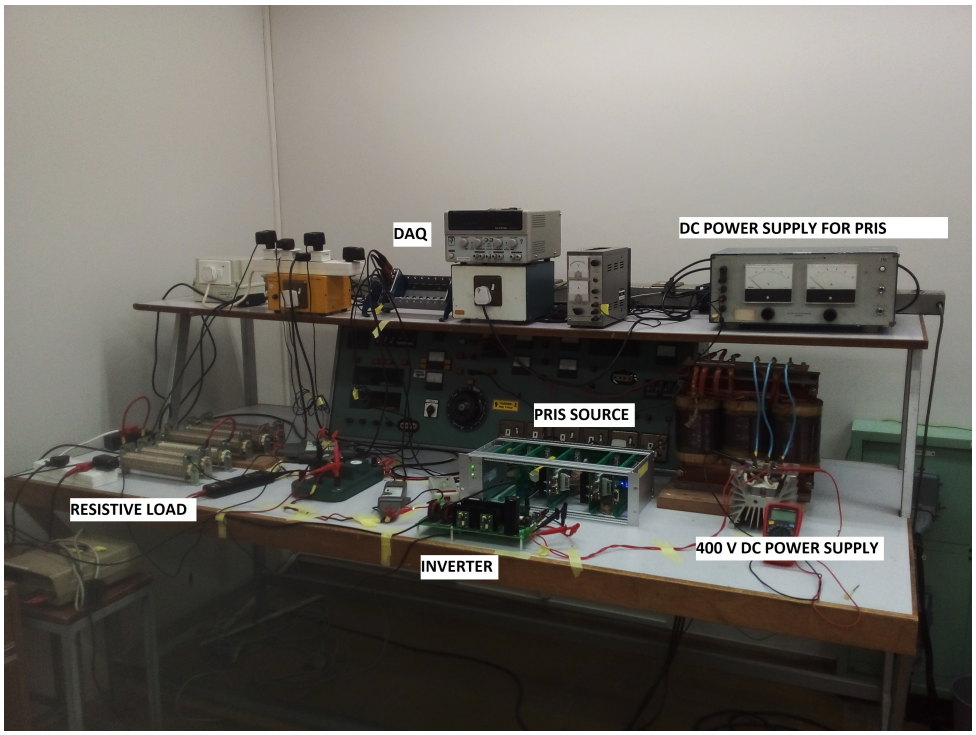

Figure F.1: The experimental arrangement.

Appendix G

Half-bridge Inverter Practical Arrangement

The half-bridge phase arm in Fig. G is utilized in appendix A [139]. It is controlled by a FPGA.